

# **Covalent immobilisation of proteins for biomaterial and biosensing applications**

Submitted for examination on 10<sup>th</sup> of December 2007 for a Doctor of Philosophy Degree at Flinders University, Faculty of Science and Engineering, School of Chemistry, Physics and Earth Sciences by **Mr Endre Jozsef Szili**.

Supervisors:

Associate Professor Nicolas H. Voelcker (Flinders University)

Associate Professor Sunil Kumar (University of South Australia)

Professor Roger St. C. Smart (University of South Australia)

Doctor Mark DeNichilo (TGR Biosciences)

# Contents

<b>Declarations</b>	I
<b>Acknowledgements</b>	II
<b>Abbreviations</b>	III
<b>Abstract</b>	1
<b>Part 1: Covalent immobilisation of IGF-1 on PECVD-Si-Ti for orthopaedic biomaterial applications</b>	
<b>1.1 Introduction</b>	
1.1.1 Overview of biomaterials	3
1.1.2 Titanium biomaterials	4
1.1.3 Osseointegration	7
1.1.4 Introduction to titanium biomaterials research	11
1.1.5 Influence of surface topography on osseointegration	11
1.1.6 Influence of surface chemistry on osseointegration	14
1.1.7 Hydroxyapatite implant coatings	16
1.1.8 Bioactive glass implant coatings	17
1.1.9 Plasma enhanced chemical vapour deposition of bioactive glass	18
1.1.10 Biological bioactive factors	22
1.1.11 Protein surface immobilisation techniques	23
1.1.12 Silane chemistry for protein surface immobilisation	26

1.1.13	Part one objectives	28
<b>1.2</b>	<b>Materials and Methods</b>	
1.2.1	Substrate preparation	30
1.2.2	Buffer preparation	31
1.2.3	Plasma enhanced chemical vapour deposition (PECVD) of silica on titanium	32
1.2.4	Characterisation of hydroxyl group surface coverage on PECVD-Si-Ti	35
1.2.5	Grafting of alkoxy silane molecules on PECVD-Si-Ti	36
1.2.6	Development of surface modification techniques on PECVD-Si-Ti for the attachment of insulin-like growth factor-1 (IGF-1)	38
1.2.7	Immunological activity of immobilised IGF-1 on PECVD-Si-Ti	39
1.2.8	Assessment of IGF-1 biological activity on PECVD-Si-Ti	41
1.2.9	X-ray photoelectron spectroscopy	45
1.2.10	Infrared spectroscopy	46
1.2.11	Atomic force microscopy	46
1.2.12	Scanning electron microscopy	46
1.2.13	Statistical analyses	47
<b>1.3</b>	<b>Results and Discussion</b>	
1.3.1	Characterisation of silica films deposited on titanium by plasma enhanced chemical vapour deposition (PECVD)	48
1.3.2	Assessment of alkoxy silane grafting methods on PECVD-Si-Ti	69
1.3.3	Development of surface modification techniques for the covalent attachment of insulin-like growth factor-1 (IGF-1) on PECVD-Si-Ti	90
1.3.4	Analysis of the immunological activity of adsorbed and covalently attached insulin-like growth factor-1 (IGF-1) on PECVD-Si-Ti	105

1.3.5	Analysis of osteoblast-like cell growth on PECVD-Si-Ti and IGF-1 functionalised PECVD-Si-Ti surfaces	112
1.3.6	Analysis of cell attachment and early cell proliferation on IGF-1 functionalised PECVD-Si-Ti	139
<b>1.4</b>	<b>Conclusion and Future Directions</b>	<b>161</b>

## **Part 2: Covalent immobilisation of anti-human IgG on porous silicon for the detection of human IgG by reflective interferometry**

<b>2.1</b>	<b>Introduction</b>	
2.1.1	Overview of porous silicon applications	163
2.1.2	Porous silicon formation	163
2.1.3	Porous silicon pore geometries	166
2.1.4	Biosensors made from porous silicon	168
2.1.5	Functionalisation of porous silicon biosensors	168
2.1.6	Patterning of biosensor platforms with biomolecules	169
2.1.7	Readout signal of porous silicon biosensors	171
2.1.8	Porous silicon optical interferometry	172
2.1.9	Interferometric porous silicon biosensors	173
2.1.10	Advantages of interferometric porous silicon biosensors	175
2.1.11	Part two objectives	176
<b>2.2</b>	<b>Materials and Methods</b>	
2.2.1	Porous silicon formation	177
2.2.2	Porous silicon oxidation	179
2.2.3	Optical interferometric reflectance spectroscopy	180
2.2.4	Mechanism of enzyme-catalysed porous silicon degradation	181
2.2.5	Immobilisation of anti-human IgG on porous silicon	181

2.2.6	Biosensing of human IgG	182
2.2.7	Infrared spectroscopy	182
2.2.8	X-ray photoelectron spectroscopy	183
2.2.9	Atomic force microscopy	183
2.2.10	Scanning electron microscopy	183
<b>2.3</b>	<b>Results and Discussion</b>	
2.3.1	Characterisation of porous silicon morphology and surface chemistry	184
2.3.2	Enzyme-catalysed porous silicon degradation	193
2.3.3	Establishment of an enzyme-based interferometric biosensor for the detection of immunoglobulin G (IgG) on a functionalised porous silicon platform	200
2.3.4	Assessing the performance of the enzyme-based interferometric biosensor on functionalised porous silicon	213
<b>2.4</b>	<b>Conclusions and Future Directions</b>	223
	<b>Overall Conclusions</b>	225

## References

Part 1: Covalent immobilisation of IGF-1 on PECVD-Si-Ti for orthopaedic biomaterial applications	i
Part 2: Covalent immobilisation of anti-human IgG on porous silicon for the detection of human IgG by reflective interferometry	xxiv

# Declarations

‘I certify that this thesis does not incorporate without acknowledgment any material previously submitted for a degree or diploma in any university; and that to the best of my knowledge and belief it does not contain any material previously published or written by another person except where due reference is made in the text.’

Endre J. Szili

Date

‘I believe that this thesis is properly presented, conforms to the specifications for the thesis and is of sufficient standard to be, *prima facie*, worthy of examination.’

Associate Professor Nicolas H. Voelcker

Date

# Acknowledgements

First, I would like to thank my PhD principle supervisor, Associate Professor Nicolas Voelcker. Under his guidance, I have acquired a lot of knowledge in biomaterials science and developed a host of new skills. Also, I am grateful to my co-supervisors, Associate Professor Sunil Kumar, Professor Roger Smart and Dr. Mark DeNichilo for their supervision and professional discussions during my PhD degree.

I also thank Dr. Robert Jones and Dr. Andrew Lewis for teaching me the operation of the XPS instruments. I am thankful to Miss Suet Peng Low and Miss Rachel Lowe for kindly taking SEM images of my samples. In addition, I am grateful for their expert discussions and the expertise of Dr. Sean Graney who taught me new skills and knowledge in chemistry during my PhD.

The support of the technical staff at Flinders University has to be credited. This includes Mr Mike Mellow, Mr Chris Price, Mr Greg Hewitt, Mr Tony Nugent, Mr Bruce Gilbert, Mr Brenton Perkins, Mr Bob Northeast, Mr John Pesor, Mr Bob de Vries, Mr Bill Drury and Mr Mark Ellis. Also, I would like to thank the assistance of the former and current supervisors of the chemical store at Flinders University, Mr Kevin Solly and Ms Tricia Butterfield.

During my PhD, I have enjoyed the company and interesting conversations with many people at Flinders University especially Sean, Rachel, Mike, Trish, Gordy, Sasha, Kevin, Chris and the rest of the guys from the workshops, which has helped fill in time between experiments.

Finally, I would like to thank the love and support of my family and friends and especially Sue for all her love, support and patience.

# Abbreviations List

A	ampere
ABTES	triethoxysilyl butyraldehyde
APTES	3-aminopropyl triethoxysilane
AFM	atomic force microscopy
anti-IGF-1	biotinylated anti-human IGF-1 antibody
ASD	anodic spark deposition
ASTM	American Society for Testing and Materials
at.%	atomic percentage
Avg	average
$A\lambda$	absorbance at a given wavelength
Bal	balance of the elemental composition (wt.%) of the metal alloy
BSA	bovine serum albumin
BSP	bone sialoprotein or BioSpark™
C	coulomb
CCD	charge-coupled device
CDS	cell dissociation solution
cm	centimetre
CPS	counts per second
C3b	complement-activated fragment
DCM	dichloromethane
DMEM	Dulbecco's modified Eagle's medium
DMSO	dimethyl sulfoxide
DNA	deoxyribonucleic acid
Dr	Doctor
ECM	extracellular matrix
EGFs	epidermal growth factors
ELISA	enzyme-linked immunosorbent assay
EOT	effective optical thickness

ERK	extracellular-signal-regulated kinase
etc	et cetera
EtOH	ethanol
eV	electronvolt
F-actin	filamentous actin
FBS	foetal bovine serum
FEAM	2,2,2-trifluoroethylamine
FFT	Fast Fourier Transform
FGFs	fibroblast growth factors
FPTMS	3,3,3-trifluoropropyl trimethoxysilane
FT-IR	Fourier transform-IR
FWHM	full-width-half-maximum
GDP	guanosine diphosphate
GPTMS	3-glycidoxypropyl trimethoxysilane
GTP	guanosine triphosphate
h	hour
HA	hydroxyapatite
HBSS	Hank's balanced salt solution
HF	hydrofluoric acid
HOB	human osteoblast-like
HQ	hydroquinone
HRP	horseradish peroxidase
HRP-Strep	peroxidase conjugated streptavidin
h $\nu$	Planck's constant (h) times by the frequency of the exciting radiation ( $\nu$ )
ICP-AES	inductively coupled plasma atomic emission spectrometry
IgA	immunoglobulin A
IgG	immunoglobulin G
IgM	immunoglobulin M
IGF-1	insulin-like growth factor-1
IGFs	insulin-like growth factors

IR	infrared
IPTES	3-isocyanatopropyl triethoxysilane
kV	kilovolt
LBNL	Lawrence Berkeley National Laboratory
M	molar
mA	milliamps
MAPK	mitogen activated protein kinase
MAPKK	MAPK kinase
MAPKKK	MAPK kinase kinase
MEM	minimal essential medium
mer	nucleotide
MFC	Mass flow controller
MG63	immortalised cell line of fibroblast morphology with adherent growth properties derived from an osteosarcoma of human bone
MHz	megahertz
min	minute
ml	millilitre
mM	millimolar
MPa	megapascal
$m\lambda$	spectral order of the Fabry-Pérot fringe ( $m$ ) times wavelength of the incident light striking the surface at an incident angle of $0^\circ$ ( $\lambda$ )
ng	nanogram
NHS	<i>N</i> -hydroxysuccinimide
nL	average refractive index of a porous silicon layer ( $n$ ) times porous silicon layer thickness ( $L$ )
nm	nanometre
n-type	phosphorous or arsenic doped
OIRS	optical interferometric reflectance spectroscopy
OPD	<i>o</i> -phenylenediamine dihydrochloride
OPG	osteoprotegerin

OX	oxidised
PBS	phosphate buffered saline
PBS-T	PBS-Tween <sup>®</sup> 20
PDEPMA	poly(3,3'-diethoxypropyl methacrylate)
PDGFs	platelet-derived growth factors
PECVD	plasma enhanced chemical vapour deposition
PECVD-Si	silica film deposited on a material by the technique of PECVD
PECVD-Si-Ti	titanium coated with a film of PECVD-Si
p-ERK	phosphorylated ERK
PGE <sub>2</sub>	prostaglandin E <sub>2</sub>
pH	potential of hydrogen
Pty Ltd	proprietary limited
p-type	boron doped
RANK	nuclear factor $\kappa$ -B
RCF	relative centrifugal force
Red	reduced
RGD	Arginine-Glycine-Aspartic acid
RMS	root mean square
SAGA	smart apertured grazing angle
sccm	standard cubic cm per min
scfh	standard cubic feet per h
SEM	scanning electron microscopy
SMP	<i>N</i> -succinimidyl-3-maleimidopropionate
Strep.-HRP	streptavidin conjugated HRP
TCPS	tissue culture polystyrene
TEOS	tetraethoxysilane
TFAA	trifluoroacetic anhydride
TGF- $\beta_1$	transforming growth factor $\beta_1$
TGFs	transforming growth factors
TM	trademark
TMB	3,3',5,5'-tetramethylbenzidine

TNBS	2,4,6-trinitrobenzenesulfonic acid
TNP	trinitrophenol
$\mu\text{g}$	microgram
$\mu\text{l}$	microlitre
$\mu\text{m}$	micrometre
$\mu\text{M}$	micromolar
UTS	ultimate tensile strength
UV-Vis	ultra-visible
v/v	volume per volume
WGFE	whey growth factor extract
wt. %	weight percentage
w/v	weight per volume
XPS	X-ray photoelectron spectroscopy
~	approximately
°	degrees
°C	degrees celsius
$\emptyset$	diameter
>	greater than
$\geq$	greater than or equal to
3T3 balb/c	immortalised cell line of fibroblast morphology with adherent growth properties derived from mouse embryo
<	less than
$\leq$	less than or equal to
3-MPTS	3-mercaptopropyl trimethoxysilane
$\varepsilon$	molar extinction coefficient
$\Omega$	ohms
%	percentage
®	registered
$\lambda$	wavelength

# Abstract

This thesis focuses on surface science and bioengineering investigations, first for the development of an improved biomaterial for orthopaedic implant applications, and second, for the development of a biosensor device for biomedical diagnostics. A key component considered in this thesis was the covalent linkage of proteins to the material's surface for retaining the protein's immunological and biological activities and for generating a functional interface.

Part 1 of this thesis investigated surface modification procedures for improving the bioactivity of titanium substrates. Titanium is first coated with a bioactive silica film grown by plasma enhanced chemical vapour deposition (PECVD), referred to as PECVD-Si-Ti. In previous studies, the bone-implant integration process was enhanced 1.6-fold for titanium implants coated with PECVD-Si films compared to uncoated titanium implants *in vivo*. However, *in vitro* studies carried out in this thesis showed that the growth of MG63 osteoblast-like cells was 7-fold higher on uncoated titanium compared to PECVD-Si coated titanium. Therefore, to improve cell growth on the surface and, by inference, the integration of PECVD-Si-Ti implants into bone tissue, the implant's surface was functionalised with a mitogenic factor, insulin-like growth factor-1 (IGF-1). This was accomplished by modifying the PECVD-Si-Ti surface with an alkoxysilane, 3-isocyanatopropyl triethoxysilane (IPTES), and then by covalent bioconjugation of IGF-1 through isocyanate-amino chemistry. After 72 h of *in vitro* cell culture in serum-free medium, the growth of MG63 cells was enhanced 1.9-fold on IPTES functionalised PECVD-Si-Ti, which was loaded with covalently immobilised IGF-1 compared to IPTES functionalised PECVD-Si-Ti without IGF-1 (isocyanate reactive groups were quenched with ethanolamine hydrochloride). The attachment and adhesion of MG63 cells were also enhanced on PECVD-Si-Ti by the covalently immobilised IGF-1 in serum-free cell culture conditions. Therefore, the bioactivity of PECVD-Si-Ti was improved by covalently linking IGF-1 to the substrate surface through isocyanate-amino chemistry.

Part 2 of this thesis involved the development of a new optical interferometric biosensor. The biosensor platform was constructed from electrochemically-prepared thin films of porous silicon that acted as a sensing matrix and transducer element. By reflective interferometry using white light, an enzyme-catalysed reaction was discovered (horseradish peroxidase (HRP) mediated oxidation of 3,3',5,5'-tetramethylbenzidine (TMB)), which led to an acceleration in the rate of porous silicon corrosion and represented the biosensor's readout signal. We discovered that another substrate, which is also oxidised by HRP, OPD, produces an even more pronounced readout signal. The HRP-OPD system was used in an immunoassay for detecting human IgG from an Intragam solution. An important part in the design of the biosensor was the surface functionalisation approach where anti-human IgG, referred to as the capture antibody, is immobilised on the porous silicon surface. The readout signal (produced from the capture of human IgG) was enhanced 4-fold on the porous silicon biosensing platform functionalised with covalently linked anti-human IgG through isocyanate-amino chemistry compared to the porous silicon biosensing platform functionalised with adsorbed anti-human IgG. The optimised biosensor was used to detect IgG from a total human protein concentration of Intragam to a sensitivity of 100 ng/ml.

In summary, isocyanate-amino bioconjugate chemistry was used to covalently link either IGF-1 to PECVD-Si-Ti for improving the biological activity of the orthopaedic implant and to covalently link IgG to porous silicon for developing a sensitive biosensor for the detection of proteins. This surface chemistry approach is very useful for biomaterial and biosensing applications.

**Part 1:**

**Covalent immobilisation of IGF-1 on  
PECVD-Si-Ti for orthopaedic  
biomaterial applications**

# 1.1 Introduction

## 1.1.1 Overview of biomaterials

The body's response to a foreign implant is dictated by a combination of biological and medical factors. These biomedical aspects require careful consideration so that biomaterial implants can be manufactured with appropriate mechanical, physical and chemical properties. Particularly, the physicochemical property of the implant's surface is of crucial importance for obtaining biological compatibility and for achieving a biomaterial with an optimised performance. When a biomaterial is first implanted in the body, its surface comes immediately in contact with biological fluids and tissue containing proteins and polysaccharides [1]. These proteins and polysaccharides adsorb on the biomaterial to form a film covering the underlying surface [2-4]. The adsorbed protein/polysaccharide film is fundamentally important for the success of the biomaterial because the structure and composition of the film determines the type and extent of the biological response towards the entire biomaterial implant [5]. Furthermore, the nature of this adsorbed film is dependant on the material surface properties [4-5].

Of particular relevance to this work, the majority of orthopaedic implants are also required to withstand load-bearing applications. For this reason most of the commercially available orthopaedic implants are made of metals, which are high in mechanical strength. Usually, the metals are alloyed to improve the mechanical and biocompatible properties of the medical device. Some of the common alloys used as orthopaedic implants include stainless steel, cobalt-chromium, titanium-aluminium-vanadium. The properties of these alloys are outlined in **Table 1.1** [6(a)-8]. These metals are suitable as biomaterials because the surfaces of these materials are considered biocompatible with the body.

In this thesis, biological terminology will be defined according to the following descriptions [9(a), 10]:

‘Biomaterial: a material intended to interface with biological systems to evaluate, treat, augment, or replace any tissue, organ, or function of the body;

Host response: the reaction of a living system to the presence of a material;

Biocompatible material: a material that has the ability to perform with an appropriate host response in a specific application; and

Bioactive material: a biomaterial designed to elicit or modulate biological activity.’

### **1.1.2 Titanium biomaterials**

Among the metals listed in **Table 1.1**, titanium possesses the best combination of mechanical and biocompatible properties. Therefore, the following discussion will focus on titanium biomaterials research. Titanium owes its good biocompatibility to a dense surface oxide layer, which is approximately 4 nm thick and forms spontaneously in the presence of oxygen [9(b)]. The titanium surface dioxide ( $\text{TiO}_2$ ) layer not only shields the bulk of the metal from the surrounding environment, but the chemical interaction of  $\text{TiO}_2$  molecules with biological fluid and tissue determines the host’s reaction to the entire titanium implant [11-12]. Because the  $\text{TiO}_2$  surface layer plays such a pivotal role in titanium implants, it is important to understand each surface characteristic that makes titanium a biocompatible material.

As mentioned above, the surface oxide film shields the underlying titanium metal from the surrounding environment. This is significantly important when the material is implanted in the body and becomes exposed to biological electrolytic fluids. As metals corrode in aqueous environments, ionic species are released into solution, which can be toxic to cells [13]. Corrosion can also result in a gradual loosening of the implant with bone, which requires corrective surgery to remedy. Therefore, the corrosion rate of metallic implants needs to be limited or ideally inhibited when possible. The native  $\text{TiO}_2$  film on titanium forms a passive layer protecting the underlying metal from electrolytic corrosion [14(a)].

Moreover, under physiological conditions of near neutral pH, the high repassivation rate of TiO<sub>2</sub> prevents the dissolution of potentially toxic ionic species from the material's surface [14(a)]. Therefore, the ability of TiO<sub>2</sub> film to spontaneously form a passive film, or quickly repassivate at neutral pH, helps protect the underlying titanium metal from electrolytic corrosion.

	Stainless steel	Cobalt-chromium	Titanium-aluminium-vanadium
Elemental composition (wt.%)	Fe (Bal.) Cr (17-20) Ni (12-14) Mo (2-4)	Co (Bal.) Cr (19-30) Mo (0-10) Ni (0-37)	Ti (Bal.) Al (6) V (4) Nb (7)
ASTM designation	F138	F75, F-799, F1537	F67, F136, F1295
UTS (MPa)	960-970	600-1795	465-950
Main Orthopaedic implant application	Temporary devices (Fracture plates, screws)	Dentistry, prostheses stems, load-bearing implant components	Long-term permanent devices (nails, pacemakers)
Advantages	Cost, availability	Wear and corrosion resistance, fatigue strength	Biocompatibility, corrosion resistance, fatigue strength
Disadvantages	Lack of long-term biocompatibility, Mechanical property (high modulus) can lead to high stress shielding locally in the bone resulting in constant bone resorption	Lack of biocompatibility, Mechanical property (high modulus) can lead to high stress shielding locally in the bone resulting in constant bone resorption	Mechanical property (low wear resistance) can lead to the abrasion of the implant surface resulting in loosening of the implant from bone

**Table 1.1.** Some properties of metallic implants. Table was adapted from Long et al. [8]. Abbreviations: ASTM – American Society for Testing and Materials, UTS – ultimate tensile strength, wt – weight, Bal – balance of the elemental composition (wt.%) of the metal alloy.

The TiO<sub>2</sub> surface layer also interacts with biological fluids and tissues in ways that promote the biocompatibility of titanium. In fact, the main reason why titanium is a biocompatible material is that the TiO<sub>2</sub> surface layer gently interacts and does not exert any strong forces on proteins in the biological fluid [12, 14(a)]. Because TiO<sub>2</sub> has a dielectric constant ( $\epsilon = 40-110$ ), which is close to that of water ( $\epsilon = 80$ ), hydrophilic proteins that come in contact with the surface are able to gently interact with TiO<sub>2</sub> without denaturing on the material's surface [12, 14(a)]. At near neutral pH, the titanium surface is only slightly negatively charged from TiO<sup>-</sup> species (TiO<sub>2</sub> has an isoelectric point of 3.5-6.7) and is unlikely to exert strong electrostatic forces on proteins that can lead to protein denaturation [9(c)]. However, the ion exchange properties of TiO<sup>-</sup> enable the binding of Ca<sup>2+</sup> ions, which are present in biological fluids. This is also relevant because some serum proteins have been shown to adsorb on TiO<sub>2</sub> via an intermediate interaction with adsorbed calcium [11].

So far it has been made apparent that titanium is an ideal material as an orthopaedic implant because of the combination of favourable mechanical and biocompatible properties. These features have resulted in titanium being exploited for bone tissue replacement therapies such as dental implants and hip prostheses [9(d-e)]. Then why is it necessary to continue titanium biomaterials research? From a scientist's view, developing a new generation of titanium implants with highly controlled surface modifications will enable specific or multiple aspects of the bone-implant integration process to be targeted. This could include functionalising the surface with proteins that regulate osteoblastic cell adhesion, differentiation and proliferation and by designing chemically modified substrate surfaces resistant to non-specific protein adsorption and hence minimise the risk of a severe inflammatory response to the implant material. Therefore, these new "designer" biomaterials will possibly lead to implants with faster and more effective integration capabilities with a reduced risk of being rejected by the body. Obviously this is also important from a clinical perspective because the healing process can be lengthy (several weeks) and orthopaedic implants that have not integrated correctly into the surrounding bone tissue, that have loosened over time or caused severe inflammatory responses, often require corrective surgery. This can be both costly and painful for the patient, particularly for larger operations such as hip-replacement surgery. Therefore, continuing research in the

field of biomaterials science is certainly warranted and development of improved titanium-based implant devices is desirable.

### **1.1.3 Osseointegration**

Before discussing developments in orthopaedic implant technology, the bone-biomaterial integration process will first be introduced. This is a complex process and the following description should only be considered as a brief overview. An excellent and comprehensive description can be found in 'Bone Engineering' edited by J.E. Davies [14(b-n)].

During implantation, blood vessels become damaged and the implant surface becomes exposed to blood. Haemorrhage leads to formation of a blood clot on the implant surface, which is often referred to as the provisional matrix. Fibrin, which is the major component of the provisional matrix, forms a cross-linked mesh network that stabilises the matrix and regulates angiogenesis that improves vascularization of the wound site. This is important to obtain sufficient transport of oxygen and nutrients to the wound site and remove toxic cellular material [15]. The provisional matrix comprises of many other proteins including fibronectin and transforming growth factors, which regulate cellular activity during the initial wound-healing process and the complex 3-dimensional structure of this matrix provides a support for the growth of blood cells [14(b), 16-18].

Blood cells are the cellular initiators of the wound healing process. Erythrocytes, platelets and leukocytes constitute the main cellular components of blood [19]. Erythrocytes are mainly responsible for transporting oxygen to the tissues. Leukocytes, involved in phagocytosis, accumulate at the wound site during inflammation and play a key role in the removal of microorganisms and foreign materials. Activated platelets secrete a variety of proteins including growth factors such as platelet-derived growth factors (PDGFs) and transforming growth factors (TGFs), which regulate cellular proliferation, activation and differentiation to direct vascular ingrowth at the wound site and promote cellular matrix deposition [14(o)].

The interaction of the implant surface with blood not only impacts on bone formation processes but also determines if the implant will be accepted or rejected by the host. Biological failure of the implant may occur at an early or late stage of the implant/bone integration process or even after the implant has integrated with the bone. After the implant is inserted in the body, the success of the implant is mainly governed by the host's inflammatory reaction, which is caused from surgical trauma and the presence of the biomaterial implant [14(k)]. Implant failures are mainly caused by microorganism infections, excessive surgical trauma, implant wear, implant overload (when the force applied to an implant exceeds the force that the surrounding bone can withstand) and prolonged or excessive inflammation [14(k)]. For example, the implant's surface may stimulate certain phagocytic events when serum factors such as immunoglobulin G (IgG) and complement-activated fragment (C3b) adsorb on the biomaterial surface [14(h)]. These factors can be recognised by macrophages (phagocytic cells). Although macrophages cannot phagocytose most biomaterial implants (because the surface area of the implant is much greater than the cell), the cells may undergo "frustrated phagocytosis" and secrete agents including proteases, oxygen metabolites and cytokines leading to chronic inflammation [14(h)].

The mechanism by which the implant surface chemistry and physics interacts with the blood proteins and cells and how this interaction impacts on the subsequent wound healing phases is only poorly understood. However, proteins such as growth factors that become adsorbed on the implant or are released by cells during the initial interaction of the implant surface with blood have been shown to influence the recruitment and cellular activity of cells involved in bone tissue formation and regeneration [20].

Bone formation on the implant surface occurs when stem or progenitor cells from the connective bone tissue are recruited, proliferate and differentiate along an osteogenic pathway to form mature osteoblast cells, the major cell type involved in bone formation. Growth factors play a key role in directing proliferation and differentiation of stem or progenitor cells along the osteogenic pathway [14(d), 21]. A non-collagenous matrix called the cement line, consisting of hydroxyapatite (HA, a bone mineral) and non-collagenous

proteins (osteopontin and bone sialoprotein), is first deposited by pre-osteoblast cells on the implant surface (**Figure 1.1**) [14(p)]. The early expression of osteopontin, a characteristic of pre-osteoblast cells, is associated with the formation of the cement line [22-23]. The formation of the cement line is an important step of the implant integration process because the newly formed bone bonds to the implant surface via the intermediate non-collagenous matrix. Pre-osteoblasts mature into osteoblast cells, which produce a mineralised bone matrix comprising of interwoven collagenous fibres, HA and other proteins, including bone sialoprotein (BSP), osteopontin, osteonectin and osteocalcin that regulate bone mineralisation, resorption and cellular activity [24-27]. The osteoblasts eventually become entrapped in the bone matrix and further differentiate into mature, non-mitotic cells called osteocytes. Although osteocytes are no longer able to undergo cell division, they play an important role in the regulation of bone structure and mass through a mechanosensory mechanism [28]. The surface of the bone not growing or being resorbed is covered with lining cells. The lining cells are thought to regulate bone resorption, which only occurs after the cells are removed from the surface of the bone [29]. Bone formed on the implant surface is also remodelled in a process involving the break down (resorption) and build-up (synthesis) of bone. This process regulates the microstructure of bone ensuring that maximal strength of bone is maintained with a minimal mass. The main cell involved in the active resorption of bone is the osteoclast [30-31]. The differentiation and activation of osteoclasts are mainly regulated by osteoprotegerin (OPG) and receptor activator of nuclear factor  $\kappa$ -B (RANK) [32-33].

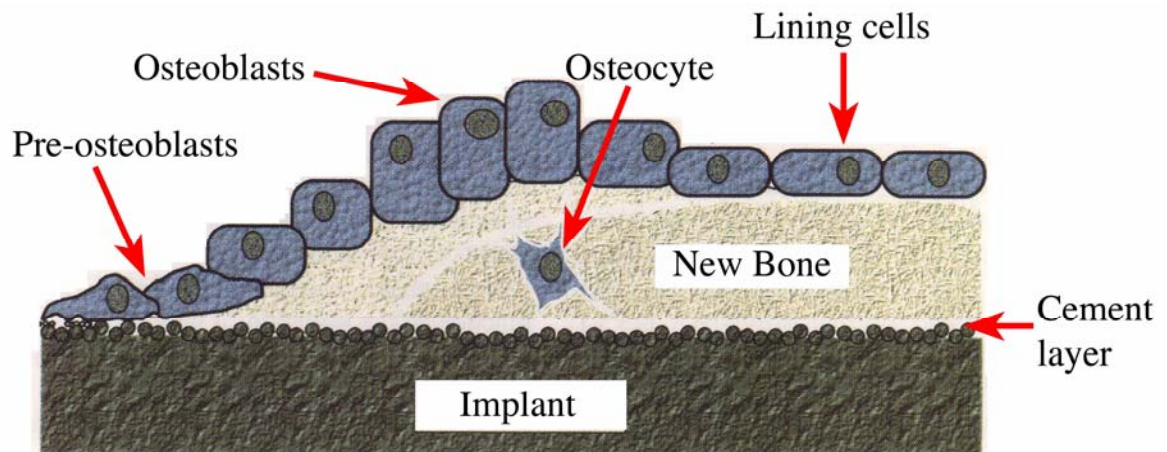


**Figure 1.1.** An illustration of bone formed on an implant surface by osteoblastic cells. The diagram was adapted from Davies [14(e)].

The above briefly described the process of vertical bone formation on the implant surface referred to as appositional bone growth (**Figure 1.2**). At the same time, osteogenic cells migrate and synthesise bone horizontally along the implant surface in a process referred to as osteoconduction (**Figure 1.2**) [14(b)]. Osteoconduction allows for a faster healing time because the synthesis of bone can begin simultaneously along many locations on the surface of the implant.

In summary, the integration process of an orthopaedic implant can be described in phases mainly regulated by protein and cellular interactions on the implant surface. The implant surface first interacts with proteins and cells in the blood, leading to a recruitment of potentially osteogenic cells, which differentiate into mature osteoblasts that control the multidirectional synthesis of bone and bone remodelling. An understanding of each phase is essential so that orthopaedic implants can be developed with enhanced bone integration performance characteristics. However, there are virtually limitless possibilities by which implants can be modified to improve the process of osseointegration (the direct structural and functional connection between the implant's surface and the living bone tissue). Moreover, it is extremely difficult, if not impossible to design an orthopaedic implant that improves each component of the complex integration process. This has led to an extraordinary amount of research being directed to developing new biomaterials to improve specific stages of the bone-implant integration process.

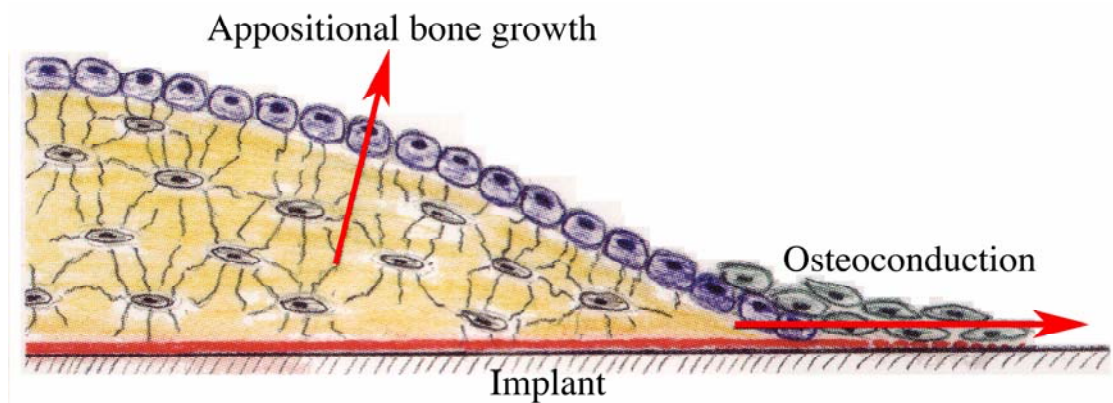


**Figure 1.2.** An illustration of bone formed on an implant surface through appositional bone growth and osteoconduction. The diagram was adapted from Davies [14(b)].

### **1.1.4 Introduction to titanium biomaterials research**

To illustrate the significant amount of research carried out on titanium biomaterials, a simple search for “titanium implant” in a PubMed database yielded nearly 3000 references in the last decade alone (for years 1997-2007). Because Part 1 of this thesis is concerned with the surface modification of titanium materials, only the literature focussed on this area of research will be discussed. Surface modification of biomaterials can be divided into two main categories: surface chemistry and surface morphology. As is often the case, the surface modification procedure usually alters both characteristics. It is debatable which surface characteristic is more important, but certainly both are known to have a strong influence on the biological response to the material’s surface [34]. The surface characteristics of the biomaterial can be changed by chemically or physically altering the atoms or molecules of the existing surface, a film having a new composition can be coated over the surface or the surface can be functionalised with biological molecules (such as proteins, peptides, deoxyribonucleic acid (DNA) or oligosaccharides). The following will discuss methods for generating titanium orthopaedic implants with improved surfaces for promoting the growth and regulating the activity of osteogenic cells. A significant amount of titanium biomaterials research was carried out in the 1990s, however more recent studies have also been carried out [35-39].

### **1.1.5 Influence of surface topography on osseointegration**

Although Part 1 of this thesis focuses on the regulation of cell behaviour through the display of chemical and biochemical cues, there is also evidence available that suggests osseointegration can be influenced by the implant’s surface topography [40-42]. The titanium surface can be modified with well-defined surface morphological characteristics through a range of methods including mechanical and electrochemical polishing, acid etching, grit blasting, laser ablation and plasma (glow discharge) processing methods, but the mechanisms by which the newly introduced surface morphologies improve bone-implant integration is not completely understood [43-46]. However, several reports have shown how the behaviour of bone cells including cell attachment, adhesion, proliferation

and differentiation can be regulated by defined morphological surface characteristics [47-52]. Recent work has shown that the osteoblast cell response can be regulated by both micron- and nanostructured surfaces [53-55].

For example, Kieswetter et al. demonstrated that the production of growth factors and cytokines from MG63 osteoblast-like cells was affected by the morphology of the titanium surface [50]. In this study, titanium surfaces were (from smoothest to roughest) electropolished, acid-etched only (not sand-blasted), fine sand-blasted/acid-etched, coarse sand-blasted/acid-etched and plasma sprayed. After MG63 cells were grown on the substrate surfaces, production of prostaglandin E<sub>2</sub> (PGE<sub>2</sub>) and transforming growth factor  $\beta_1$  (TGF- $\beta_1$ ) (important factors in bone formation) were expressed at higher levels on the rougher surfaces in comparison to the smoother surfaces and tissue culture polystyrene (TCPS). PGE<sub>2</sub> was expressed 3.4-fold, 7.6-fold and 5.9-fold on fine sand-blasted/acid-etched, coarse sand-blasted/acid-etched and plasma sprayed titanium in comparison to TCPS, respectively, whereas no significant differences were observed in the level of PGE<sub>2</sub> produced by MG63 cells grown on electropolished and acid-etched (not sand-blasted) titanium. TGF- $\beta_1$  was expressed 3-fold and 4.2-fold by MG63 cells grown on coarse sand-blasted/acid-etched and plasma sprayed titanium in comparison to TCPS, respectively, whereas no significant differences were observed in the level of PGE<sub>2</sub> produced by MG63 cells grown on electropolished, acid-etched (not sand-blasted) and fine sand-blasted/acid-etched titanium. Furthermore, the authors proposed a possible relationship between cellular activity and morphology. MG63 cells grown on the smoothest electropolished titanium surface exhibited a well-spread morphology; the cells were also well-spread on the next smoothest acid-etched titanium surface but exhibited slightly ruffled morphology and formed multiple cell layers; a lower cell density was found on the three roughest fine and coarse sand-blasted/acid-etched and plasma sprayed titanium surfaces and the cells appeared to form multiple cell layers with some cells having extensions in excess of 10  $\mu\text{m}$  (**Figure 1.3 A-E**). Therefore, the results shown in this article suggest that the differences of MG63 cell morphology observed on the titanium surfaces (with different surface roughness characteristics) was related to differences in cellular behaviour (secretion of proteins, which are important in wound healing and bone formation).

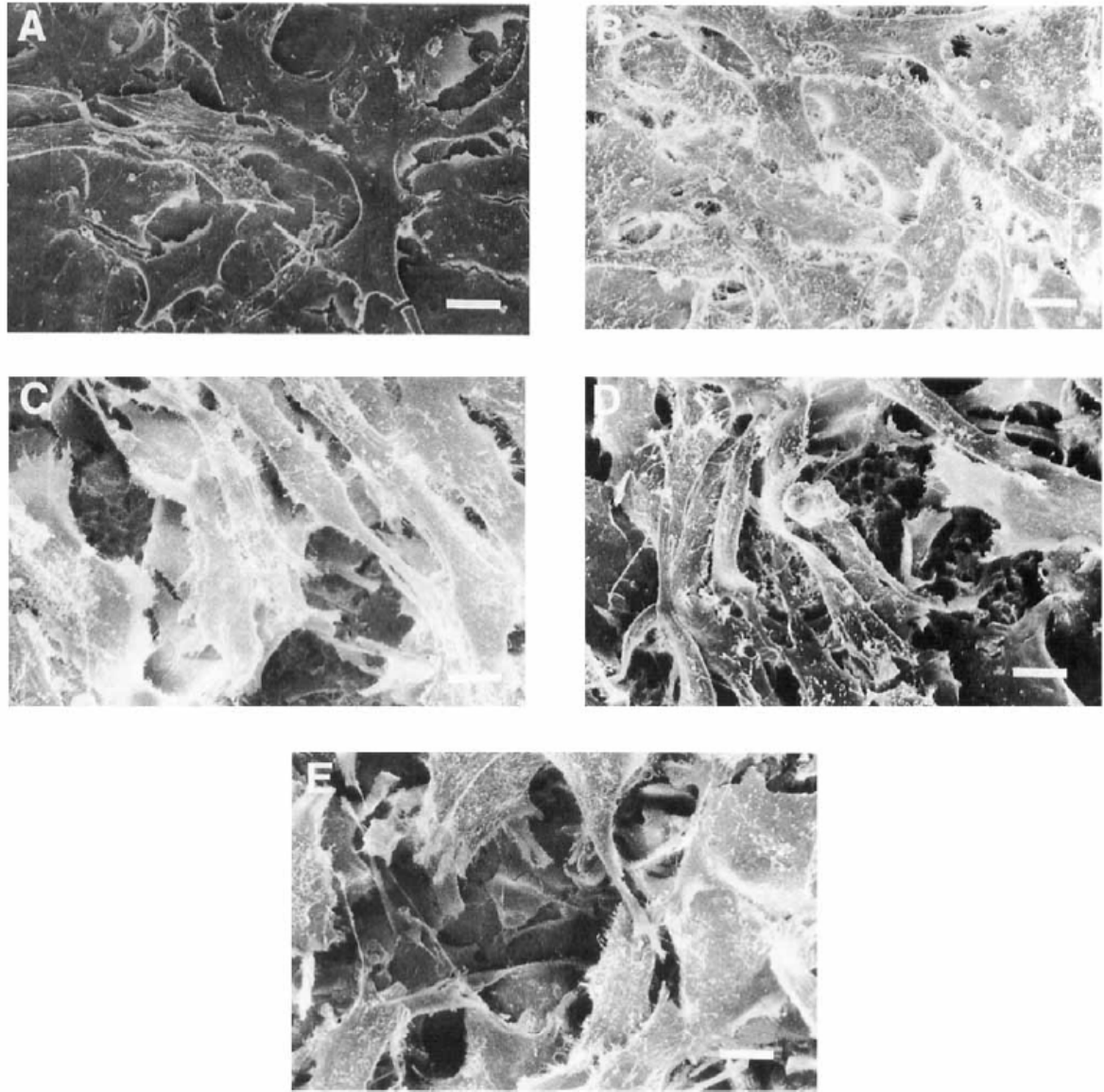


**Figure 1.3.** Scanning electron micrographs of MG63 cells grown on (from smoothest to roughest) electropolished (A), acid-etched (B), fine sand-blasted/acid-etched (C), course sand-blasted/acid-etched (D) and plasma sprayed titanium (E). Scale bars = 10 μm. Images were adapted from Kieswetter et al. [50].

### 1.1.6 Influence of surface chemistry on osseointegration

Similarly, cellular behaviour on chemically modified titanium surfaces has been extensively studied. Some common surface modifications include altering the titanium oxide surface by increasing the depth of the surface oxide layer, changing the density of surface hydroxides, incorporating new elements, covering the titanium oxide surface with a film having a new chemical composition and by functionalising the surface with biological molecules. These modifications are generally carried out in an attempt to improve the performance of the implant by improving corrosion resistance, stimulating and regulating cell growth, inducing resistance to biological fouling, limiting microbial activity or rendering biological specificity (targeting specific cell types).

Increasing the thickness, density and ultimately the passivity of the titanium oxide film is desirable to improve the corrosion resistance of the metal implant. The common methods for passivating and hydroxylating titanium include chemical treatment in strong oxidising agents such as nitric acid, sodium hydroxide and hydrogen peroxide, heat treatment or plasma (glow discharge) processing [9(f)]. These treatments can also alter the hydrophilic/hydrophobic properties of the titanium surface, which impacts on subsequent protein adsorption events and consequently on cell attachment and growth [56-57]. Some efforts have also been made to produce bioactive titanium oxide surfaces by incorporating new chemical species into the surface oxide layer [58-60]. The titanium surfaces are usually treated by ion implantation or by electrochemical processes to generate a calcium-phosphate (HA-like) mineral phase through the oxide layer [58-59, 61]. The literature suggests that implants with calcium-phosphate doped titanium oxides improve osseointegration indirectly through the conversion of calcium-phosphate into HA (by oxidation, hydrolysis, precipitation and crystallisation) during the formation of the cement layer (refer to **pages 8-9** and **Figure 1.1**) or directly by stimulating the growth and activity of osteoblastic cells. For example, Sandrini et al. compared the growth of osteoblast-like cells on calcium-phosphate doped titanium prepared using a traditional anodic spark deposition (ASD) process to a modified ASD method called BioSpark™ (BSP), which generates a thicker titanium oxide film consisting of a calcium-phosphate mineral phase

with a higher Ca:P ratio compared to the traditional ASD method [59, 62]. The higher Ca:P ratio led to a higher proliferation rate of MG63 osteoblast-like cells on BSP-modified titanium in comparison to titanium modified by the traditional ASD method. Furthermore, osteoblast-like cells grown on BSP-modified titanium showed a more intimate contact to the substrate surface in comparison to titanium modified by the traditional ASD method, which showed more elongated cellular structures (**Figure 1.4 A-B**). The authors concluded that, as an orthopaedic device, BSP treated titanium was more suitable because of the optimised osteoblast-like cell behaviour.

In other work, titanium oxide surfaces have been modified with films possessing different chemical and morphological surface characteristics. The two most common surface coatings used for enhancing the performance of titanium orthopaedic implants are HA ( $\text{Ca}_5(\text{PO}_4)_3\text{OH}$ ) and Bioglass<sup>®</sup> (the composition of 45S5 type Bioglass<sup>®</sup> by weight % is 45%  $\text{SiO}_2$ , 24.5%  $\text{Na}_2\text{O}$ , 24.5%  $\text{CaO}$ , 5%  $\text{P}_2\text{O}_5$ ). These materials are not only biocompatible with the body but also possess potent bioactive properties [63-67].

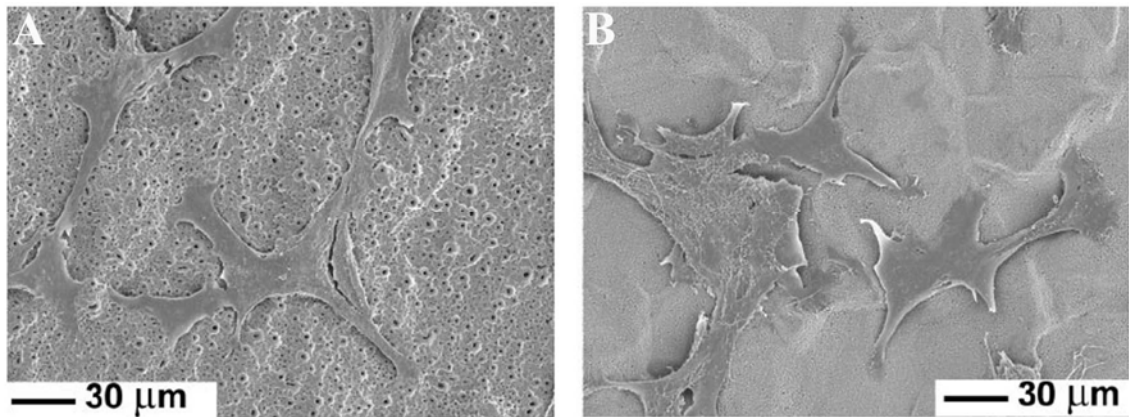


**Figure 1.4.** Scanning electron micrographs of MG63 osteoblast-like cells grown on oxidised and Ca-P doped titanium surfaces that were modified using a traditional method of ASD (A) and by BSP (B). Images were adapted from Sandrini et al. [59].

### 1.1.7 Hydroxyapatite implant coatings

Artificial HA or HA-like layers have been coated on titanium and titanium alloys by a variety of techniques including high temperature plasma spraying, chemical precipitation and electrochemical deposition [9(g), 68-70]. Of these techniques, only plasma sprayed coatings are commercially available. Clinical results have showed that plasma sprayed HA coatings make excellent orthopaedic implants [9(g)]. The success of HA implants has been attributed to their osseointegration, resulting in excellent bone contact and interfacial strength between the implant and bone [71-72]. However, there are several disadvantages associated with plasma sprayed HA coatings including non-uniformity in coating thickness and density, the presence of chemical contaminants, the lack of structural integrity and reproducibility. In some cases these pitfalls have contributed to implant failure (**Figure 1.5**) [73].

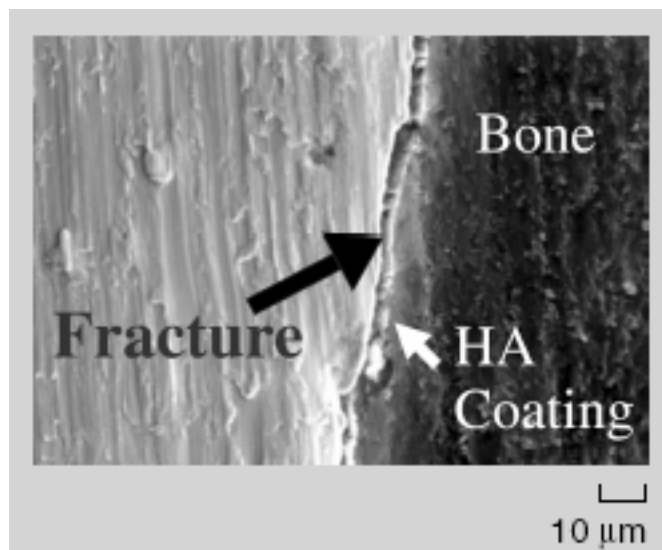


**Figure 1.5.** Scanning electron micrograph of a plasma sprayed HA titanium implant that had been implanted in a dog's mandible for 1 year followed by a pull-out test. The implant fractured at the HA-titanium interface. The image was adapted from Ong et al. [73].

### 1.1.8 Bioactive glass implant coatings

Bioglass<sup>®</sup> is another commercially available and highly bioactive biomaterial. Bone formation occurs spontaneously on Bioglass<sup>®</sup> *in vivo* with high interfacial adhesion strength [63, 74]. The bioactivity of Bioglass<sup>®</sup> (and other bioactive glasses having variations in the elemental composition to that of Bioglass<sup>®</sup>) has been reported to occur through several mechanisms. In physiological environments, bone is able to bond strongly to bioactive glass through an intermediate apatite cement layer that is formed on the implant surface (**Figures 1.1 and 1.6 A-B**).

Apatite growth begins at the Si-OH nucleation sites of the glass ceramic surface. Ionic species such as Na<sup>+</sup> and Ca<sup>2+</sup> are released from glass ceramic into the surrounding biological fluid, which increases the degree of supersaturation with respect to the apatite and accelerates the rate of apatite nucleation. Apatite continues to grow spontaneously by consuming Ca<sup>2+</sup> and PO<sub>4</sub><sup>3-</sup> in the biological fluid. This process, which is illustrated in **Figure 1.6 A**, has been described in more detail elsewhere [14(q), 75]. Interestingly, calcium and phosphorous species may not necessarily be an integral constituent of the glass ceramic because in the presence of simulated body fluid, even pure SiO<sub>2</sub> material (without Ca, P or Na) can form bone-like apatite beginning at the Si-OH nucleation sites [76].

It has also been proposed that bioactive glasses act on cellular behaviour through the release of soluble forms of silicon, such as silicate, from the glass surface [65, 77]. The soluble silicon may stimulate the production of transforming growth factor  $\beta$  by osteoblast stem or progenitor cells and consequently the proliferation and differentiation of the cells leading to enhanced bone formation [65]. Also, the leached elements of Si, Ca, and P from bioactive glasses have been shown to induce the up-regulation of genes involved in bone growth [78-79]. Therefore, enhancement of bone formation can be described on bioactive glasses through a synergistic mechanism of spontaneous growth of apatite on the material surface and stimulation of osteogenic cellular activity.

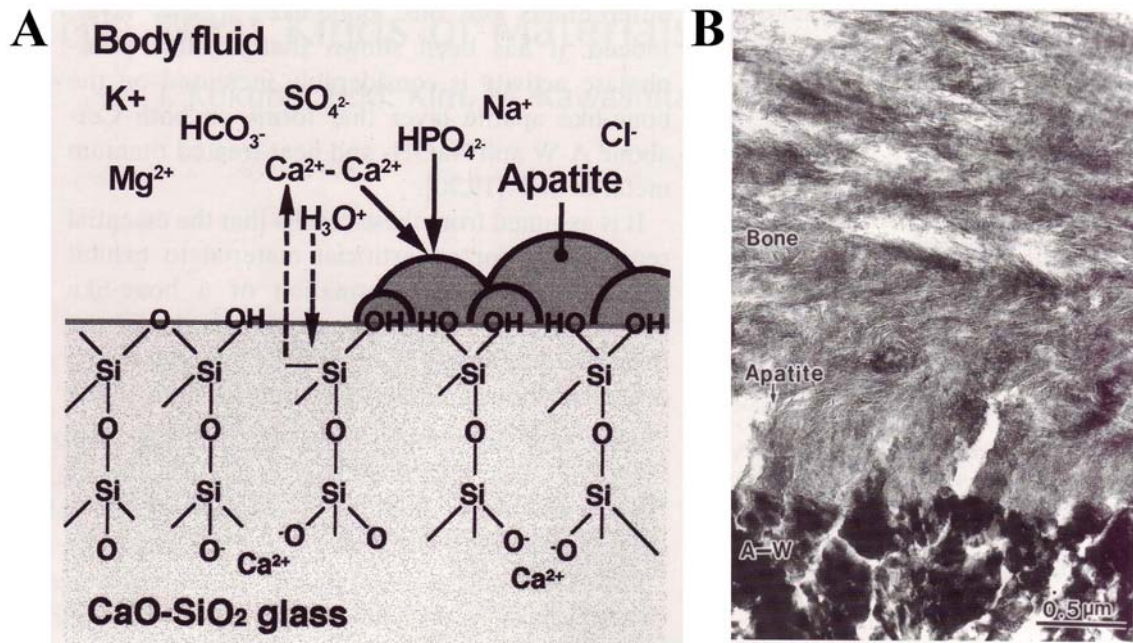


**Figure 1.6.** An example of the mechanism of apatite formation on bioactive glass (CaO-SiO<sub>2</sub> in this case) (A) and a transmission electron micrograph of the interface between a bioactive glass implant (A-W) and bone (rat tibia) (B); note the intermediate apatite layer formed between the implant and bone. Images were adapted from Davies [14(q)].

Because Bioglass<sup>®</sup> is too brittle for use in load-bearing applications, the material is usually used as a coating over the surface of metals such as titanium, which provides the structural support. The common techniques for generating bioactive glass ceramic coatings on titanium include enamelling, electrophoresis, sol-gel and plasma spraying. However, bioactive glass ceramic coatings possess some disadvantages such as poor adhesion to the substrate surface, which as discussed above, is also a problem for HA coatings [80].

### 1.1.9 Plasma enhanced chemical vapour deposition of bioactive glass

In an attempt to improve the adhesion of bioactive silica on titanium, a low temperature plasma process for depositing silica was developed by R.St.C. Smart, which was modified later to improve control over the plasma deposition parameters [81-83]. Here, silica is deposited by a plasma enhanced vapour deposition (PECVD) technique. The plasma (partially ionised gas) is generated in a commercially available Harrick radio-frequency

plasma chamber that is typically operated at 100 W and 13.56 MHz. A controlled flow of vapour into the reactor is maintained with the aid of 3 mass flow controllers, which delivers air and mixtures of tetraethoxysilane (TEOS) and air or H<sub>2</sub>O<sub>2</sub> and air into the reaction chamber at defined flow rates (**Figure 1.7**). In the first step, air plasma is generated to remove surface impurities and increase the thickness of the titanium oxide layer. Silica is then deposited from TEOS/air plasma (the reaction layer is formed by silicon-oxygen species produced in the gas phase such as SiO<sup>+</sup>, O<sup>-</sup> and SiO radicals becoming embedded in the titanium oxide layer). The third step uses H<sub>2</sub>O<sub>2</sub>/air plasma for surface hydroxylation to increase the density of surface silanol groups.

The process produces a compositionally and structurally graded metal/oxide/silicate/silica surface layer that strongly adheres to the material substrate. The silica layer deposited by the PECVD method (PECVD-Si) can withstand pull-off loads in excess of 27 MPa (**Figure 1.8**), much higher than the titanium/apatite and the bone/apatite interfaces, which have been reported to fail under loads of 12 MPa and 17 MPa, respectively [81-84]. Because the titanium/silica interface can withstand higher loads than the bone/apatite interface, the implant is unlikely to fail at the interface between the substrate surface and the coating.

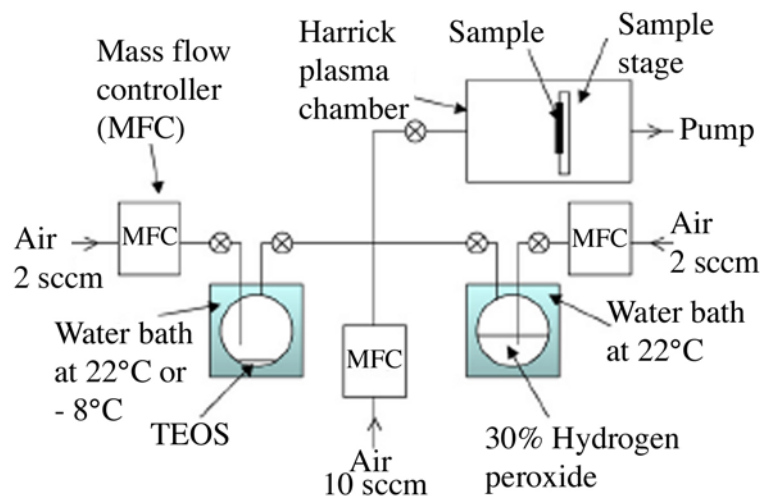


**Figure 1.7.** Schematic representation of the PECVD system used for depositing bioactive PECVD-Si coatings on titanium. Abbreviations: MFC – Mass flow controller, sccm – standard cubic cm per min. Image was adapted from Zhang et al. [83].

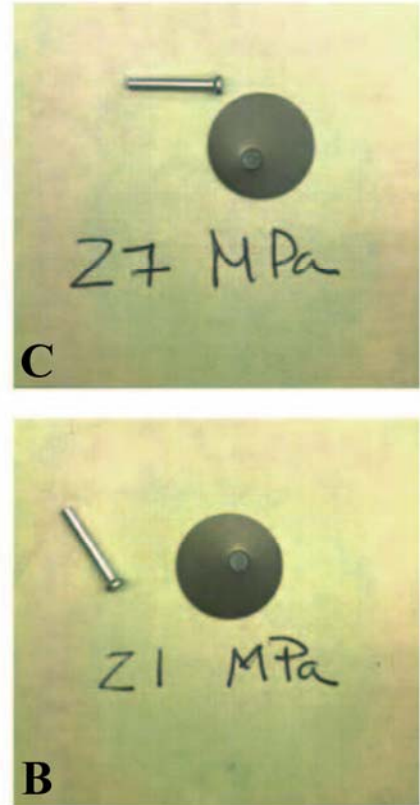
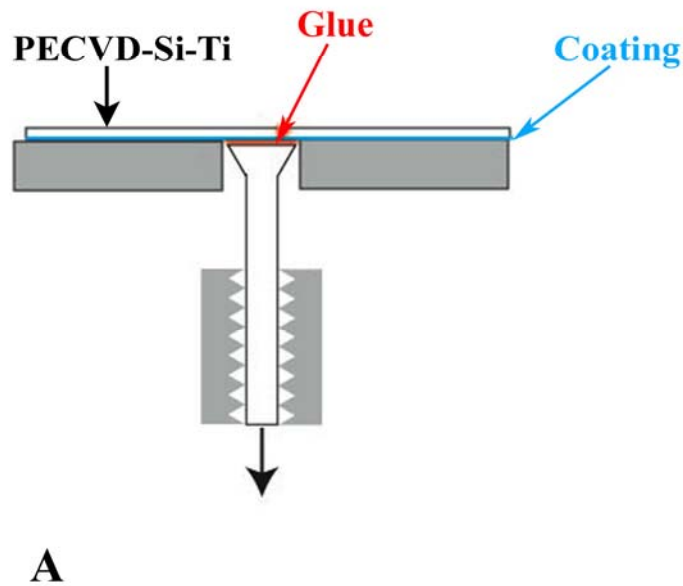


**Figure 1.8.** An illustration of the apparatus and method used for testing the adhesion (pull off force) of PECVD-Si coatings on titanium substrates (A) and photographs of titanium coated with PECVD-Si (PECVD-Si-Ti) after testing the adhesion strength of the PECVD-Si coatings (B and C). At forces of 21 and 27 MPa, failure occurred between the screw and glue interface and not at the PECVD-Si and titanium interface (B and C), indicating that PECVD-Si coatings on titanium can withstand loads in excess of 27 MPa. The adhesion test was performed by Eduardo Saiz from Lawrence Berkeley National Laboratory (LBNL). The illustration and photographs are courtesy of LBNL.

PECVD-Si has been used for several applications including corrosion resistance coatings and growing HA or HA-like layers [81-83]. More importantly, a previous study showed that titanium implants coated with PECVD-Si (PECVD-Si-Ti) exhibit a 1.6-fold increase of direct bone/implant contact (the area of the implant thread in contact with bone in comparison to soft tissue) in comparison to uncoated titanium implants after 6 weeks implantation in a sheep's mandible (**Figure 1.9 A-C**) [85].

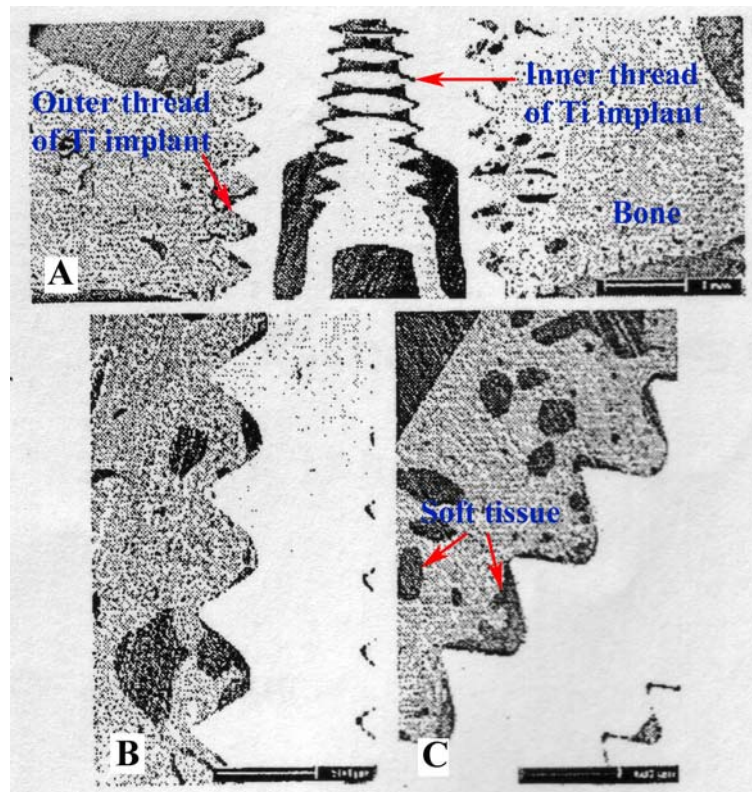


**Figure 1.9.** Scanning electron micrographs of a whole titanium screw implanted in a sheep's mandible *in situ* (**A**), part of a PECVD-Si-Ti screw after 6 weeks implantation in the sheep's mandible *in situ* (**B**) and part of an uncoated titanium screw after 6 weeks implantation in the sheep's mandible *in situ* (**C**). A higher percentage of direct bone/implant contact is seen for the coated implant (**B**) in comparison to the uncoated implant (**C**) where the bone also appears less dense. Images were adapted from Abbott et al. [85].

In a recent study, we examined the interaction between the surface of PECVD-Si-Ti and an osteoblast-like cell line (MG63) *in vitro* and discovered that cell attachment and proliferation was poor on PECVD-Si-Ti when compared to uncoated titanium and tissue culture polystyrene (TCPS) (this is discussed in detail on **pages 112-138**). Although it is difficult to make a direct correlation between the *in vivo* and *in vitro* biological behaviour of the biomaterial, the data suggested that PECVD-Si does not stimulate bone formation directly and short-term through stimulating osteoblastic cellular activity. Instead, the beneficial effect of the PECVD-Si coating more likely stems from an indirect mechanism, that is by first promoting the precipitation of apatite from the biological fluid, followed by osteoblast colonisation [76, 83]. Therefore, in an attempt to further enhance *in vivo* bone formation on PECVD-Si-Ti, Part 1 of this thesis is aimed at improving the growth of osteoblastic cells on the substrate surface through the immobilisation of a bioactive molecule.

#### **1.1.10 Biological bioactive factors**

The bioactive molecule should be a factor that osteoblastic cells can recognise and the factor should ultimately stimulate osteoblastic cellular activity on the implant material. There are a variety of growth factors that may regulate bone formation including epidermal growth factors (EGFs), TGFs, insulin-like growth factors (IGFs) and fibroblast growth factors (FGFs) [86(a)]. Bone morphogenetic proteins have also been recognised to play an important role in the regulation of osteoblast cellular activity, including differentiation [87], and for inducing the formation of both cartilage and bone [88]. In this current research, we chose to functionalise the surface with insulin-like growth factor-1 (IGF-1) because it is a highly potent mitogen to many cell types, including osteoblastic cells [89-92]. Moreover, human osteoblasts express functional IGF-1 receptors indicating that IGF-1 is possibly an important regulatory factor in bone formation [93]. We anticipated that PECVD-Si-Ti implants functionalised with IGF-1 could potentially accelerate bone formation *in vivo* through a synergistic action of the IGF-1 functionalised PECVD-Si surface promoting spontaneous apatite formation and stimulating osteoblastic cellular activity.

The biological effects of IGF-1 are mediated through a signalling cascade that is triggered when IGF-1 binds the IGF-1 receptor of the cell [94]. IGF-1 most likely induces bone formation by simultaneously stimulating proliferation (mediating the progression of the cell cycle), differentiation (matrix synthesis and collagen production) and cell survival (inhibiting apoptosis) of osteoblastic cells through this signalling cascade [95-98]. However, the main action of IGF-1 on PECVD-Si-Ti was expected to be through stimulation of cellular proliferation since the growth factor has previously been shown to be a potent mitogen even at relatively low concentrations ranging from 0.003-0.1  $\mu\text{M}$  in solution [91-92, 99-100]. This has led to IGF-1 being used for many tissue engineering and therapy applications including promoting bone tissue regeneration on polymer scaffolds and microspheres, in clinical trials for IGF-1 replacement therapy (SomatoKine) and is also found in commercially available products such as TransCyte - a wound dressing for temporary skin substitutes [101-102].

### 1.1.11 Protein surface immobilisation techniques

The next question we asked was how should we load IGF-1 onto the PECVD-Si-Ti surface? There are a variety of strategies that can be used to immobilise growth factors on surfaces (**Figure 1.10 A-H**) [103]. Growth factors can be immobilised through non-covalent mechanisms including physical entrapment (**Figure 1.10 A-C**), adsorption (**Figure 1.10 D-E**), electrostatic interaction (**Figure 1.10 F**) and by covalent mechanisms through intermediate linkers or by direct attachment to the substrate surface (**Figure 1.10 G-H**). Entrapment methods were not a suitable method for this work because entrapment involves the growth factor being immobilised in 3-dimensional delivery vehicles (**Figure 1.10 A-B**; we intended to immobilise IGF-1 on an implant possessing a 2-dimensional surface), or the growth factor being immobilised in a polymeric matrix, which significantly changes the implant's surface chemistry (**Figure 1.10 C**; the polymeric film would shield the bioactive PECVD-Si surface from the surrounding biological environment). Therefore, we chose to compare the biological performance of the PECVD-Si-Ti implant functionalised with adsorbed (non-covalently attached) IGF-1 and covalently linked IGF-1.

Protein adsorption (adhesion) occurs through a combination of hydrophilic/hydrophobic, electrostatic and physical interactions between the protein and the substrate surface. For example, human serum albumin has been reported to adsorb onto titanium substrates through a combination of these mechanisms [104]. Once adhered to the surface, the protein may also undergo several conformational changes leading to reversible or irreversible adsorption. In some cases, the conformational change can also lead to the protein becoming deactivated or denatured on the substrate surface.

To limit the possibility of protein deactivation or denaturation and improve the stability of the IGF-1 surface concentration, bifunctional linkers/spacers can be used to covalently tether IGF-1 to the substrate surface. Furthermore, more stable bioactive layers can be formed by covalently linking biological molecules to the surface in comparison to adsorption methods. For example, Müller et al. has shown that collagen, covalently linked to titanium substrates, produces more stable bioactive layers in comparison to adsorbed collagen films [105]. The adsorbed collagen film completely degraded after 6 h of collagenase digestion. In stark contrast, 47% of the residual amount of covalently bonded collagen was detected and 24% of collagen was still detected on the same surface after 24 h of enzymatic digestion.

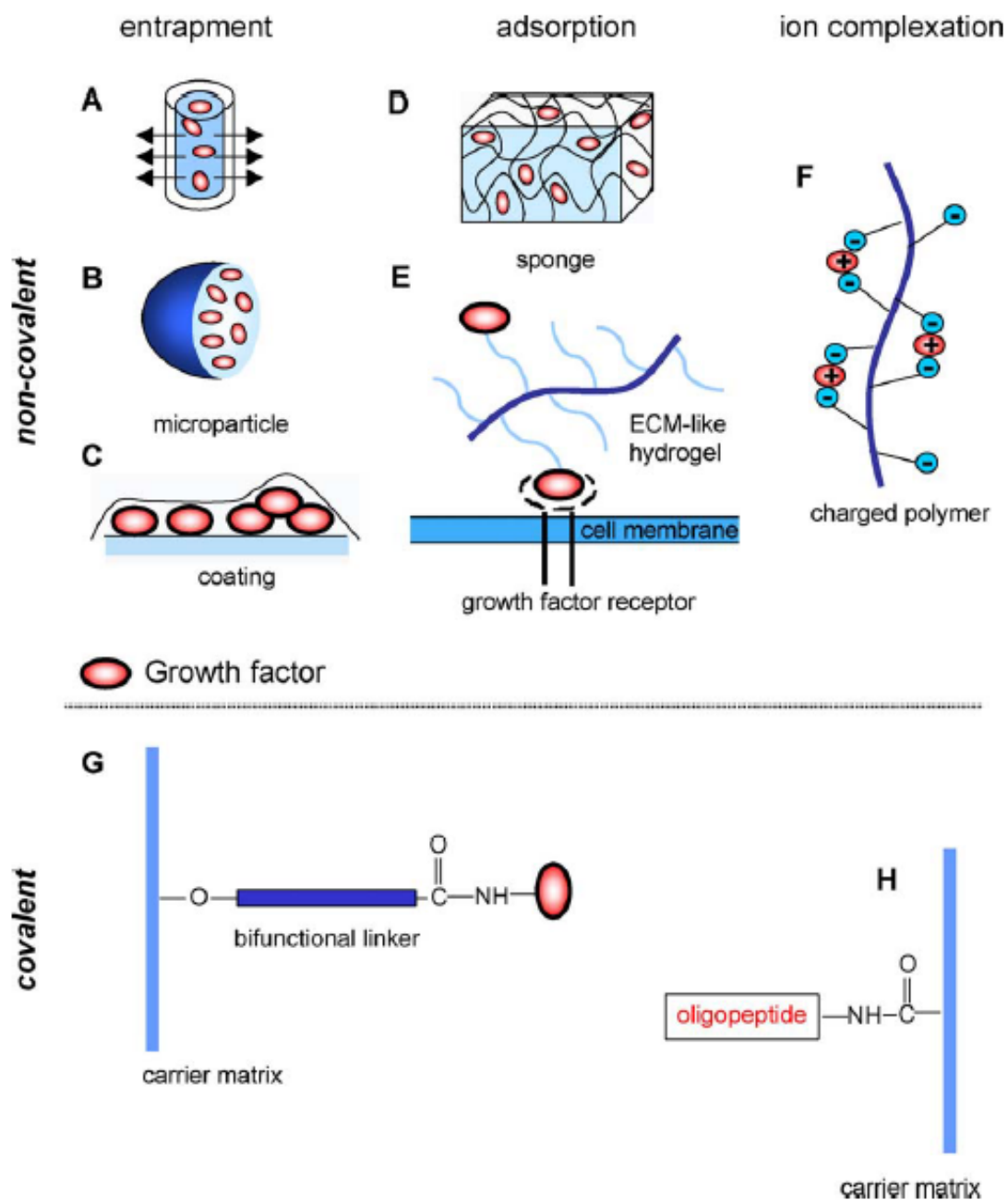


**Figure 1.10.** Non-covalent (A-F) and covalent (G-H) strategies used for the immobilisation and delivery of growth factors. Non-covalent strategies include physically entrapping the growth factor in a delivery vehicle (A), microparticle (B) or within a polymeric film (C), adsorbing the growth factor directly to the substrate surface (D), via intermediate carriers (for example, extracellular matrix (ECM)) (E) or through ion exchange mechanisms (F). Covalent immobilisation strategies include indirectly tethering the growth factor to the substrate surface by an intermediate linker (G) or by directly coupling the growth factor to the substrate surface (H). The illustrations were taken from Luginbuehl et al. [103].

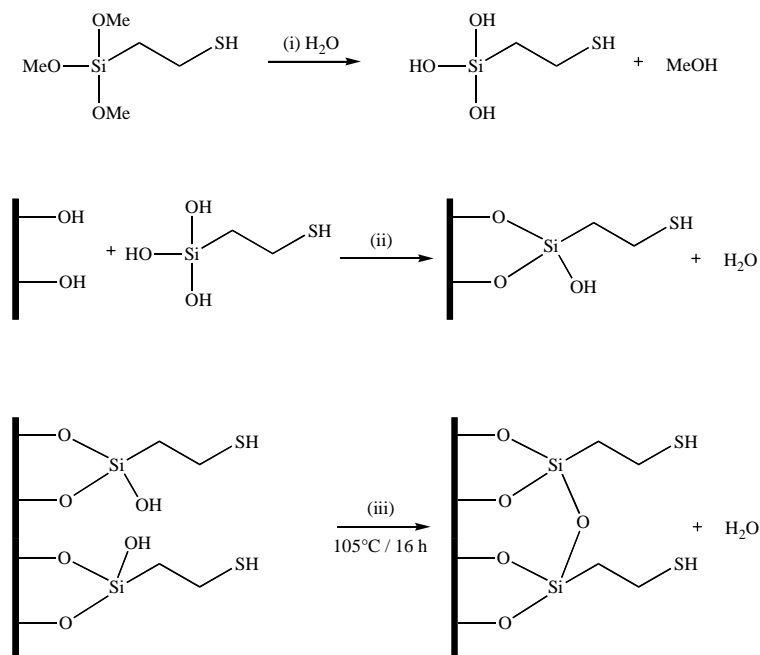
### 1.1.12 Silane chemistry for protein surface immobilisation

Since titanium and silica surfaces possess high densities of hydroxyl groups, silane chemistry has become a widely used method for introducing new functional groups (for covalent immobilisation of proteins) onto these substrate surfaces. Also, the chain of the silanes can also play an important role on the biomaterial surface. For example, silanes with protein resistant chains, such as poly(ethylene glycol), can be used to coat biomaterials to limit non-specific protein adsorption and consequently reduce the possibility of unwanted immunogenic responses to the implant [106].

Usually, mono-, di- or tri-alkoxysilanes are employed for the functionalisation of hydroxylated surfaces via a simple, rapid and very effective condensation reaction. An example of a 3-mercaptopropyl trimethoxysilane (3-MPTS) linking to a hydroxylated surface is shown in **Scheme 1.1** [107]. In the first step of the reaction, the physisorbed silane undergoes rapid hydrolysis of alkoxy (methoxy in this case) groups, liberating alcohol (methanol in this case) (**Scheme 1.1 (i)**). The silanol groups of the silane then condense with the surface silanol groups of the substrate through covalent interactions, releasing water as the by-product (**Scheme 1.1 (ii)**). In this case, the silane first reacted with adsorbed water on the substrate surface or with water in the reaction solution as depicted in **Scheme 1.1 (i)**. Under anhydrous conditions, the alkoxysilane could also directly react with surface hydroxyl groups, liberating alcohol as a by-product. This reaction would also result in a covalent linkage between the silane and the substrate surface. In the case of di- and tri-alkoxysilanes, the silane may form multiple attachment sites on the substrate surface or condense with neighbouring silanes to form multiple silane layers. Any silanol groups of the silane that have not reacted can be left and act as possible nucleation sites for apatite precipitation, or be heat treated (thermally cured) to form a more cross-linked and more stable siloxane layer (**Scheme 1.1 (iii)**) [107-109]. In the case of 3-MPTS, the siloxane layer introduces thiol functionalities on the surface. Thiols can covalently interact with the cysteine residues of proteins to form disulphide linkages. But surfaces can be functionalised with other reactive groups by silane chemistry including epoxy, carboxy and isocyanates

that are able to covalently react with the primary amino groups of the amino-terminus of proteins and of lysine side chains [110].

There are numerous reports available in the literature, which suggest covalent immobilisation strategies for biomolecules are useful for biomaterial applications [111]. For instance, biologically relevant peptides, enzymes and proteins have been covalently immobilised on amino-functionalised titanium surfaces via *N*-succinimidyl-3-maleimidopropionate (SMP) and glutaraldehyde cross-linking agents at concentrations sufficient for inducing biological activity, retaining enzyme activity and immunological reactivity, respectively [112-113]. *In vitro* mineralisation has also been enhanced on glass substrates functionalised with biologically relevant peptides after culturing osteoblast cells on the functionalised surfaces in the presence of a growth factor, osteogenic protein-1 (OP-1) [114]. *In vivo*, the performance of titanium orthopaedic implants has been enhanced by covalently attaching bioactive proteins on the substrate surface. For example, Morra et al. showed that titanium implants loaded with covalently bonded collagen exhibited a 23.8% increase in bone to implant contact (percentage of the bone apposed to the implant surface, divided by the total surface perimeter of the implant) and bone ingrowth (percentage of bone amount in the area delimited by the threaded surface, divided by the total threaded area) in comparison to uncoated controls after 4 weeks implantation in a rabbit femur [115]. To demonstrate the wide applicability of covalent immobilisation strategies via intermediate silane tethers, a stable and active concentration of antibiotic (vancomycin) has also been covalently bound to titanium making the surface bactericidal even after several repeated challenges [116].



**Scheme 1.1.** A reaction scheme depicting the condensation of 3-MPTS with surface hydroxyl groups (**i** and **ii**) and after thermally curing the siloxane layer (**iii**). Me refers to methyl ( $\text{CH}_3$ ). Scheme was adapted from Halliwell et al. [107].

### 1.1.13 Part one objectives

The main objective of Part 1 of this thesis was to improve cellular growth on PECVD-Si-Ti by functionalising the surface with the mitogenic factor IGF-1. Because PECVD-Si is already bioactive *in vivo*, we did not want to extensively alter the surface properties of the bioactive coating. Therefore, we compared the bioactivity of PECVD-Si towards promoting cellular growth on surfaces functionalised with IGF-1 by means of adsorption and covalent immobilisation. Both of these mechanisms can be controlled to not significantly change the surface characteristics of PECVD-Si. The main objectives of Part 1 of this thesis are outlined below:

- Prepare PECVD-Si coatings on titanium of high quality and reproducibility. Characterise the surface morphology and chemistry of PECVD-Si-Ti.
- Devise methods for producing stable siloxane layers on PECVD-Si-Ti.

- Introduce new functional groups through silane modification of PECVD-Si-Ti for the covalent immobilisation of IGF-1. Identify the surface functional groups and characterise the reactivity of the functional surface.
- Develop an immobilisation strategy for achieving an active concentration of IGF-1 on the functional PECVD-Si-Ti surface. Compare the immunological activity of adsorbed and covalently immobilised IGF-1.
- Analyse the biological activity of PECVD-Si-Ti surfaces functionalised with IGF-1 through *in vitro* osteoblast-like cell culture assays.

## 1.2 Materials and Methods

### 1.2.1 Substrate preparation

Titanium with a purity of 99.7% and a thickness of 0.25 mm was purchased from Sigma. The metal was carefully cut into small discs with a diameter of 15 mm. Before using the specimens for subsequent experiments, the substrates were cleaned in a surfactant solution. This involved transferring each specimen into a 20 ml glass vial (Crown Scientific) containing 5 ml of a 0.5% (w/v) Pyroneg (Diversey) detergent solution, prepared in water. The vials were sealed with a plastic cap and the samples were cleaned by ultrasonication in a Soniclean 160HT unit at 60°C for 40 min. The samples were washed 6 times in water and ultrasonicated for a further 20 min in water at 60°C. After washing another 3 times in water, each specimen was dried under a stream of N<sub>2</sub> and stored in a plastic Petri dish under vacuum.

The water used for these and all subsequent experiments was purified in a Labconco WaterPro PS system equipped with a carbon and 3 deionisation cartridges. The unit was operated at a resistivity of 18.2 Mega  $\Omega$ ·cm and the water was dispensed through a 0.2  $\mu$ m hollow fiber filter supplied by the manufacturer.

The morphological characteristics of the samples were characterised by atomic force microscopy (AFM) and scanning electron microscopy (SEM) (refer to **page 46**). The surface elemental composition was examined by X-ray photoelectron spectroscopy (XPS) (refer to **page 45**).

## 1.2.2 Buffer preparation

### *Phosphate buffered saline (PBS)*

Phosphate buffered saline (PBS) was prepared by dissolving 13.7 mM NaCl, 2.7 mM KCl, 5.3 mM Na<sub>2</sub>HPO<sub>4</sub> and 1.8 mM KH<sub>2</sub>PO<sub>4</sub> in water at 25°C for 30 min. The pH was adjusted to 7.4 with the addition of HCl and the solution was filter-sterilised through a 0.2 µm filter (PALL) and then autoclave sterilised at 125°C for 15 min.

### *Carbonate buffer*

Carbonate buffer was prepared by dissolving 15.0 mM Na<sub>2</sub>CO<sub>3</sub> and 34.9 mM NaHCO<sub>3</sub> in water at 25°C. The pH of the solution was 9.6. The solution was filter-sterilised through a 0.2 µm filter (PALL) and then autoclave sterilised at 125°C for 15 min.

### *Sodium phosphate buffer*

A 0.2 M solution of sodium phosphate, mono-sodium salt was prepared by dissolving 27.6 g of NaH<sub>2</sub>PO<sub>4</sub>·1H<sub>2</sub>O in 1000 ml of water (Solution A). A 0.2 M solution of sodium phosphate di-sodium salt was prepared by dissolving 53.62 g of Na<sub>2</sub>HPO<sub>4</sub>·7H<sub>2</sub>O in 1000 ml of water (Solution B). Solutions A and B were filter-sterilised through a 0.2 µm filter (PALL) and then autoclave sterilised at 125°C for 15 min. 0.1 M of sodium phosphate buffer with a pH of 8.0 was prepared by mixing 5.3 ml of Solution A with 94.7 ml of Solution B and 100 ml of filtered and autoclaved water.

All reagents used for the preparation of the buffers were of Analytical Grade.

### 1.2.3 Plasma enhanced chemical vapour deposition (PECVD) of silica on titanium

A photograph of the PECVD system is shown in **Figure 1.11 A**. The system can be divided into 3 major components: a vacuum line, plasma generator, and a vapour delivery system (**Figure 1.11 A and B**).

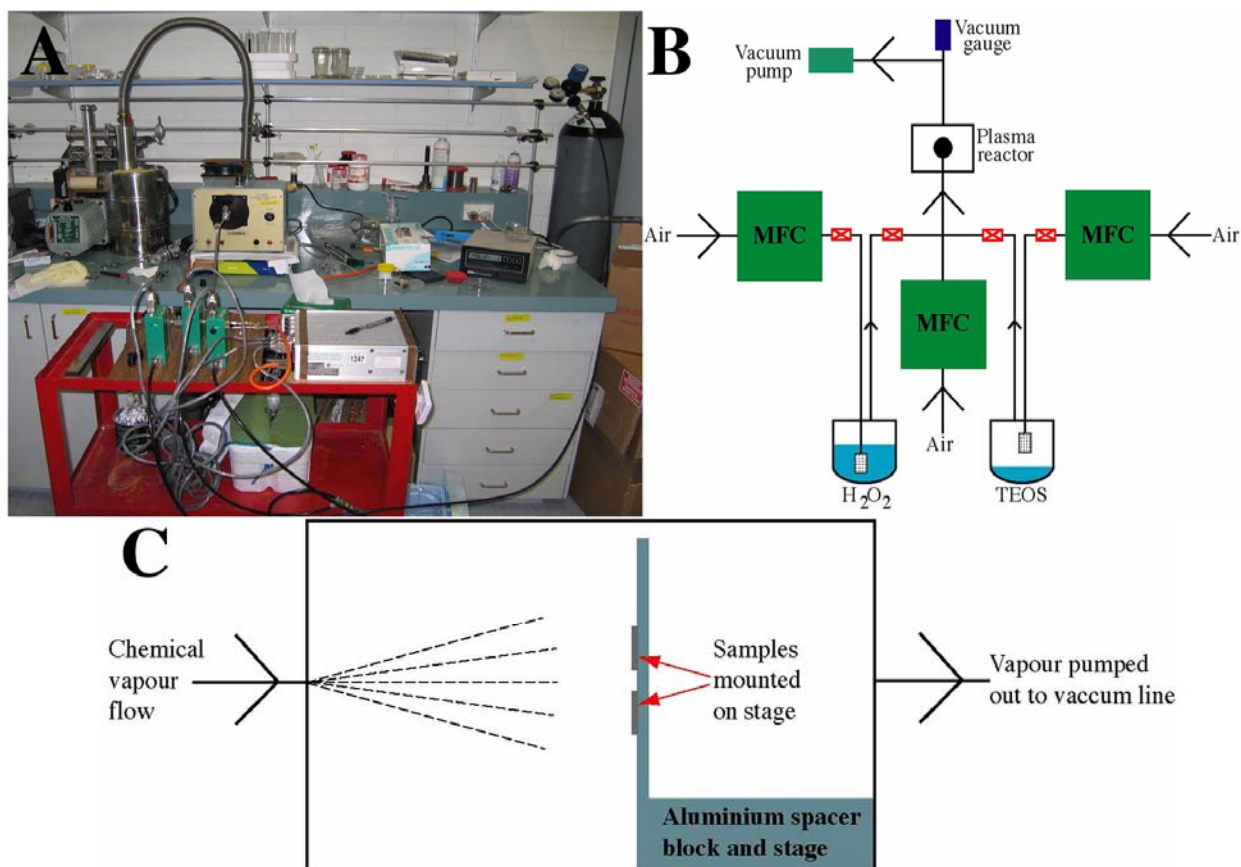


**Figure 1.11.** The PECVD experimental set-up that was used for coating PECVD-Si films on titanium substrates. A photograph of the set-up is shown in (A). An illustration of the vapour delivery system is shown in (B). MFC denotes mass flow controller. An illustration of titanium samples (for PECVD-Si coating) mounted on the stage in the glass chamber of the Harrick radio-frequency plasma generator is shown in (C).

The vacuum line consists of a Javac rotary pump (model # DD150) filled with chemically inert oil (Fomblin). A cold trap cooled in liquid N<sub>2</sub> is connected between the pump and the plasma chamber to prevent the possibility of back-streaming of contaminating hot oil vapour from the pump to the samples and the pressure was recorded between the cold trap and the plasma chamber with a piranha gauge (MKS) (**Figure 1.11 B**).

A radio-frequency plasma generator (model # PDC-32G) made by Harrick was operated at 100 W and 13.56 MHz. An external fan located at the top unit cooled the plasma chamber. The glass chamber of the Harrick unit is defined by a length of 18 cm and a diameter of 7 cm. The samples were positioned in the glass chamber according to the optimal location determined from previous studies, which was found to be 7 cm from the rear of the chamber and parallel to the centre of the inlet valve located on the chamber lid (**Figure 1.11 C**). The chamber could be isolated from the vapour delivery system by closing the inlet valve and was opened 1/2 a turn during plasma processing. The titanium substrates were held to the stage by a small piece of Scotch 3M double-sided adhesive. After plasma processing, the adhesive was carefully scraped off from the underside of the substrate with a stainless steel blade and the specimen washed in methanol. Six 15 mm diameter titanium discs were coated in each run to ensure all samples were located close to the optimal position for silica deposition.

Three MKS mass flow controllers controlled the flow of air vapour. An MKS digital readout module (model # 247D) connected to each mass flow controller (MFC) was used to set and record the flow rates through each MFC. The middle MFC (model # M100B12CS1BV) in **Figure 1.11 A-B** purged air (BOC; Instrument Grade) into the plasma chamber at a set flow rate of 10 sccm. The right MFC (model # M100B11C1SBV) purged air into the tetraethoxysilane (TEOS) vessel at 2 sccm. The MFC (model # M100B12CS1BV) on the left purged air into the H<sub>2</sub>O<sub>2</sub> flask with a setting of 2 sccm. The 2-stemmed TEOS glass container was 11 cm in height with a diameter of 4 cm. The glass frit, where air was purged through, was situated 1 cm from the bottom of the vessel. The vessel was filled with 5 ml of 98% pure TEOS (Sigma) to a level well below the frit and the vessel was kept in crushed ice (0°C) during plasma processing. 40 ml of an aqueous

solution of 30% H<sub>2</sub>O<sub>2</sub> (Chem-Supply) was filled in a 100 ml 2-stemmed round bottom flask so the frit would be submerged in the liquid. The vessel was kept at 25°C and the flask was covered with aluminium foil to shield it from ambient light.

Before plasma processing, the cold trap was allowed to cool in liquid N<sub>2</sub> and the TEOS vessel was chilled in ice for approximately 10 min. The plasma chamber would then be pumped down to base pressure ( $2 \times 10^{-2}$  Torr) defined by the pressure of the vacuum line and plasma chamber, but excluding the vapour delivery system. The TEOS vessel was then connected to the vacuum system and evacuated 3 times. The glass chamber was then cleaned in an air plasma for 20 min at an airflow rate of 10 sccm to remove impurities inside the chamber.

After transferring the samples into the chamber, the system was pumped to base pressure before air was flowed through the system. The pressure was allowed to stabilise to  $2 \times 10^{-1}$  Torr and the plasma was switched on for 20 min. At the end of this cleaning/oxidation step, the plasma was switched off and the airflow was maintained. Air was then purged through the TEOS vessel and the mixed air/TEOS vapour was slowly introduced into the chamber to obtain a pressure of  $3 \times 10^{-1}$  Torr. The plasma was then switched on for 30 min. Afterwards, air and air/TEOS supply into the chamber was stopped. For samples treated with H<sub>2</sub>O<sub>2</sub> vapour, the system would be pumped down to base pressure before introducing air/H<sub>2</sub>O<sub>2</sub> vapour into the chamber. The plasma was then switched on (usually for 5 min) after the pressure had stabilised (to  $3.2 \times 10^{-1}$  Torr). Before removing the samples the system was allowed to cool to ambient temperature under vacuum. All samples were stored in a plastic desiccator under vacuum.

The morphology of the air-plasma processed titanium samples was characterised by AFM (refer to **page 46**). Micrographs of the surface of PECVD-Si coated titanium (PECVD-Si-Ti) samples were acquired by SEM (refer to **page 46**). A profilometer (DEKTAK 6M Stylus Profilometer, Veeco) was used to measure the thickness of the PECVD-Si film. For thickness measurements, sticky tape was used to mask half the area of the titanium surface during the deposition of PECVD-Si films. The mask was then removed by ultrasonication

in acetone (Analytical Grade; Chem-Supply) until no residual tape could be seen by visual inspection. The sample was placed under the profilometer and a section analysis of the interface between the coated and the non-coated area was performed from which the thickness of the coating was determined. The surface chemistry of PECVD-Si-Ti was analysed by XPS and infrared (IR) spectroscopy (refer to **pages 45-46**).

#### **1.2.4 Characterisation of hydroxyl group surface coverage on PECVD-Si-Ti**

Hydroxylation of PECVD-Si-Ti surfaces were characterised by 3 methods. Contact angle measurements, XPS analysis after derivatisation of hydroxyl groups by trifluoroacetic anhydride (TFAA) and after fluoro or amino alkoxy silane derivatisation.

##### *Contact angle measurements*

Contact angle measurements were performed on a custom-built stage that allowed the sample to be positioned in the  $x$ ,  $y$  and  $z$  directions. Samples were spotted with 2  $\mu$ l of water with a mechanical pipette in an ambient atmosphere. Images were then quickly recorded on a Panasonic WV BP550 CCTV camera to minimise any effects as a result from water evaporation. Processing was performed using Scion Image v4.0.2 software. Measurements were taken on the left and right side of the water droplet from 2 samples (total of 4 measurements per sample type).

##### *TFAA derivatisation*

Cleaned uncoated titanium, silicon (Virginia Semiconductor Inc., Virginia) (cleaned by ultrasonication in methanol (Analytical Grade; Chem-Supply)) and PECVD-Si-Ti (with air/H<sub>2</sub>O<sub>2</sub> plasma treatment times ranging from 1-15 min) were derivatised with TFAA (Sigma) using the three methods given below.

### Method 1

Samples were placed face up at the bottom of a sealed glass container containing a separate vial of TFAA solution (1 ml). The reaction was allowed to proceed for 1 h at 25°C. The samples were then washed with methanol, dried under N<sub>2</sub> and stored under vacuum.

### Method 2

These reactions were performed in a custom-built vessel (Refer to **Figure 2.10**). The samples were attached to a glass slide that was inserted to the bottom of the vessel. The vessel was evacuated and back-filled with dry nitrogen gas (3 times) before the lid of the chamber holding the reservoir of TFAA solution was slowly opened. TFAA vapour was allowed to react with the samples for 1 h at 25°C. In one set of experiments the TFAA solution was kept at 40°C to increase the flow of TFAA vapour into the reaction chamber. All samples were washed with methanol, dried under N<sub>2</sub> and kept under vacuum.

### Method 3

Samples were incubated in TFAA solution at 25°C for 5 and 60 min time periods in 20 ml glass vials (Crown Scientific). The samples were washed with methanol, dried under N<sub>2</sub> and kept under vacuum.

## **1.2.5 Grafting of alkoxy silane molecules on PECVD-Si-Ti**

Two different alkoxy silanes were reacted on PECVD-Si-Ti samples (with and without treatments of air/H<sub>2</sub>O<sub>2</sub> plasma) through condensation reactions between the alkoxy groups of the silane and the surface hydroxyl groups of the samples. The 3 fluorine atoms of  $\geq 97\%$  pure 3,3,3-trifluoropropyl trimethoxysilane (FPTMS) (Fluka) and the nitrogen atom of 99% pure 3-aminopropyl triethoxysilane (APTES) (Aldrich) were used as marker elements in XPS analysis.

The reaction parameters that were tested are listed in **Table 1.2**. Toluene (Analytical Grade; Chem-Supply) was prepared by distilling over sodium (Reidel-deHaën) and benzophenone indicator (Chem-Supply) in an atmosphere of dry N<sub>2</sub> and the distilled solvent was stored

under dried molecular sieves. Methods 2 A and B were performed in round bottom glass flasks containing 5 ml of silane solution under a dry N<sub>2</sub> atmosphere. Methods 1 and 3-5 were performed in 20 ml glass vials containing 5 ml of silane solutions and were covered with aluminium foil. These samples were incubated at 25°C and mixed on a RATEK orbital mixer set at 3.5. All samples were washed in toluene, dried under a stream of N<sub>2</sub> and stored under vacuum. For curing, the silane-labeled samples were incubated in an oven (Binder) at the designated temperature and time as listed in **Table 1.2**.

The stability of siloxane films was tested under a physiological condition. This involved transferring the samples to a 12-well TCPS plate (Nunc) and incubating in 2 ml of sterile PBS under cell culture conditions (humidified atmosphere at 37°C and 5% CO<sub>2</sub>). These samples were then rinsed in water, dried under N<sub>2</sub> and stored under vacuum before analysis. In addition to this, the stability of the PECVD-Si film coated on titanium was tested by incubating PECVD-Si-Ti in boiling toluene at 120°C for 12 h. After this, the sample was washed in toluene, dried under a stream of N<sub>2</sub> and stored under vacuum before analysis.

Method	Solvent type	Concentration	Temperature and time	Curing step
1	Toluene	100 mM	25°C; 1 h	Not performed
2 (A and B)	Toluene	100 mM	Refluxed 1 h, then heated additional at 90°C for 12 h	Samples were not cured (A) or cured at 100°C for 12 h (B)
3	Aqueous: Methanol containing 5% (v/v) water and 1 mM of acetic acid	1% (v/v)	25°C for 2.5 h	120°C for 5 min
4	Neat	Undiluted	90°C for 1h	Not performed
5	Toluene	1% (v/v)	25°C for 2.5 h	120°C for 5 min

**Table 1.2.** Summary of the alkoxysilane grafting methods used for preparing siloxane films on PECVD-Si-Ti.

The density of amino groups generated on APTES functionalised PECVD-Si-Ti was determined using 2,4,6-trinitrobenzenesulfonic acid (TNBS) (Sigma). First, the molar extinction coefficient of the trinitrophenol (TNP)-APTES compound was determined according to the following description: 0.25% (w/v) of TNBS was incubated with 0.5 M of APTES in sodium phosphate buffer of pH 8.0 (refer to **page 31**) at 25°C for 1 h with gentle mixing; 20 µl of the reaction solution was incubated with 1.98 ml of NaOH (Analytical Grade) at 25°C for 1 h (pH of solution was 12.7); 500 µl of this solution was then incubated with 100 µl of 1 M of HCl (pH of solution was 1.0); and finally, the absorbance from 280-500 nm of the solutions was analysed in a Hewlett Packard 8452 UV-Vis spectrometer in a quartz cuvette. Second, the test samples (with a surface area of 1.78 cm<sup>2</sup>) were incubated with 0.25% (w/v) TNBS in sodium phosphate buffer of pH 8.0 at 25°C for 1 h with gentle mixing; the remainder of the reactions were performed as described above. The amino group density was calculated using the molar extinction coefficient at 350 nm for TNP-APTES at pH 1.0 and the absorbance of the test reaction solutions at 350 nm.

### **1.2.6 Development of surface modification techniques on PECVD-Si-Ti for the attachment of insulin-like growth factor-1 (IGF-1)**

PECVD-Si-Ti was functionalised with neat solutions of 90% pure triethoxysilyl butyraldehyde (ABTES) (Gelest) and 98% pure 3-glycidoxypropyl trimethoxysilane (GPTMS) (Aldrich) molecules according to Method 4 outlined in **Table 1.2**. Neat and diluted solutions of 3-isocyanatopropyl triethoxysilane (IPTES) (Fluka; purity ≥ 95%) were reacted with PECVD-Si-Ti (according to Methods 1 and 4 from **Table 1.2**). The modified surfaces were analysed by XPS (refer to **page 45**).

2,2,2-trifluoroethylamine (FEAM) (Aldrich) was reacted on PECVD-Si-Ti functionalised with epoxide, aldehyde and isocyanate reactive groups (as described above). Aldehydes and epoxides were reacted with 2 ml of 100 mM FEAM in either carbonate pH 9.6 or sodium phosphate (pH 8.0) buffers (refer to **page 31** for details of the buffers). Amino reaction solutions used for aldehyde surface functional groups were supplemented with 50 mM of NaCNBH<sub>3</sub> (Sigma). Isocyanates were reacted with 2 ml of 100 mM of FEAM prepared in

PBS, pH 7.4. Reactions were performed at 25°C for 2 h in 24-well TCPS plates (TPP) on a RATEK orbital mixer set to a mixing setting of 3.5. The samples were rinsed in a stream of water and dried under N<sub>2</sub>. Negative control samples were prepared by incubating PECVD-Si-Ti (not functionalised with alkoxysilanes) in the reaction solutions as described above for each sample type. All samples were analysed by XPS (refer to **page 45**).

### **1.2.7 Immunological activity of immobilised IGF-1 on PECVD-Si-Ti**

An immunosorbent assay was developed for analysing the immunological activity of covalently immobilised IGF-1 on non-functionalised and IPTES-functionalised PECVD-Si-Ti. The immunoassay is described below.

Lyophilised recombinant human IGF-1 (referred to as IGF-1) and a biotinylated anti-human IGF-1 antibody (anti-IGF-1) were purchased from R&D Systems. Lyophilised peroxidase conjugated streptavidin (HRP-Strep) was purchased from Rockland. IGF-1 was reconstituted in PBS to obtain a stock protein concentration of 100 µg/ml. The anti-IGF-1 molecule was reconstituted in tris-buffered saline (20 mM of tris(hydroxymethyl)aminomethane (Sigma; purity ≥ 99.9%), 150 mM NaCl (Ace Chemical Company); adjusted to pH 7.3 and sterilised by autoclaving) to a concentration of 50 µg/ml. HRP-Strep was reconstituted in autoclave-sterilised water to a concentration of 1 mg/ml. All stock solutions were stored at -80°C.

The blocking solution was prepared by dissolving 2.5% (w/v) bovine serum albumin (BSA) (Sigma; purity ≥ 96%) in PBS and syringe filtering through a sterile 0.2 µm filter (PALL) into a sterile plastic vial. Dilution buffer was made by mixing 0.05% (v/v) Tween<sup>®</sup> 20 (Sigma) in a filtered solution of 1% (w/v) bovine serum albumin (BSA) (Sigma) prepared in PBS. Working concentrations of proteins were obtained by diluting anti-IGF-1 to 0.5 µg/ml and HRP-Strep to 0.2 µg/ml (the concentration of IGF-1 was varied as described in the results and discussion section of Part 1) in the dilution buffer. Solutions of 0.5% and 0.05% (v/v) Tween<sup>®</sup> 20 (PBS-T) were prepared in PBS.

Double-sided adhesive (Scotch, 3M) was punched to the same diameter as the test samples (15 mm). The tape, with the cover left on, was inserted into the well of a 24-well TPP tissue culture polystyrene plate. The well was blocked with 600  $\mu$ l of blocking solution at 25°C for 1 h and mixed on a RATEK orbital mixer set at 3.5. The well was washed 4 times in PBS-T (0.05% (v/v)) and 4 times in PBS (using 1.5 ml/wash). The tape cover was removed and the test sample was carefully inserted into the well. 300  $\mu$ l of IGF-1 or PBS (with no IGF-1) to the same volume (for negative controls) were dispensed into the wells, incubated at 25°C for 2 h with mixing and washed 4 times with PBS-T (0.5% (v/v)) and 4 times with PBS. The plate was inverted and gently tapped on paper towel to remove excess liquid. Unreacted isocyanate groups on IPTES-functionalised samples were quenched by incubating in 1 ml of a 1 mM filtered solution of ethanolamine hydrochloride (Sigma) prepared in PBS, pH 7.4, at 25°C for 30 min with mixing. The wells were washed 4 times in PBS and blocked again with blocking solution at 25°C for 1 h with mixing and washed 4 times in PBS-T (0.05% (v/v)). 300  $\mu$ l of anti-IGF-1 was added, incubated at 25°C for 1 h with mixing and washed 4 times in PBS-T (0.05% (v/v)). 300  $\mu$ l of HRP-Strep was added, incubated at 25°C for 1 h with mixing and washed 4 times in PBS-T (0.05% (v/v)). 300  $\mu$ l of *o*-phenylenediamine dihydrochloride (OPD) (Sigma) solution (prepared according to the manufacturers instructions by dissolving the urea buffer tablet first in 20 ml of water and then the OPD tablet) was added. The plate was covered with aluminium foil to keep out ambient light and incubated at 25°C for 10 min with mixing. 100  $\mu$ l of the test solution was transferred to a 96-well plate (Iwaki) and the absorbance measurements were taken on a Molecular Devices Vmax microplate reader at 450 nm. Absorbance readings were corrected for background absorbance values measured from empty 96-well (Iwaki) plates at 450 nm and adjusted according to the absorbance measured for the negative controls.

### 1.2.8 Assessment of IGF-1 biological activity on PECVD-Si-Ti

The two cell types used in these experiments, MG63 and 3T3 Balb/c, were both donations from TGR Biosciences. MG63 cells were cultured in minimal essential medium (MEM) purchased from JRH Biosciences in powdered form. MEM was prepared according to the manufacturer's instructions by dissolving 9.61 g/l of the powder and 2.2 g/l of NaHCO<sub>3</sub> in water (pH was adjusted to 7.1) and filter-sterilizing through a 0.2 µm filter (PALL). The medium was supplemented with 10% (v/v) foetal bovine serum (FBS) (Bovogen Biologicals) and 100 units of penicillin and 100 µg of streptomycin antibiotics (Sigma). 3T3 Balb/c cells were cultured in Dulbecco's modified Eagle's medium (DMEM) (JRH Biosciences), which was prepared by dissolving 13.4 g/l of the powder and 3.7 g/l of NaHCO<sub>3</sub> in water (pH was adjusted to 7.1) and filter-sterilizing through a 0.2 µm filter (PALL). The medium was supplemented with 10% (v/v) FBS and 100 units/ml penicillin-streptomycin antibiotics. Cells were stored either in frozen stocks in FBS containing 10% (v/v) of ≥ 99.9% pure dimethyl sulfoxide (DMSO) (Sigma) at -80°C or were maintained growing in 75 ml tissue culture flasks (Iwaki) under cell culture conditions, that is, at 37°C in a humidified incubator (Lunaire) with an atmosphere of 5% CO<sub>2</sub> (BOC; food grade) and periodically passaged with the aid of trypsin (Sigma).

All PECVD-Si-Ti samples were loaded with IGF-1 as described for the enzyme-linked immunosorbent assay (ELISA) on **pages 39-40** except the samples were not glued into wells of a multi-well plate. Instead, the IGF-1 solution was dispensed over the samples so that a meniscus was formed, which covered the entire surface area. The solution was then incubated over the samples under humidity and the samples were washed three times by immersing the samples in 3 separate vials of PBS. Samples were then transferred to a 12-well plate for quenching any unreacted isocyanate groups as described for the ELISA. The samples were then used immediately for the experiments. Uncoated titanium and PECVD-Si-Ti samples not functionalised with IPTES were cleaned/sterilised by incubating in 70% (v/v) ethanol (Analytical Grade) (prepared in sterilised water) at 25°C for 15 min, and were then rinsed in sterilised water and air-dried. TCPS discs were purchased sterilised from the manufacturer (Sarstedt).

The biological activity of immobilised IGF-1 on PECVD-Si-Ti was assessed according to the following assays:

*AlamarBlue™ cell vitality assay*

Cell viability and proliferation was assessed by using an alamarBlue™ dye (purchased from Jomar Diagnostics). This involved washing cells that had grown in 96 or 24 well plates twice with 200 µl or 1 ml of PBS (warmed to 37°C), respectively. 100 or 300 µl of alamarBlue™ diluted in PBS at a ratio of 1:10 (and warmed to 37°C) was added to either 96 or 24 well plates, respectively, and incubated under cell culture conditions for 1 h. 100 µl of solution from each well was then transferred to a 96-well (Iwaki) plate for the experiments performed in 24-well plates (alamarBlue™ experiments performed in 96-well plates did not require solution transfer because these plates were suitable for the microplate reader). Absorbance readings were taken on the Molecular Devices Vmax microplate reader at 570 and 600 nm. All absorbance readings were corrected for background absorbance of empty test wells at 570 and 600 nm. The negative control samples were treated exactly the same as the test samples except that the cell culture medium (that was incubated over the samples) did not contain cells.

Cell vitality on titanium and TCPS discs was assessed in 24-well ultra-low cell attachment plates (Dow Corning). The hydrogel coated on the bottom of these wells was hydrated in serum-free MEM or DMEM (supplemented with antibiotics) under cell culture conditions for 1 h. The wells were then washed with the medium 3 times before inserting the test samples. Experiments were then conducted according to the alamarBlue™ assay procedure described above.

*AlphaScreen™ SureFire™ p-ERK assay*

The AlphaScreen™ SureFire™ p-ERK assay was performed in two ways. The first method involved analysing p-ERK concentrations from populations of cells that had attached onto the test samples (functionalised and non-functionalised with IGF-1) for a short time period.

For these experiments, cell dissociation solution (CDS; Sigma) was used instead of trypsin for dislodging cells from the 75 ml tissue culture flask (Iwaki). This involved rinsing cells 3 times with 10 ml of Hank's balanced salt solution (HBSS) (warmed to 37°C) and then incubating cells in 5 ml of CDS (warmed to 37°C) under cell culture conditions for 20 min. The cells were then scraped from the flask with a cell scraper (TPP). The solution was centrifuged at 200 RCF and 25°C for 5 min in a Sigma 3-18K fixed-rotor bench-top centrifuge. The solution was decanted and the cells were resuspended in MEM or DMEM supplemented with 1 mg/ml of BSA. The cells were incubated under cell culture conditions for 1 h before being diluted to an appropriate cell concentration as indicated in the following sections. Cell densities were determined from haemocytometer cell counts. The cells were then incubated over the test samples for 10 or 30 min time periods under cell culture conditions. The surface was washed once with medium (warmed to 37°C) and the remainder of the experiment was performed according to the manufacturer's instructions (see below).

The second method involved analysing phosphorylated extracellular-signal-regulated kinase (p-ERK) concentrations from a population of cells that had been grown to confluency in a 96-well TCPS plate (Iwaki). The test wells (with a confluent coverage of cells) were washed twice with HBSS. The cells were then serum-starved for 2 h under cell culture conditions in 200 µl of serum-free medium. 100 µl of medium was removed from the test well and the cells were stimulated with 100 µl solutions of IGF-1, whey growth factor extract (WGFE; a kind donation from TGR Biosciences) or FBS (IGF-1, WGFE and FBS were diluted in cell culture medium) for 5, 10 or 15 min time periods.

The remainder of the experiment was identical for both methods and was performed according to the manufacturer's instructions (see below).

After removing the medium from the cells, 100 µl for 96-well plates or 300 µl for 24-well plates of Lysis Buffer (diluted to 1X in sterile water) supplied in the AlphaScreen™ SureFire™ p-ERK assay kit (provided by TGR Biosciences) was incubated over the cells

and mixed on a RATEK orbital mixer set at 3.5 for 10 min at 25°C. The solutions were then stored frozen until use.

The remainder of the assay was performed at TGR Biosciences. 40 µl of the thawed cell lysate was transferred to a separate well. 10 µl of Activation Buffer (in the AlphaScreen™ SureFire™ p-ERK assay kit) was added to the cell lysate to give a final concentration of 20% (v/v) Activation Buffer. The plate was mixed for 2 min at 25°C. 5 µl of the activated lysate was transferred to a 384-well Proxiplate™ (Perkin Elmer). 6 µl of the Reaction Buffer (containing AlphaScreen™ beads) was added to the activated lysate. The plate was sealed and covered with aluminium foil to shield it from ambient light. The plate was then incubated at 25°C with gentle mixing for 2 h. Finally, fluorescence measurements in the test wells were recorded on an AlphaScreen™ plate reader using standard AlphaScreen™ settings.

#### *Fluorescence microscopy*

Cellular nuclei were stained with a Hoechst 33342 (Molecular Probes) nuclear dye. The commercial stock of Hoechst 33342 dye was diluted to 0.1 mg/ml in PBS. 100 µl of the dilution was added to 1 ml of cell culture medium and incubated with the cells under cell culture conditions for 1 h. The cells were washed twice in PBS. Fluorescence micrographs of the cells were taken as described below.

Cellular filamentous actin was stained with an Alexa Fluor® 594 phalloidin (Molecular Probes) dye. After washing cells twice in PBS warmed to 37°C, the cells were fixed with 4% (v/v) formaldehyde for 10 min at 25°C. The cells were washed twice with PBS. The cell membrane was then permeabilised by incubating in 1 ml of 0.1% (v/v) Triton X-100 (Sigma) prepared in PBS at 25°C for 5 min. The cells were washed twice with PBS. A working concentration solution of Alexa Fluor® 594 phalloidin was prepared by dissolving the dye in 1.5 ml of methanol to yield a final concentration of 6.6 µM. A working concentration dye was prepared by diluting 25 µl of Alexa Fluor® 594 phalloidin stock solution per 1 ml of PBS supplemented with 1% (w/v) of BSA. 300 µl of this solution was

incubated with the cells at 25°C for 20 min. The cells were washed twice in PBS and once with water.

Fluorescence micrographs were acquired on an Olympus IX81 microscope using 10x/0.4 or 20x/0.75 UPlanSApo objectives through an F-View II fluorescence charge coupled device (CCD). Hoechst 33342 dye fluorescence was excited through a 360-370 nm excitation filter and the emission was recorded through a 420-460 nm barrier filter. Alexa Fluor 594 dye was excited through a 530-550 nm excitation filter and the emission was recorded through a 575-625 nm barrier filter. Images were processed using AnalySIS LS Research v2.5 software (Soft Imaging Systems) and false coloured using the colours designated for each dye as provided in the database of the software.

### **1.2.9 X-ray photoelectron spectroscopy**

XPS analysis was performed on two instruments (depending on the availability of the instruments). The first was a Physical Electronics PHI 5600 ESCA system. Spectra were acquired using the non-monochromated Mg  $K_{\alpha}$  X-ray ( $h\nu = 1253.6$  eV) source at a base pressure lower than  $10^{-8}$  Torr, an accelerating potential of 15 kV and a take-off angle of 45°. The other instrument was a Kratos Axis Ultra DLD. Spectra were recorded on this instrument using the monochromated Al  $K_{\alpha}$  ( $h\nu = 1486.6$  eV) X-ray source at a base pressure better than  $10^{-9}$  Torr, accelerating potential of 15 kV and a take-off angle of 45°. The pass energy for a survey spectrum was 93.9 eV on the Physical Electronics PHI 5600 ESCA and 160.0 eV on the Kratos Axis Ultra DLD spectrometers. Elements on the surfaces were identified from the survey spectrum. Atomic concentrations were calculated from the integral peak intensities of the main photoelectron peak for each element identified in the spectrum using a Shirley-type background and the sensitivity factors supplied by the manufacturers' of the instruments. High-resolution spectra of individual elements were taken at a pass energy of 23.5 eV on the Physical Electronics PHI 5600 ESCA and 20.0 eV on the Kratos Axis Ultra DLD spectrometers. Individual components were fitted to the high-resolution spectra assuming a Gaussian-Lorentzian with a 30% Lorentzian component. The full-width-half-maximum (FWHM) was constrained to have the same value as the  $CH_X$

component in the C 1s region and the component fitted at the lower binding energy value, C 2 (assigned to NH<sub>2</sub>), in the N 1s region. Charging effects of the samples during analysis were corrected to 285.0 eV for hydrocarbon in the C 1s region. Samples were analysed in duplicate unless stated otherwise.

### **1.2.10 Infrared spectroscopy**

Fourier transform-IR (FT-IR) spectroscopy was performed on a Nicolet Avatar<sup>®</sup> 370MCT, by using a smart apertured grazing angle (SAGA) accessory supplied by the manufacturer. This accessory allows information to be obtained for thin films ranging from 1 nm to 1 µm in depth. Before analysis, the detector was cooled with liquid N<sub>2</sub> for 15 min and samples were placed face down on the aperture of the SAGA accessory. The instrument was allowed to purge with purified dried air for 1 h before analysis. The air was purified in a Norgren hydrocarbon vapour adsorption filter and dried in a Parker FT-IR purge gas generator at 10 scfh before entering the instrument. Background spectra were taken on cleaned uncoated titanium substrates. The spectrum was recorded at a resolution of 4 wavenumbers/cm and 64 scans.

### **1.2.11 Atomic force microscopy**

Samples were analysed using a Nanoscope 4 Multimode microscope (Digital Instruments) in Tapping Mode. High frequency commercial silicon cantilevers (TESP, Veeco Instruments, USA) were used. Root mean square (RMS) roughness values were calculated from height images using the Nanoscope 5.12r3 software (Digital Instruments).

### **1.2.12 Scanning electron microscopy**

Images of samples were taken on a Phillips XL30 operated at 10 kV. All samples were coated with a thin layer of platinum to a thickness of 2 nm to prevent charging effects during analysis.

### **1.2.13 Statistical analyses**

The data was processed using Kaleidegraph version 4.0 software. The raw data from each sample set was categorised into groups. Statistical analyses was performed using a Student t-Test by comparing the means of each independent group assuming that the variances of each group are equal. A  $p$  value of less than 0.05 was considered to be of significant difference.

## 1.3 Results and Discussion

### 1.3.1 Characterisation of silica films deposited on titanium by plasma enhanced chemical vapour deposition (PECVD)

To begin this study, the properties of the titanium surface will first be addressed. Because this research was based on previous investigations, high-purity titanium sheet (99.7% purity) was purchased from the same supplier (Sigma) [81-83, 85]. Typically, there are large morphological features present on the metal as shown in the height images obtained by means of atomic force microscopy (AFM) in **Figure 1.12 A-D**. Notably, there appear to be grooves present on the surface derived from the manufacturing process. Also, the AFM images of the metal surface have relatively high root mean square (RMS) height values of  $10\pm 5$ ,  $48\pm 21$ ,  $111\pm 49$  and  $137\pm 55$  nm at areas of 1, 10, 50 and  $100\ \mu\text{m}^2$ , respectively (**Figure 1.13**). This corresponds well with previous AFM measurements that have been carried out on this material [68].

The chemical compositions of untreated and cleaned titanium surfaces (analysed by X-ray photoelectron spectroscopy (XPS)) are shown in **Figure 1.14** and representative survey spectra are shown in **Figure 1.15 A and B**, with the main photoelectron peaks being labeled for each element on the graphs. Typically, there is a large amount of carbon (55 atomic % (at.%) mainly in the form of hydrocarbon contamination, acquired during the manufacturing process and subsequent handling. Also, there was a small amount of nitrogen (4 at.%) and a weak titanium signal (below 10 at.%) detected. The titanium signal was partially quenched by a contaminating layer (mainly in the form of hydrocarbons) that was present on the surface. A cleaning procedure was developed to remove the contaminating hydrocarbon layer and increase the depth of the surface oxide layer.

Substrates were cleaned by a combined physical (ultrasonication) and chemical (detergent) method. A non-ionic detergent (Pyronex), mainly comprised of alkaline salts, was used to chemically clean the substrates. Pyronex is commonly used for cleaning of medical devices,

including metallic materials. After cleaning the substrates, the level of carbon was reduced by approximately 40% and the nitrogen signal remained below 10 at.% (**Figure 1.14** and compare **Figure 1.15 A to B**). Also, the titanium signal increased to 14 at.% due to the reduced thickness of the contaminating layer (**Figure 1.14**). Oxygen increased from 33 to 47 at.% after cleaning, indicating an increase in the thickness of the titanium oxide layer that corresponded with a decrease in the hydrocarbon layer (**Figure 1.14**).

Silica was next deposited onto the cleaned titanium surfaces by a plasma enhanced chemical vapour deposition (PECVD) process. In previous studies by our research team, plasma deposited bioactive silica coatings have been applied to a variety of metals, including titanium [81-83, 85]. Importantly, the plasma silica coatings have been shown to improve the performance of metallic-based materials as implant devices [85]. The parameters employed for silica deposition on titanium in this research were adapted from former experiments involving the extensive characterisation and optimisation of the plasma processing conditions [81-83, 85]. These parameters are described in detail on **pages 32-35**.

The silica films deposited using this PECVD process are somewhat different to that of other silica films, such as those derived by sol-gel and plasma-spray methods [117]. Silica that is deposited by the PECVD process used in this thesis, produces a structurally and functionally graded metal/oxide/silicate/silica layer, which also becomes partly embedded in the titanium oxide layer, resulting in a strongly bound surface silica layer [81-82]. The remainder of the thesis will refer to titanium substrates coated by silica through this particular PECVD process as PECVD-Si-Ti. Silica was deposited at low vapour flow rates by using a low temperature (approximately 80°C) plasma processing procedure in 3 steps (see below), which has the advantages of forming a more strongly bonded film in comparison to other techniques such as sol-gel and plasma spraying used for the deposition of bioactive glass [80]. Also, these plasma parameters do not significantly alter the underlying substrate's properties and all 3 steps (described below) can be performed *in situ*, minimising sample handling.

The first step of the PECVD process involved a pre-treatment of the samples in air plasma. This step served to further clean the surface by plasma etching and increase the thickness of the surface oxide layer. This step was important because the process requires the slow growth of the coating beginning in the titanium oxide layer in order to produce a graded metal/oxide/silicate/silica layer that strongly bonds to the metal's surface. Results from XPS are shown in **Figures 1.14** and **1.15 C**. The level of carbon decreased by 30% on titanium after processing detergent-cleaned titanium substrates in air plasma (refer to **Figure 1.14** and compare **Figure 1.15 B** to **C**) and the titanium signal was increased to 17 at.%, indicating that the hydrocarbon contaminating layer had decreased in thickness. Also, the level of oxygen increased by 13%, which can be attributed to an increase in the thickness of the titanium oxide layer. A small amount of contamination from other species (nitrogen and fluorine) was present ( $\leq 1$  at.%). However, 76% of the nitrogen from untreated titanium (surface contamination derived possibly from the manufacturing process of the titanium sheet) was removed by the air plasma cleaning step, which otherwise could not be removed by the detergent-cleaning procedure (**Figure 1.14**). In addition, 5 at.% of silicon was detected. The silicon signal indicates that a small amount of silica was deposited on the surface, probably from TEOS-derived species that had adsorbed to the walls of the vapour delivery lines or the walls of the plasma chamber from previous experiments. TEOS is used as a precursor in the deposition of silica as outlined on **pages 32-35**.

Also, the air plasma treatment step did not significantly change the morphological characteristics of the titanium surface (**Figure 1.12 E-H**), with measured RMS values of  $11 \pm 5$ ,  $47 \pm 22$ ,  $77 \pm 30$  and  $103 \pm 21$  nm at areas of 1, 10, 50 and  $100 \mu\text{m}^2$  respectively, which were not significantly different to that of clean, non-plasma processed titanium (**Figure 1.13**). Therefore, a smoothing effect from plasma processing of titanium from surface etching by electron and ion bombardment, which affects the contaminating hydrocarbon layer and the outermost molecular layers of the metal/oxide, was not detected in this study. This was important since it is known that topographical features on a material's surface can influence cellular behaviour independent of surface chemistry [34, 118-120].

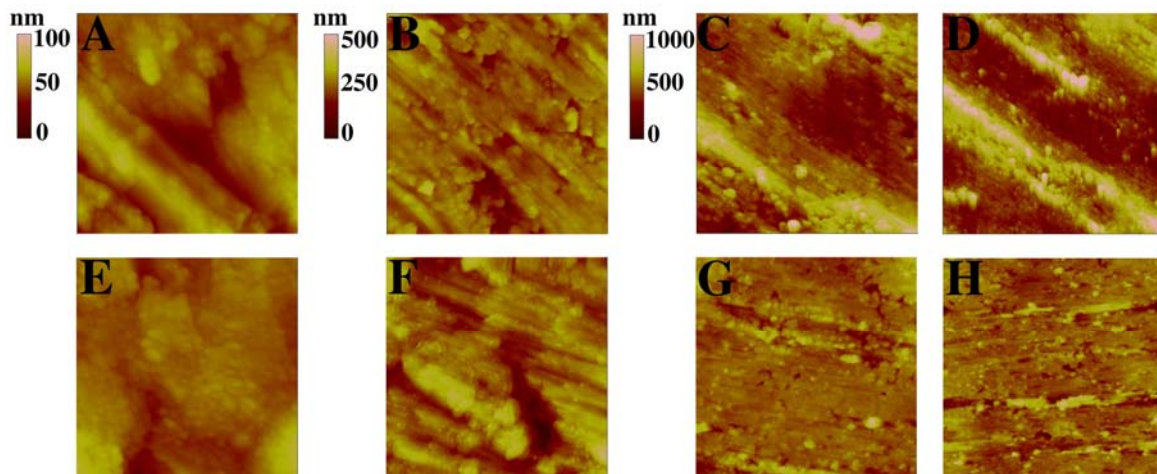


**Figure 1.12.** AFM height images of titanium surfaces. **A-D** represents detergent-cleaned titanium and **E-H** was taken on detergent-cleaned titanium subjected to 20 min of air plasma processing. Scanned areas of  $1 \mu\text{m}^2$  have a height ( $z$ ) scale bar of 100 nm (**A** and **E**); at  $10 \mu\text{m}^2$  the scale bar is 500 nm (**B** and **F**); at  $50 \mu\text{m}^2$  (**C** and **G**) and  $100 \mu\text{m}^2$  (**D** and **H**) the scale bar is 1000 nm.

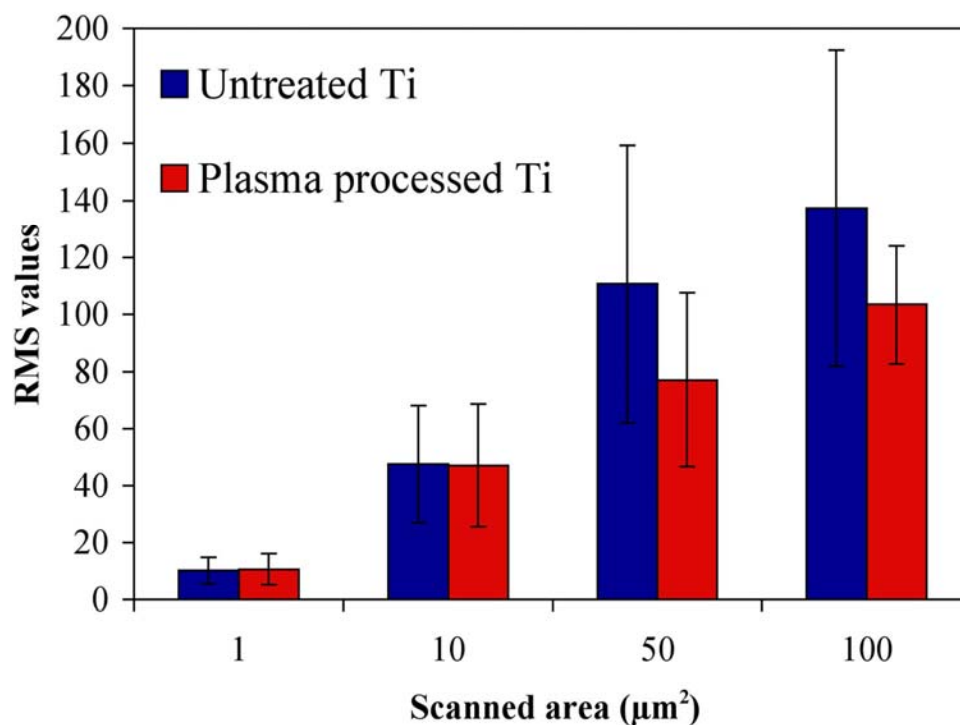


**Figure 1.13.** RMS values (nm) taken on detergent-cleaned titanium (referred to as Untreated Ti in the figure) and detergent-cleaned titanium subjected to 20 min of air plasma processing (Plasma processed Ti).

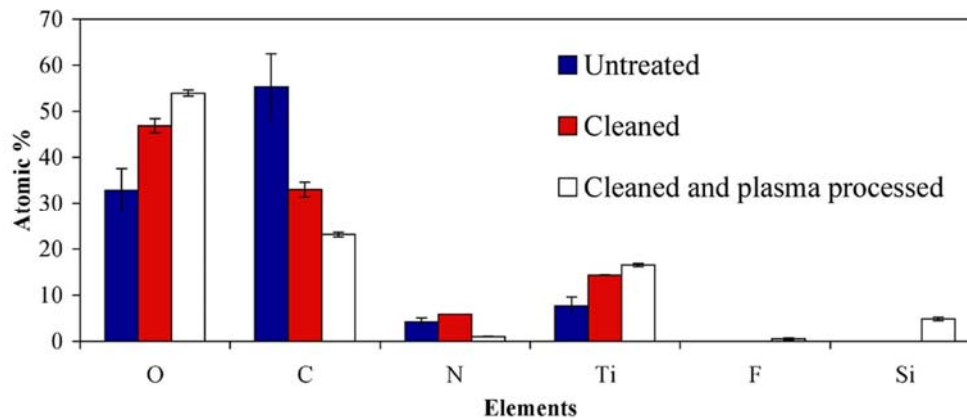


**Figure 1.14.** Elemental atomic % data of titanium surfaces (determined through XPS analysis) of untreated, cleaned (by detergent) and cleaned/plasma-processed (20 min of air plasma) titanium. Statistical analyses: Oxygen content of cleaned/plasma-processed Ti was significantly different to untreated Ti ( $p < 0.0001$ ) and detergent-cleaned Ti ( $p = 0.001$ ); carbon content of cleaned/plasma-processed Ti was significantly different to untreated Ti ( $p < 0.0001$ ) and detergent-cleaned Ti ( $p = 0.0002$ ).

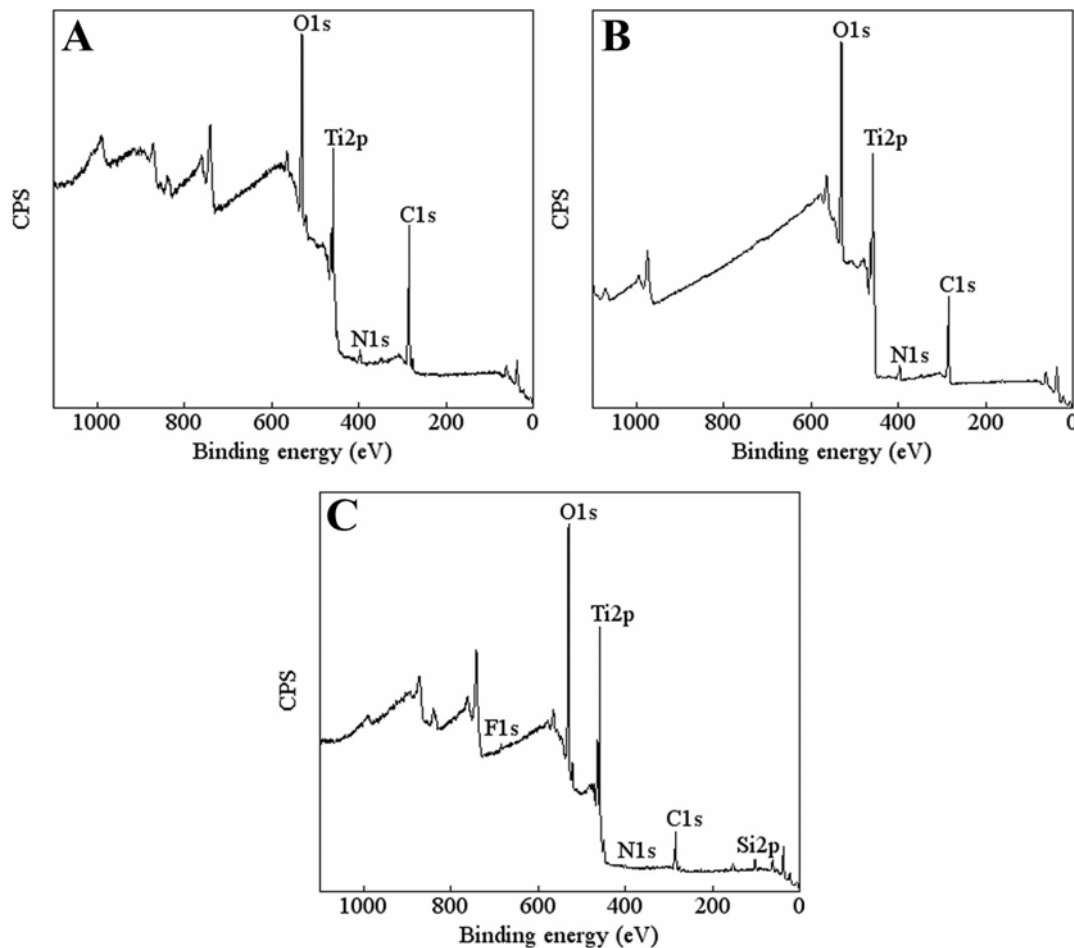


**Figure 1.15.** Representative XPS survey spectra of untreated titanium (A); after cleaning titanium in Pyroneg detergent (B) and after subjecting cleaned titanium to 20 min of air plasma treatment (C). All spectra were acquired from the centre of each sample. The main photoelectron peak for each identified element is labeled on the graphs. CPS denotes counts per second.

Next, silica was deposited onto the cleaned and oxidised substrates in the second step of the PECVD process. The thick oxide film formed in the first step is essential for obtaining well adherent silica films. This was explained in previous studies, which have showed that Si-O species, formed in the air/TEOS plasma, become embedded as silicate species in the plasma grown titanium oxide layer [81]. Also, the water present in the air supply (refer to **pages 32-35**) acts as a catalyst in the hydrolysis of TEOS. A possible hydrolysis reaction is shown in **Scheme 1.2**. Alkoxysilanes readily hydrolyse in water and the hydrolysed TEOS species can condense with each other in the gas phase or react with surface hydroxyl groups [107].

Also, other species such as  $\text{SiO}^-$  ions and  $\text{SiO}$  radicals formed in the air/TEOS plasma can react and become embedded in the titanium oxide [81-82].



**Scheme 1.2.** A possible plasma-phase hydrolysis reaction of a TEOS molecule with water.

In one set of experiments, the air carrier gas was exchanged for pure oxygen. Interestingly, silica was deposited onto titanium at a slower rate in an oxygen atmosphere compared to air. A small titanium signal ( $\sim 2$  at.%) is still found on the substrate surface after silica deposition in an oxygen atmosphere as shown in **Figure 1.16 A** (elemental at.% data) and **B** (a survey spectrum). Also, the level of silicon was found to be about 20% lower on PECVD silica coatings grown in an oxygen atmosphere compared to those grown using air (compare **Figures 1.16 A** and **1.17 B**). This data indicates that a thinner layer of silica was deposited in an oxygen atmosphere compared to air at the same PECVD treatment time.

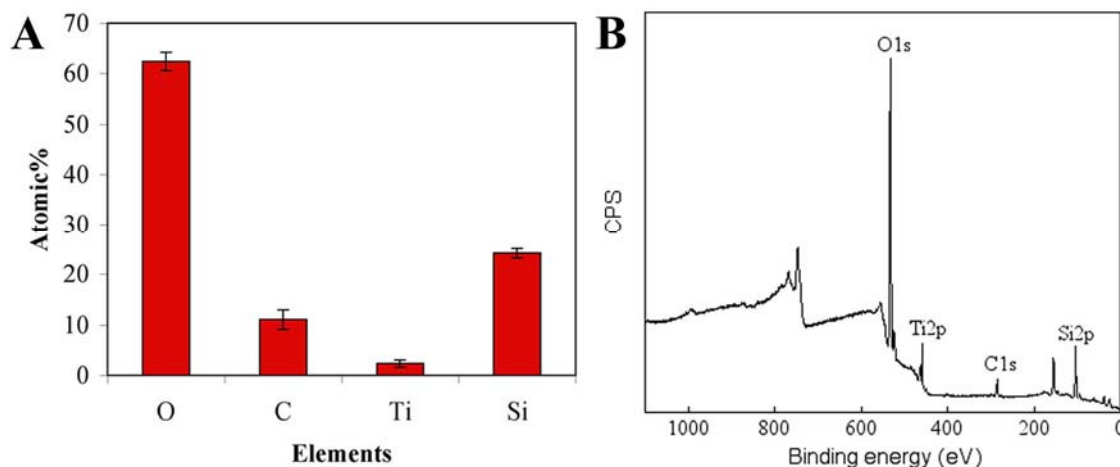


**Figure 1.16.** Elemental atomic percentages (obtained by XPS) of two PECVD-Si-Ti substrates in which silica was deposited in an oxygen atmosphere (**A**) and a survey spectrum (**B**) taken on one of those films (the main photoelectrons that were detected by the instrument are labelled). Refer to **pages 32-35** for a detailed description of the plasma silica deposition parameters. Statistical analyses: Silicon content of PECVD-SiO<sub>2</sub>-Ti was significantly different for silica deposited in an oxygen atmosphere to an air atmosphere ( $p = 0.002$ ).

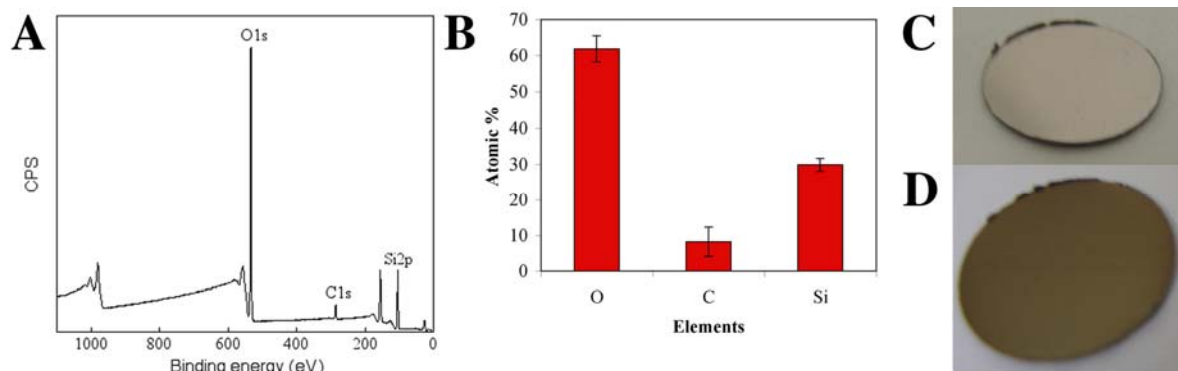


**Figure 1.17.** A representative survey spectrum (with the main photoelectron signals labeled) of PECVD-Si-Ti (treated with 5 min of air/H<sub>2</sub>O<sub>2</sub> plasma) onto which silica was deposited in an air atmosphere (A) and average XPS elemental atomic percentages of such a film (B). Photographs of an uncoated titanium disc (C) and PECVD-Si-Ti (treated with 5 min of air/H<sub>2</sub>O<sub>2</sub> plasma) (D) are also shown.

For the remainder of the experiments, silica was deposited in an air atmosphere. During the initial stages of this research, the PECVD-Si-Ti substrates were also treated with air/H<sub>2</sub>O<sub>2</sub> plasma (Step 3 of the PECVD process), which has been reported to increase the surface density of silanol groups on PECVD-Si coatings [81-83]. Generation of silanol groups is required for apatite growth and silane coupling [107, 121].

As analysed by XPS, the elemental composition of these surfaces comprised approximately of 60 at.% oxygen, 10 at.% carbon and 30 at.% silicon (**Figure 1.17 B**), which is similar to previous reports obtained using this technique [81-83]. The oxygen/silicon ratio of  $2.1 \pm 0.2$  is close to 2.0 expected for silicon dioxide. The PECVD-Si coatings on titanium are usually bronze in colour, in comparison to the uncoated grey titanium surface, attributed to optical reflective interference effects from the coating (**Figure 1.17 C-D**). The colour effect observed on PECVD-Si-Ti (caused by a change in the surface layer's refractive index) suggests that the PECVD-Si coating is relatively thick. This was confirmed by profilometry, which gave a measured film thickness in the order of 500 nm (refer to **pages 34-35** for a description of the method). Importantly, there is a complete attenuation of the underlying titanium signal, indicative of a continuous silica layer covering the substrate (**Figure 1.17 A**). Samples treated with Step 3 of the PECVD process (air/H<sub>2</sub>O<sub>2</sub> plasma) were identical in colour to the PECVD-Si-Ti surface not treated with Step 3 (data not

shown) and the surface chemistry of these samples was not significantly different, as will be discussed from **page 57** (compare **Figure 1.17 A** to **Figure 1.20** and **Figure 1.21 A** to **B**).

Micrographs of PECVD-Si-Ti were taken by scanning electron microscopy (SEM) and compared to clean, uncoated titanium surfaces at low (**Figure 1.18 (A and D)**), medium (**B** and **E**) and high (**C** and **F**) magnifications. At low magnifications, the PECVD-Si-Ti surface appeared slightly smoother than an uncoated titanium surface (compare **Figure 1.18 A** to **D**). Images taken at medium and high magnifications support this observation (compare **Figure 1.18 B-C** to **E-F**). Additionally, the PECVD-Si coating has filled cracks that are present on the titanium surface (compare **Figure 1.18 B** to **E**). There are also globular nanostructures present on PECVD-Si-Ti, which are highlighted in **Figure 1.18 E** to **F**. These may correspond to silica nanoparticles deposited during the PECVD process due to possible gas phase nucleation and growth. This is a reasonable conclusion since the formation of nanoscale aggregates is common during silica mineralisation [122-127].

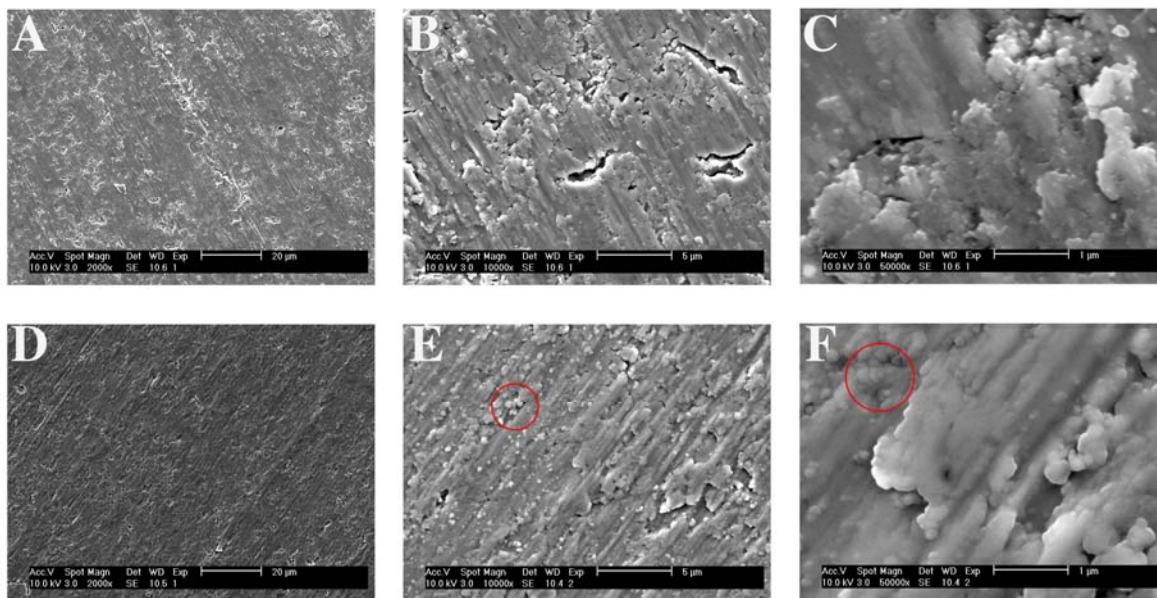


**Figure 1.18.** SEM micrographs of clean, uncoated titanium (**A-C**) and PECVD-Si-Ti (**D-F**). For both sample types, images were taken at low (**A** and **D**), medium (**B** and **E**) and high (**C** and **F**) magnifications. The red circles in **E** and **F** highlight small, globular particles that were observed only on the plasma silica films. All samples were coated with a thin layer of platinum ( $\sim 2$  nm) to prevent sample charging during SEM analysis.

More importantly, these coatings were stable under reasonably vigorous conditions developed for grafting silanes to the surface of silica (refer to **pages 36-37**). After exposing PECVD-Si-Ti substrates to boiling toluene overnight, the underlying titanium surface could still not be detected by XPS (**Figure 1.19 A and B**). This result confirmed that the sample was prepared appropriately and the plasma processing parameters were adequate for obtaining robust silica films on titanium.

Another important surface feature considered was the density of surface hydroxyl groups. These groups were required to be available to react with alkoxy silanes to form strongly (covalently) bonded siloxane layers that were subsequently used as attachment points for insulin-like growth factor-1 (IGF-1). Although hydroxylation of PECVD-Si-Ti by means of air/H<sub>2</sub>O<sub>2</sub> plasma has been used in the preparation of these substrates for inducing apatite precipitation and enhancing bone formation, the degree of hydroxylation of the PECVD-Si-Ti substrate surface has yet to be extensively investigated [83, 85].

From XPS analysis, PECVD-Si-Ti not treated with air/H<sub>2</sub>O<sub>2</sub> plasma was found to be similar in surface chemical composition compared to PECVD-Si-Ti that was treated with air/H<sub>2</sub>O<sub>2</sub> plasma (compare **Figures 1.20 to 1.17 A**). Also, no additional information could be obtained on PECVD-Si-Ti (not treated and treated with 5 min of air/H<sub>2</sub>O<sub>2</sub> plasma) substrates by infrared spectroscopy on a Nicolet Avatar<sup>®</sup> 370MCT spectrometer equipped with a smart apertured grazing angle (SAGA) accessory capable of analysing the chemistry of thin films ranging from 1 nm to 1 μm in thickness (**Figure 1.21 A and B**). The broad hydroxyl-stretching band expected at approximately 3400 cm<sup>-1</sup> was not detected and both spectra were rather featureless apart from the narrow SiO<sub>2</sub> band near 1250 cm<sup>-1</sup> [128]. Therefore, three different methods were chosen to assess the surface coverage of hydroxyl groups: contact angle measurements were taken on the substrates; hydroxyls were derivatised with trifluoroacetic anhydride (TFAA); and hydroxyl groups were derivatised with a fluorinated silane molecule (discussed in the following section of Part 1: Results and Discussion).

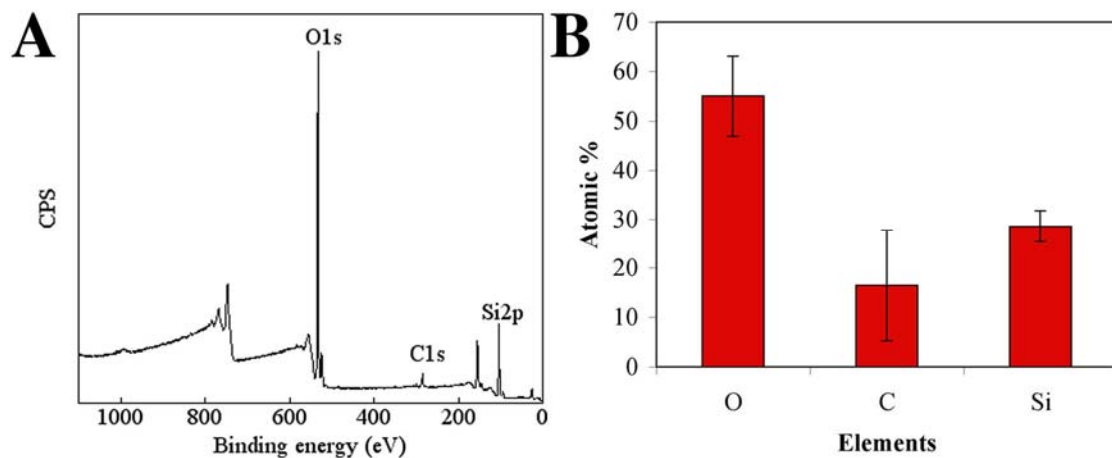


**Figure 1.19.** XPS data of PECVD-Si-Ti taken after boiling the samples in toluene overnight. A survey spectrum (with labeled photoelectrons) is shown in **A** and **B** shows the elemental atomic % of the surface.

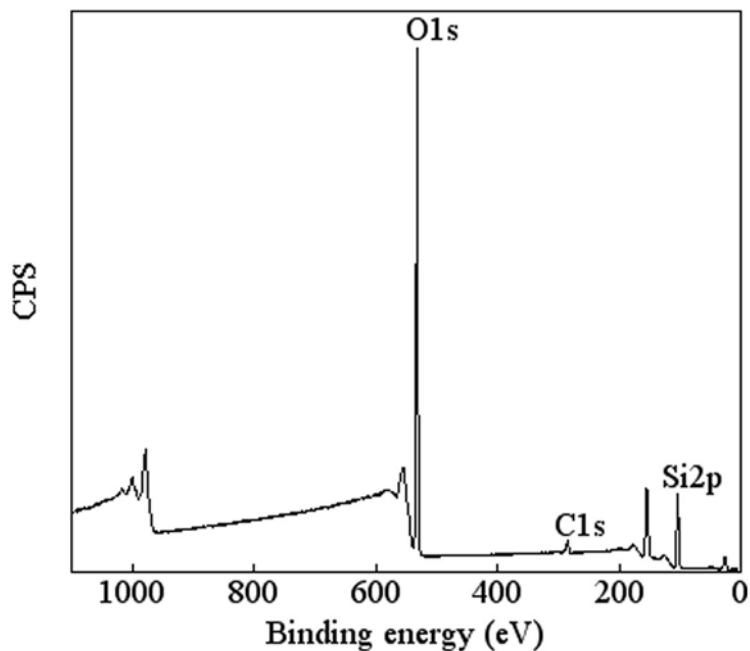


**Figure 1.20.** An XPS survey spectrum of PECVD-Si-Ti that was not subjected to an air/H<sub>2</sub>O<sub>2</sub> plasma treatment.

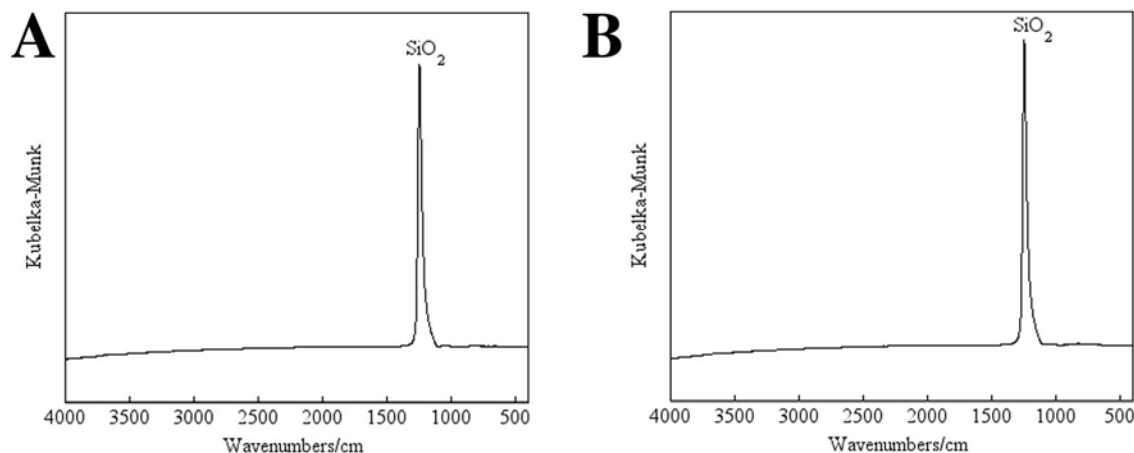


**Figure 1.21.** Infrared spectra of PECVD-Si-Ti (A) and after treating PECVD-Si-Ti with 5 min of air/H<sub>2</sub>O<sub>2</sub> plasma (B). The spectra were acquired on a Nicolet Avatar<sup>®</sup> 370MCT spectrometer equipped with a smart apertured grazing angle (SAGA) accessory.

The first method involved measuring three-phase contact angles at the interface of small (2  $\mu$ l) water droplets and the material's surface in air. This technique gave an indication of the interfacial energy at the solid-liquid interface. For a surface with a high energy, the water droplet will spread, that is, the surface will be easily wetted. This is typical for a hydrophilic surface such as one containing a high density of hydroxyls [129-130]. Conversely, a hydrophobic surface such as one contaminated with high amounts of saturated hydrocarbon, will repel water and water droplets with a high contact angle will form. There are other factors that can have a bearing on the contact angle, such as surface roughness, but to simplify the argument, these will not be considered.

Contact angle measurements were also performed to characterise the surface of detergent-cleaned, uncoated titanium. In **Figure 1.22 A**, a water droplet has formed on untreated ("as received") titanium with an average contact angle of  $71 \pm 11^\circ$ . The relatively hydrophobic surface observed here is a result of the thick hydrocarbon layer present on the material. After titanium was cleaned in detergent, some of the contaminating layer was removed and the thickness of the titanium oxide layer increased (refer to **pages 48-49**) that made the surface more hydrophilic (from an increase in the surface density of titanium-oxide species such as Ti-OH) and consequently the contact angle was reduced to  $45 \pm 2^\circ$  (**Figure 1.22 B**).

Surprisingly, the water droplet completely spread on the PECVD-Si-Ti surface (not treated with air/H<sub>2</sub>O<sub>2</sub> plasma) and could not be imaged by the charge-coupled device (CCD), which is a common problem for very hydrophilic surfaces. This is indicative of a contact angle of less than 10° and a highly hydrophilic surface with a high hydroxyl group density. Interestingly, after treating PECVD-Si-Ti with air/H<sub>2</sub>O<sub>2</sub> plasma, the contact angle was now 15±4° (**Figure 1.22 C**). This result suggests that the air/H<sub>2</sub>O<sub>2</sub> plasma post-treatment reduces the hydroxyl group density on the surface [129].

Using another method, the hydroxyls were derivatised with TFAA. TFAA reacts with surface hydroxyls to form an ester with 3 terminal fluorine atoms that can be detected by XPS (**Scheme 1.3**). The reaction has previously been used to detect hydroxyl groups on plasma deposited films, and the experimental parameters used here were adapted from these reports [131-132].

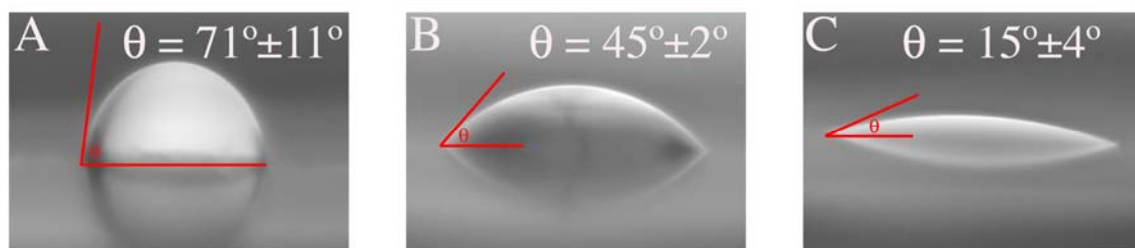
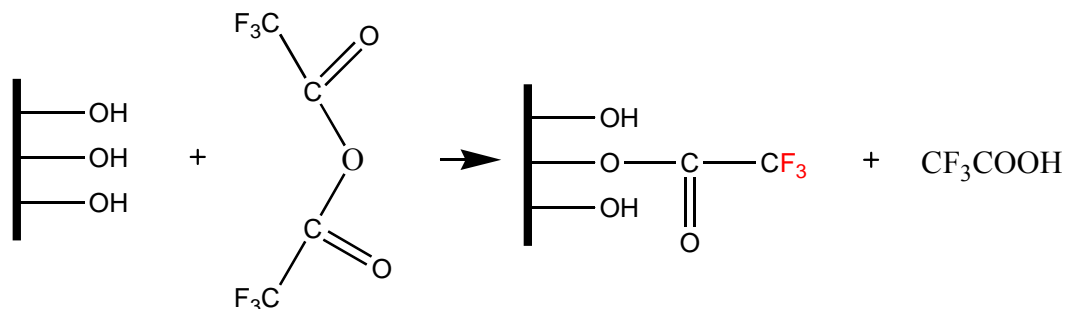


**Figure 1.22.** Photographs of water droplets (2  $\mu$ l) on untreated titanium (**A**), after cleaning titanium in detergent (**B**) and on PECVD-Si-Ti treated with 5 min of air/H<sub>2</sub>O<sub>2</sub> plasma. The contact angle ( $\theta$ ) was measured on the left (shown) and the right side of the water droplet. Statistical analyses: Contact angle of PECVD-SiO<sub>2</sub>-Ti treated with 5 min of air/H<sub>2</sub>O<sub>2</sub> plasma was significantly different to untreated Ti ( $p < 0.0001$ ) and detergent-cleaned Ti ( $p < 0.0001$ ).



**Scheme 1.3.** Reaction of TFAA molecule with a surface hydroxyl group. An ester is formed on the surface with 3 fluorine atoms (shown in red) that provide a characteristic elemental label for XPS analysis.

In attempts to optimise the TFAA/OH derivatisation reaction, surface hydroxyl groups were reacted with TFAA by a range of methods. First, clean, uncoated titanium and PECVD-Si-Ti were placed at the bottom of a closed jar containing a separate vial of TFAA solution (Method 1) and were incubated with TFAA vapour for 1 h at 25°C (refer to **pages 35-36**). The samples were subsequently analysed by XPS and the results are displayed in **Figure 1.23 A-D**. As shown in **Figure 1.23 A**, there is a small amount of fluorine (1.0 at.%) on the uncoated titanium surface after the reaction, indicating that some TFAA had reacted with the surface. Notably, fluorine was not detected on PECVD-Si-Ti treated for 1, 5 and 15 min in air/H<sub>2</sub>O<sub>2</sub> plasma after silica deposition (**Figure 1.23 B-D**). Due to the absence of the fluorine signal, the experimental parameters were adjusted in an attempt to improve the reaction yield.

Clean, uncoated titanium and PECVD-Si-Ti (treated with 5 min of air/H<sub>2</sub>O<sub>2</sub> plasma) were then reacted with TFAA vapour in a custom-built reaction vessel (shown in **Figure 2.10**) that allowed for more vigilant measures to be taken to create a dry atmosphere (Method 2) (refer to **pages 35-36**). The reaction was again performed at 25°C and at reaction times of 1 h. Additionally, in one set of experiments, the TFAA solution was maintained at 40°C to help vaporise the TFAA solution. The uncoated titanium surface produced a slightly higher fluorine signal (1.5 at.%) compared to the previous result and this signal was increased to 2.0 at.% following a reaction when the TFAA solution was heated to 40°C (**Figure 1.24 A and B**). The relatively low fluorine signal obtained on TFAA-derivatised uncoated titanium (maximum of 2.0 at.%), compared to fluorine detected at 4-27.5 at.% on TFAA-derivatised polymers in previous studies, suggests that hydroxyl groups are present on titanium only at a low surface density [132-133]. However, after reacting TFAA with PECVD-Si-Ti surfaces treated with 5 min of air/H<sub>2</sub>O<sub>2</sub> plasma, fluorine was again unable to be detected on the substrate surface (**Figure 1.24 C and D**), expected to have 2.5-3.0 OH groups per nm<sup>2</sup>, suggesting that it does not adequately represent the surface hydroxyl concentration [134].

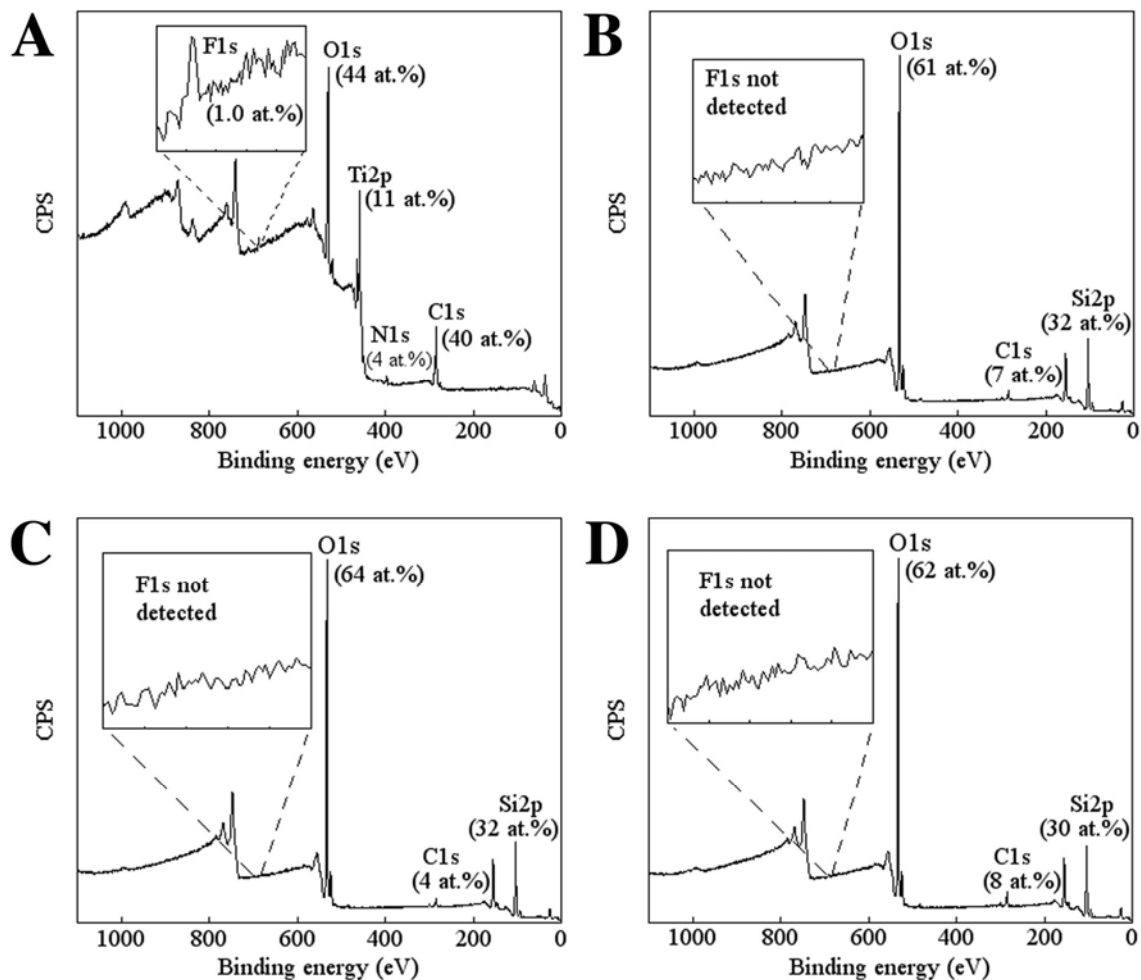


**Figure 1.23.** XPS survey spectra of clean, uncoated titanium (A) and PECVD-Si-Ti treated with 1 min (B), 5 min (C) and 15 min (D) of air/H<sub>2</sub>O<sub>2</sub> plasma. All surfaces were reacted with TFAA by Method 1 (refer to pages 35-36 for a detailed description). Elemental atomic percentages for each major photoelectron peak detected by the instrument are shown.

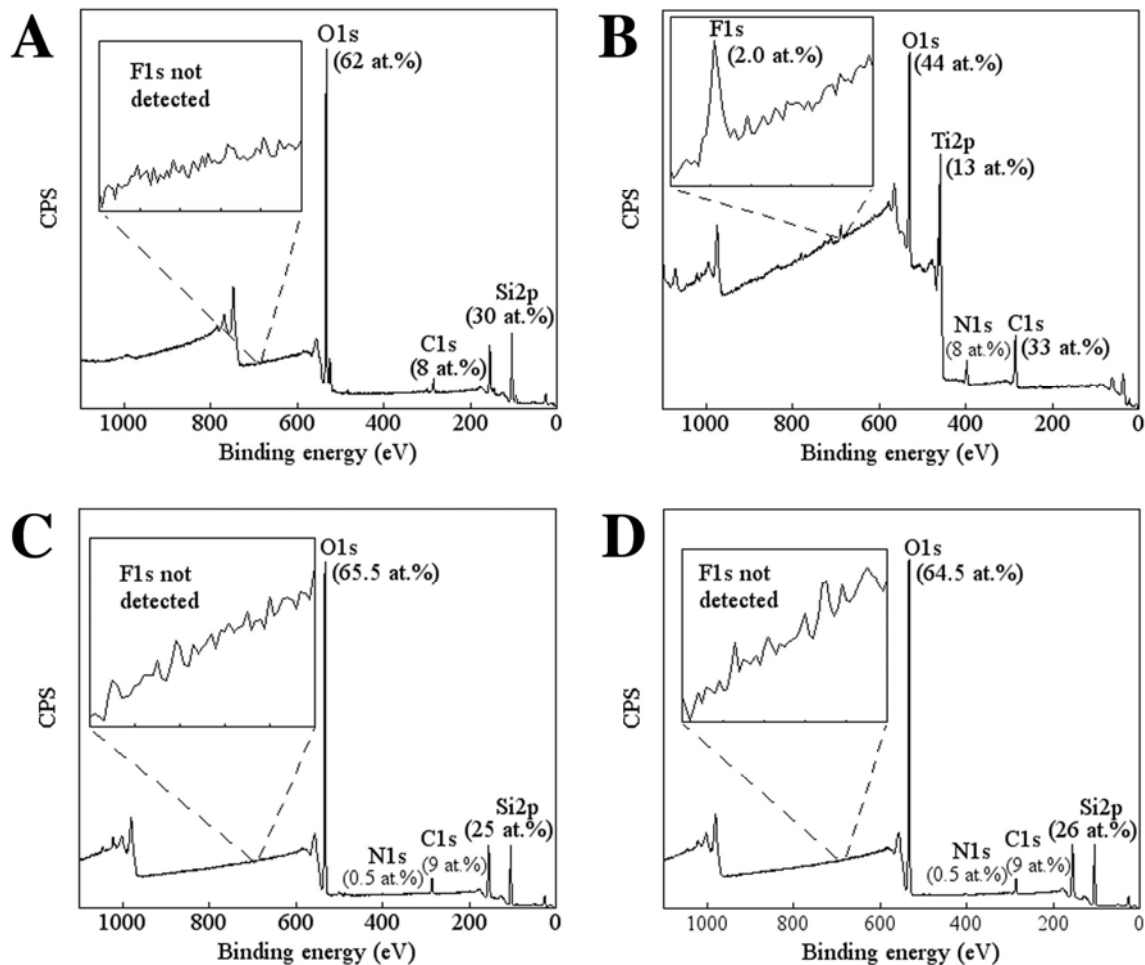


**Figure 1.24.** XPS survey spectra of clean, uncoated titanium (**A** and **B**) and PECVD-Si-Ti treated with 5 min of air/H<sub>2</sub>O<sub>2</sub> plasma (**C** and **D**). Samples were reacted with TFAA by Method 2 (refer to **pages 35-36** for a detailed description). TFAA solution was heated to 40°C in **B** and **D**.

In a more direct approach, the samples were allowed to incubate in TFAA solution for reaction times of 5 min and 1 h (Method 3) (refer to **pages 35-36**). The reaction on PECVD-Si-Ti (treated with 5 min of air/H<sub>2</sub>O<sub>2</sub> plasma) was compared to commercially available silicon (used as a control surface). After the TFAA reaction, the silicon surface produced a low fluorine signal of 0.4 at.% and 0.3 at.% for 5 min and 1 h reaction times, respectively (**Figure 1.25 A-B**). Corresponding fluorine signals on PECVD-Si-Ti were both at 0.1% (**Figure 1.25 C and D**). Only trace levels of fluorine were detected on these surfaces, which may be an indication that there are only few hydroxyl groups available to react with the TFAA molecule, the reaction did not proceed very efficiently, or that there is a side reaction that degrades the PECVD-Si film and the generated ester with it. The latter two possibilities are more probable considering that the surface of PECVD-Si-Ti (not treated and treated with 5 min of air/H<sub>2</sub>O<sub>2</sub> plasma) was shown to be hydrophilic (from contact angle data) (refer to **Figure 1.22 C and pages 59-60**). Previously, Dang et al. attempted to derivatise silanol groups using TFAA [135]. They too found that the reaction did not occur effectively on silica, and the data obtained here corroborated their results. A possible cause for this is that the acidic by-product produced in the TFAA/hydroxyl reaction (**Scheme 1.3**) may degrade the PECVD-Si coating. This can be potentially remedied by adding a volatile base such as pyridine to neutralise the reaction, however this was not performed in these experiments.

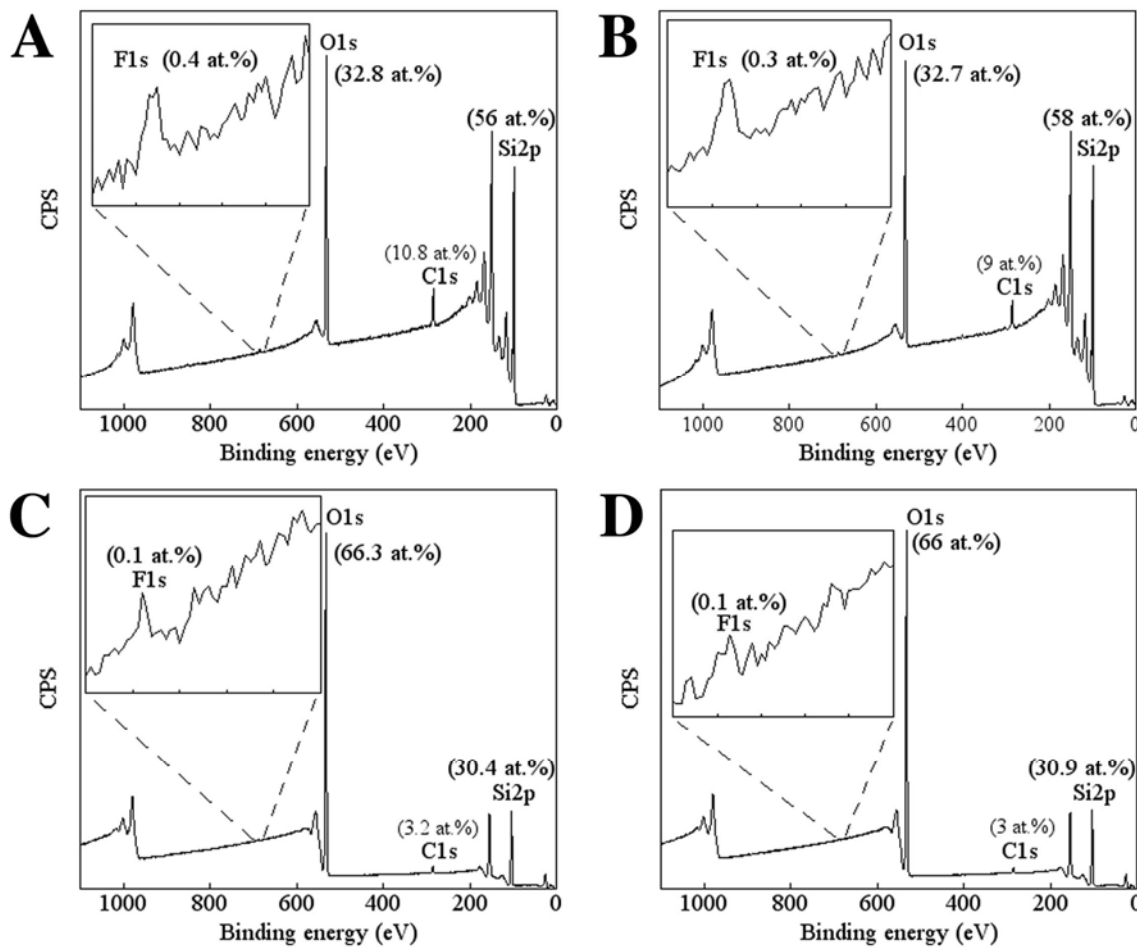


**Figure 1.25.** XPS survey spectra on commercial silicon and PECVD-Si-Ti (treated with 5 min of air/H<sub>2</sub>O<sub>2</sub> plasma) after a TFAA reaction in solution (Method 3) (refer to **pages 35-36** for a detailed description). Shown, is a spectrum of silicon reacted with TFAA for 5 min (**A**) and 1 h (**B**) and PECVD-Si-Ti reacted with TFAA for 5 min (**C**) and 1 h (**D**). The silicon used in this experiment was purchased from Virginia Semiconductor Inc. (Virginia) and was boron doped to a resistivity of 0.0005-0.001  $\Omega\cdot\text{cm}$ .

Furthermore, no additional evidence could be obtained from high-resolution C 1s spectra (**Figure 1.26**). In this figure, the C 1s spectra of clean, uncoated titanium, silicon and PECVD-Si-Ti (treated with 5 min of air/H<sub>2</sub>O<sub>2</sub> plasma) control surfaces (**Figure 1.26 A-C**) can be directly compared to corresponding surfaces after TFAA reactions (**Figure 1.26 D-G**). Notably, the broad asymmetrical C 1s photoelectron peak on all controls consisted of the expected hydrocarbon peak at 285.0 eV and the shoulder seen on all the spectra were attributed to C-O contaminant species at about 286.5 eV. The expected peak at 289.7 eV corresponding to C-F from the TFAA molecule bonded to a surface hydroxyl (OCOCF<sub>3</sub>) was absent [131]. However, this was not surprising since only traces of the molecule could be detected in the survey spectrum.

Other techniques have also been applied for detecting surface hydroxyl groups but these were not investigated in this thesis. For example, the surface coverage of hydroxyls have been directly and quantitatively analysed by XPS without any need for indirectly labeling hydroxyl groups with a marker molecule [136]. However, the disadvantage of this technique was that several assumptions were required to be made in order to model the molecular layers covering the substrate and detailed XPS procedures were required. Another indirect method described by Ivanov et al. used a fluorescent dye to label the hydroxyls of a polymer film and the density of hydroxyls was determined by comparing the fluorescence of the sample films against a carefully constructed calibration standard [137]. Another group derivatised hydroxyl groups with zinc ions that were detected by inductively coupled plasma atomic emission spectrometry (ICP-AES) [138]. Rather than investigating these procedures, in this present study, the hydroxyl groups were derivatised with model silane molecules. These samples were then analysed by XPS to confirm the presence of marker silane molecules directly bound to uncoated titanium and PECVD-Si-Ti surfaces. Similar silanes were also used later as attachment tethers for insulin-like growth factor-1 (IGF-1). The results will be discussed in the following sections of Part 1: Results and Discussion.

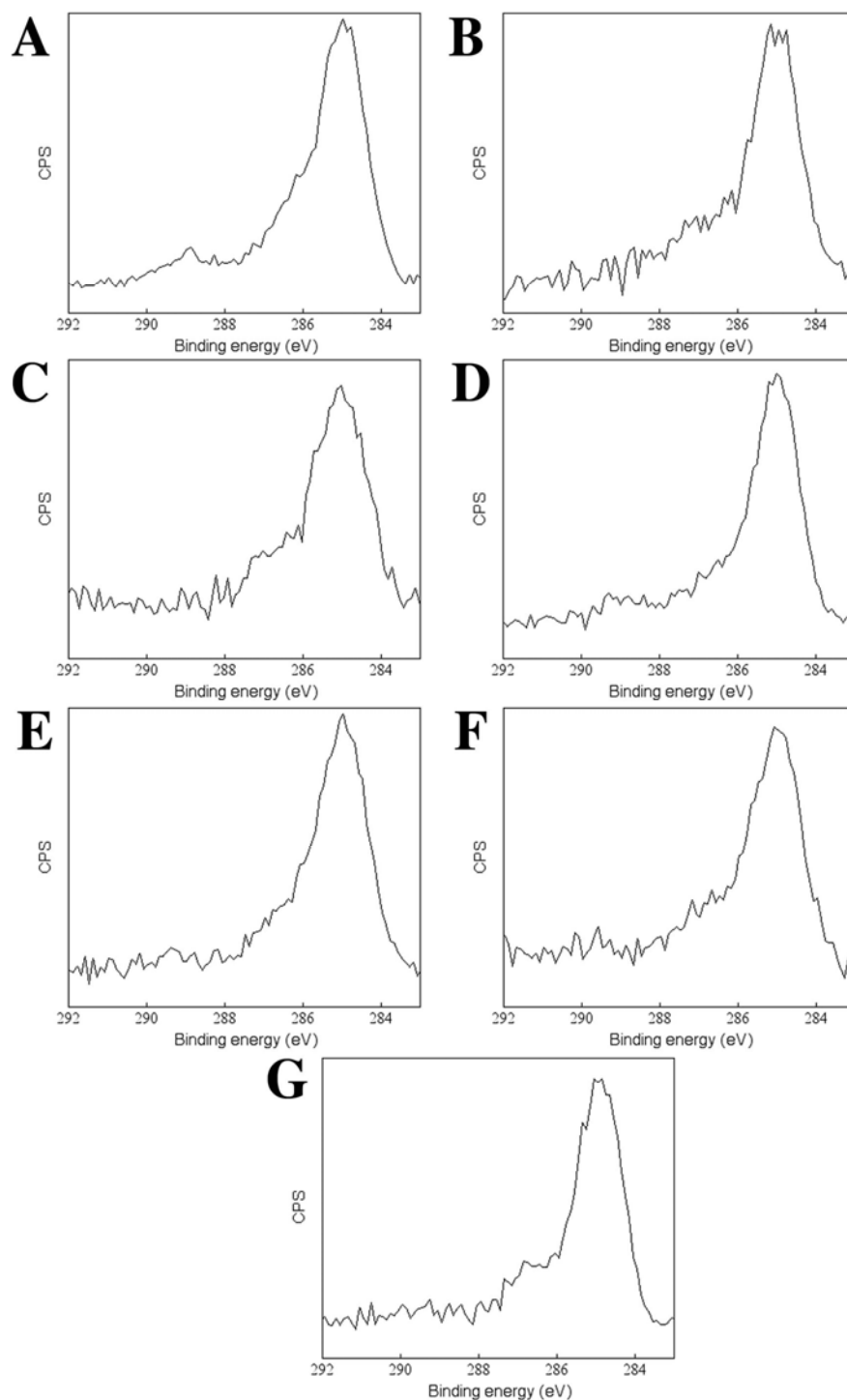


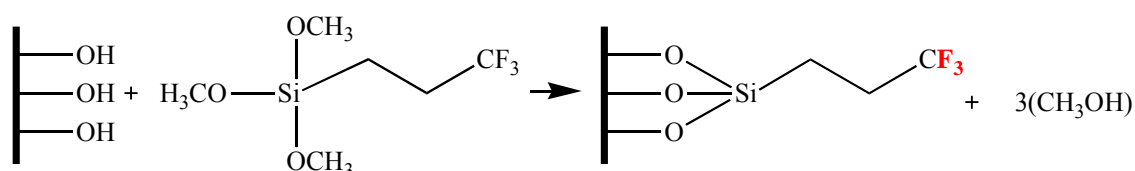
**Figure 1.26.** C 1s high-resolution XPS spectra for selected surfaces. Controls (samples not treated with TFAA) of clean, uncoated titanium (A), silicon (B) and PECVD-Si-Ti (treated with 5 min of air/H<sub>2</sub>O<sub>2</sub> plasma) (C) are shown. Clean, uncoated titanium and PECVD-Si-Ti (treated with 5 min of air/H<sub>2</sub>O<sub>2</sub> plasma) reacted with TFAA by Method 2 (TFAA solution was heated to 40°C) is shown in D and E. TFAA reactions on PECVD-Si-Ti and silicon by Method 3 (reaction time = 1 h) are shown in F and G. Refer to **pages 35-36** for detailed descriptions of TFAA derivatisation procedures.

In summary, a cleaning procedure was devised in this section for removing the contaminating hydrocarbon layer from the titanium surface in preparation for the deposition of PECVD-Si. The surface of PECVD-Si-Ti, on which silica had been deposited in an air atmosphere, is mainly silicon dioxide and the hydrophilic films adhere well to the titanium substrate. Finally, identification of hydroxyl groups could not be achieved by labeling the groups with TFAA for subsequent XPS analysis because the reaction does not proceed well on oxidised silicon or on PECVD-Si surfaces. However, the next part of the study uses another labeling method to investigate the coverage of hydroxyl groups on the PECVD-Si-Ti surface. The following section discusses the surface coverage of alkoxysilanes, which were grafted on PECVD-Si-Ti. These surfaces are also analysed by means of XPS.

### 1.3.2 Assessment of alkoxy silane grafting methods on PECVD-Si-Ti

This section addresses the loading ability of alkoxy silane molecules on PECVD-Si-Ti and the stability of siloxane films under physiological conditions. The reactions of alkoxy silanes on hydroxylated surfaces has been extensively characterised in previous work and it is known that a rapid condensation of the silane molecules occurs on the surface in the initial stages of the reaction and at longer reaction times, cross-linked multi-layers of silanes are formed [107, 139]. However, under different reaction conditions, silanes can also form a range of other different molecular surface orientations, which can have a major impact on their stability in solution [108, 125, 140-145]. Because silanes will be used to tether IGF-1 to PECVD-Si-Ti, as will be described in the following sections, both the density of silane molecules and the stability of the siloxane films will be important factors for sustaining IGF-1 bioactivity on the biomaterial surface. Both of these factors will be qualitatively examined here under different reaction conditions (silane concentrations, temperature and time) and solvent systems (organic, aqueous, anhydrous, neat and pH).

PECVD-Si-Ti was first reacted with a 3,3,3-trifluoropropyl trimethoxysilane (FPTMS) under different conditions. A simplified schematic of the silane attached to a surface containing hydroxyl groups is shown in **Scheme 1.4**. After the reaction, the surface becomes terminated with three fluorine atoms per silane molecule (shown in red in **Scheme 1.4**). Since fluorine is absent on both PECVD-Si-Ti and cleaned, uncoated titanium surfaces, fluorine could be used as a distinct marker element to indicate that FPTMS had attached on the surfaces (by XPS analysis). This is a similar approach to that described for the surface reactions involving trifluoroacetic anhydride (TFAA) in the previous section.



**Scheme 1.4.** Schematic of a possible surface reaction between a FPTMS and three hydroxyl groups. The surface becomes terminated with three fluorine atoms (shown in red).

FPTMS was first grafted onto PECVD-Si-Ti (treated with 5 min of air/H<sub>2</sub>O<sub>2</sub> plasma) and uncoated titanium (as a control surface) in toluene at a concentration of 100 mM and a reaction temperature of 25°C (Method 1 – **pages 36-37**). The aim of this experiment was to comparatively examine a silane reaction on the titanium oxide surface, which is known to readily react with alkoxysilanes [146], to PECVD-Si-Ti (treated with 5 min of air/H<sub>2</sub>O<sub>2</sub> plasma), which is thought to contain a high surface density of hydroxyl groups [83] and therefore should also react with alkoxysilanes.

Typical XPS survey spectra taken on both the surfaces after the reaction are shown in **Figure 1.27 A and B** with atomic percentages in **Table 1.3**. On the uncoated titanium surface, a relatively strong fluorine (F 1s) signal was detected after the surface was labeled with FPTMS (**Figure 1.27 A**). 6 at.% of fluorine was detected on uncoated titanium after reacting the surface with FPTMS (**Table 1.3**). On PECVD-Si-Ti, a much lower percentage of fluorine was detected (2.0 at.%), which indicates that fewer FPTMS molecules were attached to PECVD-Si-Ti in comparison to titanium (**Table 1.3**).

At a high-resolution, the C 1s photoelectron spectra was curve-fitted with 4 components for both FPTMS-labeled uncoated titanium and PECVD-Si-Ti, respectively (**Figure 1.28**): C 1 at 292.7-292.9 eV is assigned to the CF<sub>3</sub> group of the silane; C 2 and 3 are carbon atoms bonded to oxygen at 288.8-289.0 eV for C-O-Si; 286.2-286.7 eV for C-O groups; and C 4 is saturated hydrocarbon at 285.0 eV [131, 147]. C-O and C-O-Si species may be from contaminants as well as unreacted methoxy groups of FPTMS [131, 147]. Finally, the contribution of C 1 (CF<sub>3</sub>) in the C 1s high-resolution spectra for FPTMS-labeled uncoated titanium (10.3%) was higher compared to PECVD-Si-Ti (treated with 5 min of air/H<sub>2</sub>O<sub>2</sub> plasma) (7.7%), which supports the higher concentration of fluorine detected on uncoated titanium in **Table 1.3** and the conclusion that a higher coverage of silane was achieved on the uncoated titanium samples (compared to PECVD-Si-Ti samples).

After 12 h of incubation in PBS under physiological conditions, the fluorine signal was reduced by 65% and 50% on uncoated titanium and PECVD-Si-Ti, respectively (**Figure 1.27 C and D** and **Table 1.3**). This result shows that Method 1 produced a FPTMS siloxane film mixed with unstably and stably bound FPTMS molecules on both uncoated titanium and PECVD-Si-Ti (treated with 5 min of air/H<sub>2</sub>O<sub>2</sub> plasma). Also, traces of sodium from the PBS and nitrogen (contamination from additional handling) were occasionally detected on these surfaces (**Table 1.3**).

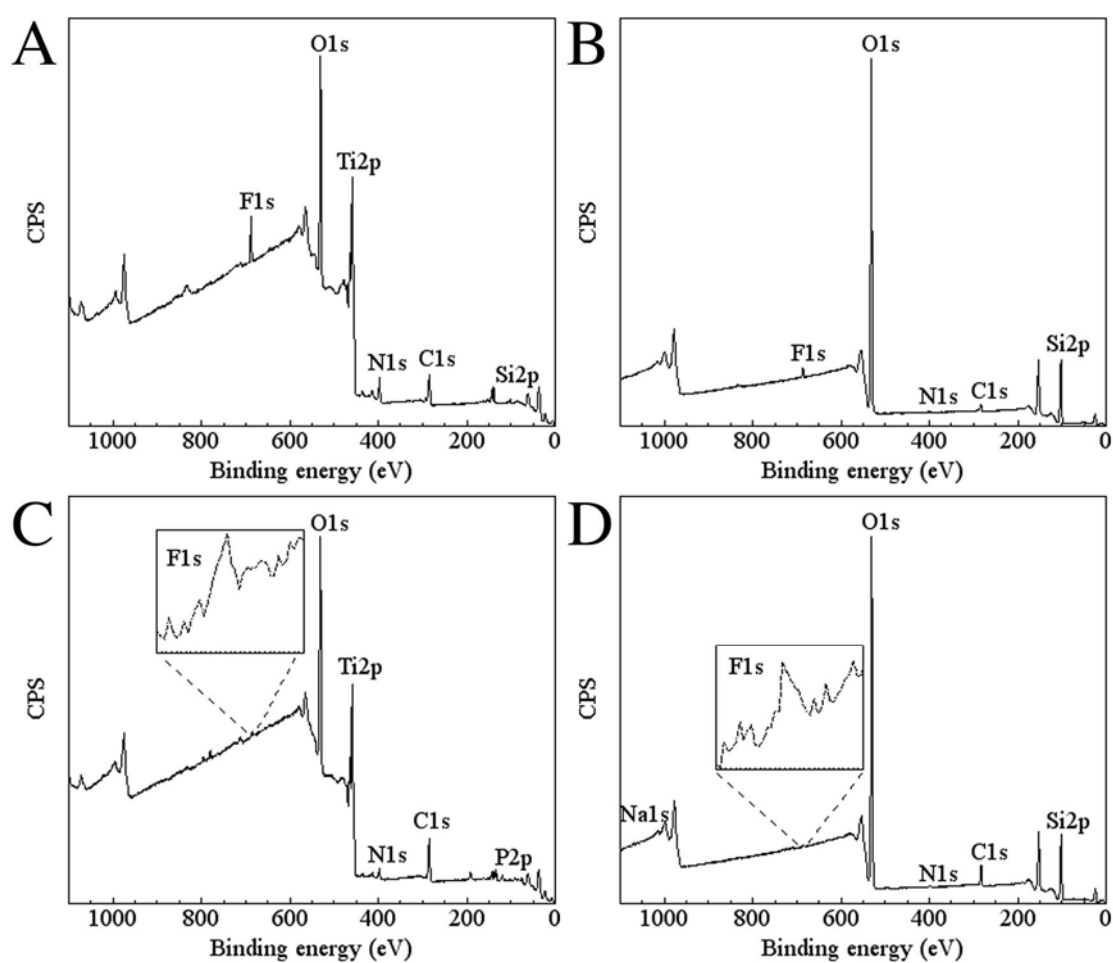


**Figure 1.27.** Typical XPS survey spectrum from uncoated titanium (**A** and **C**) and PECVD-Si-Ti (treated with 5 min of air/H<sub>2</sub>O<sub>2</sub> plasma) (**B** and **D**) surfaces functionalised with FPTMS (100 mM in toluene for 1 h at 25°C) according to Method 1 (refer to **pages 36-37**) before (**A** and **B**) and after (**C** and **D**) 12 h of incubation in PBS at 37°C and 5% CO<sub>2</sub>.

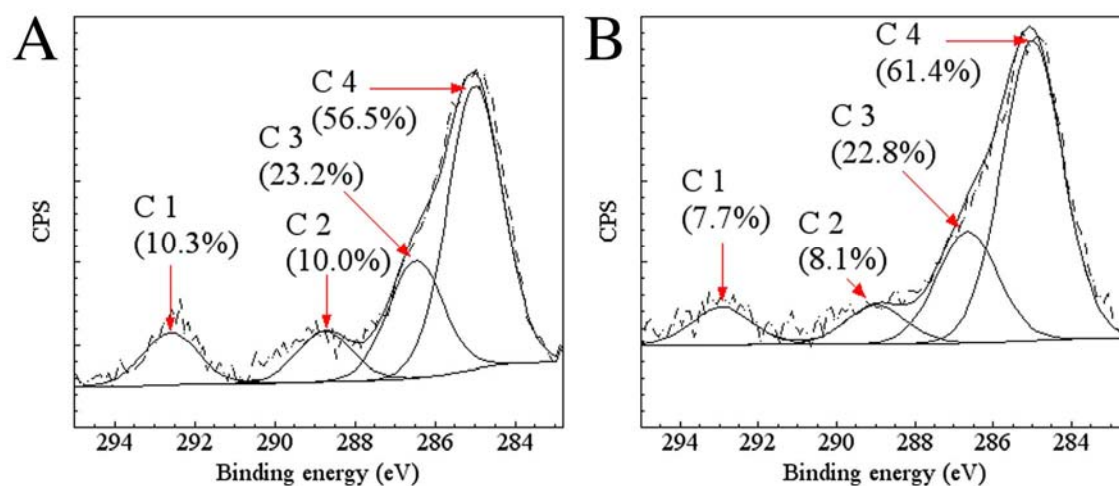


**Figure 1.28.** High-resolution C 1s spectra (dashed lines) and curve-fitted spectra (solid lines) taken on uncoated titanium (A) and PECVD-Si-Ti (treated with 5 min of air/H<sub>2</sub>O<sub>2</sub> plasma) (B) surfaces functionalised with FPTMS (100 mM in toluene for 1 h at 25°C) according to Method 1 (refer to pages 36-37).

Atomic % for samples labeled with FPTMS							
	O	C	N	F	Ti	Si	Na
Uncoated titanium	47.7	24.9	6.4	6.0	13.7	1.3	0.0
PECVD-Si-Ti (treated with 5 min of air/H <sub>2</sub> O <sub>2</sub> plasma)	60.7	9.0	0.2	2.0	0.0	28.1	0.0
Atomic % for samples labeled with FPTMS and incubated in PBS at 37°C and 5% CO <sub>2</sub> for 12 h							
	O	C	N	F	Ti	Si	Na
Uncoated titanium	51.6	31.2	4.5	2.1	10.1	0.5	0.0
PECVD-Si-Ti (treated with 5 min of air/H <sub>2</sub> O <sub>2</sub> plasma)	63.2	9.6	0.4	1.0	0.0	25.6	0.2

**Table 1.3.** Elemental atomic percentages for uncoated titanium and PECVD-Si-Ti samples (treated with 5 min of air/H<sub>2</sub>O<sub>2</sub> plasma) labeled with FPTMS (100 mM in toluene for 1 h at 25°C) according to Method 1 (refer to pages 36-37) and after 12 h of incubation in PBS at 37°C and 5% CO<sub>2</sub>.

In previous studies, hydroxylation of PECVD-Si by air/H<sub>2</sub>O<sub>2</sub> plasma was employed to improve the biological activity of the films deposited on titanium substrates [83, 85]. This was seen to produce an acceleration of bone growth on the implant surface *in vivo*, or HA-like precipitation *in vitro*. However, none of the data in these studies has directly measured an increase in the density of hydroxyl groups. Hydroxyl species were unable to be detected on PECVD-Si-Ti not treated or treated with air/H<sub>2</sub>O<sub>2</sub> plasma by XPS or IR spectroscopy (refer to the previous section). Furthermore, PECVD-Si-Ti that was not treated with air/H<sub>2</sub>O<sub>2</sub> plasma was found to be more hydrophilic in comparison to PECVD-Si-Ti treated with 5 min of air/H<sub>2</sub>O<sub>2</sub> plasma by contact angle (refer to **pages 59-60**). This result suggested that the PECVD-Si-Ti surface contains more hydroxyl groups in comparison to PECVD-Si-Ti treated with 5 min of air/H<sub>2</sub>O<sub>2</sub> plasma. Therefore, in the next set of experiments, PECVD-Si-Ti samples treated in air/H<sub>2</sub>O<sub>2</sub> plasma for different times were labeled with FPMTS and the surfaces were analysed by XPS.

This time, more vigorous reaction conditions were used to graft FPTMS onto PECVD-Si-Ti. This involved refluxing 100 mM of FPTMS in toluene over the PECVD-Si-Ti samples for 1 h, followed by a heating step at 90°C for 12 h according to Method 2 (A) (refer to **pages 36-37**). FPTMS was reacted on PECVD-Si-Ti for a longer time and at an elevated temperature in an attempt to increase the coverage of FPTMS molecules on PECVD-Si-Ti.

After FPTMS was grafted on PECVD-Si-Ti treated for 5 min in air/H<sub>2</sub>O<sub>2</sub> plasma, according to Method 2 (A), the fluorine signal (by XPS) was 4.3 at.%, which was higher than the atomic percentage of fluorine detected on the same surface functionalised with FPTMS according to Method 1 (2.0 at.%) (compare **Tables 1.3** and **1.4**). This result shows that a greater surface coverage of FPTMS molecules can be obtained on PECVD-Si-Ti by increasing the reaction time and temperature of the silane grafting conditions. After treating PECVD-Si-Ti with 15 min of air/H<sub>2</sub>O<sub>2</sub> plasma treatment, the fluorine signal was 4.4 at.%, which was similar to the concentration of fluorine detected on FPTMS-labeled PECVD-Si-Ti treated with 5 min of air/H<sub>2</sub>O<sub>2</sub> plasma (4.3 at.%) (**Table 1.4**). This result indicated that a PECVD-Si-Ti surface processed with 5 min of air/H<sub>2</sub>O<sub>2</sub> plasma contains a similar density of hydroxyl groups as one treated with 15 min of air/H<sub>2</sub>O<sub>2</sub> plasma. After grafting FPTMS (according to

Method 2 (A)) onto PECVD-Si-Ti treated with 1 min of air/H<sub>2</sub>O<sub>2</sub> plasma, only 1.7 at.% of fluorine was detected (**Table 1.4**). This was much lower than the concentration of fluorine (of 4.3 at.% and 4.4 at.%) detected on FPTMS-labeled PECVD-Si-Ti treated with 5 and 15 min of air/H<sub>2</sub>O<sub>2</sub> plasma, respectively (**Table 1.4**). The highest amount of fluorine (5.4 at.%) and therefore the highest coverage of FPTMS molecules was achieved on PECVD-Si-Ti not treated with air/H<sub>2</sub>O<sub>2</sub> plasma (**Table 1.4**). These results suggest that air/H<sub>2</sub>O<sub>2</sub> plasma processing of PECVD-Si-Ti does not increase the density of surface hydroxyl groups and therefore is not needed for promoting the condensation of alkoxy silanes on PECVD-Si-Ti.

To confirm these results, FPTMS was grafted (according to Method 2 (A)) on PECVD-Si-Ti that had not been treated with air/H<sub>2</sub>O<sub>2</sub> plasma and PECVD-Si-Ti treated with 5 min of air/H<sub>2</sub>O<sub>2</sub> plasma. Consistent with the results discussed above, the concentration of fluorine on PECVD-Si-Ti not treated with air/H<sub>2</sub>O<sub>2</sub> (5.8 at.%) was approximately 1 at.% higher than on PECVD-Si-Ti treated with 5 min of air/H<sub>2</sub>O<sub>2</sub> plasma (4.6 at.%) (**Table 1.5**). This data, together with contact angle measurements discussed in the previous section, suggest that the density of hydroxyl groups is reduced on PECVD-Si-Ti by air/H<sub>2</sub>O<sub>2</sub> plasma processing compared to PECVD-Si-Ti not processed with air/H<sub>2</sub>O<sub>2</sub> plasma. Possibly, the surface density of hydroxyl groups was reduced in the early stages of the air/H<sub>2</sub>O<sub>2</sub> plasma treatment ( $\leq 1$  min) before new hydroxyl groups were formed following longer processing times ( $\geq 5$  min) [129].

Air/H <sub>2</sub> O <sub>2</sub> plasma treatment time	O at.%	C at.%	N at.%	F at.%	Si at.%
0 min	58.1	10.7	0.2	5.4	25.6
1 min	52.1	15.9	1.2	1.7	29.1
5 min	59.3	9.8	0.1	4.3	26.5
15 min	53.9	13.0	0.0	4.4	28.7

**Table 1.4.** Elemental atomic percentages of FPTMS-labeled PECVD-Si-Ti that had been treated with different times of air/H<sub>2</sub>O<sub>2</sub> plasma, as indicated in the above table. 100 mM of FPTMS, prepared in toluene, was grafted on PECVD-Si-Ti by refluxing at 120°C for 1 h, followed by heating at 90°C for 12 h according to Method 2 (A) (refer to **pages 36-37**).

After incubating FPTMS-labeled PECVD-Si-Ti not treated and treated with 5 min of air/H<sub>2</sub>O<sub>2</sub> plasma in PBS under physiological conditions, the percentage of fluorine decreased by 62% and 72%, respectively (**Table 1.5**). These results suggest that PECVD-Si-Ti not treated with air/H<sub>2</sub>O<sub>2</sub> plasma, supports the highest coverage of alkoxy silanes and more stable siloxane films in comparison to PECVD-Si-Ti treated with air/H<sub>2</sub>O<sub>2</sub> plasma. Since PECVD-Si-Ti not treated with air/H<sub>2</sub>O<sub>2</sub> was found to be a more optimal surface for grafting alkoxy silanes compared to PECVD-Si-Ti surfaces treated with air/H<sub>2</sub>O<sub>2</sub> plasma, for the remainder of this thesis, we abandoned the air/H<sub>2</sub>O<sub>2</sub> plasma-processing step.

Atomic % for PECVD-Si-Ti labeled with FPTMS						
	O	C	N	F	Si	Na
PECVD-Si-Ti not treated with air/H <sub>2</sub> O <sub>2</sub> plasma	57.7	10.7	0.0	5.8	25.8	0.0
PECVD-Si-Ti treated with 5 min of air/H <sub>2</sub> O <sub>2</sub> plasma	58.7	9.8	0.0	4.6	26.9	0.0
Atomic % for PECVD-Si-Ti labeled with FPTMS and incubated in PBS at 37°C and 5% CO <sub>2</sub> for 12 h						
	O	C	N	F	Si	Na
PECVD-Si-Ti not treated with air/H <sub>2</sub> O <sub>2</sub> plasma	59.1	11.9	0.8	2.2	25.9	0.1
PECVD-Si-Ti treated with 5 min of air/H <sub>2</sub> O <sub>2</sub> plasma	60.4	11.2	0.9	1.3	26.1	0.1

**Table 1.5.** Elemental atomic percentages of FPMTS-labeled PECVD-Si-Ti not treated or treated air/H<sub>2</sub>O<sub>2</sub> plasma and after 12 h of incubation in PBS at 37°C and 5% CO<sub>2</sub>. FPTMS at 100 mM in toluene was refluxed at 120°C for 1 h and then heated at 90°C for 12 h according to Method 2 (A) (refer to **pages 36-37**).

So far we found that grafting of an alkoxy silane (FPTMS) according to Method 1 (100 mM of FPTMS for 1 h at 25°C) results in a relatively low coverage of FPTMS molecules and a FPTMS siloxane film that is relatively moderately stable under an aqueous physiological condition. Method 2 (A) (100 mM of FPTMS refluxed at 120°C for 1 h followed by heating at 90°C for 12 h) produced a greater coverage of FPTMS molecules and a FPTMS siloxane film that is similar in stability (under an aqueous physiological environment) to that of a FPTMS siloxane film produced according to Method 1. Also, PECVD-Si-Ti not treated with air/H<sub>2</sub>O<sub>2</sub> plasma was found to be a more effective surface for functionalising with alkoxy silanes than air/H<sub>2</sub>O<sub>2</sub> plasma-processed PECVD-Si-Ti. In the next set of experiments, a few more parameters will be investigated to determine if we can further control the grafting density of alkoxy silanes on PECVD-Si-Ti (not treated with air/H<sub>2</sub>O<sub>2</sub> plasma) and analyse the stability of the siloxane films under physiological conditions.

The coverage of FPTMS molecules on PECVD-Si-Ti (not treated with air/H<sub>2</sub>O<sub>2</sub> plasma) was assessed under different silane grafting conditions: Method 2 (described above), with siloxane films not cured (Method 2 (A)) or cured at 100°C for 12 h (Method 2 (B)); 1% (v/v) FPTMS in an aqueous environment (in a methanolic solution containing 5% (v/v) water and 1 mM acetic acid) at 25°C for 2.5 h and then cured at 120°C for 5 min – Method 3); and in an undiluted form (neat) at 90°C for 1 h – Method 4 (refer to **pages 36-37**).

We first compared the coverage of FPTMS molecules grafted on PECVD-Si-Ti according to Method 2 before and after curing. As shown in **Table 1.6**, the fluorine signal (by XPS) on FPTMS-labeled PECVD-Si-Ti was increased from 4.8 at.% before curing to 5.9 at.% after curing the siloxane films at 100°C for 12 h. This result can be explained by free silanol groups of FPTMS molecules reacting to form a more cross-linked and therefore more tightly packed siloxane film [107]. After incubating these samples in PBS under physiological conditions, the atomic percentage of fluorine was 3.8 at.% and 4.0 at.% on non-cured and cured samples, respectively (**Table 1.6**). This result was interesting because it showed that the stability between cured and non-cured siloxane films was similar in this study. According to the literature, this result was not expected because cured siloxane films should be more resistant to hydrolytic degradation than non-cured films [107, 142]. But the results from this study imply that

the method by which the siloxane film is grafted on PECVD-Si-Ti may influence the stability of the siloxane films more than the cross-linking procedure.

The lowest atomic percentage of fluorine (1.4 at.%) was detected on PECVD-Si-Ti that was functionalised with FPTMS by Method 3 in comparison to all of the other methods tested in this study, which indicated that this method produced the lowest coverage of FPTMS molecules on PECVD-Si-Ti and most likely, the thinnest siloxane film (**Table 1.6**). This result was expected because monolayer or near monolayer siloxane films are more readily formed in aqueous medium in comparison to multi-layered siloxane films usually formed in organic solvents [123, 148-149]. After labeling PECVD-Si-Ti with FPTMS by heating a neat (undiluted) solution of FPTMS over the sample at 90°C for 1 h (Method 4), 4.3 at.% of fluorine was detected by XPS, which was similar to FPTMS films deposited by Method 2 (**Table 1.6**). Therefore, the results in this study so far have shown that the grafting density of alkoxy silanes on PECVD-Si-Ti is mainly dependant on reaction time, temperature and solvent type and to a lesser degree on the concentration of silane.

The high-resolution C 1s curve-fitted XPS spectra supported the above conclusions. C 1 was assigned to the CF<sub>3</sub> group of FPTMS, C 2 and 3 to C-O-Si and C-O species and C 4 to saturated hydrocarbons. The CF<sub>3</sub> contribution in the C 1s region was similar between PECVD-Si-Ti labeled with FPTMS according to Method 2 (A) (13.4%; **Figure 1.29 A**) and Method 4 (11.8%; **Figure 1.29 D**) supporting the conclusion that both surfaces had a similar coverage of FPTMS molecules. The CF<sub>3</sub> contribution was increased from 13.4% to 20.3% in the C 1s region after the siloxane film (deposited by Method 2 (A)) was cured (Method 2 (B)) due to the FPTMS molecules forming a more tightly packed cross-linked network (**Figure 1.29 A and B**). CF<sub>3</sub> comprised 1.4% of the C 1s region for PECVD-Si-Ti labeled with FPTMS in aqueous medium (Method 3), which was the lowest of all the FPTMS-labeled PECVD-Si-Ti samples analysed in this study and confirmed that this method produced the lowest coverage of FPTMS molecules on PECVD-Si-Ti (compared to the other methods analysed in this study) (**Figure 1.29 C**). Finally, the contribution of CF<sub>3</sub> on FPTMS-labeled PECVD-Si-Ti (according to Method 2) after incubation in PBS was 9.0% and 8.8% for cured and non-cured samples, respectively, which confirmed that the curing step did not improve the stability of the film (in aqueous medium under physiological conditions) (**Figure 1.29 E and F**).

In summary, by means of XPS analysis, the surface coverage of a model silane (FPTMS) was compared after grafting the silane on PECVD-Si-Ti under different reaction conditions. A relatively low surface density of FPTMS molecules was deposited in aqueous medium according to Method 3. A higher density of FPTMS was deposited in anhydrous organic solvent (toluene) at 25°C for 1 h (according to Method 1) and the density of FPTMS molecules was increased yet again at elevated temperatures of 120°C and 90°C and at longer reaction times (according to Method 2 (A)). But the grafting density of FPTMS molecules on PECVD-Si-Ti was not significantly affected by the concentration of the silane (for the range used in this study) because a similar density of FPTMS molecules were grafted on PECVD-Si-Ti from an undiluted silane solution (according to Method 4) compared to the coverage of FPTMS molecules on PECVD-Si-Ti produced from 100 mM silane reaction solutions (according to Method 2 (A)). To confirm these conclusions, the coverage and stability of a different silane will be analysed on PECVD-Si-Ti under the same reaction conditions that were used for grafting the FPTMS.

Atomic % for PECVD-Si-Ti labeled with FPTMS						
	O	C	N	F	Si	Na
100 mM in toluene; Refluxed at 120°C for 1 h, then heated at 90°C for 12 h (Method 2)	62.0	8.2	0.0	4.8	25.0	0.0
100 mM in toluene; Refluxed at 120°C for 1 h, then heated at 90°C for 12 h (Method 2 (A)) and cured at 100°C for 12 h (Method 2 (B))	61.6	6.9	0.0	5.9	25.6	0.0
1% (v/v) in methanol containing 5% (v/v) water and 1 mM acetic acid for 2.5 h at 25°C; cured at 120°C for 5 min (Method 3)	62.3	12.0	0.5	1.4	23.8	0.0
Neat at 90°C for 1 h (Method 4)	58.5	11.7	0.4	4.3	25.1	0.0
Atomic % for PECVD-Si-Ti labeled with FPTMS and incubated in PBS at 37°C and 5% CO <sub>2</sub> for 12 h						
	O	C	N	F	Si	Na
100 mM in toluene; Refluxed at 120°C for 1 h, then heated at 90°C for 12 h (Method 2 (A))	59.7	11.6	0.7	3.8	23.8	0.4
100 mM in toluene; Refluxed at 120°C for 1 h, then heated at 90°C for 12 h and cured at 100°C for 12 h (Method 2 (B))	60.2	10.6	0.5	4.0	24.3	0.4

**Table 1.6.** Elemental atomic percentage data derived from PECVD-Si-Ti (not treated with air/H<sub>2</sub>O<sub>2</sub> plasma) samples labeled with FPTMS using different grafting conditions as outlined in the above table and described in detail on **pages 36-37**. Additionally, FPTMS-labeled PECVD-Si-Ti (according to Method 2) samples with siloxane films not cured (Method 2 (A)) or cured (Method 2 (B)) were analysed by XPS after 12 h of incubation in PBS under physiological conditions.

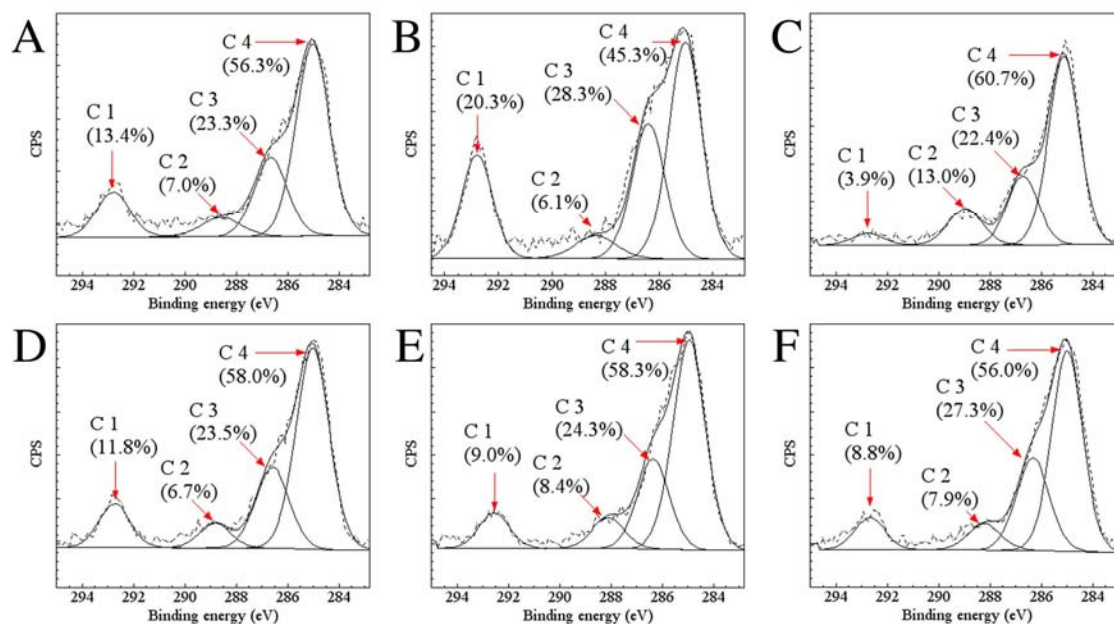
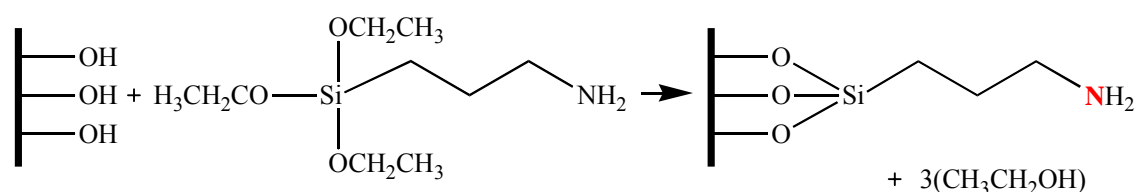


**Figure 1.29.** XPS high-resolution C 1s spectra (dashed lines) and curve-fitted spectra (solid lines) taken on PECVD-Si-Ti (not treated with air/H<sub>2</sub>O<sub>2</sub> plasma) that was functionalised with FPTMS by: refluxing 100 mM of FPTMS at 120°C in toluene for 1 h, followed by heating at 90°C for 12 h (Method 2) before (A) and after (B) curing at 100°C for 12 h; incubating 1% (v/v) FPMTS in methanol containing 5% (v/v) water and 1 mM acetic acid at 25°C for 2.5 h and curing at 120°C for 5 min (Method 3) (C); and undiluted at 90°C for 1 h (Method 4) (D). Two samples functionalised by Method 2 were also incubated in PBS for 12 h at 37°C and 5% CO<sub>2</sub> for non-cured (E) and cured (F) siloxane films. Refer to **page 36-37** for more detail of alkoxy silane grafting procedures.

PECVD-Si-Ti (not treated with air/H<sub>2</sub>O<sub>2</sub> plasma) was next modified with 3-aminopropyl triethoxysilane (APTES) under the reaction conditions described above. APTES is commonly used in the modification of hydroxyl-bearing materials for generating functional surfaces [113, 150-151]. In these experiments, the nitrogen atom of the amino group of APTES was used as a marker element for the detection of the silane by XPS (**Scheme 1.5**).

A typical XPS survey spectrum of a APTES-labeled PECVD-Si-Ti sample is shown in **Figure 1.30 A**. This sample was labeled with the APTES according to Method 2 (B). Notably, a strong nitrogen signal (which is otherwise absent on PECVD-Si-Ti as shown in the previous section) of 7.0 at.% is detected in the spectrum (**Figure 1.30 A**). This nitrogen signal, derived from one nitrogen atom per APTES molecule, was higher than the fluorine signal derived from 3 fluorine atoms per FPTMS (of 5.9 at.%) after both silanes were grafted on PECVD-Si-Ti by the same method (Method 2 (B)) (**Table 1.6** and **Figure 1.30 A**). Also, the concentration of carbon (attributed to the hydrocarbon chain of APTES and FPTMS) was nearly 6-fold higher on APTES-labeled PECVD-Si-Ti (48.5 at.%) in comparison to FPTMS-labeled PECVD-Ti-Si (8.2 at.%) (**Table 1.6** and **Figure 1.30 A**). These results indicate that the APTES reacts more efficiently on PECVD-Si-Ti in comparison to the FPTMS.

The above conclusion was supported by the high-resolution C 1s XPS spectrum. The spectrum was fitted with 3 components. C 1 at 288.0 eV was attributed to C-O-Si possibly from unreacted ethoxy groups of the silane; C 2 at 286.2 eV was attributed to C-O and C-N species from unreacted ethoxy groups and the amino group of the APTES; and C 3 at 285.0 eV was attributed to adventitious hydrocarbons and C-H species from the hydrocarbon chain of the APTES (**Figure 1.30 B**) [112, 152]. The extensive contribution from C 2 (25.6%) partly from C-N species of APTES and C 3 (64.9%) partly from the hydrocarbon chain of the APTES indicates a high surface coverage of APTES molecules on PECVD-Si-Ti. Also, the amino group of the APTES was mainly in the form of NH<sub>2</sub> groups as indicated in the XPS N 1s region: C 2 at 399.6 eV assigned to NH<sub>2</sub> that comprised 72.2% of the N 1s spectrum and a smaller percentage of C 1 (27.8%) at 401.1 eV from protonated amino (NH<sub>3</sub><sup>+</sup>) groups comprised the remainder of the N 1s spectrum (**Figure 1.30 C**) [112].



**Scheme 1.5.** Schematic of a possible surface reaction between a APTES molecule and a hydroxylated surface. The surface becomes terminated with an amino group and the nitrogen atom is used as a marker element for the detection of the silane by XPS (shown in red).

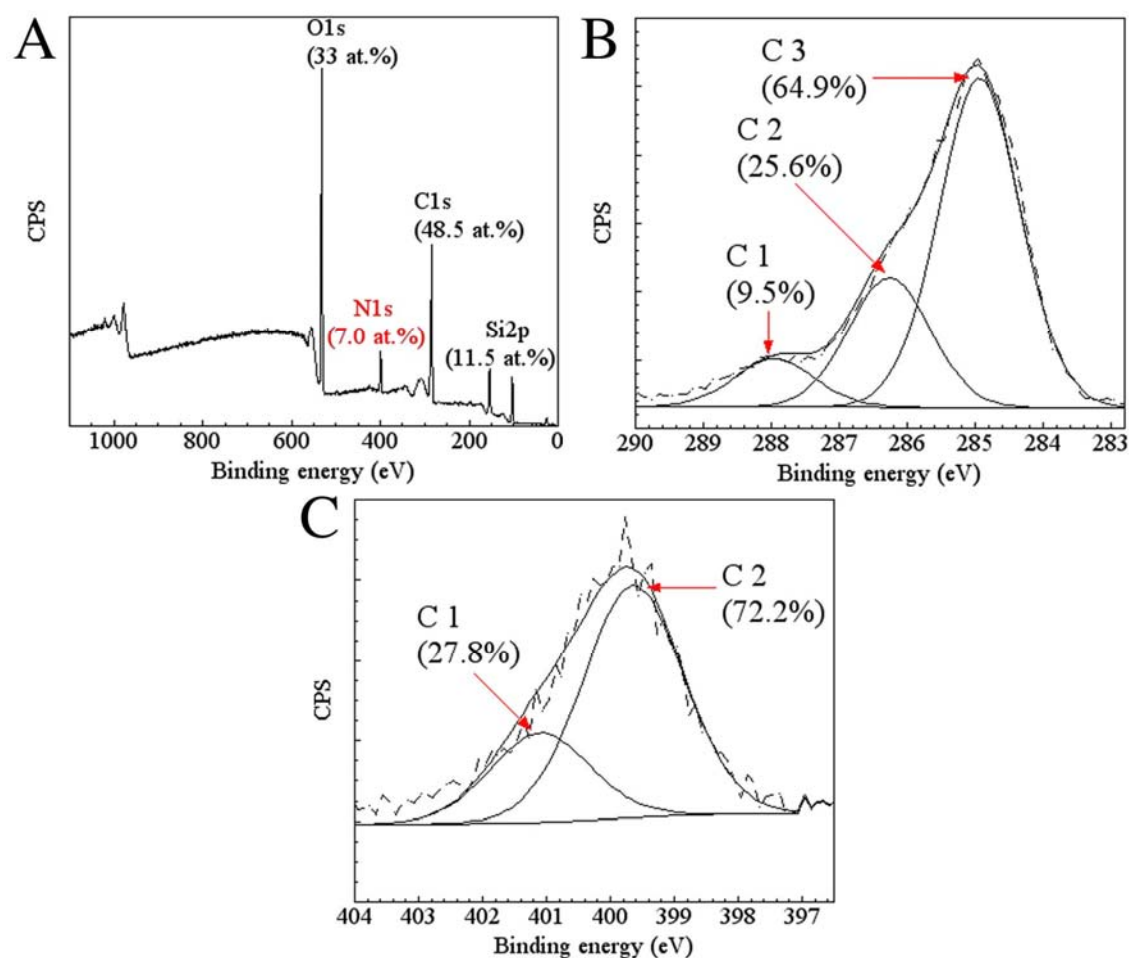


**Figure 1.30.** An example XPS survey spectrum (A), high-resolution C 1s spectrum (B) and N 1s spectrum (C) of a APTES-labeled PECVD-Si-Ti sample. 100 mM of APTES was refluxed over PECVD-Si-Ti for 1 h and then heated at 90°C for 12 h cured at 100°C for 12 h (Method 2 (B) (refer to [pages 36-37](#) for a more detailed description)). Nitrogen from the amino group of APTES is used as a marker element to indicate the molecule is present on the PECVD-Si-Ti surface (shown in red).

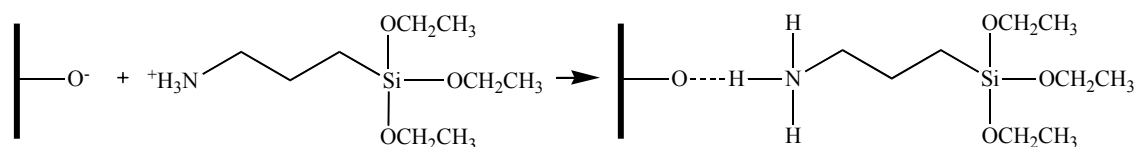
**Table 1.7** outlines the elemental atomic percentages on PECVD-Si-Ti (not treated with air/H<sub>2</sub>O<sub>2</sub> plasma) labeled with APTES according to Methods 1-5 (refer to **pages 36-37** for detailed descriptions) and after the APTES-labeled samples were incubated in PBS under physiological conditions. 2.8 at.% of nitrogen was detected on PECVD-Si-Ti reacted with 100 mM of APTES at 25°C for 1 h according to Method 1 (**Table 1.7**). Similar to the results obtained with the FPTMS, the coverage of APTES was increased (indicated by an increase in the concentration of nitrogen to 7.0 at.%) when the sample was reacted with the silane at a higher temperature and a longer time period (refluxed at 120°C for 1 h, then heated at 90°C for 12 h and cured at 100°C for 12 h according to Method 2 (B)) (**Table 1.7**). The coverage of silane was found to be similar to Method 2 (B) (7.0 at.% of nitrogen) after 1% (v/v) of APTES in toluene was grafted on PECVD-Si-Ti for 2.5 h at 25°C and cured at 120°C for 5 min (7.4 at.% of nitrogen) (Method 5) (**Table 1.7**). This result suggested that the reaction time had a greater influence on the coverage of APTES on PECVD-Si-Ti in comparison to the temperature. Additionally, a slightly higher coverage of APTES on PECVD-Si-Ti was obtained by grafting an undiluted solution of the silane at 90°C for 1 h (Method 4) (3.9 at.% of nitrogen) in comparison to when 100 mM of APTES (in toluene) was grafted on PECVD-Si-Ti at 25°C for 1 h according to Method 1 (2.8 at.% of nitrogen). Also, the coverage of APTES on PECVD-Si-Ti was directly compared between grafting Methods 3 and 5. APTES was grafted on PECVD-Si-Ti under the same experimental conditions according to Methods 3 and 5, except Method 3 used an aqueous medium and Method 5 used an anhydrous organic solvent (toluene). After grafting APTES on PECVD-Si-Ti, the atomic percentage of nitrogen was much lower when the silane was grafted in aqueous medium (1.9 at.% of nitrogen) in comparison to anhydrous toluene (7.4 at.% of nitrogen) (**Table 1.7**). Therefore, the nature solvent significantly influenced the grafting density of APTES on PECVD-Si-Ti. Finally, in contrast to FPTMS siloxane films, APTES siloxane films were much more stable under aqueous physiological conditions. Approximately 93%, 99%, 95%, 85% and 66% of the nitrogen signal was retained on APTES-labeled PECVD-Si-Ti according to Methods 1-5, respectively, after the samples had been incubated in PBS under physiological conditions.

Atomic % for PECVD-Si-Ti labeled with APTES					
	O	C	N	Si	Na
100 mM in toluene; 1 h at 25°C (Method 1)	50.9	26.0	2.8	20.3	0.0
100 mM in toluene; Refluxed at 120°C for 1 h, then heated at 90°C for 12 h and cured at 100°C for 12 h (Method 2 (B))	33.0	48.5	7.0	11.5	0.0
1% (v/v) in methanol containing 5% (v/v) water and 1 mM acetic acid at 25°C for 2.5 h; cured at 120°C for 5 min (Method 3)	61.7	15.4	1.9	21.0	0.0
Neat at 90°C for 1 h (Method 4)	51.1	26.3	3.9	18.7	0.0
1% (v/v) in toluene at 25°C for 2.5 h; cured at 120°C for 5 min (Method 5)	36.5	43.1	7.4	13.0	0.0
Atomic % for PECVD-Si-Ti labeled with APTES and incubated in PBS at 37°C and 5% CO <sub>2</sub>					
	O	C	N	Si	Na
100 mM in toluene; 1 h at 25°C (Method 1)	59.6	18.2	2.6	19.6	0.0
100 mM in toluene; Refluxed 1 h and heated at 90°C for 12 h and cured at 100°C for 12 h (Method 2 (B))	34.6	49.8	6.9	8.7	0.0
1% (v/v) in methanol containing 5% (v/v) water and 1 mM acetic acid at 25°C for 2.5 h; cured at 120°C for 5 min (Method 3)	61.0	17.6	1.8	19.6	0.0
Neat at 90°C for 1 h (Method 4)	52.3	27.2	3.3	16.7	0.5
1% (v/v) in toluene at 25°C for 2.5 h; cured at 120°C for 5 min (Method 5)	45.1	36.2	4.9	13.8	0.0

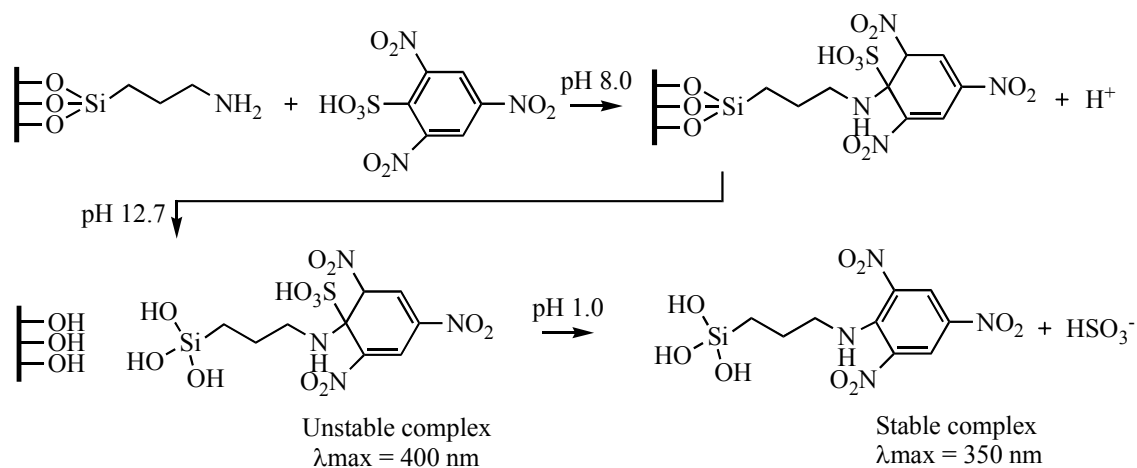
**Table 1.7.** XPS elemental atomic percentage data on PECVD-Si-Ti (no air/H<sub>2</sub>O<sub>2</sub> plasma treatment) after the surface was functionalised with APTES using the different methods outlined in the above table and described on **pages 36-37** and after 12 h of incubation in PBS under physiological conditions.

Protonated amino groups were detected on all PECVD-Si-Ti samples labeled with APTES. Approximately 25% of  $\text{NH}_3^+$  species contributed the N 1s region by XPS. The remainder comprised of  $\text{NH}_2$  species. A typical N 1s high-resolution XPS spectrum with two fitted components attributed for  $\text{NH}_2$  and  $\text{NH}_3^+$  species was shown in **Figure 1.30 C**. Amino groups on APTES-functionalised surfaces are generally found in both  $\text{NH}_2$  and  $\text{NH}_3^+$  forms and the latter can form hydrogen or ionic bonds with oxidised surfaces (**Scheme 1.6**) [125, 145]. This phenomenon could result in a weakly adsorbed APTES siloxane film.

Therefore, in the next set of experiments, we tested if we could label and ultimately detect  $\text{NH}_2$  groups on APTES-modified PECVD-Si-Ti. This was accomplished by labeling APTES-modified PECVD-Si-Ti with 2,4,6-trinitrobenzenesulfonic acid (TNBS), which selectively reacts with amino nucleophiles [153-159]. The reaction is shown in **Scheme 1.7**. TNBS first attaches to an amino group in a moderately basic buffered solution (pH 8.0). The complex is hydrolysed from the surface in a basic solution of pH 12.7. This complex, which has a  $\lambda_{\text{max}}$  of 400 nm (**Figure 1.31**), is unstable. The unstable complex is then converted into a stable complex by lowering the pH to 1.0 [144]. The concentration of the stable complex, with a  $\lambda_{\text{max}}$  of 350 nm (**Figure 1.31**), can then be determined by ultraviolet-visible (UV-Vis) spectroscopy. The molar extinction coefficient at 350 nm for (trinitrophenol) TNP-APTES (from **Figure 1.31**) was calculated to be  $1.3394 \times 10^4 \text{ M}^{-1}\text{cm}^{-1}$ , which is in good agreement with that reported for a similar TNP compound [153].



**Scheme 1.6.** Schematic of a protonated amino group of an APTES molecule hydrogen bonding (dashed line) to an oxidised surface.



**Scheme 1.7.** A proposed reaction of a TMBS molecule with a APTES functionalised surface. The amino-terminated surface is first reacted under mildly alkaline conditions, the product is then hydrolysed from the surface in a basic solution and finally the solution is acidified to produce a stable complex with a  $\lambda_{\text{max}}$  of 350 nm.

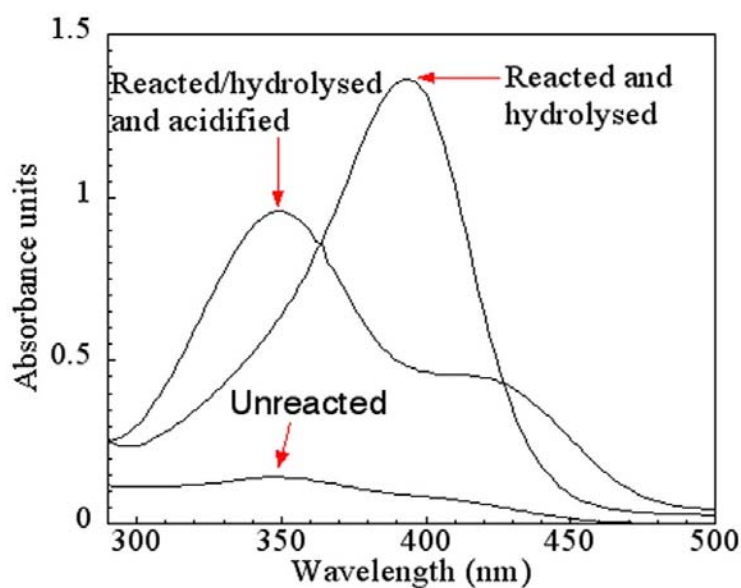


**Figure 1.31.** A UV-Vis spectrum of TNBS solution (Unreacted, that is a spectrum of the commercial stock of TNBS), a spectrum of hydrolysed TNP-APTES solution (Reacted and hydrolysed) and after acidifying the solution containing the hydrolysed TNP-APTES compound (Reacted/hydrolysed and acidified). Refer to **page 38** for a description of the experimental procedure.

Next, we examined the availability of amino groups from two PECVD-Si-Ti surfaces that had been functionalised with APTES by two different methods. One surface was functionalised with an undiluted solution of APTES at 90°C for 1 h according to Method 4 and the other sample was functionalised with 1% (v/v) APTES in toluene at 25°C for 2.5 h and cured at 120°C for 5 min (Method 5). UV-Vis spectra of acidified TNBS reaction solutions are shown for both samples in **Figure 1.32 A and B**. The absorbance measured at 350 nm in the spectra corresponded with 67 and 92 NH<sub>2</sub> groups per nm<sup>2</sup> for APTES-functionalised PECVD-Si-Ti according to Methods 4 and 5, respectively (**Figure 1.32 A and B**). Organic APTES silanisation methods usually produce much larger densities compared to other methods, such as silanisation in aqueous medium. For example, Puleo found that APTES silanisation of a Co-Cr-Mo metal alloy using a silane concentration of 82 mM in acetone for 10 min at room temperature resulted in 92 NH<sub>2</sub> groups per nm<sup>2</sup>, whereas a much lower density of NH<sub>2</sub> groups (6.7 NH<sub>2</sub> groups per nm<sup>2</sup>) was detected on the metal alloy silanised with 1.02 M of APTES in deionised water for 3 h at room temperature [149]. However, the higher surface density of NH<sub>2</sub> groups detected on APTES-functionalised PECVD-Si-Ti by Method 5 in comparison to Method 4 was in accordance with the XPS measurements for both samples. A higher atomic percentage of nitrogen (related to the surface density of APTES molecules) was measured for APTES-labeled PECVD-Si-Ti by Method 5 (7.4 at.%) compared to Method 4 (3.9 at.%) (**Table 1.7**). The expected surface density of amino groups for a monolayer surface coverage of APTES is 2-3 NH<sub>2</sub> groups/nm<sup>2</sup> and densities above this are representative of APTES multilayered films [160]. A much higher surface density of NH<sub>2</sub> groups were detected on APTES-functionalised PECVD-Si-Ti in this work because the roughness of the titanium substrate was not considered and therefore the surface area of PECVD-Si-Ti was underestimated and a high density of APTES molecules had attached on the PECVD-Si-Ti samples as indicated by XPS analysis.

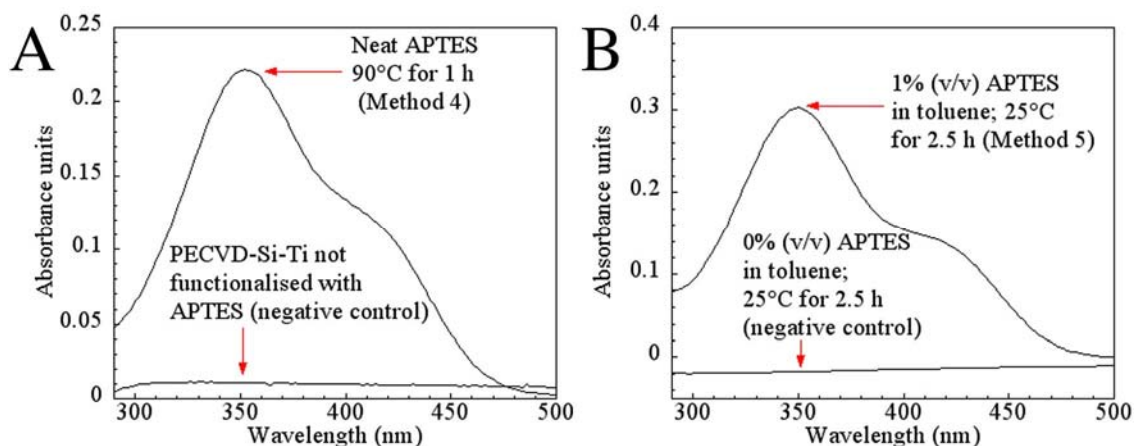


**Figure 1.32.** UV-Vis spectra of acidified TNBS reaction solutions from two APTES-functionalised PECVD-Si-Ti samples. PECVD-Si-Ti was functionalised with an undiluted solution of APTES at 90°C for 1 h according to Method 4 (A) and 1% (v/v) of APTES in toluene at 25°C for 2.5 h followed by a curing step at 120°C for 5 min according to Method 5 (B). Spectra were also taken of acidified TNBS reaction solutions incubated on negative control samples prepared for each sample type (that contain no amino functionalities). Refer to **page 38** for a detailed description of the experimental procedure.

In summary, by means of XPS, we assessed the coverage of FPTMS and APTES on PECVD-Si-Ti. A similar coverage of FPTMS was obtained on PECVD-Si-Ti not treated or treated with 5 or 15 min of air/H<sub>2</sub>O<sub>2</sub> plasma. This result suggested that the air/H<sub>2</sub>O<sub>2</sub> plasma did not increase the density of hydroxyl groups on PECVD-Si-Ti. The grafting density of FPTMS was significantly affected by the nature of the solvent, reaction time and temperature. The grafting density was increased in anhydrous toluene in comparison to aqueous medium and at elevated temperatures and longer reaction times. FPTMS siloxane films on PECVD-Si-Ti were relatively unstable under aqueous physiological conditions and the stability of the siloxane film was not improved after thermal treatment (curing). In comparison to FPTMS, APTES reacted much more efficiently on PECVD-Si-Ti. Similar to reactions involving FPTMS, the grafting density of APTES on PECVD-Si-Ti was higher in anhydrous toluene compared to aqueous medium. Furthermore, the grafting density of APTES was also influenced by the reaction temperature and time. All of the APTES siloxane films grafted on PECVD-Si-Ti by the 5 methods tested in this section were relatively stable under aqueous conditions. Finally, we determined that the APTES molecules grafted on PECVD-Si-Ti by two grafting methods (Methods 4 and 5) had formed an appropriate conformation so that the functional end amino group could be labeled with TNBS and subsequently

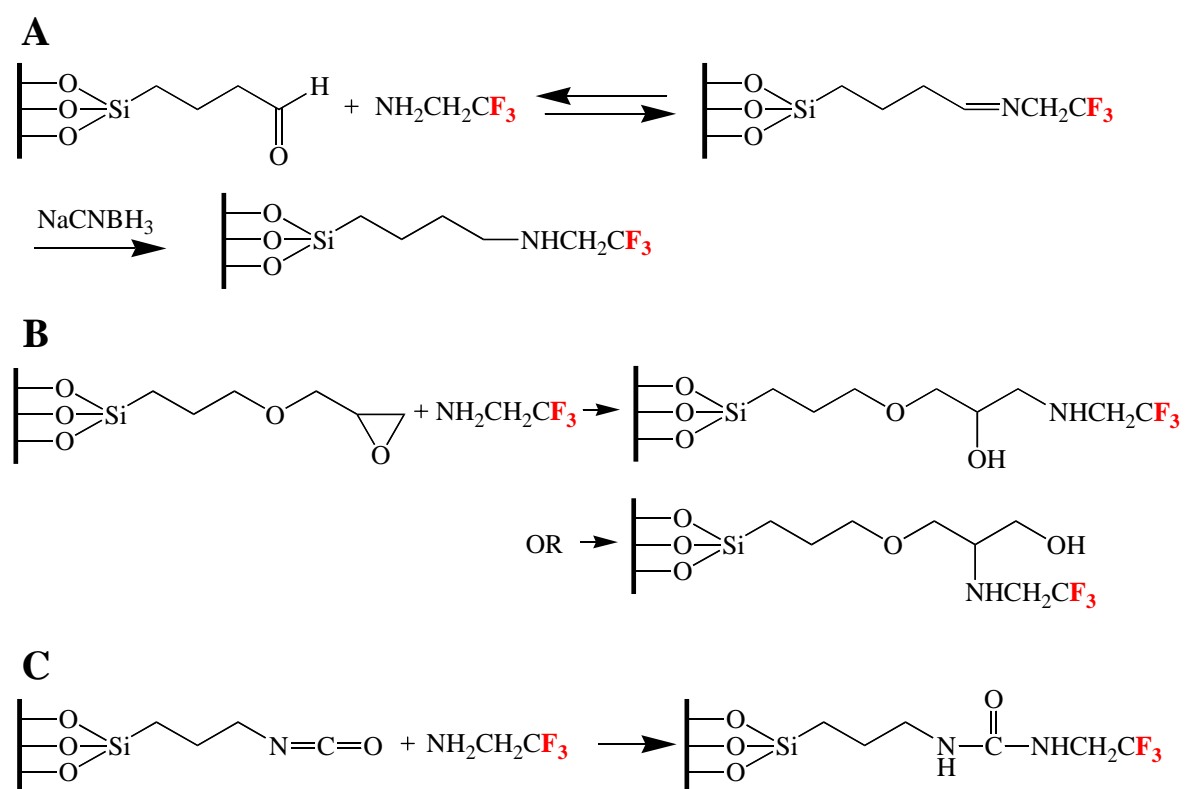
detected by UV-Vis spectroscopy. In the following sections we will use some of the alkoxy silane grafting conditions described in this section for introducing new functional groups (via intermediate silane tethers) that will be used to immobilise IGF-1 on PECVD-Si-Ti.

### 1.3.3 Development of surface modification techniques for the covalent attachment of insulin-like growth factor-1 (IGF-1) on PECVD-Si-Ti

This section focuses on the preparation of surfaces presenting three different functional groups that can react with amino groups of amino acids that make up the polypeptide chains of proteins. 2,2,2-trifluoroethylamine (FEAM) was chosen as a model amino molecule for this study. The amino group of FEAM can react with an amino-reactive surface functional group to form a surface terminated with 3 fluorine atoms per FEAM molecule that can be detected by XPS (**Scheme 1.8**). This is a similar approach to reactions described using TFAA and FPTMS in the previous two sections of Part 1: Results and Discussion.

The advantage of studying the immobilisation of this model molecule by XPS before the immobilisation of IGF-1 is that the performance of these reactions could be easily analysed by measuring a distinct (fluorine) signal on the PECVD-Si-Ti surface derived from the model FEAM molecule. Surface reactions involving IGF-1 are more difficult to interpret by XPS due to the lack of a sensitive and characteristic marker element. Furthermore, a low amount of IGF-1 was reacted on PECVD-Si-Ti in this study (refer to the following section of Part 1: Results and Discussion), resulting in a low maximum surface coverage. The reasoning behind this is that IGF-1 molecules have been shown to be mitogenic agonists at relatively low concentrations ranging from 0.003-0.1  $\mu\text{M}$  in solution [99-100]. Hence, a relatively low amount of IGF-1 was reacted on PECVD-Si-Ti in this study (340  $\text{ng}/\text{cm}^2$ , refer to the following section of Part 1: Results and Discussion) to obtain a low surface coverage of the growth factor, which was deemed to be appropriate for the immobilised IGF-1 molecules to sustain bioactivity on the material's surface. By analysing techniques used for protein attachment with the FEAM model molecule, a successful method was found and later adapted for tethering IGF-1 molecules to the functionalised PECVD-Si-Ti surface.

Functional groups were introduced onto the PECVD-Si-Ti surface by grafting silane molecules with short hydrocarbon-chains containing aldehyde, epoxide and isocyanate reactive groups (**Scheme 1.8**). Similar to FPTMS and APTES molecules that were used to model silane reactions on the PECVD-Si-Ti surface in the previous section, these silane molecules also contain reactive trialkoxy groups that can condense with the surface silanol groups on PECVD-Si-Ti (these reactions were discussed in the previous section).



**Scheme 1.8.** Possible reactions of FEAM with aldehyde (**A**), epoxide (**B**) and isocyanate (**C**) reactive groups on hydroxylated surfaces that were functionalised with triethoxysilyl butyraldehyde (ABTES) (**A**), 3-glycidyloxypropyl trimethoxysilane (GPTMS) (**B**), and 3-isocyanatopropyl triethoxysilane (IPTES) (**C**). Each attached FEAM molecule contains 3 fluorine atoms (shown in red) that can be detected by XPS.

Aldehyde groups were generated on the PECVD-Si-Ti surface by grafting triethoxysilyl butyraldehyde (ABTES) (**Scheme 1.8 A**). After this reaction took place, the surface chemistry (analysed by means of XPS) appears to be very similar to that of PECVD-Si-Ti not reacted with the silane (compare **Figure 1.33 A** to **1.20**). However, at high-resolution, the deconvoluted C 1s XPS spectrum gave an indication that the silane had reacted with the surface. The spectrum was fitted with 3 components (**Figure 1.34 A**): C1 at 287.9 eV was assigned to C=O present in the aldehyde group; C2 at 286.7 eV was assigned to C-O groups from the alkoxy groups of the silane or from adsorbed contaminants; and C3 at 285.0 eV was assigned to saturated hydrocarbons either adsorbed on the surface or from the hydrocarbon chain of the silane. The carbon species assigned to the peaks here have also been identified in previous reports and at similar binding energies for other aldehyde-modified materials [161-162].

Epoxide groups were generated on the PECVD-Si-Ti surface by grafting 3-glycidoxypropyl trimethoxysilane (GPTMS) (**Scheme 1.8 B**). This surface was similar in elemental composition to that of PECVD-Si-Ti, which had not been reacted with the silane and the ABTES-functionalised PECVD-Si-Ti surface (compare **Figures 1.33 A** and **C** and **1.20**). Again, the C 1s spectrum was used to distinguish the characteristic features of this surface. The spectrum was curve-fitted with 3 components (**Figure 1.34 B**): C1 at 286.7 eV and C2 at 285.0 eV was assigned to aliphatic C-O and C-H species, respectively; and C3 at 283.2 eV was assigned to carbon of the epoxide ring structure [163].

A prominent nitrogen signal (of 3 at.%) was detected after grafting 3-isocyanatopropyl triethoxysilane (IPTES) (shown in **Scheme 1.8 C**) to the PECVD-Si-Ti surface (**Figure 1.33 E**). The nitrogen signal was derived from the isocyanate group and was used as a characteristic marker element (in XPS) to indicate the silane had attached to the surface. Also, the much higher atomic percent of carbon (17.9 at.%) compared to 9.9 at.% and 10.2 at.% for ABTES and GPTMS functionalised PECVD-Si-Ti surfaces, respectively, attributed to the hydrocarbon chain of the silane, indicates that more IPTES molecules had attached to PECVD-Si-Ti in comparison to ABTES and GPTMS (**Table 1.8**). Consistent with the above observation, grafting of IPTES partly quenched the underlying signal from the PECVD-Si-Ti surface resulting in lower atomic percentages of oxygen and silicon compared to the ABTES and GPTMS functionalised PECVD-Si-

Ti surfaces (**Table 1.8**). At a high resolution, the C 1s XPS spectrum was curve-fitted with 5 components: C1 at 289.2 eV was assigned to carbon in an isocyanate group (N=C=O); C2 at 287.8 eV was assigned to C=O species derived from the isocyanate group; C3 at 286.6 eV was attributed to adsorbed C-O species or from unreacted ethoxy groups of the silane molecule; C4 at 285.7 eV was probably amine (C-N) species that had formed as a result of the reaction of some isocyanate groups with atmospheric moisture prior to analysis; C5 at 285.0 eV was assigned to saturated hydrocarbons either adsorbed on the surface or from the hydrocarbon chain of the silane [164].

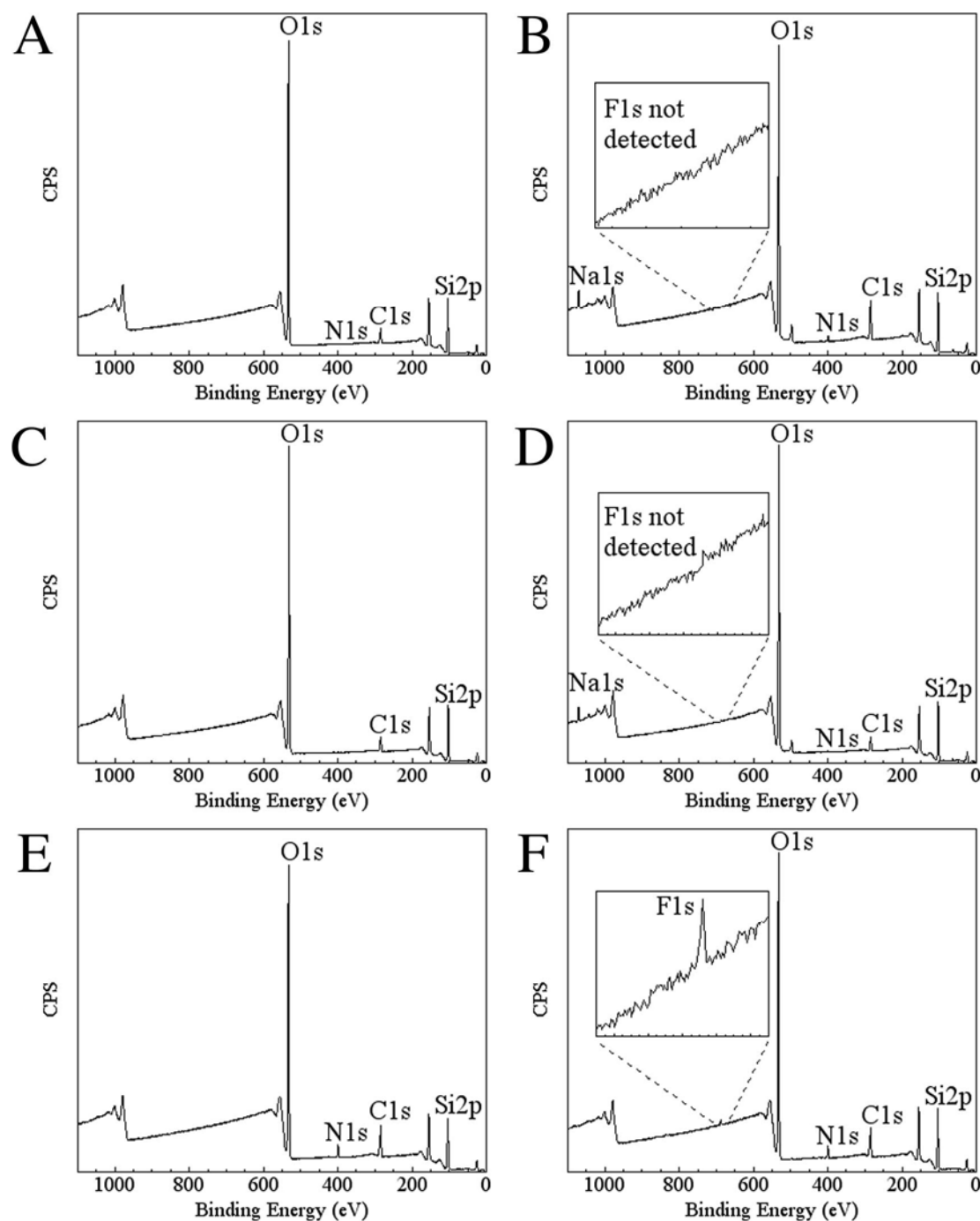


**Figure 1.33.** XPS survey spectra of PECVD-Si-Ti surfaces functionalised with ABTES (**A** and **B**), GPTMS (**C** and **D**) and IPTES (**E** and **F**) before (**A**, **C**, **E**) and after (**B**, **D**, **F**) labeling with FEAM. PECVD-Si-Ti surfaces were coated with the silanes at 90°C for 1 h according to Method 4 (refer to **pages 36-37**). Functionalised surfaces were reacted with 2 ml of 100 mM FEAM for 2 h at 25°C in carbonate buffer (pH 9.6) containing 50 mM NaCNBH<sub>3</sub> (**B**); in carbonate buffer (pH 9.6) (**D**); and in PBS (pH 7.4) (**F**) (refer to **pages 38-39** for a more detailed description).

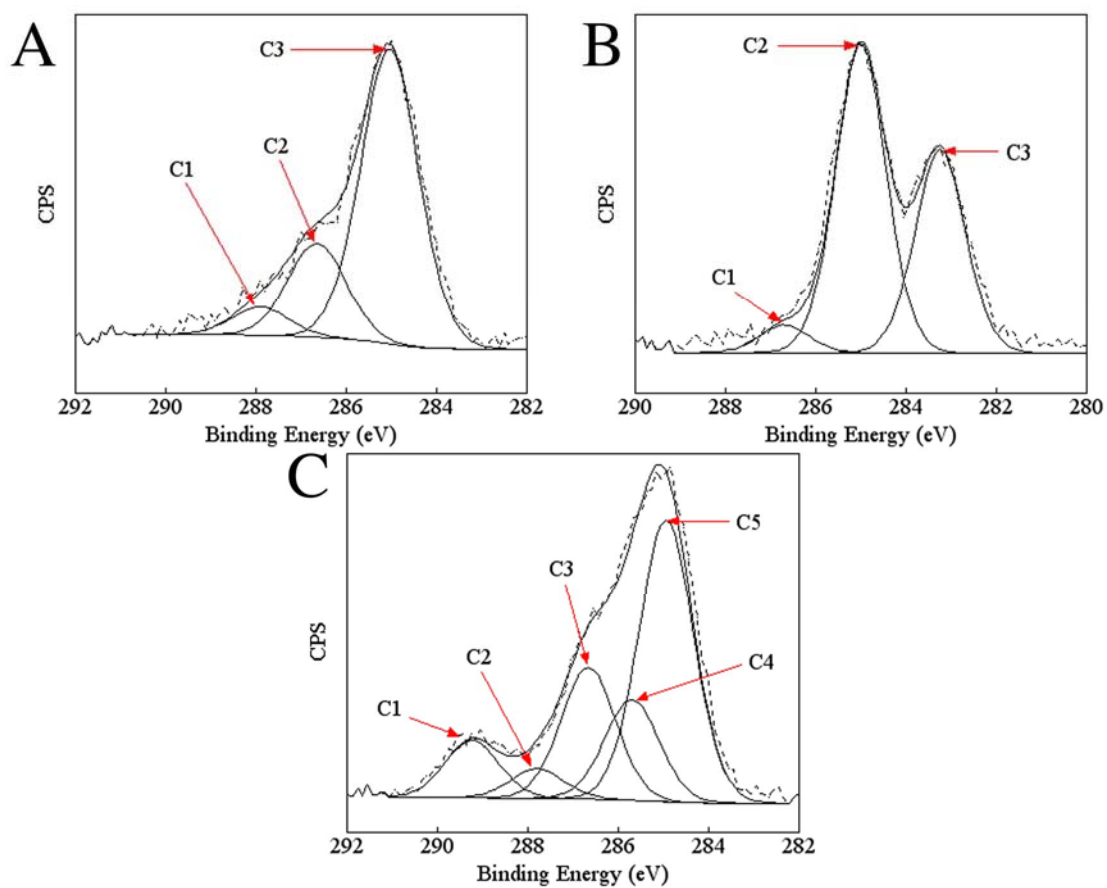


**Figure 1.34.** XPS high-resolution spectra (dashed lines) and curve-fitted spectra (solid lines) of PECVD-Si-Ti reacted with neat solutions of ABTES (A), GPTMS (B) and IPTES (C) according to Method 4 (refer to [page 38](#) for a more detailed description).

<b>After silanisation (Neat at 90°C for 1 h according to Method 4 (refer to pages 36-37))</b>						
	O at.%	C at.%	N at.%	Si at.%	Na at.%	F at.%
Aldehyde	63.7	9.9	0.2	26.2	0.0	0.0
Epoxide	64.2	10.2	0.0	25.6	0.0	0.0
Isocyanate	56.0	17.9	3.0	23.1	0.0	0.0
<b>After labeling with FEAM</b>						
	O at.%	C at.%	N at.%	Si at.%	Na at.%	F at.%
Aldehyde	51.8	20.9	1.5	23.9	1.9	0.0
Epoxide	62.8	10.0	0.1	25.5	1.6	0.0
Isocyanate	54.8	16.9	3.1	24.4	0.0	0.8
<b>Negative controls (non-silanised PECVD-Si-Ti) reacted with FEAM</b>						
	O at.%	C at.%	N at.%	Si at.%	Na at.%	F at.%
Control reaction for aldehyde surface	55.9	18.4	1.7	23.8	0.2	0.0
Control reaction for epoxide surface	62.2	10.0	1.1	26.5	0.2	0.0
Control reaction for isocyanate surface	62.3	10.3	1.0	26.1	0.3	0.0

**Table 1.8.** Elemental atomic percentage data (from XPS) taken after grafting ABTES, GPTMS and IPTES onto PECVD-Si-Ti (Top panel). The middle panel shows elemental atomic percentages after surface reactions with 2 ml of 100 mM FEAM for 2 h at 25°C in carbonate buffer (pH 9.6) containing 50 mM NaCNBH<sub>3</sub> (for aldehydes); in carbonate buffer (pH 9.6) (for epoxides); and in PBS (pH 7.4) (for isocyanates). The atomic percentages derived from the negative controls for each corresponding surface are shown in the bottom panel. Refer to **pages 38-39** for more detailed descriptions of methods.

Having characterised the surface chemistry of ABTES, GPTMS and IPTES functionalised PECVD-Si-Ti by means of XPS, the functionalised PECVD-Si-Ti surfaces were next reacted with FEAM under different reaction conditions after careful consideration of the required reaction conditions. Firstly, aldehydes are known to react with amino groups to form a Schiff base intermediate product (shown in **Scheme 1.8 A**) [165]. This reversible reaction preferentially occurs under alkaline conditions and the intermediate product can be reduced by reductive amination with a mildly reducing agent such as sodium cyanoborohydride to form a stable secondary amine bond (**Scheme 1.8 A**) [166]. Similarly, epoxides also react with amines in alkaline pH environments, but by a ring-opening process to form a secondary amine bond (**Scheme 1.8 B**) [165]. Isocyanates react readily with amines to form urea bonds (**Scheme 1.8 C**) [165]. The reactions do not require an acid or base as a catalyst and therefore can be performed at neutral pH. However, the isocyanate groups can also be hydrolysed by water, which may result in a reduction of the number of available surface reactive groups for protein coupling [167]. Taking the above information into consideration, an alkaline carbonate buffer (pH 9.6) was chosen for (FEAM) reactions with aldehyde and epoxide surface functional groups and isocyanate surface functional groups were reacted in a neutral PBS solution (pH 7.4). Additionally, amino reaction solutions used for aldehyde surface functional groups were supplemented with NaCNBH<sub>3</sub> to reduce the Schiff base to a secondary amine bond.

As negative controls, non-silanised PECVD-Si-Ti samples were reacted with identical reaction mixtures and under the same reaction conditions as the test samples. Importantly, no fluorine was detected on these samples after such reactions (**Table 1.8**). This demonstrated that FEAM does not react non-specifically with the PECVD-Si-Ti surface. However, no fluorine was detected (by XPS) on ABTES or GPTMS functionalised PECVD-Si-Ti (**Figure 1.33 B and D** and **Table 1.8**). This indicates that FEAM had also not reacted with these samples. The carbonate buffer with a relatively high pH of 9.6 may have hydrolysed the silane molecules from the surface [168]. Therefore, even if FEAM had reacted with the aldehyde and epoxide functional groups, the molecules would have been removed as the silane was hydrolysed from the surface prior to XPS analysis. FEAM labeling of the IPTES functionalised PECVD-Si-Ti surface was more successful. After reacting FEAM on this surface, 0.8 at.% of fluorine was detected, which indicates that FEAM had attached to the surface (**Figure 1.33 F**

and **Table 1.8**). Therefore, one possible method of covalently attaching IGF-1 to PECVD-Si-Ti (by isocyanate chemistry) was found in this set of experiments.

In another set of experiments, ABTES and GPTMS functionalised surfaces were reacted in a sodium phosphate buffer with a milder alkaline pH of 8.0 in comparison to the carbonate buffer of pH 9.6 used in the previous experiment. Again, NaCNBH<sub>3</sub> was added as a reducing agent in the case of ABTES functionalised PECVD-Si-Ti. Similar to the previous experiments, no fluorine (from FEAM) was detected by XPS on the ABTES and GPTMS functionalised PECVD-Si-Ti that was not reacted with FEAM or on non-silanised PECVD-Si-Ti that had been reacted with FEAM (negative control samples) (**Table 1.9**). After labeling with FEAM, 0.9 at.% of fluorine was detected on the ABTES functionalised PECVD-Si-Ti surface but no fluorine was detected on the GPTMS functionalised PECVD-Si-Ti surface (**Figure 1.35 A-B** and **Table 1.9**). This indicates that FEAM had attached to ABTES functionalised PECVD-Si-Ti but not to GPTMS functionalised PECVD-Si-Ti. Therefore, FEAM could not be coupled to GPTMS functionalised PECVD-Si-Ti under the experimental parameters that were tested here, but the model amino compound could be successfully coupled to ABTES and IPTES functionalised PECVD-Si-Ti samples.

Although only low fluorine signals (of less than 1.0 at.%) were detected (by XPS) on the FEAM-labeled ABTES and IPTES functionalised PECVD-Si-Ti surfaces (**Tables 1.8** and **1.9**), the method did indicate that FEAM molecules could be coupled onto ABTES and IPTES functionalised PECVD-Si-Ti. Therefore, the reaction conditions for the immobilisation of FEAM that were identified in this study are also possibly suitable for the immobilisation of other amino-functional molecules, including IGF-1.

After silanisation						
(Neat at 90°C for 1 h according to Method 4 (refer to pages 36-37))						
	O%	C%	N%	Si%	Na%	F%
Aldehyde	61.5	12.6	0.0	25.9	0.0	0.0
Epoxide	63.7	10.1	0.0	26.2	0.0	0.0
After labeling with FEAM						
	O%	C%	N%	Si%	Na%	F%
Aldehyde	57.7	15.5	1.4	24.5	0.0	0.9
Epoxide	62.8	12.2	0.0	25.0	0.0	0.0
Negative controls (non-silanised PECVD-Si-Ti) reacted with FEAM						
	O%	C%	N%	Si%	Na%	F%
Control reaction for aldehyde surface	61.5	12.6	0.0	25.9	0.0	0.0
Control reaction for epoxide surface	59.3	14.1	1.4	25.2	0.0	0.0

**Table 1.9.** Elemental atomic percentage data (from XPS) of ABTES and GPTMS functionalised PECVD-Si-Ti (by Method 4) before (top panel) and after (middle panel) reacting the surfaces with 2 ml of 100 mM FEAM for 2 h at 25°C in sodium phosphate buffer (pH 8.0) containing 50 mM NaCNBH<sub>3</sub> (for aldehydes) or in sodium phosphate buffer (pH 8.0) (for epoxides). The elemental atomic percentages from negative controls for both surface types are shown in the bottom panel. Refer to **pages 38-39** for a more detailed description of the methods.

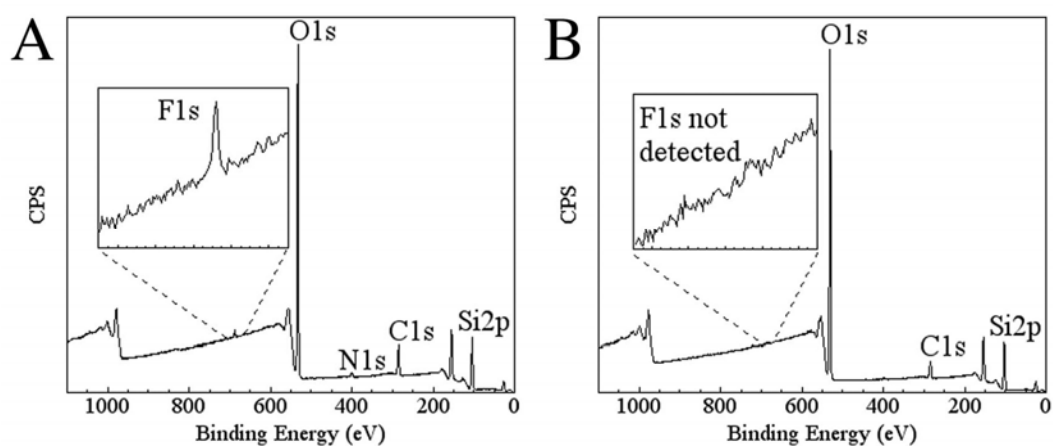


**Figure 1.35.** XPS survey spectra of aldehyde (A) and epoxide (B) functionalised PECVD-Si-Ti (by Method 4) after reacting the surfaces with 2 ml of 100 mM FEAM for 2 h at 25°C in sodium phosphate buffer (pH 8.0) containing 50 mM NaCNBH<sub>3</sub> (A) or in sodium phosphate buffer (pH 8.0) (B). Refer to **pages 38-39** for more detailed descriptions of methods.

In another experiment we tested if PECVD-Si-Ti that was functionalised with IPTES by Method 1 (for 1 h at 25°C in toluene; refer to **pages 36-37**) could also be used as a surface for the covalent immobilisation of the amino FEAM molecule. The reason for this investigation was that the coverage of another silane, FPTMS, which was grafted onto PECVD-Si-Ti by Method 1 in the previous section, was shown to be lower than that achieved after grafting FPTMS onto PECVD-Si-Ti by Method 4 (refer to **pages 69-80**). Therefore, silanisation by Method 1 does not alter the surface chemistry of the bioactive PECVD-Si coating as significantly compared to silanisation by Method 4. This was found to be the case also after grafting IPTES onto PECVD-Si-Ti by Methods 1 and 4. After grafting IPTES onto PECVD-Si-Ti by Methods 1 and 4, the nitrogen signal from the isocyanate group of the silane (detected by XPS) was 1.7 at.% and 3.0 at.%, respectively (**Tables 1.8** and **1.10**). This indicated that the surface coverage of IPTES on PECVD-Si-Ti, grafted according Method 1, was approximately 50% compared to the coverage of IPTES obtained by Method 4 on PECVD-Si-Ti. Once again, fluorine was not detected by XPS on the surface of PECVD-Si-Ti that was functionalised with IPTES by Method 1 (**Table 1.10**). After FEAM labeling of IPTES functionalised PECVD-Si-Ti (by Method 1), fluorine was detected at 0.8 at.%, which was the same as on PECVD-Si-Ti functionalised with IPTES by Method 4 (**Tables 1.8** and **1.10**). Therefore, this experiment showed that a lower surface coverage of IPTES on PECVD-Si-Ti (achieved after grafting the silane onto the surface by Method 1) was equally as effective for the immobilisation of the amino compound FEAM, in comparison to the PECVD-Si-Ti surface that was functionalised with IPTES by Method 4. Because the loading capacity of FEAM was the same on IPTES functionalised PECVD-Si-Ti by Methods 1 and 4, Method 1 is possibly more suitable for functionalising the PECVD-Si-Ti surface (compared to Method 4) because the surface chemistry of the bioactive coating is not as extensively modified by this method.

<b>After silanisation</b>				
<b>(100 mM in toluene for 1 h at 25°C according to Method 1 (refer to pages 36-37))</b>				
O at.%	C at.%	N at.%	Si at.%	F at.%
60.2	12.5	1.7	25.6	0.0
<b>After labeling with FEAM</b>				
O at.%	C at.%	N at.%	Si at.%	F at.%
58.9	12.8	1.9	25.6	0.8

**Table 1.10.** Elemental atomic percentage data from PECVD-Si-Ti surfaces functionalised with IPTES (by Method 1) before (top panel) and after reacting the surfaces with 2 ml of 100 mM FEAM for 2 h at 25°C in PBS (pH 7.4). Refer to **pages 38-39** for more detailed descriptions of methods.

From the solid phase reactions using the FEAM model molecule, ABTES functionalised PECVD-Si-Ti was shown to react with FEAM at a pH of 8.0 and IPTES functionalised PECVD-Si-Ti reacted with FEAM at a pH of 7.4. GPTMS functionalised PECVD-Si-Ti did not react with FEAM under the experimental conditions tested here. Also, as XPS data revealed, a similar surface concentration of FEAM attached on ABTES and IPTES functionalised PECVD-Si-Ti (determined by the measured fluorine atomic percentages of 0.9 at.% and 0.8 at.%, respectively, from **Tables 1.9** and **1.10**). Since no additional reagents are required to be added to amine reaction solutions developed for IPTES functionalised PECVD-Si-Ti (which could inhibit protein activity), isocyanate chemistry was first chosen to immobilise the growth factor IGF-1 on PECVD-Si-Ti. Also, we chose to examine the immobilisation of IGF-1 on PECVD-Si-Ti that was functionalised with IPTES by Method 1 because the reaction does not significantly alter the bioactive PECVD-Si surface chemistry in comparison to Method 4, and because the surface yield of the amino-containing compound was shown to be the same on both surfaces.

IPTES functionalised PECVD-Si-Ti (by Method 1) was reacted with 340 ng/cm<sup>2</sup> of IGF-1 (prepared in PBS) for 2 and 12 h at 25°C. For both reaction times, control samples (IPTES functionalised PECVD-Si-Ti) were prepared by incubating the substrates in PBS containing no protein. Nitrogen was used as a marker element for IGF-1 in the XPS characterisation. As shown in the XPS survey spectra in **Figure 1.36 A-D**, nitrogen was detected on all samples and at a similar intensity. This result was expected since nitrogen was already present on the surface of IPTES functionalised PECVD-Si-Ti (from the surface isocyanate groups) and only a small increase in the surface content of nitrogen would be possible from the low amount of protein (340 ng/cm<sup>2</sup>) that was used to react with the surface. However, after measuring the atomic percentages for each element on these surfaces by means of XPS, a marginally higher atomic percent of nitrogen was found on both surfaces that were reacted with IGF-1 for 2 and 12 h (2.3 and 2.2 at.%) compared to their respective controls (1.6 and 1.7 at.%), indicating that the protein was indeed attached on the surface (**Table 1.11**). This reaction appeared to have reached completion within 2 h since similar nitrogen percentages were detected (by XPS analysis) on samples incubated with IGF-1 for either 2 or 12 h.

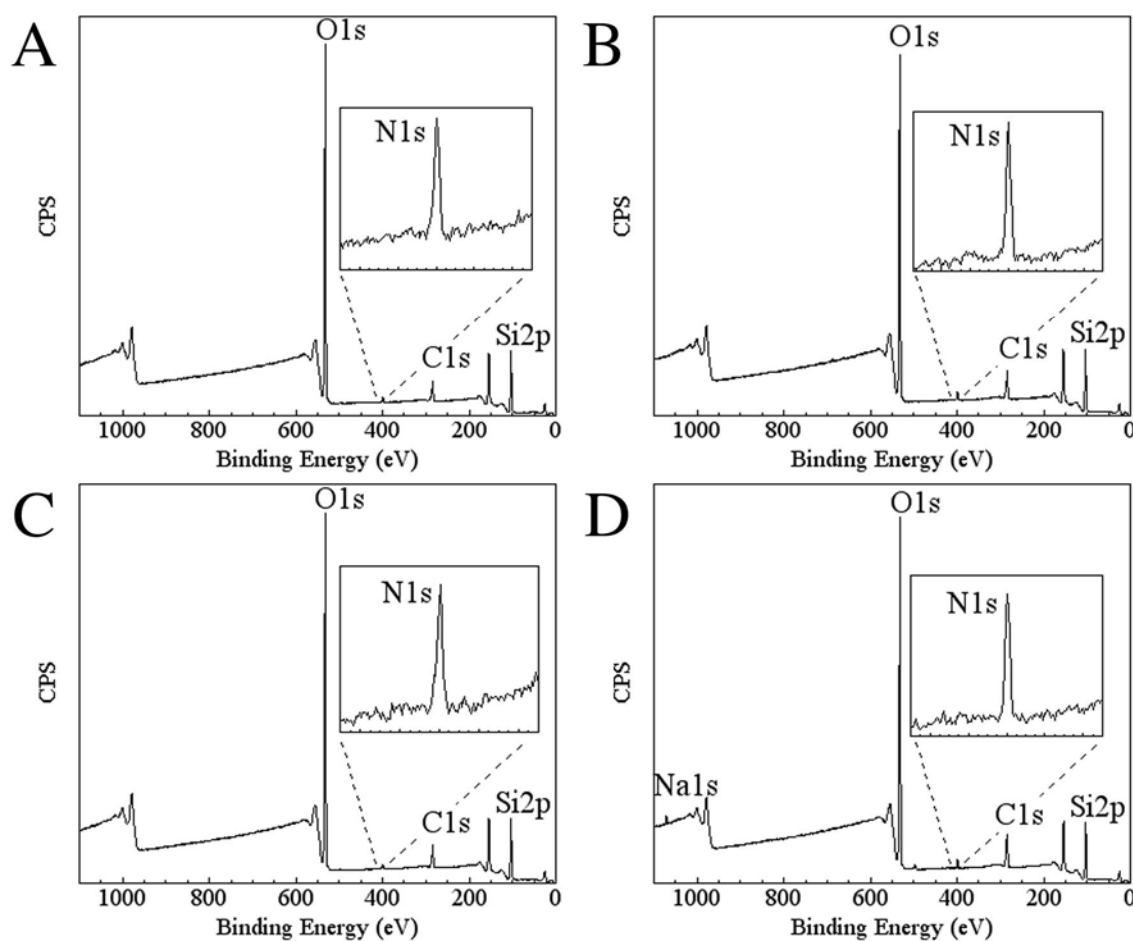


**Figure 1.36.** XPS survey spectra taken on IPTES functionalised PECVD-Si-Ti after incubation in PBS (pH 7.4) for 2 h (A) or 12 h (C) and after incubation with 600 ng of IGF-1 in 300  $\mu$ l of PBS for 2 h (B) or 12 h (D).

	O at. %	C at. %	N at. %	Na at. %	Si at. %
340 ng/cm <sup>2</sup> of IGF-1; 2 h at 25°C	59.6	14.6	2.3	0.0	23.5
PBS; 2 h at 25°C	63.2	11.4	1.6	0.0	23.8
340 ng/cm <sup>2</sup> of IGF-1; 12 h at 25°C	57.0	18.1	2.2	0.9	21.8
PBS; 12 h at 25°C	61.8	12.5	1.7	0.0	24.0

**Table 1.11.** Elemental atomic percentage data (from XPS) for IPTES functionalised PECVD-Si-Ti after incubation in PBS (pH 7.4) for 2 h or 12 h and after incubation with 600 ng of IGF-1 in PBS (in a volume of 300  $\mu$ l and a surface area concentration of 340 ng/cm<sup>2</sup>) for 2 h or 12 h at 25°C.

In summary, by means of XPS, we characterised three different surface chemistries (aldehyde, epoxide and isocyanate surface functionalities), which can be used for the covalent immobilisation of proteins. The surface chemistries were generated on PECVD-Si-Ti by grafting ABTES, GPTMS or IPTES onto the substrate surfaces through silane chemistry. We investigated the immobilisation of an amino FEAM molecule on these surfaces under different experimental conditions. By means of XPS analysis, we identified two suitable experimental conditions for coupling of FEAM onto ABTES and IPTES functionalised PECVD-Si-Ti. A suitable experimental condition for coupling FEAM to GPTMS functionalised PECVD-Si-Ti was not found in this study. Furthermore, we determined that the surface coverage yield of FEAM was the same on PECVD-Si-Ti that was functionalised with a higher and lower density of IPTES molecules by Methods 1 and 4, respectively. Finally, a procedure developed for the immobilisation of FEAM on IPTES functionalised PECVD-Si-Ti (according to Method 1) was successfully adapted for the immobilisation IGF-1. The immunological activity of covalently attached immobilised IGF-1 molecules will be assessed in the following section.

### 1.3.4 Analysis of the immunological activity of adsorbed and covalently attached insulin-like growth factor-1 (IGF-1) on PECVD-Si-Ti

In the previous section, XPS was used to detect IGF-1 that had been covalently immobilised on IPTES functionalised PECVD-Si-Ti. The results from this XPS study gave an indication that the protein was present on the surface. However, no information has been obtained to determine if the protein remained in the correct conformation to retain biological activity. To test if covalently attached IGF-1 had not been denatured by the immobilisation method, an enzyme-linked immunosorbent assay (ELISA) was used to analyse the immunological activity (immuno-reactivity) of insulin-like growth factor-1 (IGF-1) on functionalised titanium substrates.

These experiments were performed in commercially available 24-well plates, enabling multiple samples to be analysed in each experiment. After inserting double-sided adhesive tape into the wells of a 24-well tissue culture polystyrene (TCPS) plate (used for holding the titanium substrates), each well was blocked with bovine serum albumin (BSA), the cover of the tape was then removed and the titanium discs were glued into place. After incubation with IGF-1, any isocyanate functional groups that had not reacted with the protein were subsequently quenched with ethanolamine hydrochloride. A second blocking step with BSA was performed to reduce the amount of non-specific protein binding sites on the titanium substrate surface. The remainder of the experiment involved a standard ELISA protocol provided by TGR BioSciences Pty. Ltd. In this experiment, IGF-1 was reacted with a biotinylated IGF-1 antibody before labeling this “detection” antibody with a horseradish peroxidase (HRP) enzyme that was conjugated to streptavidin. The enzyme catalysed the oxidation of a colourless *o*-phenylenediamine dihydrochloride (OPD) substrate to produce a yellow-coloured end product with a  $\lambda_{\max}$  of 450 nm. The intensity of this yellow-coloured product is related to the surface concentration of immuno-reactive IGF-1 on the titanium substrate surface. Absorbance measurements were recorded in a standard 96-well microplate reader. An illustration of this ELISA procedure is shown in **Figure 1.37**.

The experimental protocol provided TGR BioSciences Pty. Ltd. had been developed for a 96-well format. These assays are usually performed in polystyrene wells that have been modified to obtain maximum protein adsorption such as on Nunc-Maxisorp™ plates [169]. To test whether this method could be scaled up to a 24-well format, the IGF-1 ELISA was first used to detect IGF-1 that had been adsorbed to wells of a 24-well TCPS plate at a protein surface concentration of 0-340 ng/cm<sup>2</sup>. The resulting calibration curve showed a sigmoidal shape and a saturation level was reached between 170-340 ng/cm<sup>2</sup> (**Figure 1.38**). A maximum absorbance of approximately 0.1 was obtained in the test wells that were reacted with a higher concentration (170-340 ng/cm<sup>2</sup>) of IGF-1 (from **Figure 1.38**). The measured background absorbance that was recorded in empty test wells by the microplate reader was typically 0.03-0.04 units (data not shown), which was about half of the maximum absorbance recorded in the above experiment. Therefore, to enable IGF-1 to be easily detected on the titanium substrates (by obtaining high signal to noise ratio) in the subsequent ELISA experiments, IGF-1 was reacted on the test samples at 340 ng/cm<sup>2</sup> that reflected a complete coverage of protein from the calibration curve (**Figure 1.38**).

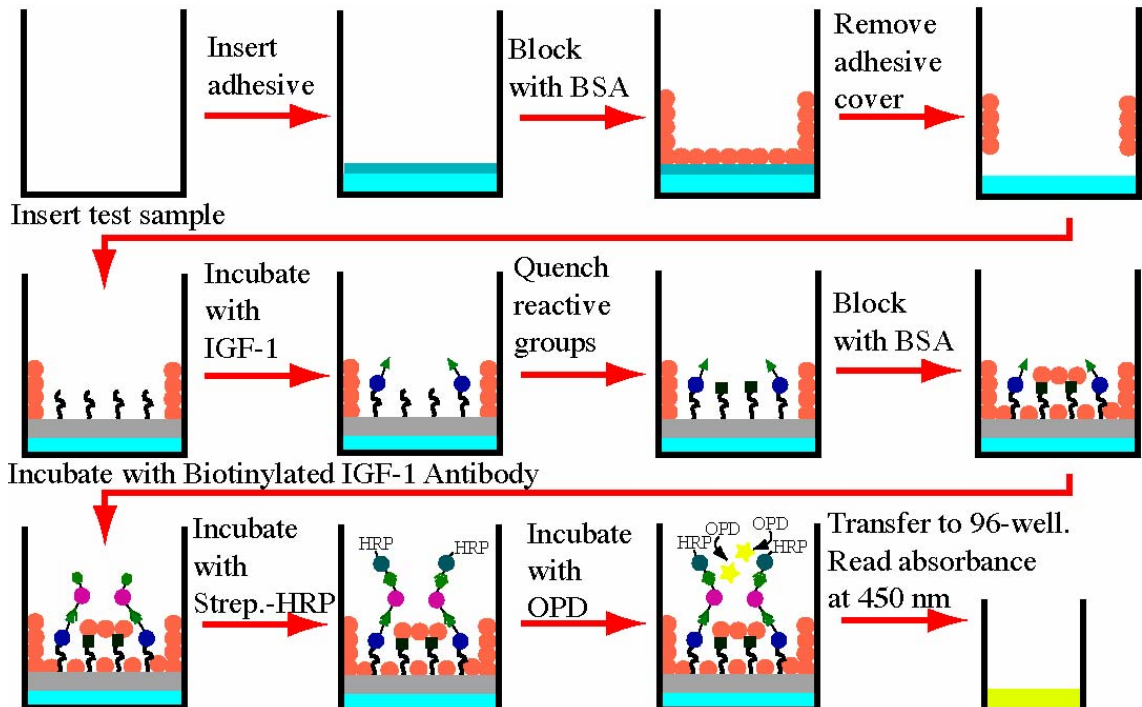


**Figure 1.37.** A cartoon illustrating each step of the ELISA used to analyse the immuno-reactivity of IGF-1 on functionalised titanium substrates in a 24-well format. Abbreviations: Strep.-HRP - streptavidin conjugated HRP; OPD - *o*-phenylenediamine dihydrochloride; and BSA - bovine serum albumin.

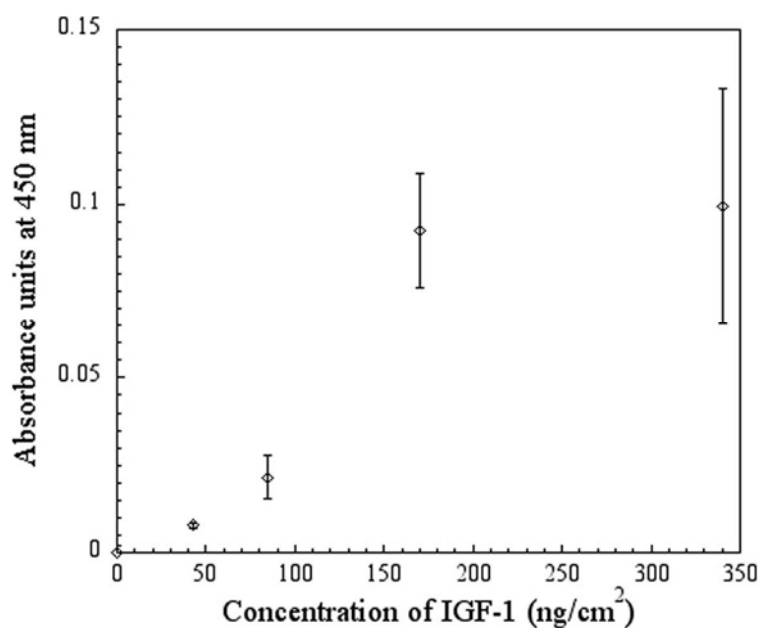
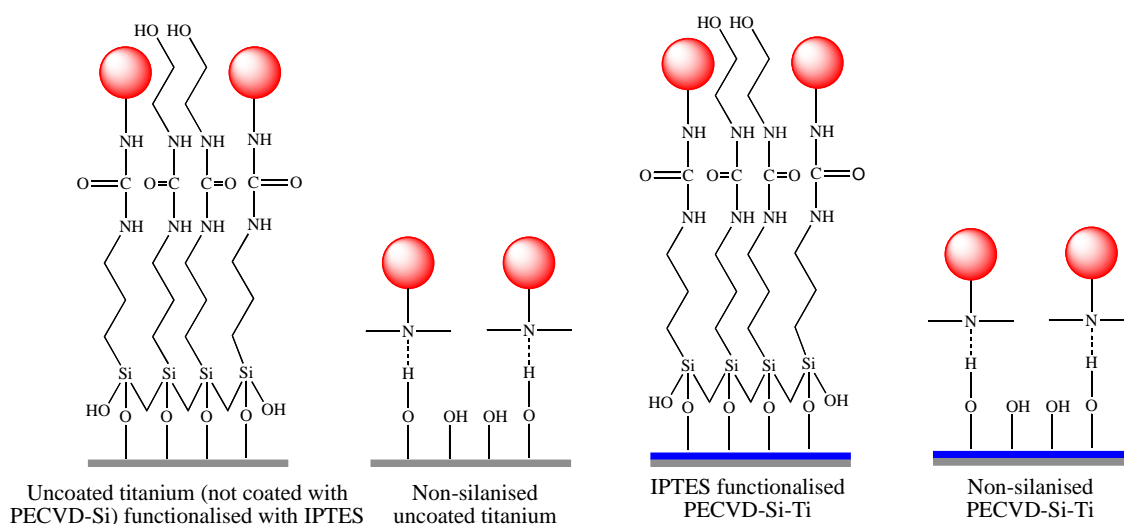


**Figure 1.38.** A calibration curve of adsorbed IGF-1 in a 24-well plate. Absorbance readings were adjusted according to the absorbance recorded in the negative (minus IGF-1) control wells. IGF-1 dilutions were prepared in PBS and incubated in the test wells at 25°C for 2 h.

The ELISA was next used to compare IGF-1 reactivity on PECVD-Si-Ti to uncoated titanium samples not functionalised with IPTES (**Scheme 1.9**). Only low absorbance values of approximately 0.03 and 0.02 at 450 nm (for oxidised OPD) were measured from the test wells when IGF-1 was adsorbed either to uncoated titanium or PECVD-Si-Ti, respectively (**Figure 1.39**). This indicated a low coverage of immuno-reactive protein on these surfaces. The immune reaction may have been hindered due to a combination of factors including topographical and chemical characteristics that can influence the molecular interaction between the protein and biomaterial surface during protein adsorption [170-171], significant removal of adsorbed IGF-1 by the vigorous (detergent-based) wash steps [172], protein denaturation on the surface or blocking of IGF-1 active sites that had adsorbed to the material surface [110].

A low coverage of immuno-reactive IGF-1 was also found when the protein was covalently attached to IPTES functionalised titanium (not coated with the PECVD-Si film) substrates, but a much higher concentration of immuno-reactive IGF-1 was observed when the protein was covalently linked to PECVD-Si-Ti (**Scheme 1.9** and **Figure 1.39**). This suggests that more IGF-1 had attached to IPTES functionalised PECVD-Si-Ti in comparison to IPTES functionalised uncoated titanium (that is not coated with PECVD-Si) and/or a greater percentage of IGF-1 became denatured on IPTES functionalised uncoated titanium in comparison to IPTES functionalised PECVD-Si-Ti. Nonetheless, these ELISA results showed that PECVD-Si-Ti could be loaded with IGF-1 through an isocyanate-amine coupling chemistry and that the growth factor retained its immunological activity.



**Scheme 1.9.** An illustration of the possible surface chemistry obtained after immobilising IGF-1 (red circles) on uncoated titanium substrates (grey rectangle) and PECVD-Si-Ti (grey and blue rectangles). These samples were analysed by an IGF-1 ELISA (results are shown in **Figure 1.39**). The illustration shows IGF-1 covalently linked to isocyanate groups, followed by quenching with ethanolamine, or IGF-1 adsorbed through hydrogen interactions between an amino group of the protein and the surface oxide layer (broken lines).

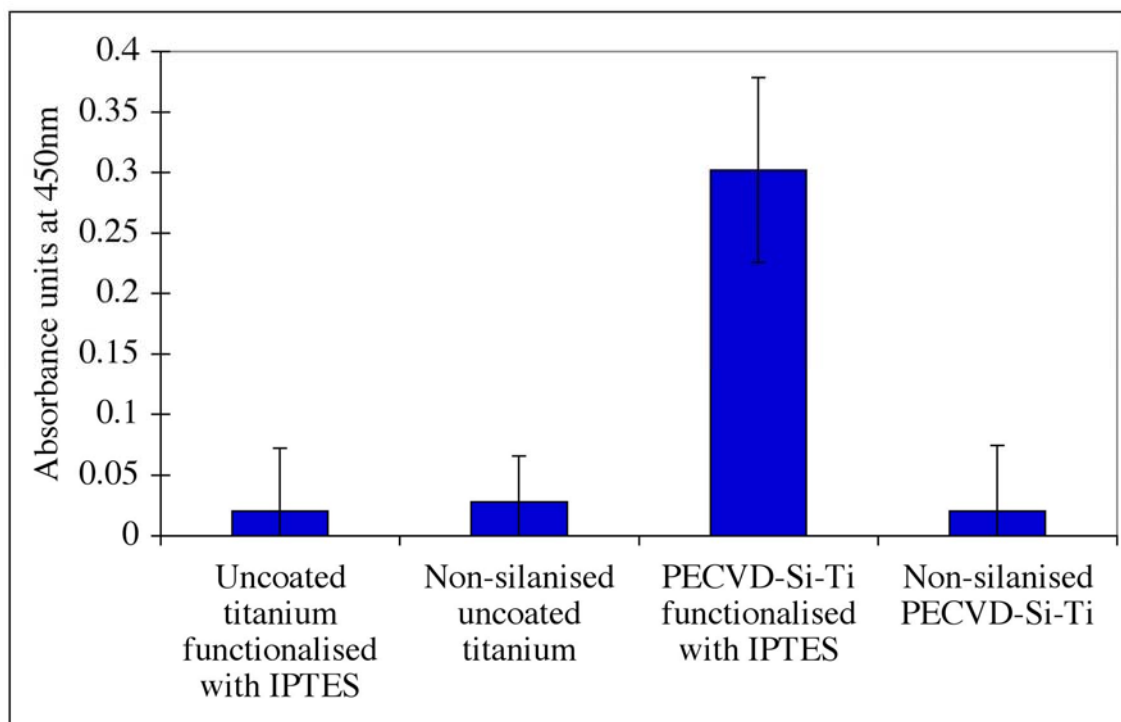
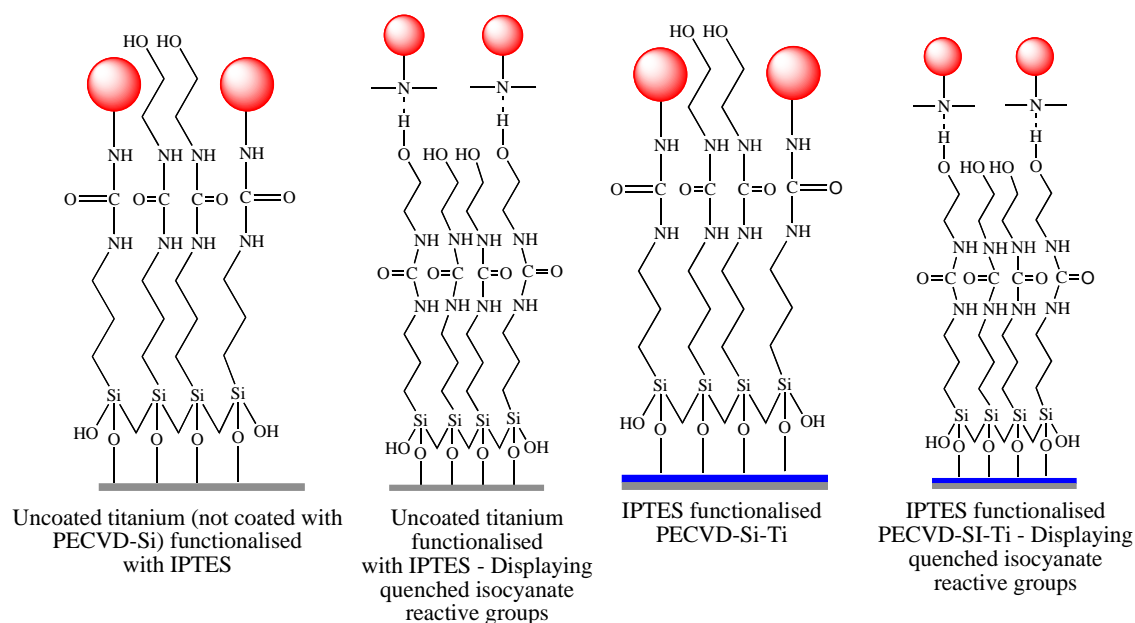


**Figure 1.39.** Results from an IGF-1 ELISA experiment performed on non-silanised and IPTES functionalised uncoated titanium and PECVD-Si-Ti (600 ng of IGF-1 (in 300  $\mu$ l of PBS) was reacted on each sample (at 340 ng/cm<sup>2</sup>) at 25°C for 2 h). The functionalised samples were reacted with IPTES according to Method 1. Refer to **pages 36-37** for the silanisation protocol and to **pages 39-40** for the ELISA method.

One more experiment was conducted to confirm the above results. This time IGF-1 reactions were compared on IPTES functionalised uncoated titanium and PECVD-Si-Ti before and after quenching the reactive groups with ethanolamine hydrochloride (**Scheme 1.10**). Ethanolamine has previously been used to block amine-reactive functional groups on biomaterial surfaces [173]. Variations in absorbance measurements were observed between **Figures 1.39** and **1.40**, which were attributed to the possibility of liquid becoming entrapped between the titanium disc and the adhesive. However, the trends in the absorbance measurements were consistent between the two graphs. Again, the surface concentration of immuno-reactive IGF-1 was much higher (by approximately 5-fold) on IPTES functionalised PECVD-Si-Ti compared to uncoated titanium (**Figure 1.40**). Also, a higher concentration of immuno-reactive IGF-1 was detected when the protein was covalently attached on IPTES functionalised uncoated titanium or IPTES functionalised PECVD-Si-Ti in comparison to when the protein was adsorbed on these surfaces displaying quenched reactive groups (over 5-

fold and 15-fold differences in the measured absorbance was observed on IPTES functionalised uncoated titanium and IPTES functionalised PECVD-Si-Ti, respectively) (**Figure 1.40**). Therefore, these experiments confirmed that a higher density of immuno-reactive IGF-1 could be retained on functionalised titanium substrates by using covalent attachment in comparison to non-specific protein adsorption.



**Scheme 1.10.** An illustration of the possible surface chemistry obtained after immobilising IGF-1 (red circles) on titanium substrates (grey rectangles) and PECVD-Si-Ti (grey and blue rectangles). These samples were analysed by an IGF-1 ELISA (results are shown in **Figure 1.40**). The illustration shows IGF-1 covalently linked to isocyanate groups, followed by quenching with ethanolamine, or IGF-1 adsorbed through hydrogen interactions between an amino group of the protein and the quenched isocyanate group (broken lines).

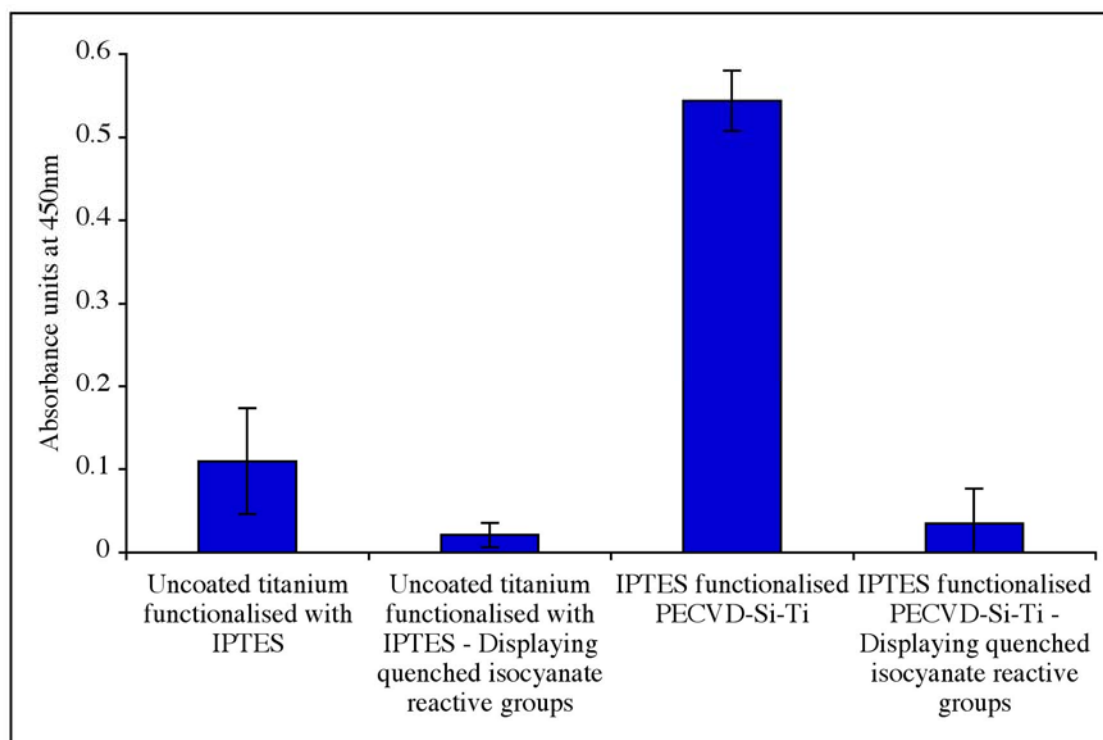


**Figure 1.40.** Results from an IGF-1 ELISA experiment performed on IPTES functionalised uncoated titanium and PECVD-Si-Ti (600 ng of IGF-1 (in 300  $\mu$ l of PBS) was reacted on each sample (at 340 ng/cm<sup>2</sup>) for 2 h at 25°C). Functionalised samples were reacted with IPTES according Method 1. In this chart, a comparison can be made in the immuno-reactivity of IGF-1 reacted on IPTES functionalised uncoated titanium and PECVD-Si-Ti before and after quenching the reactive groups with ethanolamine hydrochloride. Refer to **pages 36-37** for the silanisation protocol and to **pages 39-40** for the ELISA method.

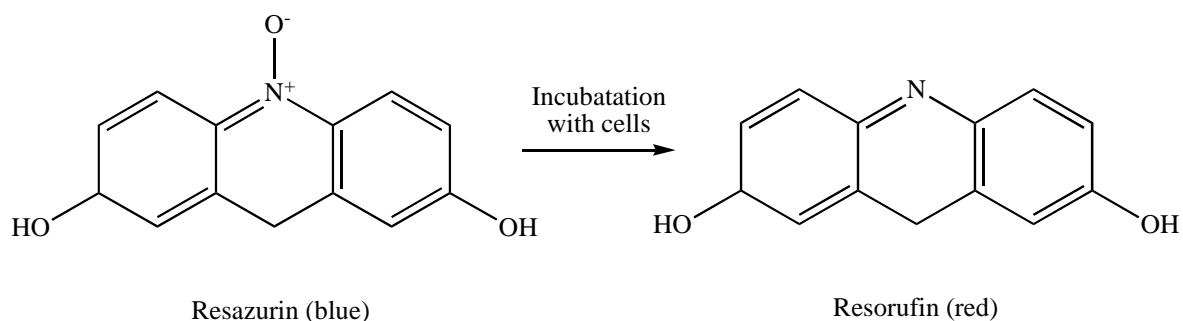
In summary, an IGF-1 immunoassay was employed in this section for detecting adsorbed and covalently immobilised IGF-1 on uncoated titanium and PECVD-Si-Ti. A higher amount of immunologically active IGF-1 was retained when the protein was covalently linked, compared to when the protein was adsorbed on both uncoated titanium and PECVD-Si-Ti. The highest amount of immuno-reactive IGF-1 was observed when the protein was covalently immobilised on IPTES functionalised PECVD-Si-Ti. The biological activity of the functionalised PECVD-Si-Ti substrates will be tested through *in vitro* cell-based assays in the following sections.

### 1.3.5 Analysis of osteoblast-like cell growth on PECVD-Si-Ti and IGF-1 functionalised PECVD-Si-Ti surfaces

The discussion will now focus on testing the biological performance of PECVD-Si-Ti in an *in vitro* cell culture study. In previous studies, PECVD-Si-Ti was shown to enhance bone formation *in situ* and bone like mineral deposition was promoted *in vitro* [83, 85]. This present study is concerned with further improving the bioactivity of PECVD-Si-Ti by tethering insulin-like growth factor-1 (IGF-1) to the surface. It is envisaged that the immobilised IGF-1 will improve the growth of cells (including bone-forming cells) on PECVD-Si-Ti, which in turn may further enhance bone formation on the substrate surface [174].

A human osteosarcoma MG63 cell line (an osteoblast-like cell) was used for testing the biocompatibility and bioactivity of the modified titanium surfaces *in vitro* [175]. Osteoblasts are the predominant cell-type involved in bone formation on the implant surface [14(d-e)]. The MG63 osteoblast-like cells possess adherent growth properties enabling these cells to be grown on the titanium substrates prepared with different surface chemistries and functional IGF-1, as will be described, or on tissue culture polystyrene (TCPS) for comparison. The major focus in this study was on the initial stage of cell attachment and early cellular proliferation on the modified substrate surfaces.

An alamarBlue™ cellular viability assay was chosen to monitor the growth of MG63 cells on the substrate surfaces. Briefly, this assay involved incubating cells that were growing on the biomaterial substrate in 10% (v/v) alamarBlue™ prepared in PBS, pH 7.4 for 1 h. The absorbance of the dye was then read spectrophotometrically at 570 and 600 nm. The alamarBlue™ dye is essentially used to monitor the reducing environment of proliferating cells. The active component of alamarBlue™ is resazurin, a blue-coloured compound [164]. After incubating alamarBlue™ with proliferating cells, the dye becomes reduced to resorufin, a red-coloured product (refer to **Scheme 1.11**). O'Brien et al. discovered that alamarBlue™ is likely reduced intracellularly by an enzymatic process [176].



**Scheme 1.11.** Reduction of resazurin (AlamarBlue™) to resorufin in the presence of live cells. Scheme was adapted from O'Brien et al. [176].

Previously, the growth of MG63 osteoblast-like cells on modified titanium surfaces has been assessed using the AlamarBlue™ assay [58, 60, 177]. In these previous studies, cellular vitality was examined between 1-21 days of culture. The endpoint signal, that is the reduction of the AlamarBlue™ dye, was calculated by subtracting the absorbance of the oxidised form of the dye at 600 nm from the reduced form at 570 nm. The AlamarBlue™ assay was sensitive for monitoring changes in cellular proliferation in response to different surface chemical cues. For example, in comparison to untreated titanium and tissue culture polystyrene (TCPS) surfaces, Giordano et al. detected a higher rate of MG63 cell proliferation after 3 days of culture on titanium modified with a thickened oxide layer that was doped with calcium and phosphorous (in order to mimic bone minerals) [58].

In this thesis, the percentage of the reduced AlamarBlue™ dye was used as an endpoint measurement to determine the comparative viability of cells that were growing on the test samples. In particular, the assay was used to gain information regarding cell growth on PECVD-Si-Ti and on surfaces functionalised with IGF-1. The percentage of the reduced AlamarBlue™ dye (related to cell density) was calculated according to the manufacturer's instructions by using the following equation [178]:

$$\% \text{ reduced} = \frac{((^{\epsilon}\text{OX})\lambda_2 \times A\lambda_1) - ((^{\epsilon}\text{OX})\lambda_1 \times A\lambda_2)}{((^{\epsilon}\text{Red})\lambda_1 \times A'\lambda_2) - ((^{\epsilon}\text{Red})\lambda_2 \times A'\lambda_1)} \times 100$$

where:

$(^{\epsilon}\text{Red})\lambda_1$  = 155677 M<sup>-1</sup>cm<sup>-1</sup>; molar extinction coefficient of reduced dye at 570 nm

$(^{\epsilon}\text{Red})\lambda_2$  = 14652 M<sup>-1</sup>cm<sup>-1</sup>; molar extinction coefficient of reduced dye at 600 nm

$(^{\epsilon}\text{OX})\lambda_1$  = 80586 M<sup>-1</sup>cm<sup>-1</sup>; molar extinction coefficient of oxidised dye at 570 nm

$(^{\epsilon}\text{OX})\lambda_2$  = 117216 M<sup>-1</sup>cm<sup>-1</sup>; molar extinction coefficient of oxidised dye at 600 nm

$A\lambda_1$  = Measured absorbance of test sample at 570 nm

$A\lambda_2$  = Measured absorbance of test sample at 600 nm

$A'\lambda_1$  = Measured absorbance of negative control (test samples that were incubated in medium containing no cells) at 570 nm

$A'\lambda_2$  = Measured absorbance of negative control (test samples that were incubated in medium containing no cells) at 600 nm

Also, the surface areas of the wells, TCPS and titanium discs were slightly different to one another. To normalise the cellular growth areas on the test specimens, the percentage of alamarBlue™ reduced by the cells was divided by the surface area of the test specimen, expressed as %/cm<sup>2</sup>.

Before analysing cell growth on the test specimens, MG63 cells were first cultured on TCPS to establish an ideal cell seeding density for monitoring cell attachment and early stages of proliferation by the alamarBlue™ assay. 1 ml of MG63 cells was seeded into the wells of a 24-well plate (having a surface area of approximately 2 cm<sup>2</sup> at the bottom of each well) at 4 different cell densities of 1.2 x 10<sup>2</sup>, 1.2 x 10<sup>3</sup>, 1.2 x 10<sup>4</sup> and 1.2 x 10<sup>5</sup> cells/ml. These wells are similar to the surface area of the titanium and TCPS test specimens of 1.8 and 1.3 cm<sup>2</sup>, respectively. After culturing the cells for time periods of 4, 24 and 72 h, the wells were washed with PBS and 300 µl of the diluted alamarBlue™ dye (in PBS) was added and incubated with the cells for 1 h under cell culture conditions (37°C in a humidified atmosphere of 5% CO<sub>2</sub>). 100 µl of the solution was then transferred to a 96-well microplate and the absorbance at 570 and 600 nm was measured in a microplate reader (refer to **page 42** for a more detailed description). Because this study was primarily

concerned with cell attachment and the initial stages of proliferation on the modified titanium surfaces, only short cell culture times of between 4-72 h were investigated.

At the two lowest cell seeding densities of  $1.2 \times 10^2$  and  $1.2 \times 10^3$  cells/ml, there was no significant increase in the percentage of reduced alamarBlue™ following 4, 24 and 72 h of cell culture (**Figure 1.41**). But at a seeding density of  $1.2 \times 10^4$  cells/ml, the percentage of reduced alamarBlue™ was significantly increased from 4 to 8 %/cm<sup>2</sup> after culturing cells between 4 and 24 h and even further to over 20 %/cm<sup>2</sup> after 72 h (**Figure 1.41**). This simply showed that the proliferation of MG63 cells during 72 h of cellular growth could be monitored by the alamarBlue™ assay at a cell seeding density of  $1.2 \times 10^4$  cells/well and above in a 24-well plate, but not at  $1.2 \times 10^2$  and  $1.2 \times 10^3$  cells/well. As expected, the greatest reduction in alamarBlue™ of approximately 25 %/cm<sup>2</sup> was observed at the highest cell seeding density of  $1.2 \times 10^5$  cells/ml after the initial 4 h cell attachment time period, which increased to 35 %/cm<sup>2</sup> after 24 h of cell culture (**Figure 1.41**). No further increase in the percentage of reduced alamarBlue™ was found between 24 and 72 h because a nearly confluent monolayer of cells had formed at the bottom of the well after 24 h as confirmed by light microscopy analysis. At higher cell densities, the proliferation of cells stagnates due to cell-cell contact inhibition of cell division [179-182]. The confluency of the cells covering the bottom of the TCPS wells was estimated by observing attached cells through a light microscope immediately before performing each alamarBlue™ experiment. These estimations were then compared to the percentage of reduced alamarBlue™ dye at each incubation time period. As expected, a greater percentage of alamarBlue™ was reduced as the cell density increased (**Table 1.12**). This confirmed that the efficiency in the reduction of alamarBlue™ correlated directly with the relative cell density in this study.

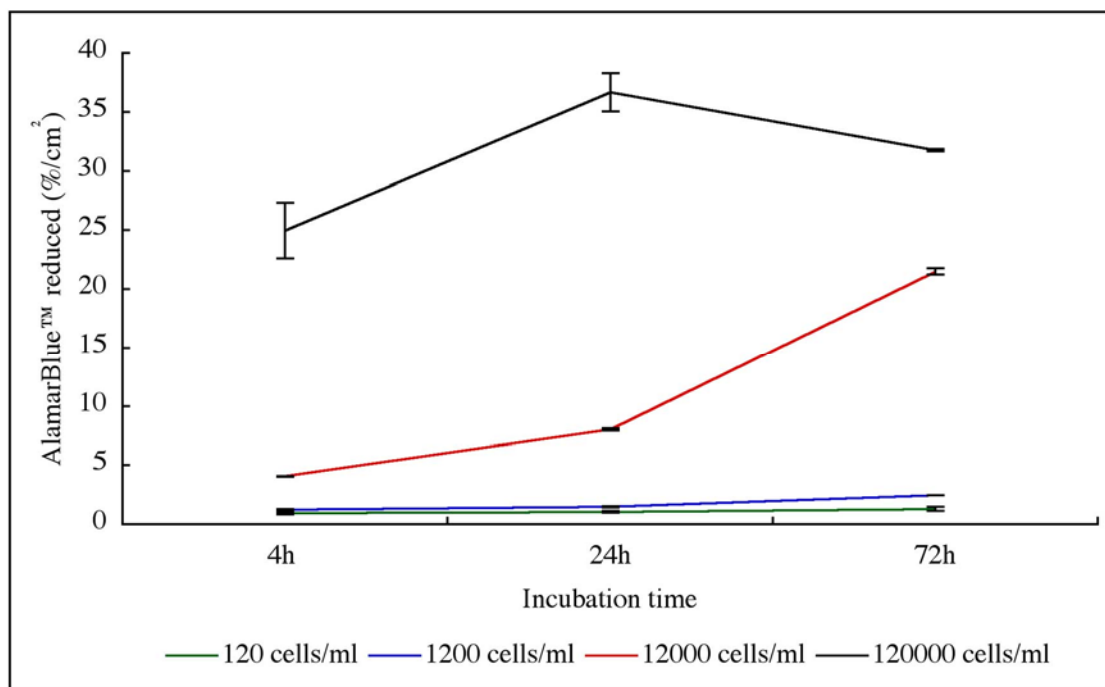


**Figure 1.41.** Percentage of alamarBlue™ reduced by MG63 cells grown in wells of a 24-well TCPS plate (TPP). Cells were removed from a T75 culture flask (Iwaki) using trypsin solution. 1 ml of cells were seeded into the wells at densities of  $1.2 \times 10^2$ ,  $1.2 \times 10^3$ ,  $1.2 \times 10^4$  and  $1.2 \times 10^5$  cells/ml. After 4 h, the wells were washed twice in PBS (pH 7.4) and the wells designated for the 4 h incubation period were examined by the alamarBlue™ assay. For the longer cell culture time periods of 24 and 72 h, the medium was decanted and replenished after an initial cell attachment period of 4 h and replenished every subsequent 24 h until the final alamarBlue™ assay was performed. Cells were grown in minimal essential medium (MEM) (pH of 7.1) supplemented with 10% (v/v) of foetal bovine serum (FBS), 100 units of penicillin and 100  $\mu$ g of streptomycin under cell culture conditions (37°C in a humidified incubator in an atmosphere of 5% CO<sub>2</sub>). The alamarBlue™ assay procedure is described in detail on **page 42**.

AlamarBlue™ reduced (%/cm <sup>2</sup> )	Surface coverage estimation (%) of MG63 cells covering the bottom of the TCPS well (Surface area = 2.01 cm <sup>2</sup> )
< 1.5	< 5
1.5-2.5	5-20
2.5-4	20-30
4-8	30-50
8-20	50-95
> 20	95-100

**Table 1.12.** A table of the percentage of alamarBlue™ reduced by MG63 cells (from **Figure 1.41**) and the corresponding percentage of cells covering the bottom of the well of the 24-well TCPS plate. An estimation of the cells covering the bottom of each well was established from visual inspection of attached cells at the bottom of the wells through a light microscope.

In summary, a significant increase in the percentage of alamarBlue™ reduced by MG63 cells was observed between cell culture times of 4-24 h and 24-72 h after seeding  $1.2 \times 10^4$  cells into wells of a 24-well TCPS plate. A much higher percentage of reduced alamarBlue™ was observed after seeding  $1.2 \times 10^5$  cells into the wells at 4, 24 and 72 h of cell culture, but cells reached near confluency after 24 h (**Figure 1.41** and **Table 1.12**). Therefore, in the next experiment a cell seeding density of  $2.4 \times 10^4$  cells/ml (between  $1.2 \times 10^4$  and  $1.1 \times 10^5$  cells/ml) was chosen to assess the growth of MG63 cells on the test titanium samples after 4, 24 and 72 h of cell culture.

The attachment and proliferation of MG63 cells was first compared between uncoated titanium, PECVD-Si-Ti and TCPS (**Figure 1.42**). All of the cell culture experiments were performed using PECVD-Si-Ti that was not treated with the third plasma-processing step of air/H<sub>2</sub>O<sub>2</sub> plasma. This treatment was abandoned because none of the data presented in this thesis suggested that the plasma-processing step of air/H<sub>2</sub>O<sub>2</sub> plasma significantly influenced the surface chemical characteristic of PECVD-Si-Ti (refer to **pages 57-60, 73-74**). After cells had attached on titanium and TCPS for 4 h, approximately 5 %/cm<sup>2</sup> of alamarBlue™ was reduced by the MG63 cells on both surfaces. This corresponds to 30-

50% of cell surface coverage (from **Table 1.12**). Interestingly, a lower percentage of alamarBlue™ was reduced at approximately 2.5 %/cm<sup>2</sup> on PECVD-Si-Ti, corresponding to a lower cell confluency of 5-20% (**Figure 1.42** and **Table 1.12**). AlamarBlue™ was reduced further by approximately 2-fold on titanium and TCPS after 24 h of cell culture, but interestingly not on PECVD-Si-Ti (**Figure 1.42**). After 72 h, the percentage of reduced alamarBlue™ significantly increased again to 38-40 %/cm<sup>2</sup> on titanium and TCPS that corresponded to a complete monolayer coverage of cells (**Figure 1.42** and refer to **Table 1.12**). However, at 72 h the percentage of reduced alamarBlue™ on PECVD-Si-Ti remained low at approximately 5 %/cm<sup>2</sup>. These results indicated that cells attached and proliferated equally well on titanium and TCPS. This result was expected because titanium is well known to be a biocompatible material [14(a), 9(a-c)]. Conversely, poor cell attachment and proliferation was observed on PECVD-Si-Ti. This result was not expected because PECVD-Si-Ti was previously shown to promote bone deposition *in situ* and therefore was considered to be a biocompatible and bioactive material [85].

Poor cell attachment and proliferation on PECVD-Si-Ti could have been due to two contributing factors. The material may be toxic to cells *in vitro* or the hydrophilic surface coating may prevent the adsorption of proteins in the FBS supplement. The first scenario is unlikely since PECVD-Si-Ti has been shown to be biocompatible *in situ* [85]. However, the highly hydrophilic PECVD-Si-Ti surface is probably protein-resistant compared to the moderately hydrophilic titanium surface with contact angles of < 10° and 71°, respectively (refer to **pages 59-60**) [183]. This effect would also apply to the adsorption of serum proteins on PECVD-Si-Ti, including fibronectin and vitronectin that are known to facilitate and depending on cell type, to be essential to cell attachment [184]. Furthermore, reducing the period of adsorption of serum proteins and cell adhesion by replacing the medium after 4 h may exacerbate this effect.

The following experiment was performed to determine if poor cell growth on PECVD-Si-Ti was attributed to the initial low density of cells that had attached to the substrate surface. MG63 cells were seeded onto the same type of samples as analysed in **Figure 1.42** but at a higher cell density of  $4.7 \times 10^4$  cells/ml (compared to  $2.4 \times 10^4$  cells/ml) and were allowed to attach for a longer time period of 24 h (compared to 4 h). These conditions were expected to increase the initial density of cells attached on the substrate surface by allowing for more protein adsorption and cell attachment even on more protein-resistant surfaces. If the percentage of alamarBlue™ reduced by the cells still remained low on PECVD-Si-Ti under these conditions, the sample may then be exhibiting some toxicity towards cells *in vitro*. However, this time the percentage of alamarBlue™ reduced on PECVD-Si-Ti was comparable to that on TCPS and titanium (**Figure 1.43**). The percentage of alamarBlue™ reduced after 24 h of cell attachment and growth was approximately 34 %cm<sup>2</sup>, 31 %cm<sup>2</sup> and 27 %cm<sup>2</sup>, which increased by 1.5-fold, 1.4-fold and 1.5-fold after 72 h of culturing the cells on TCPS, titanium and PECVD-Si-Ti, respectively (**Figure 1.43**). This experiment was significant since it demonstrated that PECVD-Si-Ti is non-toxic to MG63 cells and that cell growth (proliferation) was similar to that on the titanium and TCPS control samples.

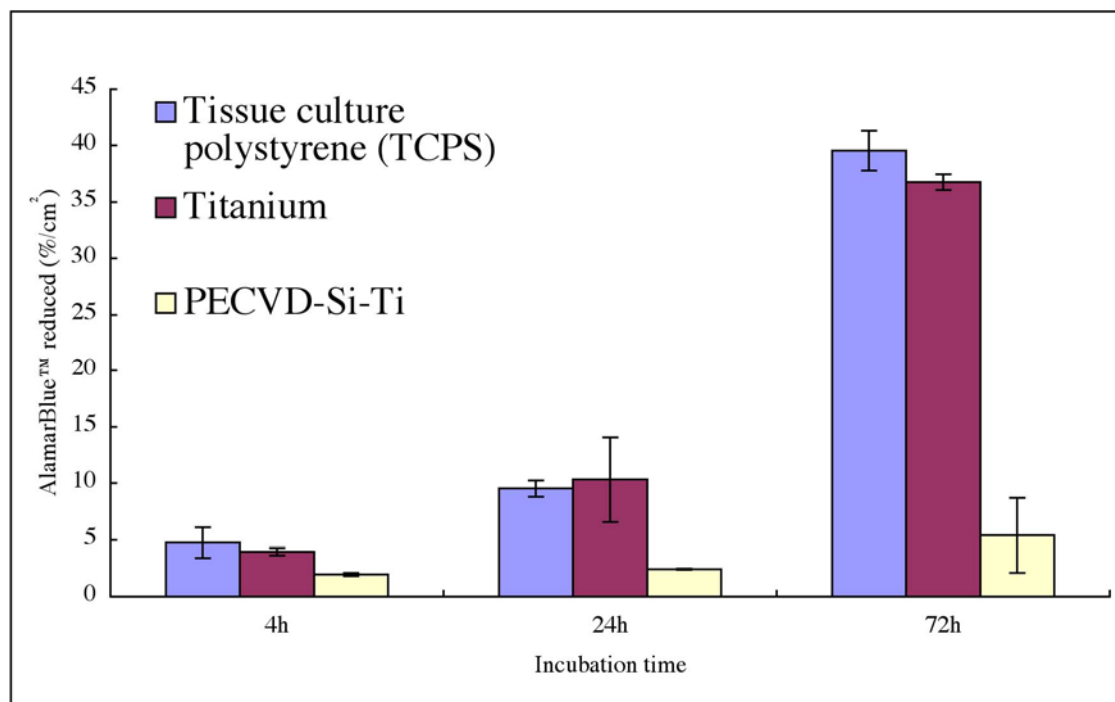


**Figure 1.42.** Percentage of alamarBlue™ reduced by MG63 cells that were grown on TCPS, titanium and PECVD-Si-Ti discs. Experiments were performed in 24-well ultra-low cell attachment plates (Dow Corning). Titanium and PECVD-Si-Ti discs were cleaned/sterilised as described on **pages 30** and **41**. TCPS discs (Sarstedt) were purchased sterile from the manufacturer and were used as received. 1 ml of trypsinised  $2.4 \times 10^4$  MG63 cells/ml were seeded and incubated over the surfaces for 4 h (under cell culture conditions). The wells were replenished with 2 ml of medium after the first 4 h of incubation and at 24 h intervals until the final measurement was taken. The cells were grown in MEM adjusted to pH 7.1 and supplemented with 10% (v/v) FBS, 100 units of penicillin and 100  $\mu$ g of streptomycin. The 2-dimensional surface area of the TCPS disc was 1.3 cm<sup>2</sup> and the surface areas of titanium and PECVD-Si-Ti were both 1.8 cm<sup>2</sup>. The alamarBlue™ assay was performed according to the protocol described on **page 42**. Statistical analyses: Percentage of alamarBlue™ reduced by MG63 cells grown on uncoated titanium was not statistically different to TCPS at 4 and 72 h of cell culture ( $p = 0.497$  and  $p = 0.171$ , respectively) but was statistically different to PECVD-Si-Ti at 4 and 72 h of cell culture ( $p = 0.015$  and  $p = 0.006$ , respectively).

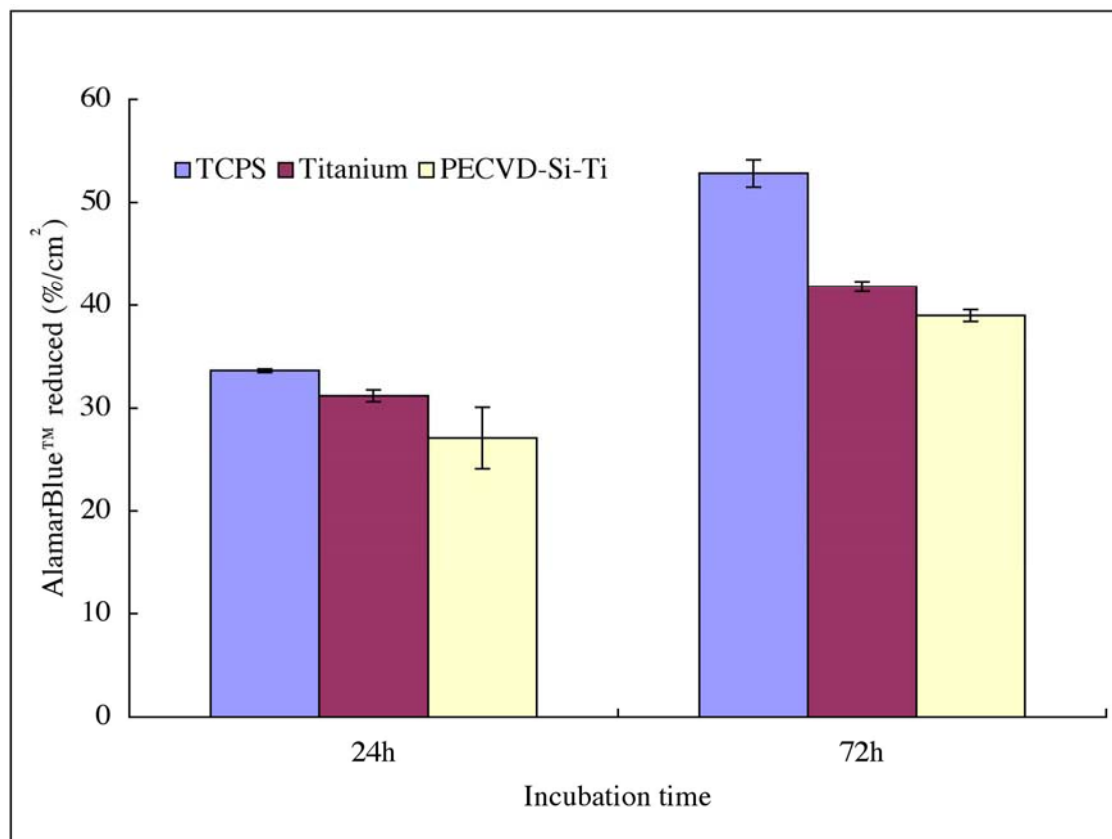


**Figure 1.43.** Percentage of alamarBlue™ reduced by MG63 cells that were grown on TCPS, titanium and PECVD-Si-Ti discs. This experiment was identical to that outlined in **Figure 1.42**, except samples were seeded with a higher cell density of  $4.7 \times 10^4$  cells/ml (compared to  $2.4 \times 10^4$  cells/ml in **Figure 1.42**) and the cells were allowed to attach for 24 h (compared to 4 h in **Figure 1.42**) before the medium was replaced by new medium. The medium was replaced every 24 h time period until the final alamarBlue™ assay was performed. Statistical analyses: Percentage of alamarBlue™ reduced by MG63 cells grown on PECVD-Si-Ti was not statistically different to TCPS or uncoated titanium after 24 h of cell attachment/growth ( $p = 0.091$  and  $p = 0.197$ , respectively) but was statistically different to TCPS and uncoated titanium after 72 h of cell culture ( $p = 0.005$  and  $p = 0.033$ , respectively).

Next, the growth of MG63 cells in response to IGF-1 was assessed on PECVD-Si-Ti by means of the alamarBlue™ assay. IGF-1 is known to be highly mitogenic to many cell types and the protein can regulate many cellular functions including the cell-division cycle, apoptosis and differentiation [89-90]. Importantly, IGF-1 also regulates the biological activity of bone cells [91-92]. Specifically, this includes stimulating the proliferation of bone cells and consequently enhanced bone formation [92]. The aim of the following experiments was to test if covalently immobilised IGF-1 could stimulate cellular attachment and/or proliferation of MG63 cells on PECVD-Si-Ti, similar to other studies that investigated the bioactivity of IGF-1 functionalised surfaces [174].

IGF-1 was adsorbed onto PECVD-Si-Ti or covalently linked to IPTES functionalised PECVD-Si-Ti (unreacted isocyanate groups were quenched with ethanolamine hydrochloride) (refer to **Scheme 1.9** and **page 41**). 1 ml of  $2.4 \times 10^4$  MG63 cells/ml was seeded onto each sample. The cells were allowed to attach for 4 h before removing any cells that had not attached or were loosely attached by a washing step (refer to **page 42**). The cell density was analysed by the alamarBlue™ assay after 24 h of cell growth on PECVD-Si-Ti, PECVD-Si-Ti loaded with adsorbed IGF-1, IPTES functionalised PECVD-Si-Ti loaded with covalently attached IGF-1, IPTES functionalised PECVD-Si-Ti with quenched reactive isocyanate groups as well as TCPS and titanium control samples. Additionally, the MG63 cell density on IPTES functionalised PECVD-Si-Ti (loaded and not loaded with IGF-1) was investigated after a longer incubation time of 72 h.

Once again, a low percentage of reduced alamarBlue™ ( $4 \text{ \%}/\text{cm}^2$ ) was recorded for PECVD-Si-Ti corresponding to a low cell surface density (**Figure 1.44**). Cell attachment and/or proliferation did not improve on PECVD-Si-Ti when the surface was functionalised with adsorbed IGF-1 (**Figure 1.44**). This result confirmed that the hydrophilic, plasma silica coating deposited on titanium (PECVD-Si-Ti - no air/H<sub>2</sub>O<sub>2</sub> plasma treatment) in this study resisted the adsorption of proteins and consequently cell attachment. This conclusion was corroborated by ELISA analysis, which showed only a low surface concentration of IGF-1 adsorbed onto PECVD-Si-Ti (refer to **Figure 1.39**).

However, cell attachment/growth was improved on PECVD-Si-Ti after functionalising the surface with IPTES. In fact, the percentage of reduced alamarBlue™ was virtually identical on IPTES functionalised PECVD-Si-Ti (11.1 %/cm<sup>2</sup>) compared to titanium (11.3 %/cm<sup>2</sup>) and slightly better than TCPS (8.7 %/cm<sup>2</sup>) in this experiment (**Figure 1.44**). This result was attributed to a decrease in the surface hydrophilicity on PECVD-Si-Ti due to the introduction of hydrophobic hydrocarbons from the IPTES (data not shown). By converting the very hydrophilic PECVD-Si-Ti surface to a moderately hydrophilic one, protein adsorption and consequently cell attachment improved, which was expected from the literature [183].

Interestingly, no further improvement in cell growth was induced by the covalently attached IGF-1 on IPTES functionalised PECVD-Si-Ti. The percentage of reduced alamarBlue™ on this sample was 11.3 %/cm<sup>2</sup>, which was similar to the amount of dye reduced on IPTES functionalised PECVD-Si-Ti not loaded with IGF-1 (with quenched reactive groups) of 11.1 %/cm<sup>2</sup> (**Figure 1.44**). After 72 h of cell culture, the percentage of reduced alamarBlue™ was again almost identical on IPTES functionalised PECVD-Si-Ti functionalised with covalently immobilised IGF-1 compared to the sample not treated with IGF-1 (graph inset in **Figure 1.44**). This showed that the immobilised IGF-1 had no influence on cell attachment and/or proliferation on IPTES functionalised PECVD-Si-Ti in this experiment. One possible explanation for this result is that IGF-1 is rendered biologically inactive when the protein is tethered to the surface. However, IGF-1 was shown to be immunologically reactive when covalently tethered to IPTES functionalised PECVD-Si-Ti (refer to **pages 105-111**). Therefore, another and more likely possibility may be that the relatively high serum (containing cell attachment and growth factors) concentration in the medium of 10% (v/v) may initiate a more significant biological response to cell attachment and/or proliferation on PECVD-Si-Ti than the surface tethered IGF-1 alone; or alternatively a thick serum protein layer adsorbed on the surface of IPTES coated PECVD-Si-Ti (functionalised with IGF-1) could shield IGF-1 and render it inaccessible to the IGF-1 receptors of cells, which are also expressed by osteoblast-like cells [93].

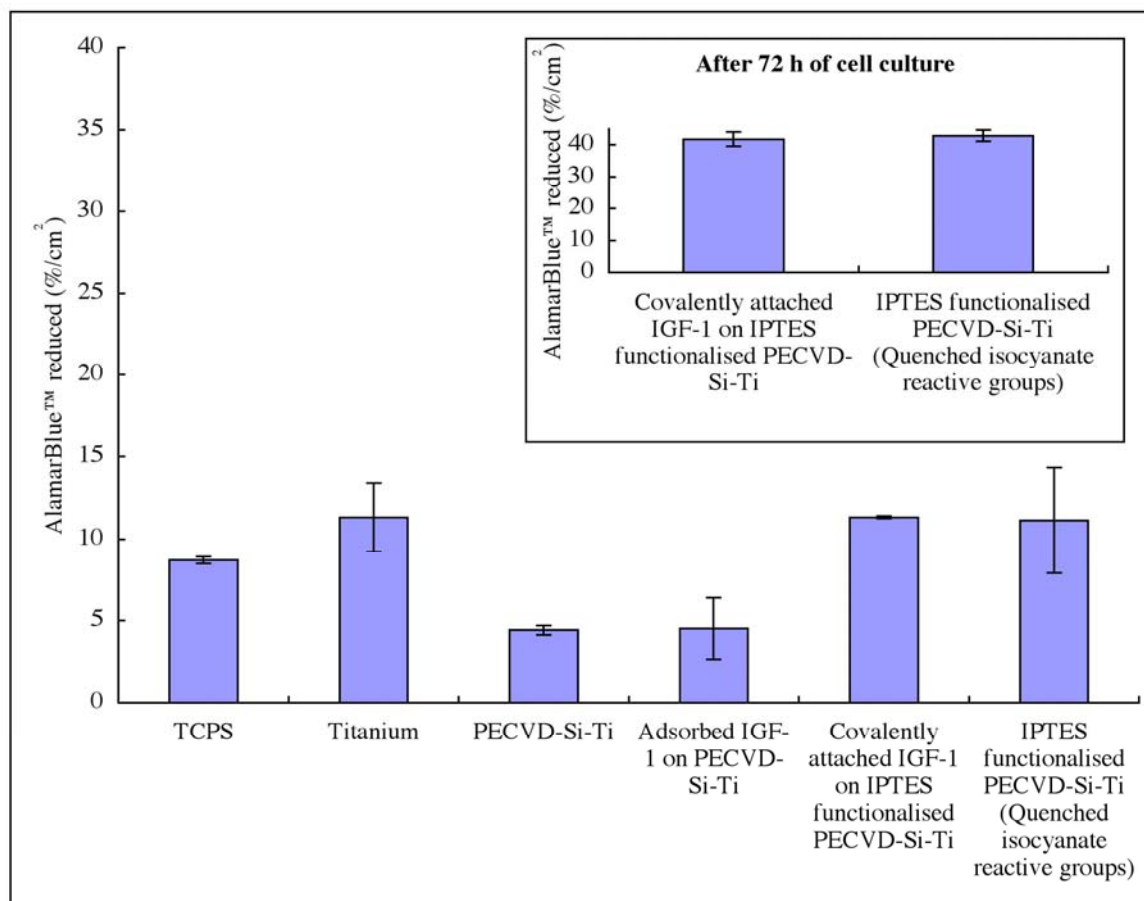


**Figure 1.44.** Percentage of alamarBlue™ reduced by MG63 cells that were grown on TCPS, titanium and PECVD-Si-Ti discs in a 24-well ultra-low cell attachment microplate. Additionally, the growth of cells was tested on PECVD-Si-Ti substrates that were loaded with adsorbed IGF-1 (600 ng for 2 h) and covalently attached IGF-1 (600 ng for 2 h) on IPTES functionalised PECVD-Si-Ti. PECVD-Si-Ti was functionalised with IPTES by Method 1 (refer to **pages 36-37**). Isocyanate groups were quenched with ethanolamine hydrochloride (refer to **page 41**). 1 ml of trypsinised  $2.4 \times 10^4$  MG63 cells/ml were seeded and incubated over the surfaces for 4 h under cell culture conditions. Following 4 h of incubation, the wells were washed twice in PBS (pH 7.4) and replenished with 2 ml of medium and then incubated for an additional 24 h. The cells were grown in MEM adjusted to a pH of 7.1 and supplemented with 100 units of penicillin and 100  $\mu$ g of streptomycin and 10% (v/v) FBS. MG63 cells were also cultured on IPTES functionalised PECVD-Si-Ti (loaded and not loaded with IGF-1) for a longer time period of 72 h (Graph inset). Refer to **page 42** for the alamarBlue™ assay procedure. Statistical analyses: Percentage of alamarBlue™ reduced by MG63 cells grown on IPTES and IGF-1 functionalised PECVD-Si-Ti was statistically different to TCPS, unmodified PECVD-Si-Ti and PECVD-Si-Ti loaded with adsorbed IGF-1 after 24 h of cell growth ( $p = 0.004$ ,  $< 0.001$  and  $0.036$ , respectively) but was not statistically different to uncoated titanium and IPTES functionalised PECVD-Si-Ti (not containing IGF-1) after 24 h of cell culture ( $p = 0.992$  and  $0.942$ , respectively) and to IPTES functionalised PECVD-Si-Ti (not containing IGF-1) after 72 h of cell culture ( $p = 0.650$ ).

The following experiment aimed to solve the uncertainty as to whether FBS was quenching the biological activity of IGF-1 by addressing the following question: Does IGF-1 enhance the proliferation of MG63 cells in the presence (or in the absence) of 10% (v/v) serum *in vitro*? In this experiment, 1 ml of  $2.4 \times 10^4$  MG63 cells/ml (prepared in serum-free medium) was seeded into wells of a 24-well plate, so that each test well contained the same number of cells (20-25% surface coverage from **Table 1.13**). After allowing the cells to attach for 4 h, the wells were washed and replenished with serum-containing (10% v/v) or serum-free medium supplemented or not supplemented with IGF-1. Cells were cultured for 72 h.

As shown in **Figure 1.45**, the growth of MG63 cells was limited in the absence of FBS. MG63 cells grown in 10% (v/v) serum reduced alamarBlue™ by approximately 3.7-fold more than cells grown in the absence of serum (**Figure 1.45**). However, no significant difference in the reduction of alamarBlue™ was obtained from cells that were cultured in medium supplemented with 10% (v/v) serum and IGF-1 compared to cells cultured in serum-supplemented medium without the addition of IGF-1 (**Figure 1.45**). But alamarBlue™ was reduced approximately 2-fold by MG63 cells grown in serum-free medium supplemented with IGF-1 compared to cells grown in serum-free medium without IGF-1 (**Figure 1.45**). Estimates made from the surface coverage of MG63 cells growing at the bottom of each well supported the results of the alamarBlue™ assay (**Table 1.13**). At each 24 h incubation time interval, the surface coverage of MG63 cells was estimated to be 5% higher in wells with serum-free medium supplemented with IGF-1 compared to wells with serum-free medium without IGF-1. In stark contrast, the coverage of cells grown in serum-containing medium was found to be the same after each incubation time period regardless of whether or not the medium was supplemented with additional IGF-1 (refer to **Table 1.13**).

As illustrated in this study, FBS was found to enhance the proliferation of cells more effectively than IGF-1 (**Figure 1.45**). FBS was more mitogenic than IGF-1, potentially because the serum has a more complete range of factors necessary for cell survival and proliferation (IGF-1 being only one of these factors). This enabled cells to proliferate much

better in serum-containing medium than in serum-free medium supplemented with IGF-1. Also, cell proliferation (after 72 h of cell culture) was only enhanced by IGF-1 in serum-free medium and not in serum-containing medium. Therefore, the experiment below tested if cell attachment and growth could be stimulated by immobilised IGF-1 in a serum-free environment on the surface modified titanium substrates.

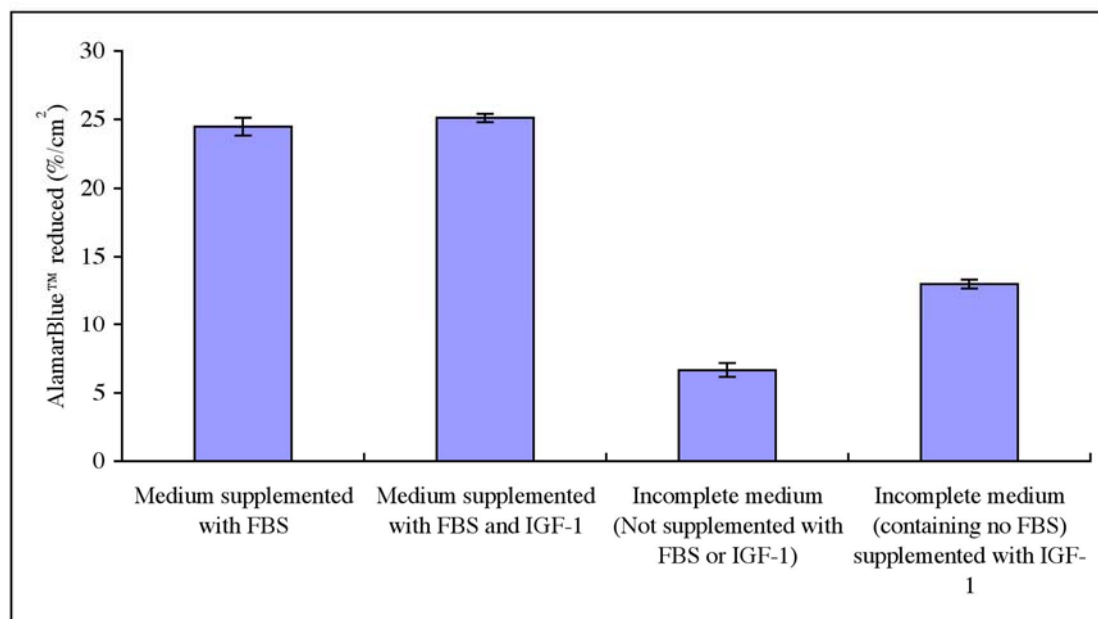


**Figure 1.45.** Percentage of alamarBlue™ reduced by MG63 cells grown in a 24-well TCPS plate (TPP). 1 ml of trypsinised  $2.4 \times 10^4$  MG63 cells/ml (prepared in serum-free MEM adjusted to a pH of 7.1 and supplemented with 100 units of penicillin and 100  $\mu$ g of streptomycin) were seeded and incubated over the surfaces for 4 h under cell culture conditions. After the first 4 h of cell attachment, the wells were washed twice in PBS (pH 7.4) and replenished with 2 ml of serum-containing (10% v/v FBS) or serum-free MEM (containing 100 units of penicillin and 100  $\mu$ g of streptomycin) supplemented or not supplemented with 600 ng of IGF-1 as indicated in the graph. The alamarBlue™ assay was performed after 72 h of cell culture. Refer to **page 42** for the alamarBlue™ assay procedure.

Surface coverage estimation (in %) of MG63 cells covering the bottom of the TCPS well (Surface area = 2.01 cm <sup>2</sup> ) at incubation times listed below				
Sample type	4 h	24 h	48 h	72 h
Medium supplemented with 10% (v/v) FBS (Not supplemented with IGF-1)	20-25	40-45	75-80	> 95
Medium supplemented with 10% (v/v) FBS and 600 ng of IGF-1	20-25	40-45	80	100
Incomplete medium (Not supplemented with FBS or IGF-1)	20-25	30	40	45
Incomplete medium (Not supplemented with FBS) supplemented with 600 ng of IGF-1	20-25	35	45	50

**Table 1.13.** A table of estimated percentages of MG63 cells covering the bottom of the well of a 24-well TCPS plate that was derived from the same experiment outlined in **Figure 1.45**. An estimation of the percentage of cells covering the bottom of the wells was established through visual inspection of attached cells at the bottom of the plate through a light microscope.

The growth of MG63 cells was next analysed with the alamarBlue™ assay to determine if immobilised IGF-1 could induce a cellular response on titanium and PECVD-Si-Ti in a serum-free environment. After 72 h of cell culture, a much higher cell density was again observed on TCPS when cells were grown in the presence of serum in comparison to cells grown in serum-free medium. AlamarBlue™ was reduced approximately 4.6-fold more on TCPS when cells were cultured in serum-containing medium compared to cells cultured in serum-free medium (**Figure 1.46**). This is in good agreement with the data in **Figure 1.45**.

Similar to alamarBlue™ reduced by MG63 cells grown on TCPS in the absence of serum (6.5 %/cm<sup>2</sup>), a low percentage of alamarBlue™ of 5.7 %/cm<sup>2</sup> was reduced on uncoated titanium after culturing MG63 cells on this sample in the absence of serum for 72 h. A low percentage of reduced alamarBlue™ typified a low cell density on TCPS and uncoated titanium, which was expected because the medium did not contain the necessary biological factors for promoting cellular attachment or proliferation (in particular IGF-1, vitronectin and fibronectin) [174, 184].

A slightly higher cell density was detected (with the alamarBlue™ assay) on uncoated titanium that was loaded with adsorbed IGF-1. AlamarBlue™ was reduced by 7.7 %/cm<sup>2</sup> on this sample, which was approximately 1.4-fold more compared to that on uncoated titanium without IGF-1 (**Figure 1.46**). Interestingly, alamarBlue™ was reduced even further to 10.8 %/cm<sup>2</sup> (1.9-fold compared to non-functionalised uncoated titanium) when IGF-1 was covalently tethered to IPTES functionalised uncoated titanium (**Figure 1.46**). Also, alamarBlue™ was reduced by 10.3 %/cm<sup>2</sup> when IGF-1 was covalently attached to IPTES functionalised PECVD-Si-Ti, which was 1.9-fold compared to alamarBlue™ reduced on IPTES functionalised PECVD-Si-Ti without IGF-1 (**Figure 1.46**). These results indicated that cell attachment and/or proliferation could be significantly improved on uncoated titanium and PECVD-Si-Ti by covalently linking an appropriate growth factor (IGF-1) to these surfaces.

As previously discussed, the immunological activity of IGF-1 was much higher when the protein was covalently immobilised on PECVD-Si-Ti compared to when the protein was covalently attached directly to titanium (refer to **Figure 1.40**). But as shown in **Figure 1.46**, the biological activity of IGF-1 was similar when the growth factor was covalently attached on both titanium and PECVD-Si-Ti. This means that a direct comparison could not be made between the immunological reactivity and the biological activity of IGF-1 on titanium and PECVD-Si-Ti. This outcome could be a result of several possibilities.

First, the ELISA (used to assess the immunological activity of immobilised IGF-1) incorporated multiple stringent wash steps with a PBS-Tween® 20 mixed solution to remove non-specifically attached proteins. But the samples that were loaded with IGF-1 in preparation for cell culture were only washed once in PBS (without Tween® 20) to exclude any adverse effects that residual detergent may have on cell attachment and survival. Therefore, if IGF-1 was not strongly tethered to titanium, it would have been washed from the surface during the ELISA preparation, resulting in a low readout signal. But a higher surface concentration of the protein would remain on titanium after a single wash in PBS (without Tween® 20), leaving the surface biologically active. Alternatively, the biological activity of IGF-1 may still be relatively high even if the protein is present at a low surface

density. This would be the case if a large spacing between the immobilised factor is required for cell surface recognition. This is a reasonable assumption considering IGF-1 is highly mitogenic at relatively low protein concentrations [89-90].

Also, MG63 cells were previously shown to attach and proliferate much better on titanium compared to PECVD-Si-Ti, which was attributed to the very hydrophilic PECVD-Si-Ti surface resisting the adsorption of serum proteins that facilitate cellular attachment (refer to **Figures 1.39, 1.42 and 1.44**). Similarly in this experiment, extracellular matrix proteins produced by the MG63 cells would adsorb much better on the underlying moderately hydrophilic titanium surface (functionalised with IPTES and IGF-1) than on the underlying very hydrophilic PECVD-Si-Ti surface (also functionalised with IPTES and IGF-1). This scenario may result in cellular attachment and proliferation stimulatory effects, induced by IGF-1 immobilised on IPTES functionalised PECVD-Si-Ti, being cancelled by inhibitory effects from the underlying hydrophilic surface resisting cellular adhesion. This argument is valid because the coverage of IGF-1 was low (suitable for cell surface recognition) in these studies. If the coverage was large, the surface wettability would be that of IGF-1, not the underlying surface. Therefore, for future studies it may be worthwhile filling the gaps on the surface after IGF-1 immobilisation with an extracellular matrix protein (such as fibronectin) to improve cellular adhesion. Nonetheless, this study did show that covalently tethered IGF-1 on both IPTES functionalised titanium and PECVD-Si-Ti was biologically active towards promoting cellular attachment.

MG63 cells were also grown on several control samples to confirm that the covalently immobilised IGF-1 improved cellular growth on PECVD-Si-Ti. The percentage of alamarBlue™ reduced by MG63 cells was compared between IPTES functionalised PECVD-Si-Ti loaded with IGF-1, IPTES functionalised PECVD-Si-Ti that was not loaded with IGF-1 possessing quenched reactive groups (quenched with ethanolamine hydrochloride) and IPTES functionalised PECVD-Si-Ti possessing reactive isocyanate groups. As shown in **Figure 1.46**, after 72 h of culturing MG63 cells on all these surfaces, alamarBlue™ was reduced 1.9-fold and 1.5-fold on IPTES functionalised PECVD-Si-Ti reacted with IGF-1 in comparison to IPTES functionalised PECVD-Si-Ti samples not

reacted with IGF-1 displaying quenched isocyanate groups and reactive isocyanate groups, respectively. Because a significantly greater percentage of alamarBlue™ was reduced on PECVD-Si-Ti with immobilised IGF-1 compared to the controls that were not reacted with IGF-1, cell attachment and or proliferation was improved on PECVD-Si-Ti, presumably as a direct result of cells responding to the immobilised growth factor.

So far the results have shown and confirmed that cell growth could be improved on PECVD-Si-Ti by functionalising the surface with IPTES, followed by coupling IGF-1 to the reactive isocyanate groups and then quenching any unreacted isocyanate groups with ethanolamine hydrochloride. But what if a different quenching agent was used? A short Arginine-Glycine-Aspartic acid (RGD) peptide, instead of ethanolamine hydrochloride, was also used to quench unreacted isocyanate groups. The RGD motif, which is recognised by cell membrane receptors such as integrins, has been widely demonstrated to be an important cell-binding domain for promoting cellular attachment and regulating cellular behaviour from interactions between cells and RGD-containing proteins and peptides, including integrin-mediated osteoblast cell adhesion [173, 185-190].

After covalently attaching IGF-1 onto IPTES functionalised PECVD-Si-Ti, any unreacted isocyanate groups were quenched by incubating the sample in PBS containing 200 µg/ml of RGD for 30 min. As shown in **Figure 1.46**, alamarBlue™ was reduced by 10.3 %/cm<sup>2</sup> and 9.3 %/cm<sup>2</sup> on IPTES functionalised PECVD-Si-Ti reacted with IGF-1 and quenched with ethanolamine hydrochloride and RGD, respectively. The similar percentage of alamarBlue™ reduced by the MG63 cells indicated that there was similar density of cells growing on these samples, which showed that both ethanolamine hydrochloride and RGD worked equally well as a quenching agent in this experiment. Alternatively, it cannot be excluded that most of the isocyanate groups may have reacted with IGF-1 or were quenched in the aqueous buffer before the reactive groups were capped with the amine-containing compounds.

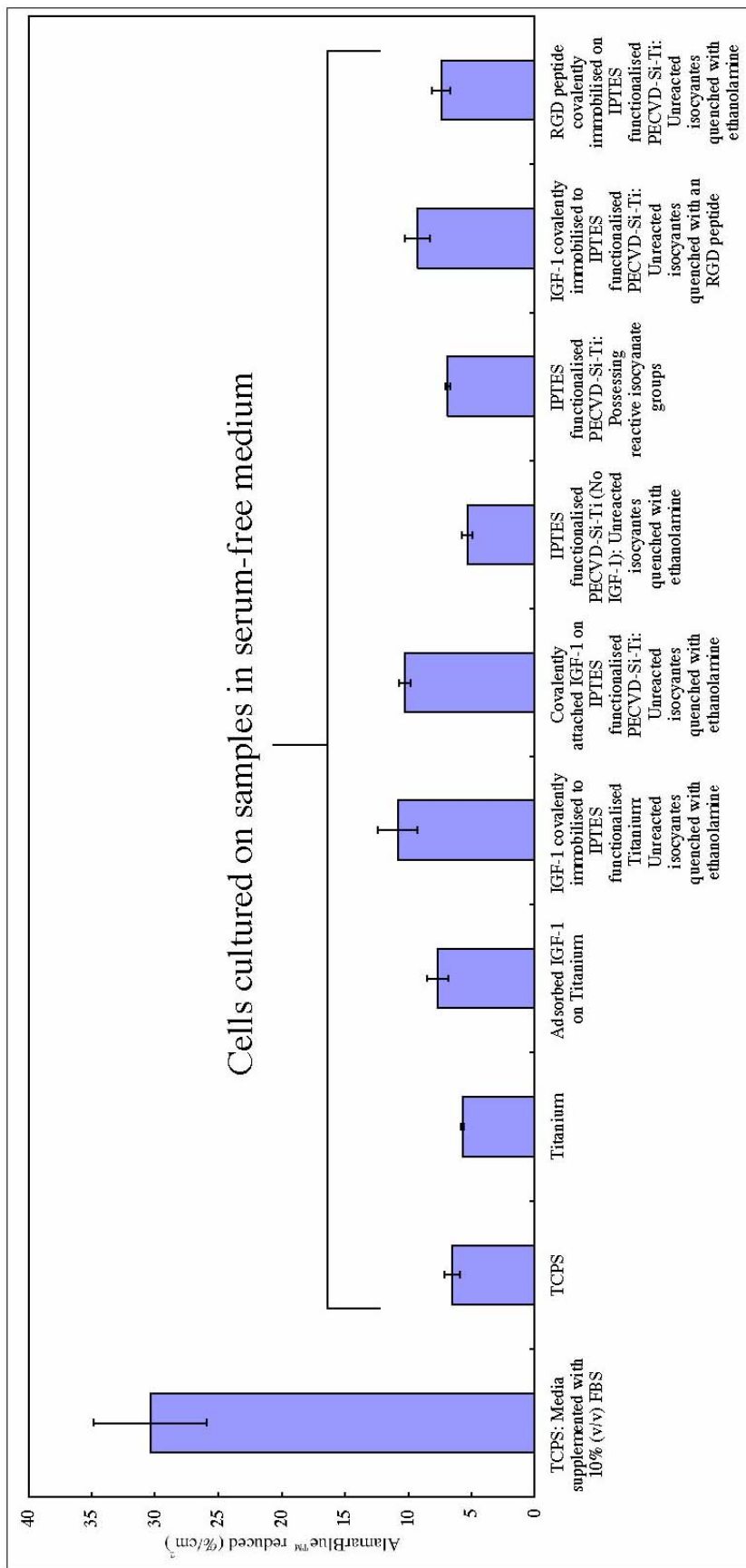


**Figure 1.46.** Refer to following page (page 132)

**Figure 1.46.** Percentage of alamarBlue™ reduced by MG63 cells after 72 h of culture in serum-free MEM. 1 ml of  $2.4 \times 10^4$  trypsinised MG63 cells/ml were seeded onto the substrates and allowed to attach for a period of 4 h. Cells that were not attached were washed from the substrate by two washes in PBS (pH 7.4) and the medium was replenished with fresh serum-free medium. TCPS discs were used as received and titanium and PECVD-Si-Ti were prepared as previously described (refer to **pages 30, 32-35 and 41**). Titanium and PECVD-Si-Ti were functionalised with a IPTES by following Method 1 (refer to **pages 36-37**). Surfaces were loaded with 600 ng of IGF-1 (refer to **page 41**). Unreacted isocyanate groups were quenched with ethanolamine hydrochloride by following the procedure on **page 41** or with 200 µg/ml of an RGD peptide according to the same experimental method. Cells were also grown on a TCPS disc in MEM (pH 7.1) supplemented with 10% (v/v) FBS for comparison. Both of the medium formulations (serum-containing or serum-free) were supplemented with 100 units of penicillin and 100 µg of streptomycin. The alamarBlue™ assay was performed after 72 h of cell culture by following the procedure described on **page 42**. Statistical analyses: Percentage of alamarBlue™ reduced by MG63 cells grown on IPTES/IGF-1 functionalised PECVD-Si-Ti (reactive groups quenched with ethanolamine) was statistically different to TCPS ( $p = 0.019$ ), uncoated titanium ( $p = 0.005$ ), IPTES functionalised PECVD-Si-Ti (not reacted with IGF-1 and having reactive groups quenched with ethanolamine) ( $p = 0.007$ ), IPTES functionalised PECVD-Si-Ti displaying reactive isocyanate groups ( $p = 0.009$ ) and IPTES/RGD functionalised PECVD-Si-Ti (reactive groups quenched with ethanolamine) ( $p = 0.039$ ). IPTES/IGF-1 functionalised PECVD-Si-Ti (reactive groups quenched with ethanolamine) was not statistically different to IPTES/IGF-1 functionalised uncoated titanium ( $p = 0.669$ ), IPTES/IGF-1 functionalised PECVD-Si-Ti (reactive groups quenched with RGD) ( $p = 0.318$ ) or titanium loaded with adsorbed IGF-1 ( $p = 0.059$ ) (at a lower confidence limit of 94%, IPTES/IGF-1 functionalised PECVD-Si-Ti (reactive groups quenched with ethanolamine) was statistically different to titanium loaded with adsorbed IGF-1).

Therefore, as a final control, RGD (as a substitute for IGF-1) was covalently attached onto IPTES functionalised PECVD-Si-Ti and unreacted isocyanate groups were quenched with ethanolamine hydrochloride. After 72 h of MG63 cell culture, alamarBlue™ was reduced 1.4-fold on PECVD-Si-Ti loaded with covalently attached IGF-1 in comparison to PECVD-Si-Ti loaded with covalently attached RGD (**Figure 1.46**). This showed that a more significant biological response was elicited by IGF-1 compared to RGD after covalently attaching the molecules on IPTES functionalised PECVD-Si-Ti. Therefore, immobilised IGF-1 exerted a greater stimulatory effect on cellular growth in comparison to the RGD peptide.

The results showed that cell growth could be stimulated in serum-free medium on both titanium and PECVD-Si-Ti by covalently immobilising IGF-1 to the surfaces. Furthermore, IGF-1 was shown to retain its biological activity after covalently tethering the growth factor to PECVD-Si-Ti. But in a previous study, Schleicher et al. reported that attachment and proliferation of human osteoblast-like cells could be further improved on TCPS by functionalising the surface with both vitronectin and IGF-1 [174]. The cell density after 72 h of cell proliferation was approximately 1.3-fold on TCPS functionalised with both IGF-1 and vitronectin compared to TCPS with vitronectin alone. Therefore, if both the proteins (IGF-1 and vitronectin) were co-immobilised on PECVD-Si-Ti, it would be likely that cell growth would be significantly improved. However, this present study focussed solely on analysing the biological activity of immobilised IGF-1 alone on PECVD-Si-Ti and no investigation, as yet, has been conducted by our research team on the co-immobilisation of cellular growth promoting factors, but would certainly be worthwhile pursuing in the future.

Since immobilised IGF-1 on PECVD-Si-Ti was shown to be biologically active in serum-free medium, but not in 10% (v/v) FBS, the next experiment was conducted to test the biological activity of IPTES functionalised PECVD-Si-Ti loaded with covalently attached IGF-1 in medium containing a reduced concentration of serum. We hypothesised that the mitogenic effect of IGF-1 may become even more enhanced in the presence of a small concentration of serum proteins, some of which are vital for cellular growth.

Before testing the growth of MG63 cells on PECVD-Si-Ti, a calibration curve was first constructed to assess the proliferation of MG63 cells grown on TCPS in a range of serum concentrations. The aim of this preliminary experiment was to determine a serum concentration that produces a reduced rate MG63 cell proliferation. After 72 h of cell culture, the density of MG63 cells had increased linearly in MEM supplemented with 0-1.25% (v/v) of serum (**Figure 1.47**). Cell proliferation levelled out at a serum concentration range of 1.25% (v/v) after 72 h of cell culture. A serum concentration of 0.2% (v/v) was chosen from this calibration curve to assess if covalently attached IGF-1 on IPTES functionalised PECVD-Si-Ti is able to stimulate cell attachment and proliferation in a reduced serum environment. It was anticipated that MG63 cell attachment and proliferation would also be similar (in comparison to TCPS) on IPTES functionalised PECVD-Si-Ti in 0.2% (v/v) serum-containing medium and that cell growth would be well below the more optimal serum concentration of 1.25-10% (v/v) when compared to IPTES functionalised PECVD-Si-Ti loaded with covalently attached IGF-1, after 72 h of cell culture. Therefore, the next experiment tested if covalently immobilised IGF-1 on IPTES functionalised PECVD-Si-Ti could induce a stimulatory effect of cell growth in 0.2% (v/v) serum-containing medium close to that of the stimulatory effect exerted by FBS on cells cultured in a higher concentration (1.25-10% (v/v)) of serum.

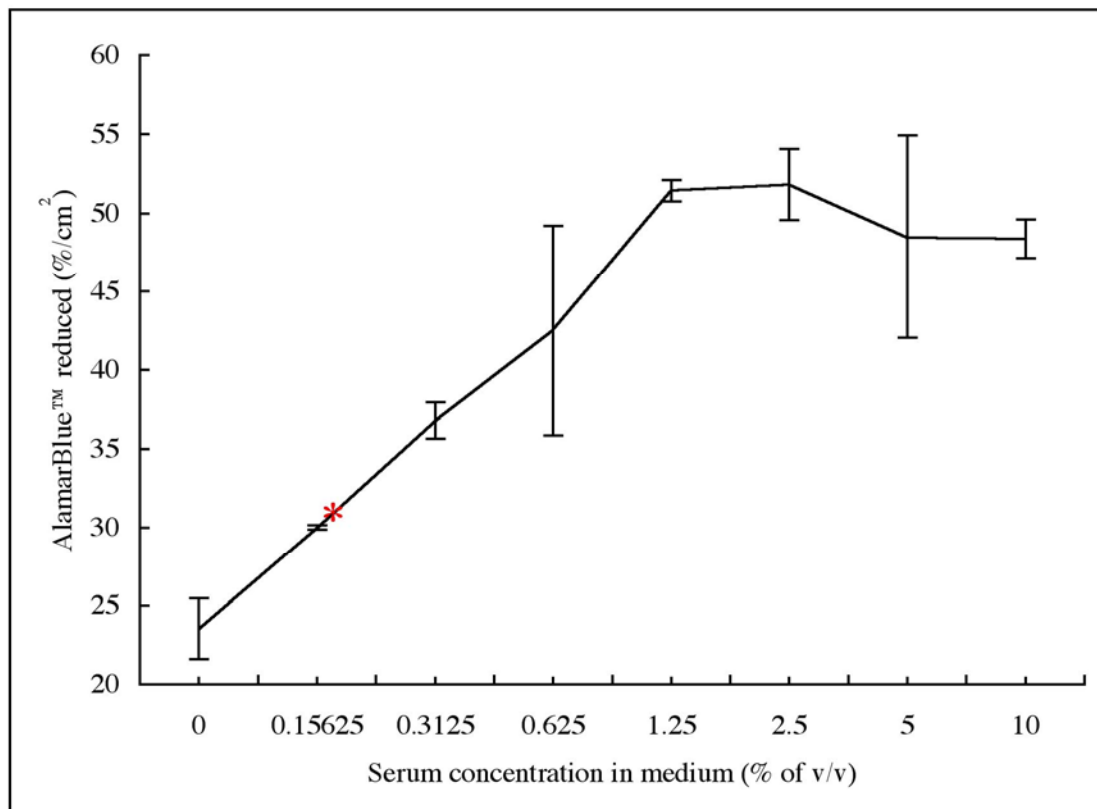


**Figure 1.47.** Calibration curve of the percentage of alamarBlue™ reduced by MG63 cells grown in MEM (pH 7.1 and supplemented with 100 units of penicillin and 100  $\mu$ g of streptomycin) at a range of serum concentrations. 200  $\mu$ l of trypsinised  $2.4 \times 10^4$  cells/ml was added to wells of an Iwaki 96-well TCPS plate (the surface area at the bottom of each well equals  $0.32 \text{ cm}^2$ ). The cells were allowed to attach for 4 h and any cells that had not attached after this period of time were washed away from the wells by two washes in PBS (pH 7.4). The wells were then replenished with 200  $\mu$ l of the test MEM solutions (indicated in the graph). The cells were then cultured in the wells for 72 h before performing the alamarBlue™ assay. Cells were cultured under cell culture conditions. \* Indicates the position on the calibration curve at a serum concentration of 0.2% (v/v) and 30 %/cm<sup>2</sup> of reduced alamarBlue™ that was used to assess cell growth in response to IGF-1 covalently linked to IPTES functionalised PECVD-Si-Ti (refer to **Figure 1.48**). Refer to **page 42** for a description of the alamarBlue™ assay procedure.

MG63 cellular growth was next compared on IPTES functionalised PECVD-Si-Ti loaded with covalently attached IGF-1 and IPTES functionalised PECVD-Si-Ti not loaded with IGF-1 in MEM supplemented with 0.2% (v/v) FBS. Isocyanate groups on both of these samples were quenched with ethanolamine hydrochloride. For comparison, the proliferation of MG63 cells grown in MEM supplemented with 0%, 0.2% and 10% (v/v) serum was monitored on TCPS. As shown in **Figure 1.48**, MG63 cells that had been cultured on TCPS for 72 h, reduced alamarBlue™ by a factor of 6.3 when grown in 0.2% compared to 0% (v/v) serum and 1.4-fold when grown in 10% compared to 0.2% (v/v) serum. This result was expected from the calibration curve shown in **Figure 1.47**. However, there was no significant difference in the percentage of alamarBlue™ reduced by MG63 cells grown in 0.2% (v/v) serum on IPTES functionalised PECVD-Si-Ti loaded with covalently attached IGF-1 and IPTES functionalised PECVD-Si-Ti not loaded with IGF-1 (**Figure 1.48**). Therefore, cellular growth was not enhanced on PECVD-Si-Ti by the covalently tethered IGF-1 in medium supplemented with a reduced concentration of serum.

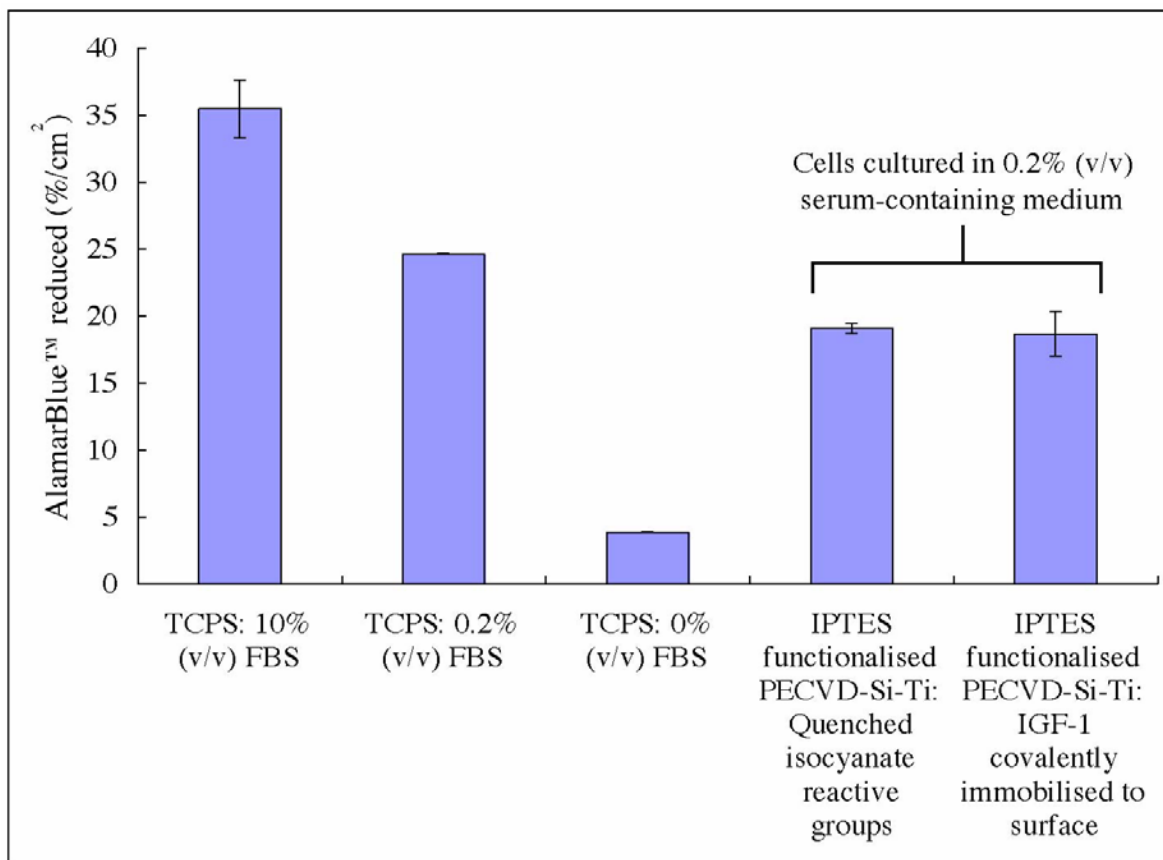


**Figure 1.48.** AlamarBlue™ reduced by MG63 cells grown on TCPS and on IPTES functionalised PECVD-Si-Ti loaded with or without 600 ng of IGF-1 (refer to **page 41**). PECVD-Si-Ti was functionalised with a IPTES by following Method 1 (refer to **pages 36-37**). Unreacted isocyanate groups were quenched with ethanolamine hydrochloride (refer to **page 41**). Additionally, cell growth was compared after culturing cells on TCPS discs in 0%, 0.2% and 10% (v/v) serum-containing medium. 1 ml of trypsinised  $2.4 \times 10^4$  cells/ml were seeded onto each substrate in serum-free MEM (pH 7.1) supplemented with 100 units of penicillin and 100  $\mu$ g of streptomycin and incubated for 4 h. Any cells that had not attached after this period time were washed from the wells by two washes in PBS (pH 7.4). The medium was replenished with 2 ml of the test MEM solutions (indicated in the graph) and the cells were cultured for 72 h before performing the alamarBlue™ assay. Refer to **page 42** for more detail about the alamarBlue™ assay procedure. Experiments were performed in a 24-well ultra-low cell attachment plate.

In summary, poor cell attachment of MG63 osteoblast-like cells was observed on PECVD-Si-Ti. This was attributed to the hydrophilic surface resisting the adsorption of extracellular proteins and consequently inhibiting cell attachment. Cell attachment was improved on PECVD-Si-Ti by functionalising the surface with IPTES. Furthermore, cell growth in a serum-free environment was further enhanced on PECVD-Si-Ti by covalently attaching IGF-1 to the surface. However, no enhancement in cellular growth was induced by IGF-1 when the cells were cultured in high-serum (10% v/v) or low-serum (0.2% v/v) environments. This discovery is very important if IPTES functionalised PECVD-Si-Ti loaded with covalently attached IGF-1 is to be used as an implant *in situ*. The implant would obviously come in contact with human serum proteins and other biological compounds, which would adsorb on the surface of the implant. It would be a reasonable assumption that these proteins would also quench the biological activity of IGF-1 towards promoting cellular growth.

However, since PECVD-Si-Ti has previously been shown to accelerate bone formation *in situ*, the possibility of IGF-1 further enhancing the bone remodelling process on this material should not be excluded. This outcome is possible even if cellular proliferation was similar on implants functionalised with and without IGF-1 because a range of other cellular pathways are also stimulated by IGF-1 including the synthesis of extracellular matrix proteins by osteoblasts, which become mineralised during bone formation on the implant surface [91]. Also, other factors such as extracellular matrix proteins could be co-immobilised with IGF-1 that could further enhance cell attachment/growth and regulate cell activity [174]. These factors have not been tested at this stage of the research. Instead, the influence of IGF-1 on the early stages of cell attachment, adhesion and proliferation in FBS-free medium was further investigated in the next section. The approach that was taken investigated the role of IGF-1 in the regulation of an intercellular mitogen activated protein kinase (MAPK) signalling pathway involved with cellular proliferation and fluorescence microscopy, which was used to visualise cell density and cellular structure in response to IGF-1.

### 1.3.6 Analysis of cell attachment and early cell proliferation on IGF-1 functionalised PECVD-Si-Ti

The next experiments were performed with a view to developing an assay that examines the regulation of a mitogen activated protein kinase (MAPK) signalling pathway in cells stimulated with immobilised IGF-1. A number of fundamental cellular processes including cellular proliferation, differentiation, development and apoptosis are controlled by the MAPK signalling pathway [191-192]. A simplified schematic of the general MAPK signalling pathway (taken from Kolch) is shown in **Figure 1.49 A** [191]. Briefly, upon stimulation with an extracellular signal, a transmembrane receptor with a cytoplasmic tyrosine kinase domain undergoes a conformational change allowing the receptor to couple to a G-protein. The G-protein becomes activated through an exchange of guanosine diphosphate (GDP) and guanosine triphosphate (GTP) leading to the activation of MAPK kinase kinase (MAPKKK) that phosphorylates and activates MAPK kinase (MAPKK), which in turn phosphorylates and activates MAPK. MAPK alters the activities of transcription factors and consequently the transcription of genes, some of which are important for the cell cycle [193].

The extracellular-signal-regulated kinase (ERK) pathway, a particular example of a MAPK pathway, is implicated in nearly every fundamental cellular activity. The ERK pathway is shown in **Figure 1.49 B** [191]. Upon stimulation with a growth (or differentiation) factor, the transmembrane growth factor receptor couples to a Ras protein (a G-protein), which becomes activated. The Ras protein then activates Raf (a MAPKKK) that in turn phosphorylates and activates MEK (a MAPKK), which in turn phosphorylates and activates ERK (a MAPK). Activated ERK may then translocate to the cell nucleus and phosphorylate nuclear transcription factors such as Elk, which is an important factor in the cell division cycle [194].

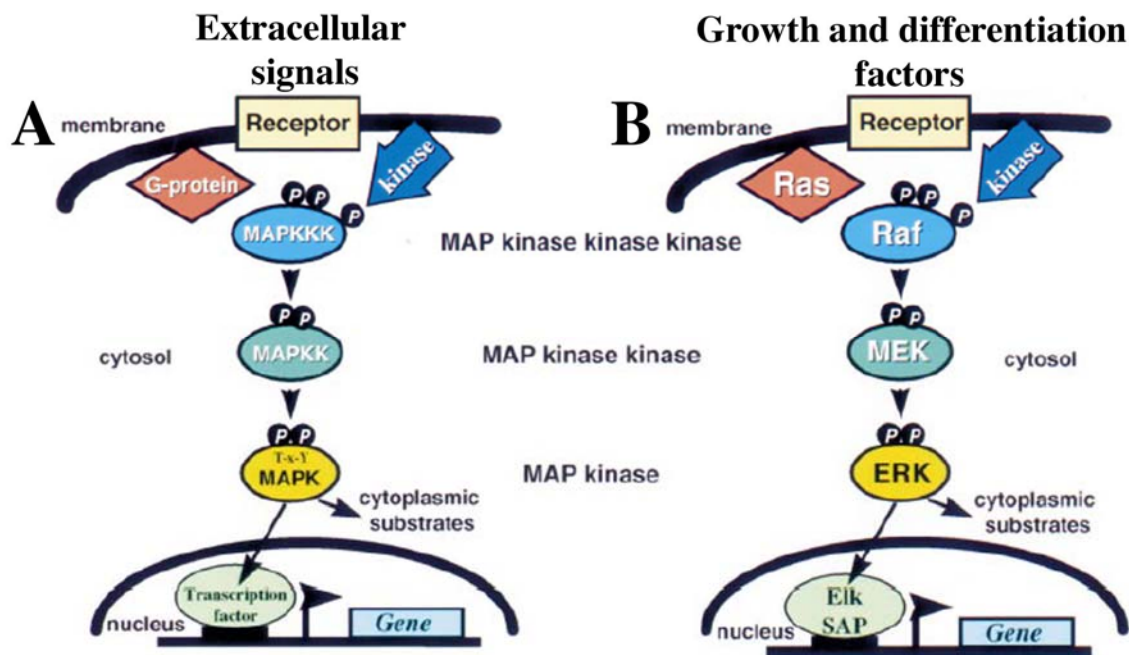


**Figure 1.49.** A general schematic of the MAPK pathway (A) and a relevant example, the ERK pathway (B). The images were taken from Kolch [191].

Activation of a MAPK signalling pathway was analysed using a commercially available kit from TGR Biosciences Pty Ltd. The assay utilises Surefire™ technology developed by TGR Biosciences Pty Ltd and Alphascreen™ technology developed by PerkinElmer to measure the phosphorylation of ERK (**Figure 1.50**) [195]. During a typical assay, a population of cells is stimulated with the agonist usually for a short period of time (5-15 min). The cells are lysed and the intracellular components are analysed through an immunological reaction. Briefly, ERK is first labelled with a donor bead complex. The donor bead contains a photosensitising agent. A monoclonal antibody specific for p-ERK (conjugated to an acceptor bead) then binds the phosphorylated region of p-ERK. The acceptor bead contains a thioxene derivative and fluorophores. When the antibody binds, the two beads are brought into close proximity. Upon excitation with a laser at 680 nm, oxygen in the aqueous medium is converted into its singlet state by the photosensitiser. The singlet state oxygen molecules diffuse across to the nearby acceptor bead eventually reacting with thioxene to form an unstable intermediate that becomes rapidly converted into a stable dioxetane derivative, generating chemiluminescence at approximately 370 nm

[196]. Other chemicals (anthracene and rubrene) in the acceptor bead shift the emission of light at approximately 370 nm to a higher wavelength of 520-620 nm by an intermolecular energy transfer process, which is recorded by the instrument [196]. Intermolecular energy transfer occurs only if the donor and acceptor beads are in close proximity with one another because singlet oxygen is unstable and at longer diffusion distances cannot excite the thioxene species. This signal mechanism ensures that an increase in fluorescence emission at 520-620 nm correlates with the p-ERK titre.

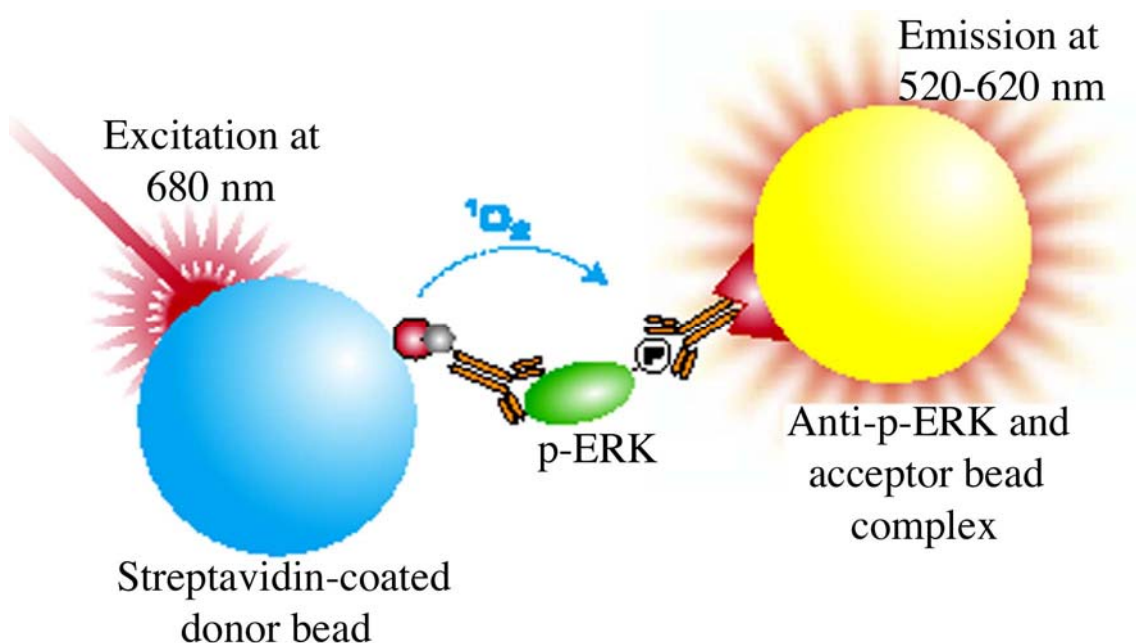


**Figure 1.50.** Overview of the AlphaScreen™ SureFire™ p-ERK assay. The image was taken from an AlphaScreen™ SureFire™ ERK assay brochure [195].

Typically, the MAPK assay is performed on an adherent and confluent monolayer of cells. The cells are usually stimulated with a 'free' agonist (spiked into the medium) for a short time period of 5-15 min. But in this study, the up-regulation of p-ERK in MG63 cells needed to be analysed after stimulating cells with an immobilised agonist (IGF-1) during the cellular attachment stage. This raised some potential problems. Firstly, non-specific cell binding and spreading on the substrate surface may trigger the up-regulation of p-ERK even in the absence of IGF-1. As cells adhere on to the substrate surface, cellular membrane integrins could cluster and trigger the MAPK cascade [197]. Secondly, the cell attachment time needed to be limited to reduce the interaction time between the cell and IGF-1. At longer interaction times, the MAPK signalling pathway is likely to be down regulated and the intracellular concentration of p-ERK is consequently reduced to a normal level [197]. However, shortening the cellular attachment time may result in a much lower surface density of cells attached to the substrate surface in comparison to a confluent layer of cells typically analysed in this assay. This could produce a false negative result because the concentration of p-ERK is also dependent on the cell density. Also, the cells would not attach to the surface at the same time resulting in cells being stimulated by IGF-1 for different time periods on the substrate surface. Both of these scenarios would probably result in a lower density of cells being stimulated by IGF-1 for the appropriate period of time. Therefore, an investigation was first conducted to determine if the immobilised IGF-1 could effectively stimulate the attachment of MG63 cells at relatively short cell attachment times.

These cellular attachment experiments were again performed using the alamarBlue™ assay. In the previous cell culture experiments described in this thesis, cells growing in the tissue culture flask were detached from the surface with the aid of trypsin. Although cells can be conveniently detached quickly from the plastic surface of the flask by means of the enzymatic trypsin solution, the enzyme can also damage cell membrane receptors (including of course the IGF-1 receptor, which is of relevance here). Therefore, in the following assays, the cells were detached from the surface of the culture flask by incubating in a non-enzymatic and protein-free cell dissociation solution (CDS). CDS contains chelating agents, which act by chelating calcium and magnesium from intercellular bridges.

Cells then dissociate from each other as well as from the TCPS surface. This solution has the advantage of gently removing the entire cell population from the growing surface of the culture vessel without giving rise to the modification of cellular proteins by enzymes or to the adsorption of foreign proteins. Therefore, this method of cell dissociation is particularly useful when studying cell-material interactions such as integrin-mediated cellular adhesion, morphology, cytoskeletal organisation and gene expression in response to distinct surface morphological and biochemical cues on material surfaces [198].

The wells of a 96-well Nunc-Maxisorp™ plate were incubated with 600 ng IGF-1, prepared in 100 µl of PBS (pH 7.4), or in PBS without IGF-1 as a negative control, and then subsequently washed in PBS to remove any unbound (or loosely bound) protein. As indicated in **Figure 1.51**, both the temperature and time were varied in an attempt to establish an optimal protein adsorption procedure. After detaching cells slowly (20-30 min using CDS compared to 5-10 min with trypsin) from the surface of the culture vessel, 100 µl of  $6 \times 10^5$  cells/ml diluted in FBS-free MEM (pH 7.1) supplemented with 2 mg/ml of BSA was added to the treated wells. BSA was added to the cell dilution medium to reduce the chance of cells binding non-specifically to the polystyrene surface. The cells were incubated in the wells for 30 min. Cells that had not attached were washed from the wells (in PBS, pH 7.4) before analysis with the alamarBlue™ assay. The highest level of cell attachment was found in wells treated with IGF-1 for the longest time period of 12 h. As shown in **Figure 1.51**, the reduction of alamarBlue™ was significantly greater (approximately 2.5-fold) in the wells incubated with IGF-1/PBS solution for 12 h at 25°C or 4°C compared to wells that had been incubated in PBS (minus IGF-1). However, no significant difference in the reduction of alamarBlue™ was found in the wells incubated with IGF-1/PBS solution for 2 h at 25°C compared to the wells incubated in PBS for the same time period. Therefore, the optimal IGF-1 adsorption time on polystyrene (for promoting MG63 cellular attachment) was found to be 12 h at either 25°C or 4°C. To the best of our knowledge, no studies have been carried out that examine cell attachment on IGF-1 functionalised surfaces. However, enhancement of cell attachment on IGF-1 functionalised TCPS was expected because cell attachment is generally improved on nitrogenous surfaces [197].

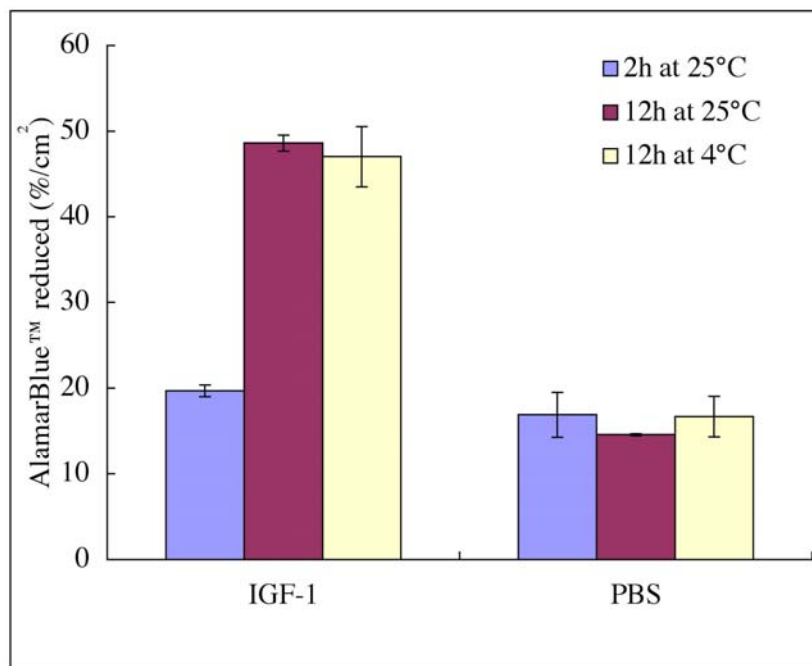


**Figure 1.51.** Percentage of reduced alamarBlue™ after an MG63 cell attachment experiment performed in a 96-well Nunc-Maxisorp™ plate that was treated by incubation with 100  $\mu$ l of 600 ng of IGF-1 prepared in PBS or 100  $\mu$ l of PBS into each well for various times and various temperatures, which are indicated in the graph. 100  $\mu$ l of  $6 \times 10^5$  MG63 cells/ml was seeded into the wells. The cells were incubated in the wells for 30 min. Cells that had not attached were removed from the wells in two PBS (pH 7.4) washes. FBS-free MEM (containing 100 units of penicillin and 100  $\mu$ g of streptomycin) was supplemented with 2 mg/ml of BSA. The attachment assay was performed under cell culture conditions. The alamarBlue™ assay procedure is described on **page 42**.

AlamarBlue™ was reduced by over 10 %/cm<sup>2</sup> by MG63 cells attached to the wells that had been incubated in PBS alone (without IGF-1) in **Figure 1.51**. Therefore, some of the cells had attached to polystyrene non-specifically. Non-specific cell attachment could potentially interfere with the p-ERK assay. Therefore, another experiment was conducted to determine if the non-specific attachment of cells on polystyrene could be further reduced. This was performed by blocking wells with BSA (prior to seeding the cells into the wells) and by further reducing the cellular attachment time. Non-specific cell attachment was found to be similar for the cell attachment times of 10 and 30 min tested in this experiment. But BSA was found to be a successful blocking agent for reducing non-specific cell attachment (**Figure 1.52**). The reduction of alamarBlue™ was decreased by approximately 25% in

wells that were blocked with BSA compared to wells that had not been blocked with BSA after allowing cells to attach for 10 or 30 min (**Figure 1.52**). Also, no significant decrease in cell attachment was observed in wells that were blocked with 0.5 to 4 mg of BSA indicating that the protein had completely covered the surface at these concentrations. Therefore, in the next experiment, untreated wells and wells loaded with adsorbed IGF-1 were blocked using 1 mg of BSA/well to further reduce non-specific cell attachment.

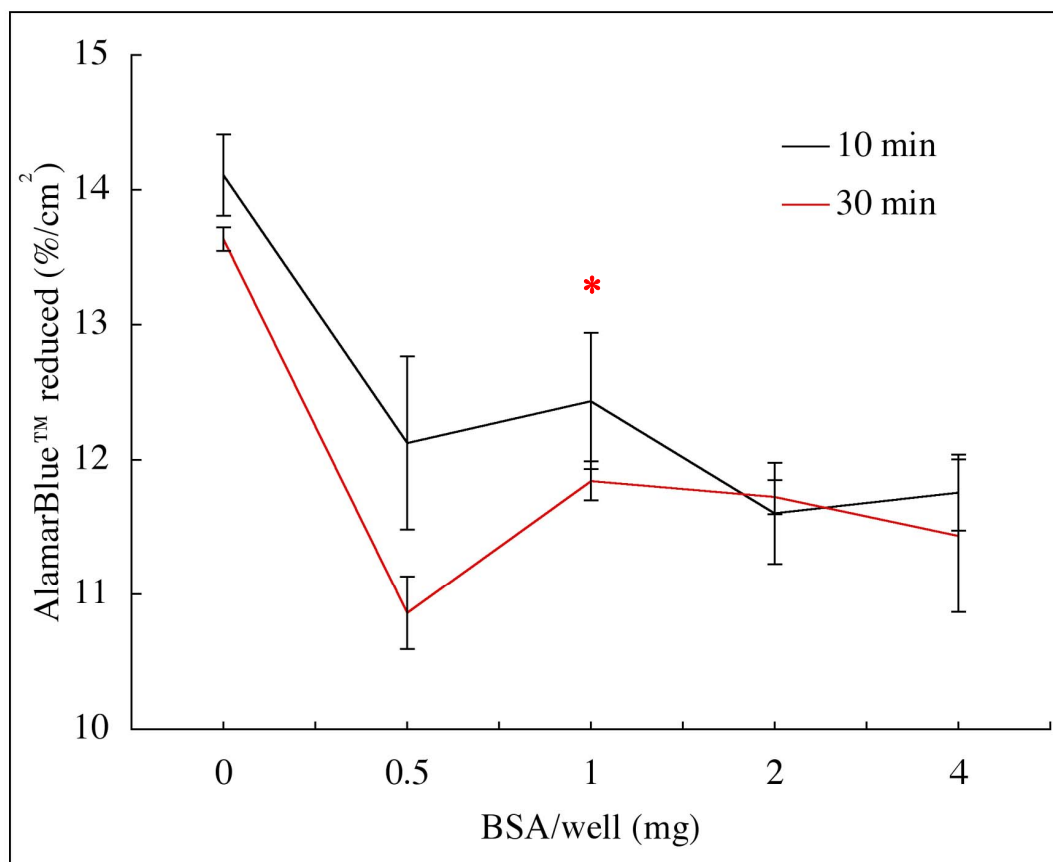


**Figure 1.52.** AlamarBlue™ reduced by MG63 cells attached to wells that were blocked with different amounts of BSA. The experiment was performed in a Nunc-Maxisorp™ 96-well plate blocked with 0-4 mg/well of BSA in a volume of 150  $\mu$ l for 1 h at 25°C. Cells were dislodged from the T75 culture flask in CDS. 100  $\mu$ l of  $6 \times 10^5$  MG63 cells/ml were incubated in the wells for 10 or 30 min. Cells that had not attached were removed from the wells in two PBS (pH 7.4) washes. FBS-free MEM (containing 100 units of penicillin and 100  $\mu$ g of streptomycin) was supplemented with 2 mg/ml of BSA. The attachment assay was performed under cell culture conditions. \* Indicates the position on the calibration curve at 1 mg/well of BSA that was used to block wells to reduce non-specific cell attachment in the experiment shown in **Figure 1.53**. The alamarBlue™ assay procedure is described on **page 42**.

Once again, a high density of cells attached to wells that were loaded with IGF-1 and not blocked with BSA. AlamarBlue™ was reduced by 27 %/cm<sup>2</sup> and 47 %/cm<sup>2</sup> after allowing cells to attach for 10 and 30 min, respectively (**Figure 1.53**). Conversely, only about 10 %/cm<sup>2</sup> of alamarBlue™ was reduced in wells loaded with IGF-1 and blocked with BSA (**Figure 1.53**). Also, the percentage of reduced alamarBlue™ was slightly higher in untreated wells (not treated with IGF-1 and not blocked with BSA) in comparison to wells blocked with BSA but not treated with IGF-1 (**Figure 1.53**). Therefore, although adsorbed BSA used at 1 mg/well was shown to inhibit non-specific cell attachment, the protein could not be used at this concentration as a blocking agent for reducing non-specific cell attachment in the p-ERK assay because the protein quenched the binding capacity of cells to IGF-1. A possible explanation is that the adsorbed BSA film covered IGF-1 ligand sites, preventing the binding of cell surface receptors. Nonetheless, a significant increase in MG63 cell attachment was detected in wells only treated with IGF-1 (no BSA) at both 10 and 30 min attachment times, in comparison to untreated wells in this study.

The response of 3T3 fibroblast cell attachment to IGF-1 on polystyrene was also examined. 3T3 cells were tested together with MG63 cells because the up-regulation of p-ERK in 3T3 cells had previously been successfully analysed using this particular p-ERK assay [199]. Similarly to MG63 cells, the attachment of 3T3 cells was also enhanced on polystyrene loaded with IGF-1 (**Figure 1.54**). After 10 min incubation (which in the experiment above was found to be a sufficient cell attachment time), the percentage of reduced alamarBlue™ was 43 %/cm<sup>2</sup> by 3T3 cells and 29 %/cm<sup>2</sup> by MG63 cells. In contrast, alamarBlue™ reduction was only 10 %/cm<sup>2</sup> and 7 %/cm<sup>2</sup>, respectively, in wells without adsorbed IGF-1 (**Figure 1.54**). This experiment showed that adsorbed IGF-1 could stimulate cell attachment on polystyrene for both MG63 and 3T3 cells.

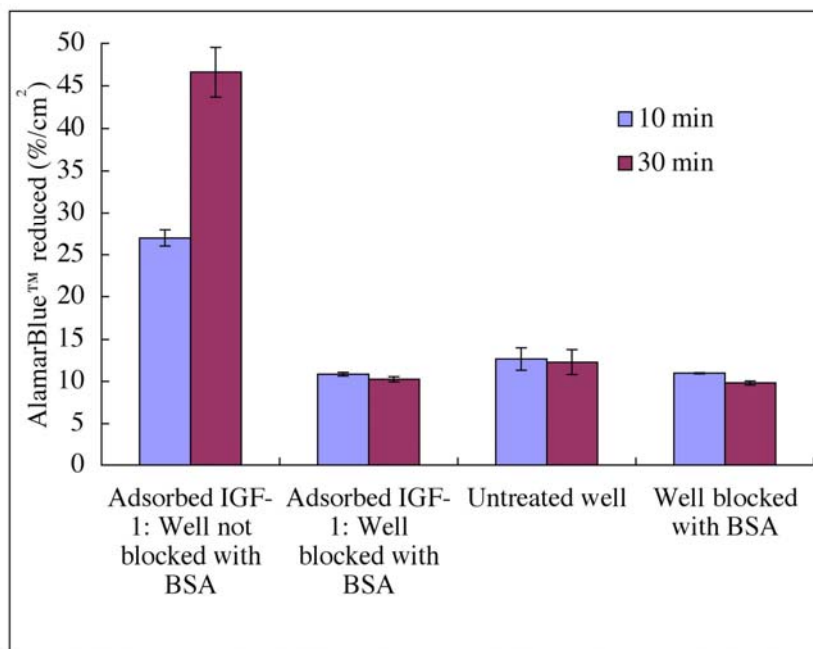


**Figure 1.53.** Percentage of alamarBlue™ reduced by MG63 cells after  $6 \times 10^5$  cells/ml (in a volume of 100  $\mu$ l) was incubated in wells of a 96-well Nunc-Maxisorp™ plate for 10 and 30 min. The wells were either left untreated (without IGF-1 or BSA), blocked with 1 mg of BSA (prepared in PBS in a volume of 150  $\mu$ l) for 1 h at 25°C, loaded with 600 ng of IGF-1 (prepared in 100  $\mu$ l of PBS) for 12 h at 25°C and loaded with IGF-1 and blocked with BSA. Cells were removed from the culture flask using CDS. FBS-free MEM (containing 100 units of penicillin and 100  $\mu$ g of streptomycin) was supplemented with 2 mg/ml of BSA. The attachment assay was performed under cell culture conditions. The alamarBlue™ assay procedure is described on **page 42**.

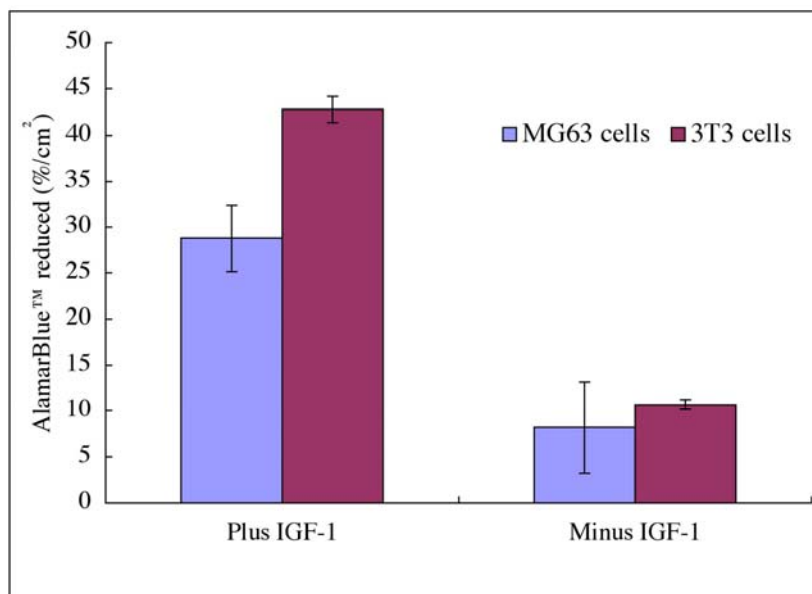


**Figure 1.54.** Percentage of alamarBlue™ reduced by MG63 and 3T3 cells attached to wells of a 96-well Nunc-Maxisorp™ plate in response to adsorbed IGF-1. The wells were incubated with 600 ng of IGF-1 in a volume of 100  $\mu$ l (prepared in PBS) (plus IGF-1) or incubated in PBS without IGF-1 (minus IGF-1) for 12 h at 25°C. 100  $\mu$ l of  $6 \times 10^5$  cells/ml were incubated in the wells for 10 min. Cells were diluted in FBS-free MEM (for MG63 cells) or FBS-free DMEM (for 3T3 cells) (containing 100 units of penicillin and 100  $\mu$ g of streptomycin). Both medium formulations were supplemented with 2 mg/ml of BSA. The attachment assay was performed under cell culture conditions. The alamarBlue™ assay procedure is described on **page 42**.

In the next experiment, the intracellular up-regulation of p-ERK in 3T3 and MG63 cells was compared after the cells had attached to polystyrene wells loaded with adsorbed IGF-1 (prepared in PBS) or to wells incubated in PBS with no IGF-1. The fluorescence signal was slightly higher for MG63 or 3T3 cells that attached to wells loaded with IGF-1 for 10 or 30 min compared to cells that had attached to wells not treated with IGF-1 for the same period of time (**Figure 1.55**). However, this difference was not significant. Therefore, an increase in the intracellular concentration of p-ERK induced by IGF-1 at the initial stage of cell attachment could not be detected in MG63 or 3T3 cells with this procedure. Similarly, no significant difference in the fluorescence signal was found for MG63 cells attached to IPTES and IGF-1 functionalised PECVD-Si-Ti compared to cells attached to IPTES functionalised PECVD-Si-Ti not treated with IGF-1 (data not shown). Therefore, the up-regulation of p-ERK induced by both adsorbed and covalently immobilised IGF-1 could not be detected in this study. This could be due to the reasons already discussed on **page 142**.

In a previous study, IGF-1 in solution was shown to induce the *in vitro* proliferation of MG63 osteoblast-like cells [200]. In the same article, IGF-1 was shown to act through the ERK signal transduction pathway. The authors demonstrated this by using an inhibitor of MEK, which is involved with the phosphorylation and activation of ERK (refer to **Figure 1.49 B**). IGF-1 was shown to enhance the proliferation of MG63 cells, but not when the growth factor was used in combination with the MEK inhibitor. Since the authors of this study demonstrated that IGF-1 does indeed up-regulate the ERK pathway, one more experiment was conducted to confirm those results for the MG63 cell line. This time, cells that were already growing on polystyrene were stimulated with IGF-1 in solution. In addition, the activity of IGF-1 was compared to FBS and a whey growth factor extract (WGFE) (supplied by TGR Biosciences Pty Ltd). FBS and WGFE were also tested because of their excellent growth-promoting properties [201-203].

Briefly, 200  $\mu\text{l}$  of  $1 \times 10^5$  3T3 or MG63 cells/ml were cultured in a 96-well TCPS microplate (Iwaki) for 12 h under cell culture conditions in medium supplemented with 10% (v/v) FBS. The medium was then decanted from the wells and the wells were washed with Hank's balanced salt solution (HBSS). The medium was then replaced with serum-free medium and the cells were serum-starved for 2 h. The agonist (IGF-1, FBS or WGFE) was added into the medium and incubated with the cells for 5, 10 or 15 min. The cells were then lysed and the p-ERK assay was performed according the manufacturers instructions. Refer to **pages 42-44** for a more detailed description.

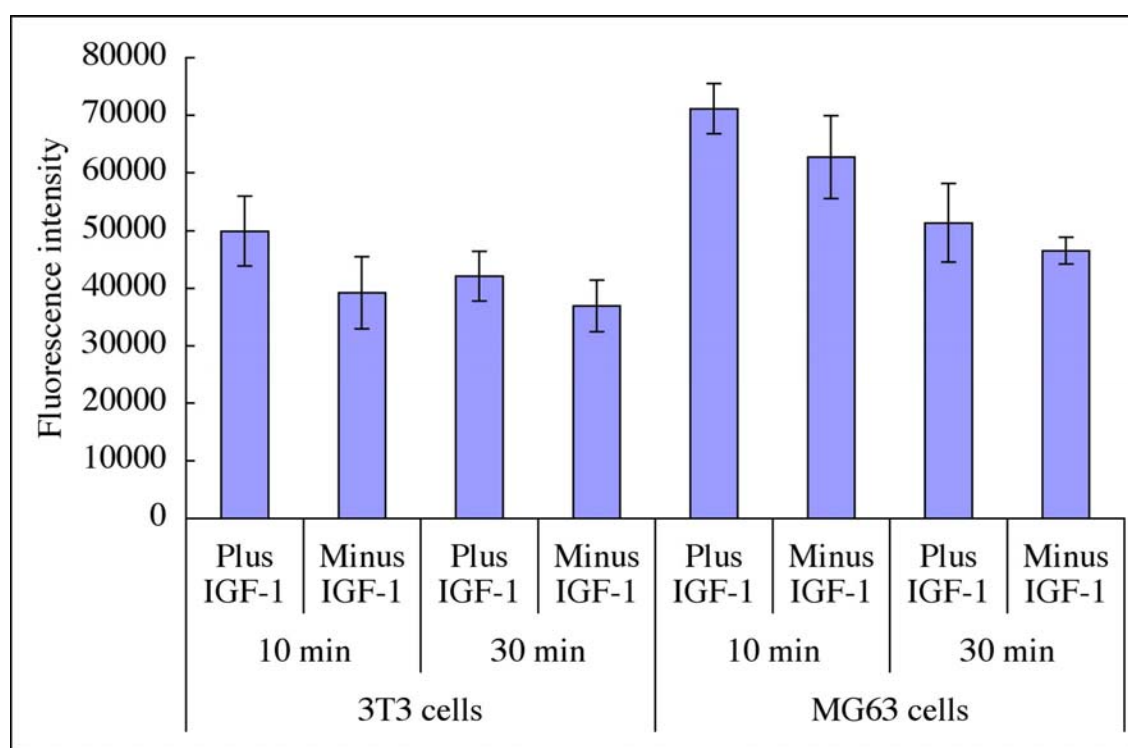


**Figure 1.55.** Results of an p-ERK assay performed in a 96-well Nunc-Maxisorp™ plate with wells containing 600 ng of adsorbed IGF-1 (prepared in 100  $\mu\text{l}$  of PBS, pH 7.4) for 12 h at 25°C (Plus IGF-1) and negative control wells incubated with PBS containing no IGF-1 (Minus IGF-1). MG63 and 3T3 cells were dislodged from a T75 tissue culture vessel (Iwaki) with the aid of CDS. 200  $\mu\text{l}$  of  $1 \times 10^5$  cells/ml in FBS-free MEM (for MG63 cells) or FBS-free DMEM (for 3T3 cells) (containing 100 units of penicillin, 100  $\mu\text{g}$  of streptomycin and 2 mg/ml of BSA) were seeded into the wells and allowed to attach for 10 or 30 min. The MAPK assay was performed using the AlphaScreen™ SureFire™ p-ERK assay kit from TGR BioSciences Pty Ltd. Refer to **pages 42-44** for a detailed description of the experimental protocol.

IGF-1, FBS and WGFE were all shown to stimulate the up-regulation of p-ERK in both MG63 and 3T3 cells (**Figure 1.56 A-F**). Elevated levels of p-ERK were observed after 5 min of incubating the cells with IGF-1, declining for longer exposure times (**Figure 1.56 A-B**). Similarly, MG63 and 3T3 cells stimulated by WGFE, exhibited elevated levels of p-ERK after 5 min of incubation with the agonist. However, in the case of WGFE, a pronounced decline in the fluorescence signal was not observed for 10 and 15 min incubation time periods (compare **Figure 1.56 C-D** to **A-B**). The multiple types of growth factors found in WGFE probably maintained ERK activity in cells over a longer time frame [202]. After stimulating cells with FBS, the maximum fluorescence signal (related to the concentration of p-ERK) was achieved after 5-10 min of incubation with FBS. Similarly to WGFE, the intracellular concentration of p-ERK remained elevated after incubating cells for 15 min with FBS (**Figure 1.56 E-F**). These results showed that IGF-1 stimulated the ERK signalling pathway in the first 5 min of binding the cell membrane receptor. Also, the activity of IGF-1 was shown to be comparable to other known mitogenic compounds (FBS and WGFE). After 15 min of incubation with IGF-1, no significant difference in fluorescence to the negative control was detected. In contrast, the result obtained for FBS and WGFE, showed that fluorescence remained well above the background level even after 15 min. Within the 5 min time frame required for strong ERK activation by IGF-1, a sufficient density of cells is unlikely to have attached to IGF-1/IPTES functionalised PECVD-Si-Ti samples. Therefore, the AlphaScreen™ SureFire™ assay could not be used to detect the biological activity of immobilised IGF-1 on the functionalised titanium samples.

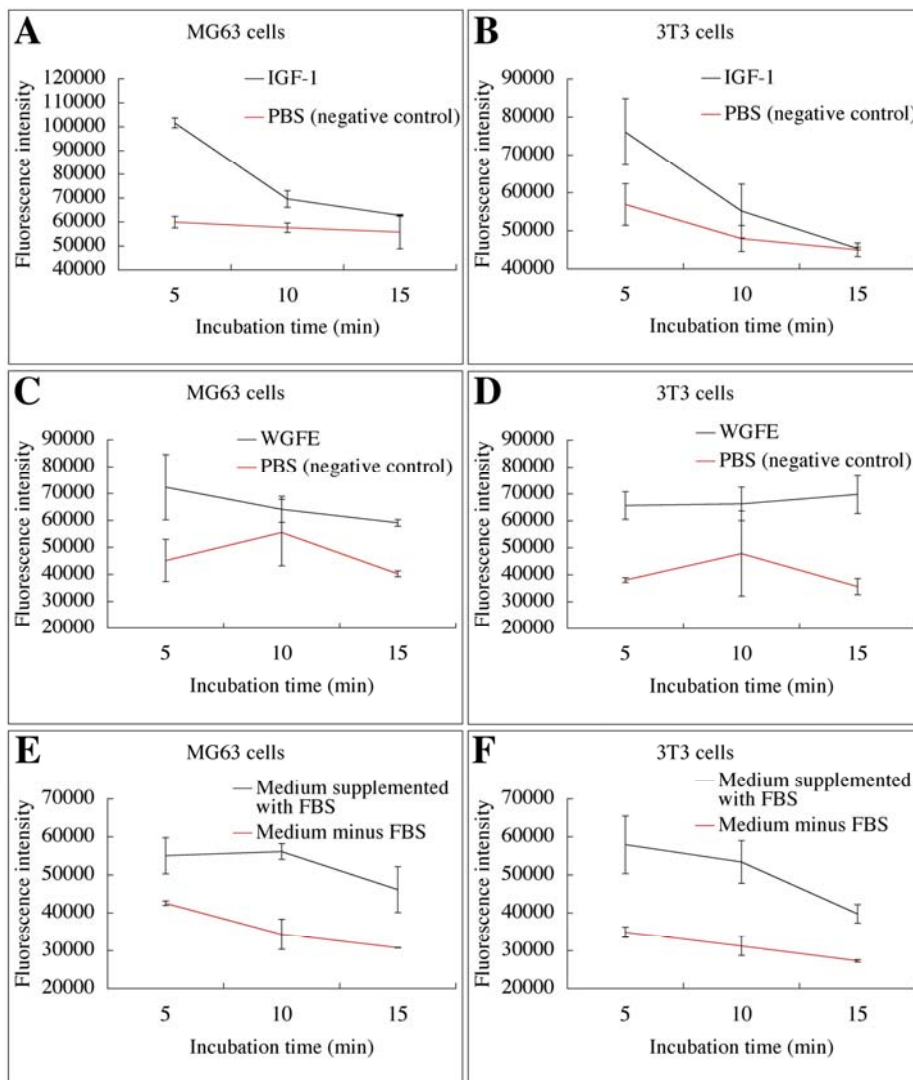


**Figure 1.56.** Results of a p-ERK assay performed using MG63 (**A**, **C**, **E**) and 3T3 (**B**, **D**, **F**) cells. 200  $\mu$ l of  $1 \times 10^5$  cells/ml (dislodged in CDS) were seeded into wells of a 96-well TCPS microplate (Iwaki) and were incubated for 12 h under cell culture conditions. The medium was decanted from the wells and the wells were washed twice with HBSS. 100  $\mu$ l of serum-free MEM (for MG63 cells) or DMEM (for 3T3 cells) was added to the wells and the cells were serum-starved for 2 h under cell culture conditions. 100  $\mu$ l of serum-free MEM or DMEM supplemented with 600 ng of IGF-1 (6  $\mu$ l of a 100  $\mu$ g/ml IGF-1/PBS stock solution added to 94  $\mu$ l of serum-free medium) (**A** and **B**), 4 mg/ml of WGFE (10  $\mu$ l of a 40 mg/ml WGFE/PBS stock solution added to 90  $\mu$ l of serum-free medium) (**C** and **D**) and 20% (v/v) FBS (to achieve a final serum concentration of 10% v/v) (**E** and **F**) was added to the 100  $\mu$ l serum-free medium already in the wells. Alternatively, 94 or 90  $\mu$ l of serum-free medium spiked with 6 or 10  $\mu$ l of PBS was used as negative control solutions for IGF-1 (**A** and **B**) and WGFE (**C** and **D**) samples or undiluted serum-free MEM or DMEM was used as a negative control for the FBS (**E** and **F**) samples. The cells were incubated with the test solutions for 5, 10 and 15 min before the cells were lysed and analysed using the AlphaScreen™ SureFire™ p-ERK assay kit according to the manufacturer's instructions. Refer to **pages 42-44** for more detail.

Although the up-regulation of p-ERK could not be detected in cells during the initial cell attachment phase on surfaces functionalised with IGF-1, the preliminary alamarBlue™ attachment experiments that were conducted for developing the p-ERK assay did show that IGF-1 could specifically stimulate cellular attachment. This was seen as an increase in the percentage of alamarBlue™ reduced by cells that had attached to polystyrene wells loaded with adsorbed IGF-1 compared to wells not loaded with IGF-1 at the early stages of cell attachment (10 and 30 min) (refer to **Figure 1.51** and **1.53-1.54**). Instead of analysing cell attachment indirectly by comparing the concentration of alamarBlue™ reduced by cells attached on the substrate surface, attached cells were stained and imaged by fluorescence microscopy.

In this cellular attachment experiment, MG63 cells were diluted in FBS-free MEM and were allowed to attach onto the substrate surfaces for 30 min. After removing cells that had not adhered or were loosely attached, the cellular nuclei were stained with a Hoechst 33342 nuclear dye (Molecular Probes). Cell attachment was compared between IPTES functionalised PECVD-Si-Ti loaded with covalently tethered IGF-1 and IPTES functionalised PECVD-Si-Ti loaded with adsorbed IGF-1 (refer to **Scheme 1.10**). IGF-1 was immobilised on the surfaces for 2 and 12 h time periods and the unreacted isocyanate groups were quenched with ethanolamine hydrochloride. This experiment was performed to determine if cell attachment is indeed enhanced on PECVD-Si-Ti by functionalising the surface with IGF-1 through a covalent attachment mechanism.

As anticipated, cells attached at a higher density on IPTES functionalised PECVD-Si-Ti that was loaded with covalently attached IGF-1 in comparison to IPTES functionalised PECVD-Si-Ti not treated with IGF-1 or loaded with adsorbed IGF-1 (**Figure 1.57 A-F**). This conspicuously showed that cell attachment could be improved on PECVD-Si-Ti by functionalising the surface with IGF-1 through a covalent attachment mechanism. A higher density of cells attached on IPTES functionalised PECVD-Si-Ti that had been reacted with IGF-1 for 12 h compared to the same surface reacted with IGF-1 for 2 h (compare **Figure 1.57 A to C**). This result was interesting because it showed that a longer incubation time (of 12 h in comparison to 2 h) was required to achieve a higher surface concentration of

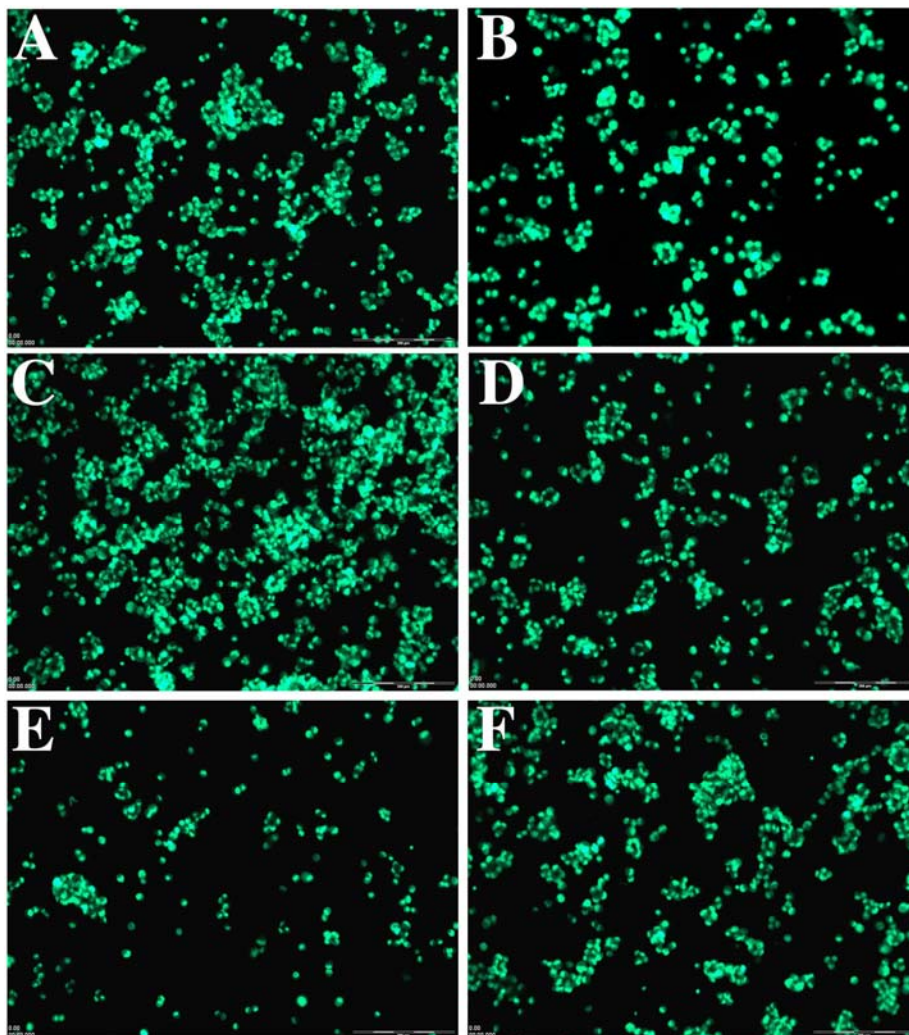


**Figure 1.57.** Fluorescence micrographs of Hoechst 33342 stained MG63 cells attached to IPTES functionalised PECVD-Si-Ti. Samples were loaded with 600 ng of IGF-1 (prepared in PBS) for 2 h (A) or 12 h (C) or incubated in PBS (without IGF-1) for 2 h (B) or 12 h (D). Any unreacted isocyanate groups were then quenched using 1 mM of ethanolamine hydrochloride (prepared in PBS) for 30 min. Additionally, IGF-1 was adsorbed on IPTES functionalised PECVD-Si-Ti with quenched isocyanate groups (by incubating in 1 mM of ethanolamine hydrochloride for 30 min) for 2 h (E) and 12 h (F). MG63 cells were dislodged from a T75 tissue culture vessel (Iwaki) in CDS.  $1 \times 10^5$  MG63 cells/ml were diluted in FBS-free MEM (containing 100 units of penicillin and 100  $\mu$ g of streptomycin) supplemented with 2 mg/ml of BSA. 1 ml of cells was added to each well of a 12-well TCPS plate containing the test samples and the cells were incubated in the wells for 30 min. Cells that had not attached were washed from the substrate surface in two PBS (pH 7.4) washes. The wells were replenished with FBS-free MEM supplemented with 2 mg/ml of BSA and 0.01 mg/ml of Hoechst 33342 (Molecular Probes) nuclear dye. After 1 h, the samples were washed twice in PBS. The images shown are a compilation of 5 superimposed images taken on 5 separate random areas on each sample. Scale bars = 200  $\mu$ m. Images were taken and processed as described on pages 44-45.

biologically active immobilised IGF-1 molecules (from a reaction solution containing the same concentration of IGF-1 protein) on IPTES functionalised PECVD-Si-Ti, assuming that cell attachment was mainly mediated by the growth factor. Therefore, the performance of the PECVD-Si-Ti biomaterial towards promoting cell attachment could be further enhanced by immobilising IGF-1 on the surface for a longer time period of 12 h compared to 2 h.

So far the data indicated that attachment of MG63 cells could be stimulated on PECVD-Si-Ti by functionalising the surface with a cellular attachment cue (IGF-1). As a final measure of characterising the attachment cells on PECVD-Si-Ti functionalised with IGF-1, the cytoskeletal structure of MG63 cells was examined at the early stages of cell attachment by analysis of filamentous actin (F-actin) structure. Previously, the reorganisation of actin has been studied in cells stimulated with a range of biological compounds including growth factors, kinases and hormones [204-206]. Furthermore, important information can be obtained on the biomaterial's cell adhesion properties because the early arrangement of the cellular cytoskeleton provides direct information of the cell-substrate interface [185, 207]. For example, Thian et al. examined the actin cytoskeleton of human osteoblast-like (HOB) cells cultured on titanium coated with silicate-substituted HA [208]. In this study, the authors found that HOB cells grown on silicate-substituted HA formed more ordered and elongated actin filaments in comparison to HOB cells grown on HA alone (not substituted with silicate). Furthermore, a higher rate of cell growth and enhanced biomineralisation was detected on silicate-substituted HA compared to HA alone. The authors proposed that these effects were caused by silicate-substituted HA (compared to HA alone) promoting a higher level of protein adsorption (in particularly extracellular matrix proteins) resulting in differences between the interaction of cellular integrins and the adsorbed protein molecules on the surface of the various coatings. When proteins bind cell surface integrin receptors, actin filaments undergo conformational changes due to mechanical stresses exerted by the integrins through the plasma membrane and consequently trigger specific signals, which regulate cellular activity. Therefore, an indication of cell function (such as adhesion, proliferation, differentiation) can be derived by organisation of the cell's actin structure. In

summary, this article showed that the difference in the organisation of the cell's actin structure is correlated with differential cellular behaviour.

In a separate investigation, Gronowicz et al. studied cell attachment of osteoblast-like cells on orthopaedic implant materials [209]. The authors analysed integrin-mediated cell attachment on both titanium and cobalt-chromium alloyed implant surfaces. Cell attachment was inhibited both on titanium (by 28%) and cobalt-chromium (by 40%) alloyed surfaces when the cellular integrin receptors were blocked by means of RGD in solution. Blocking the fibronectin cell receptor reduced cell attachment by 63% and 49% on the titanium and cobalt-chromium alloyed surfaces, respectively. Cell spreading was similar on the both alloys, however, F-actin stress fibers were more evident on the cobalt-chromium alloy and the fibers formed a more angular shape on the alloy compared to the titanium alloy. Therefore, this studied showed that the substrate material can also significantly influence cell attachment and consequently cell differentiation and bone formation.

In our present study, the F-actin of MG63 cells at the early stages of cell growth on the substrate surface was visualised by staining F-actin with Alexa Fluor<sup>®</sup> 594 phalloidin fluorescence probe (Molecular Probes) and counterstaining the cellular nuclei with Hoechst 33342 before imaging the cells by fluorescence microscopy. In this experiment the cytoskeletal structure of MG63 cells was compared between non-functionalised PECVD-Si-Ti, IPTES functionalised PECVD-Ti-Si loaded with covalently attached IGF-1 (for 12 h at 25°C), IPTES functionalised PECVD-Ti-Si incubated in PBS (for 12 h at 25°C), untreated TCPS and TCPS loaded with adsorbed IGF-1 (for 12 h at 25°C). IGF-1 was adsorbed or covalently linked to the samples for 12 h (instead of 2 h) because this reaction time produced a more significant response to cell attachment (refer to **Figures 1.51** and **1.57**).

No difference in F-actin structure of MG63 cells was observed on TCPS loaded with adsorbed IGF-1 compared to TCPS that had not been incubated with IGF-1 (**Figure 1.58 A** and **B**). MG63 cells on both samples exhibited mesh-like F-actin structure, which protruded

well out from the cellular nuclei. Therefore, MG63 cells appeared to adhere equally well on TCPS and TCPS treated with IGF-1 after 4 h of cell culture. Although cell attachment was improved by adsorbing IGF-1 on polystyrene (refer to **Figures 1.51** and **1.53-1.54**) the extracellular matrix proteins produced by the MG63 cells spread equally well on TCPS loaded with or without IGF-1 after 4 h of cell culture because the commercial TCPS used in this study was surface-modified for promoting the adsorption of extracellular matrix proteins. This enabled cellular integrins, which link the extracellular matrix to the actin cytoskeleton, to transmit comparable mechanical forces across the cell membrane inducing cells to form a similar F-actin structure.

However, F-actin spreading was not as significant on PECVD-Si-Ti (**Figure 1.58 E**). F-actin appeared localised around the cellular nuclei and irregular in shape. Also, a lower density of cells was observed on this surface in comparison to the other samples tested in this experiment (compare **Figure 1.58 E** to **A-D**). This showed that cells adhered poorly on PECVD-Si-Ti, which confirms the cell culture assay results shown in **Figures 1.42** and **1.44**. F-actin spread more on IPTES functionalised PECVD-Si-Ti (having isocyanate groups quenched by ethanolamine hydrochloride) (compare **Figure 1.58 D** to **E**). This result was probably due to the adsorption of extracellular matrix proteins during cell adhesion being enhanced on IPTES functionalised PECVD-Si-Ti in comparison to non-functionalised PECVD-Si-Ti because of the change in surface hydrophilicity as discussed on **page 123**. However, F-actin did not spread as well on IPTES functionalised PECVD-Si-Ti compared to TCPS suggesting the surface could still be further improved for cell growth (compare **Figure 1.58 B** to **D**). This result corresponded well with a slightly lower level of MG63 cell growth detected on IPTES functionalised PECVD-Si-Ti (not reacted with IGF-1 but having isocyanate groups quenched by ethanolamine hydrochloride) compared to TCPS in serum-free medium after 72 h of cell culture (refer to **Figure 1.46**). Cell adhesion was further improved by functionalising the surface with IGF-1 through a covalent attachment mechanism (compare **Figure 1.58 C** to **D**). MG63 cells showed very similar F-actin patterns on TCPS loaded with adsorbed IGF-1 compared to IPTES functionalised PECVD-Si-Ti reacted with IGF-1 (compare **Figure 1.58 A** to **C**). Therefore, it is plausible that immobilised IGF-1 plays an important role in modulating the cytoskeletal organisation of

osteoblast cells during cell adhesion on PECVD-Si-Ti. Furthermore, IGF-1 could also become an important factor in regulating the motility of cells during bone remodelling processes on PECVD-Si-Ti because changes in the F-actin cytoskeleton influence cellular motility [207].

In summary, IGF-1 in solution induced the up-regulation of p-ERK in MG63 cells after exposing the cells to the growth factor for 5 min. But up-regulation of p-ERK activity was not detected in MG63 cells during the cellular attachment phase on samples functionalised with immobilised IGF-1. One possibility is that the ERK pathway may be up-regulated in MG63 cells by integrin-mediated autophosphorylation of kinases during the cell attachment phase in the absence of IGF-1. Alternatively, the correct experimental conditions (cell density, reaction time, medium formulation etc) were not identified in this study. However, cell attachment and adhesion were both enhanced on PECVD-Si-Ti surfaces functionalised by covalently attached IGF-1. Therefore, IGF-1 may be a key factor for enhancing bone formation on PECVD-Si-Ti implants.

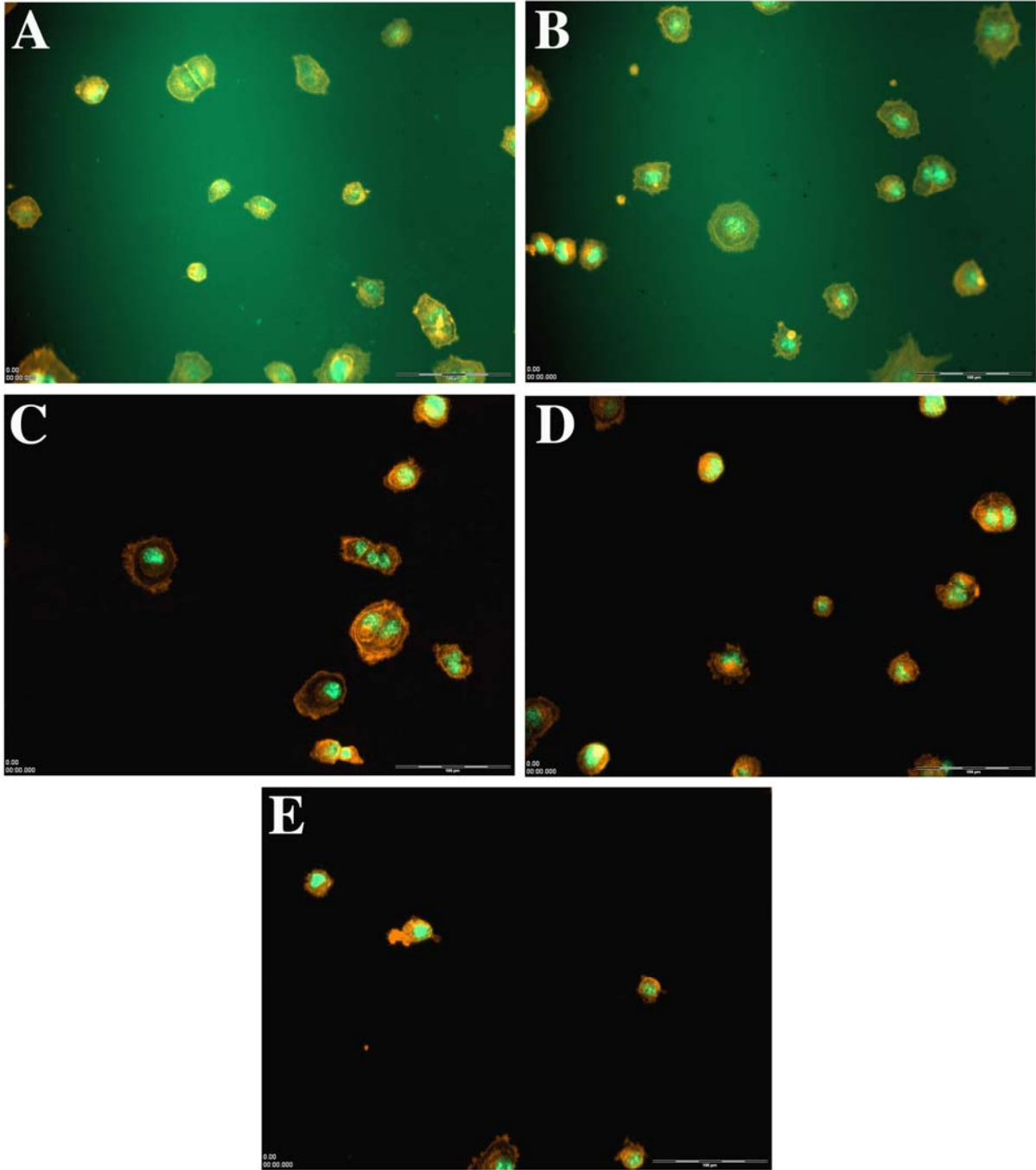


Figure 1.58. Refer to following page (page 160).

**Figure 1.58.** Fluorescence micrographs of MG63 cellular F-actin (orange) and nuclei (green). MG63 cells were removed from a T75 tissue culture flask (Iwaki) in CDS. The cells were resuspended in FBS-free MEM (containing 100 units penicillin and 100 µg of streptomycin) supplemented with 2 mg/ml of BSA. 1 ml of  $4 \times 10^4$  cells/ml were seeded onto the substrates in 12-well TCPS plates (Nunc) for 3 h. Then, cells that had not attached or were loosely attached were removed from the substrate surface in two PBS (pH 7.4) washes. The wells were replenished with FBS-free MEM supplemented with 2 mg/ml of BSA and 0.01 mg/ml of Hoechst 33342 (Molecular Probes) DNA minor groove binder. After a further 1 h of cell culture, the samples were washed twice in PBS. The cells were fixed in 4% formaldehyde for 10 min at 25°C and the samples were washed twice in PBS. The cells were then stained with an Alexa Fluor<sup>®</sup> 594 phalloidin fluorescence probe (Molecular Probes) according to the manufacturers instructions (refer to **pages 44-45**). Sample descriptions: TCPS incubated with 600 ng of IGF-1 in 300 µl of PBS for 12 h (**A**) or incubated in PBS (without IGF-1) for 12 h (**B**) at 25°C; IPTES functionalised PECVD-Si-Ti incubated with 600 ng of IGF-1 in 300 µl of PBS for 12 h (**C**) or incubated in PBS (without IGF-1) for 12 h (**D**) at 25°C (any unreacted isocyanate groups were then quenched using 1 mM of ethanolamine hydrochloride (prepared in PBS) for 30 min at 25°C); and untreated PECVD-Si-Ti (**E**) (refer to **pages 30, 32-35, 41** for more detailed descriptions of sample preparation). Images were taken and processed as described on **pages 44-45**. The light green background in **A** and **B** is attributed to autofluorescence from the TCPS disc. Scale bars = 100 µm.

## 1.4 Conclusions and Future Directions

PECVD-Si has previously been coated on titanium implants for improving the integration of the implant with bone. Titanium implants coated with PECVD-Si (PECVD-Si-Ti) exhibit a 1.6-fold increase of direct bone/implant contact (the area of the implant in contact with bone in comparison to soft tissue) compared to uncoated titanium implants. In contrast to the high level of bioactivity of PECVD-Si-Ti (compared to uncoated titanium) *in vivo*, the growth of MG63 osteoblast-like cells on uncoated titanium was 7-fold to that on PECVD-Si-Ti *in vitro*. Therefore, in an attempt to further enhance the integration process of PECVD-Si-Ti implants with bone, Part 1 of this thesis aimed to improve cellular growth on PECVD-Si-Ti by functionalising the surface with a bioactive factor, IGF-1.

First we showed that the PECVD-Si coatings strongly adhered to titanium substrates (by withstanding pull-off loads in excess of 27 MPa) and were resistant to delamination in relatively harsh conditions (toluene at 120°C). We also showed that the PECVD-Si surface was highly hydrophilic (contact angle  $< 10^\circ$ ) and mainly contained SiO<sub>2</sub>. Alkoxysilanes were next grafted on PECVD-Si-Ti using different reaction temperatures and times, silane concentrations and solvent systems. Generally, the grafting density of silane molecules was increased when the reaction temperature and time was increased. Also, the grafting density of APTES was significantly higher in anhydrous toluene (3.9-fold) in comparison to aqueous medium. Depending on the grafting method employed, 66-99% of the APTES siloxane films was retained on PECVD-Si-Ti after incubation in PBS at 37°C indicating that the siloxane films were stable under aqueous physiological conditions.

We used the grafting conditions developed for producing siloxane films on PECVD-Si-Ti for functionalising the surface with IPTES. IGF-1 was covalently immobilised on IPTES functionalised PECVD-Si-Ti through isocyanate-amino chemistry. The growth factor was shown not only to retain its immunological reactivity on IPTES functionalised PECVD-Si-Ti, but also the immunological reactivity of IGF-1 was 5-fold on this sample in comparison

to when the growth factor was covalently immobilised on IPTES functionalised uncoated titanium.

IGF-1 was also shown to be biologically active when covalently immobilised on IPTES functionalised PECVD-Si-Ti. After 72 h of *in vitro* MG63 cell culture in serum-free medium, cell growth was 1.9-fold on IPTES functionalised PECVD-Si-Ti with covalently bonded IGF-1 compared to IPTES functionalised PECVD-Si-Ti with no IGF-1 (isocyanate reactive groups were quenched with ethanolamine hydrochloride). The attachment and adhesion of MG63 cells were also enhanced on PECVD-Si-Ti by the covalently immobilised IGF-1. However, no improvement in the attachment and proliferation of MG63 cells was shown for IPTES functionalised PECVD-Si-Ti loaded with covalently immobilised IGF-1 compared to IPTES functionalised PECVD-Si-Ti with no IGF-1 in serum-containing medium. Therefore, we assume that the adsorption of human serum proteins on the PECVD-Si-Ti implant *in situ* would also quench the biological activity of IGF-1 towards promoting cellular growth. However, we do not exclude the possibility that the bone-implant integration process could be further enhanced on PECVD-Si-Ti implants by covalently immobilising IGF-1 to the surface. This could occur by IGF-1 stimulating other cellular pathways of osteoblastic cells such as the secretion of extracellular matrix proteins, which become mineralised during bone formation.

For future work, it would be worthwhile investigating the surface concentrations of IPTES and IGF-1 required for achieving optimal mineral deposition from osteoblastic cells on bioactive PECVD-Si-Ti *in vitro* and then testing these implants *in vivo* to determine if implant-bone integration is enhanced by the surface modifications. Also, it would be interesting to measure and compare the kinetics of adsorption and covalent attachment of IGF-1 on PECVD-Si-Ti and uncoated titanium. This study could be used to determine why covalently immobilised IGF-1 is more immunologically active on PECVD-Si-Ti compared to uncoated titanium. Furthermore, we only tested the biological activity of one immobilised bioactive molecule (IGF-1) on PECVD-Si-Ti at this stage of the research. Therefore, it would be worthwhile investigating the bioactive properties of PECVD-Si-Ti implants functionalised with multiple bioactive species (such as vitronectin and IGF-1),

which can stimulate several biological pathways on the implant surface in concert. To test whether transmembrane signalling is upregulated in osteoblasts by tethered IGF-1, an alternative approach to the solid support system could be to test if IGF-1 bioconjugated titanium microspheres or particles upregulate p-ERK in cells. This experiment could be performed in a similar way as used for soluble IGF-1, which was shown to enhance ERK activation in cells. Finally, we believe that by further optimising the bioactive surface properties of PECVD-Si-Ti implants and continuing investigations of bone-implant integration processes, a new generation of orthopaedic implants will be developed with superior osseointegration rates.

## **Part 2:**

**Covalent immobilisation of anti-human IgG on porous silicon for the detection of human IgG by reflective interferometry**

## 2.1 Introduction

### 2.1.1 Overview of porous silicon applications

Porous silicon has captured the attention and imagination of many materials scientists over the last few decades. The material has been shown to possess unique photoluminescence and a range of other optical properties in solution or air and the properties have been extensively characterised [1-8]. The foundations laid from the early work on porous silicon have led to the development of new silicon-based technologies such as novel optoelectronic devices [9-10]. However, porous silicon is far from being limited to electronics. Porous silicon-based devices are now used in numerous applications including biomaterials, biosensors and catalytic micro-reactors [4(a-b), 11-17]. This part of the thesis will focus on the application of porous silicon for the development of optical biosensors. First, the manufacturing process of this versatile material will be described.

### 2.1.2 Porous silicon formation

Porous silicon is most commonly formed from conductive, polished silicon by electrochemically etching in an electrolyte (also referred to as anodisation). The reaction can be performed in a simple electrochemical set-up shown in **Figure 2.1**. A silicon piece is placed on the bottom of the cell: an O-ring seals the polished side and the underside is contacted by aluminium foil. The polished side of the silicon wafer (anode) becomes immersed in the electrolyte and a platinum electrode serves as a counter electrode (cathode). The silicon material is typically doped with boron (p-type) or either phosphorous or arsenic (n-type) to increase conductivity. The electrochemical reaction on n-type silicon is catalysed by light that allows patterns of porous silicon islands to be made by illuminating the surface with white light through a patterned mask during the etching procedure (**Figure 2.2**) [18-19]. Typically, the composition of the electrolyte includes hydrofluoric acid (HF) and an organic solvent such as ethanol. HF is essential for the dissolution of generated oxidised silicon species and the alcohol increases the wettability of the substrate surface, which facilitates HF penetration into

the pores and also helps remove attached hydrogen bubbles (that are generated during anodisation) from the substrate surface.

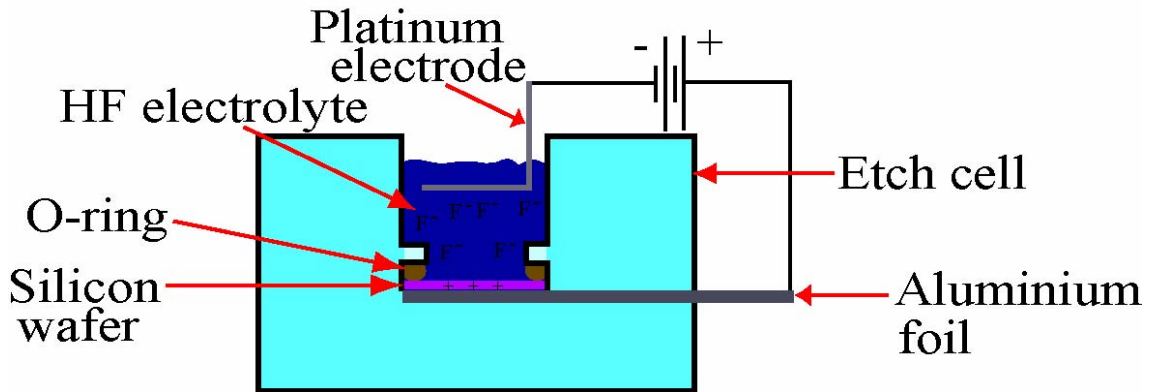


**Figure 2.1.** Schematic of a typical electrochemical set-up that can be used to prepare porous silicon.

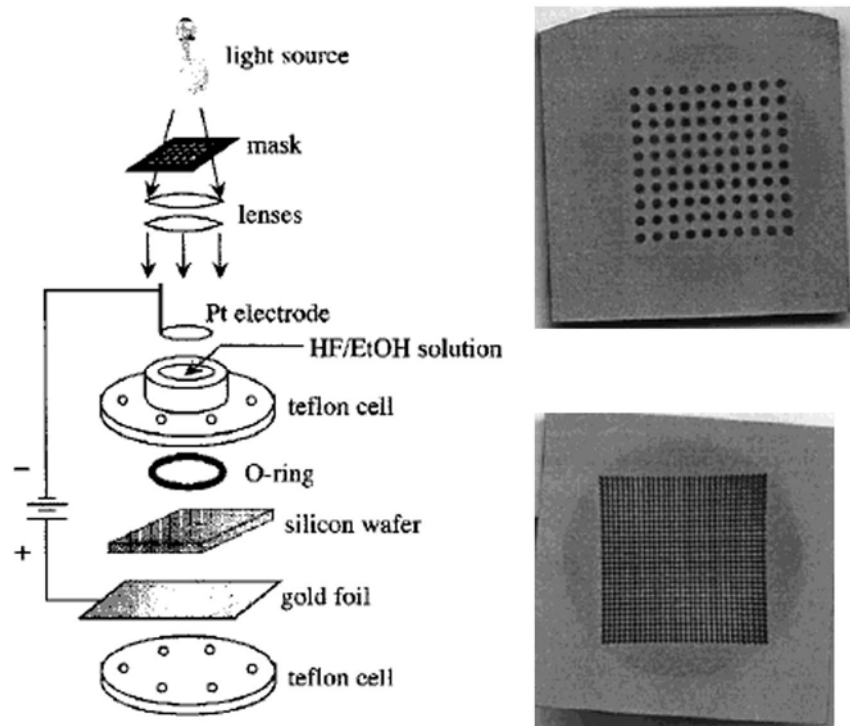
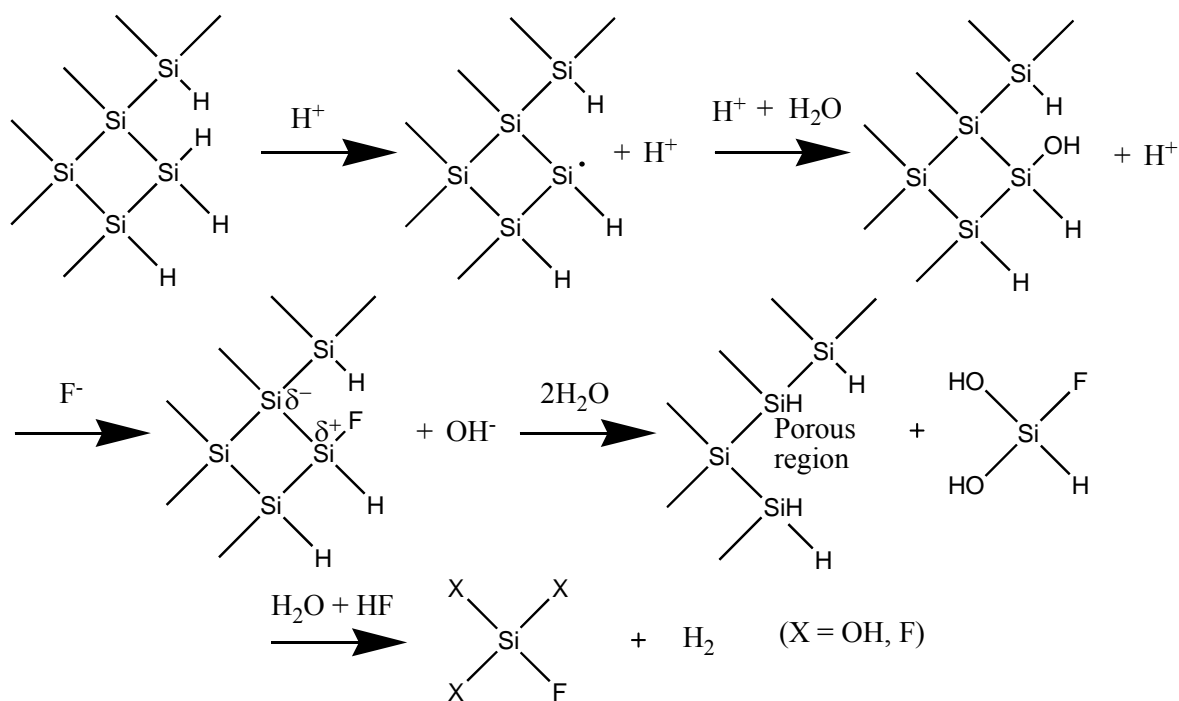


**Figure 2.2.** An apparatus that is used for preparing patterned porous silicon from n-type silicon is shown on the left. A patterned porous silicon wafer with an array of 100 individual porous silicon islands is shown in the upper right hand corner and a higher density array is shown below on a wafer patterned with 1000 porous silicon spots. Illustration and photographs were adapted from Lewis et al. and Shen et al. [18-19]. EtOH denotes ethanol.

Pore formation is understood to begin at the defect sites ('holes') at the surface of silicon. The accepted theoretical reaction mechanism for pore formation (silicon dissolution) is shown in **Scheme 2.1** [4(c), 20-22]. This reaction requires a faster rate of fluorine substitution (Si-H conversion to Si-F) than hydrolysis (Si-H conversion to Si-OH) at the initial stages of etching. After fluorine substitution, the polarised Si-Si back-bonds become broken by subsequent attack from more HF and water molecules, generating a porous silicon hydride surface and hydrogen bubbles. The SiF<sub>4</sub> species liberated from the surface become converted to H<sub>2</sub>SiF<sub>6</sub> by the remaining HF molecules and this complex finally forms a water-soluble [SiF<sub>6</sub>]<sup>2-</sup> ion and 2H<sup>+</sup> that can be washed from the substrate surface.



**Scheme 2.1.** Proposed reaction mechanism for porous silicon dissolution in aqueous HF. The scheme was adapted from Allongue [4(c)].

### 2.1.3 Porous silicon pore geometries

Pore sizes made by the electrochemical etching procedure have been reported from below 10 nm to over 1  $\mu\text{m}$  in diameter (**Figure 2.3**) [23-24]. The pores, which are generally classified in terms of geometry (diameter), can be categorised as micropores (Avg.  $\phi \leq 2$  nm; shown in **Figure 2.3 A**), mesopores (Avg.  $\phi = 2$ -50 nm; shown in **Figure 2.3 B**) or macropores (Avg.  $\phi > 50$  nm; shown in **Figure 2.3 C-E**). Well-defined pore sizes can be obtained by simply adjusting the applied current density. By keeping the current density constant, the depth of the porous layer can simply be controlled by varying the etching time (charge density) [4(d)]. An increase in current density results in an increase in the flow of negatively charged fluoride ions to the positively charged silicon surface and pore corrosion is accelerated. This results in larger pores being formed compared to those at a lower current density. At a higher charge density, the Si-Si back-bonds are attacked for a longer period of time, resulting in a deeper porous layer. There is an upper limit to pore size, which is reached when the current density enters the electro-polishing regime. The available pore size range depends on a range of factors including the applied current and charge density, dopant type and level, the crystal face, the electrolyte concentration and the nature of the organic solvent [25].

Many different types of porous silicon networks can be manufactured by judicious variation of the electrochemical-etching procedures. The architecture of the porous network formed is also dependent on the applied current and charge density as well as on the material type (dopant type, concentration of dopant and surface orientation of the crystalline silicon) and electrolyte composition [4(d), 25]. Some of these, which are shown in **Figure 2.4 A-C**, include independent single channels, branched and multi-layered porous networks [23,26-27]. Furthermore, the porous films can be removed from the silicon substrates as whole porous silicon membranes or in the form of small porous silicon particles [28-30]. These diverse forms of porous silicon offer exciting new approaches for developing new biosensors, biomaterials and other devices. As a specific example, Coffey et al. demonstrated the biomedical application of porous silicon microparticles by developing new forms of porous silicon-based biodegradable biomaterials [31].

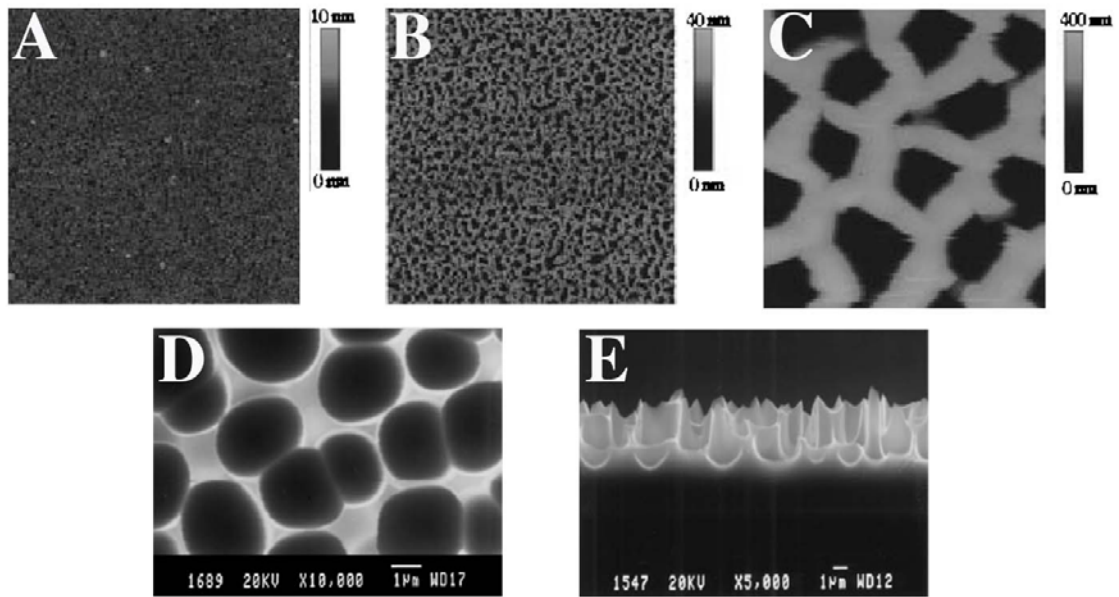


**Figure 2.3.** Micrographs of porous silicon generated by electrochemically anodising p-type silicon with a crystal orientation of (100). Atomic force microscopy (AFM) step-height images ( $5 \mu\text{m}^2$ ) of porous silicon are shown in the top row, illustrating surfaces with micropores (A), mesopores (B) and macropores (C). These surfaces were generated from  $0.0001 \Omega\cdot\text{cm}$  silicon in a 25% ethanolic HF solution at current densities of 295, 370 and  $600 \text{ mA}/\text{cm}^2$ , respectively, and to a constant charge of  $4.5 \text{ C}/\text{cm}^2$  (Images were adapted from Janshoff et al.) [23]. Below are scanning electron micrographs of larger ( $\sigma > 1 \mu\text{m}$ ) macropore types showing a top view (D) and a cross-sectional perspective (E). Porous silicon was formed from  $10 \Omega\cdot\text{cm}$  silicon in an aqueous HF solution supplemented with acetonitrile, at a current density of  $10 \text{ mA}/\text{cm}^2$  and a charge density of  $18 \text{ C}/\text{cm}^2$ . These images were adapted from Ponomarev et al. [24].

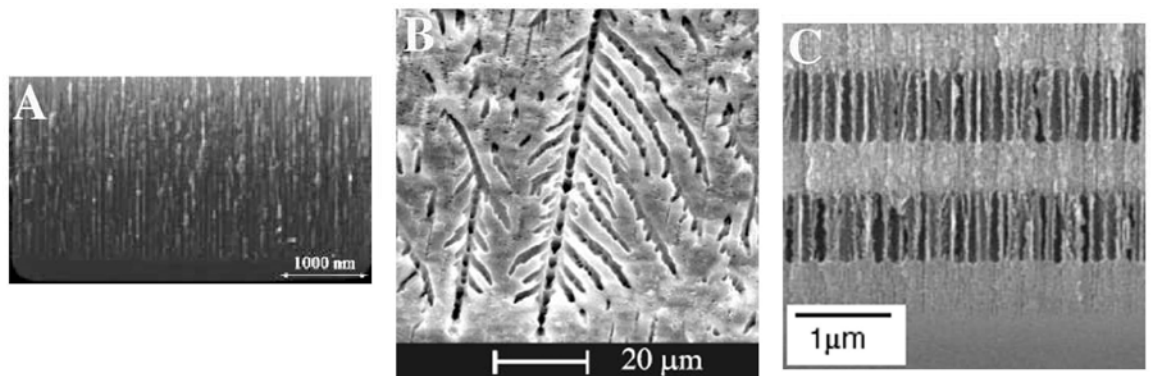


**Figure 2.4.** Scanning electron cross-sectional micrographs of different porous silicon networks achieved through electrochemical anodisation procedures. Single-channelled, vertically oriented pores obtained from p-type silicon are shown in (A); an example of branched pore formation from n-type silicon is shown in (B); and a porous silicon sample with alternating layered porous networks manufactured from n-type silicon is shown in (C). These images were adapted from Janshoff et al. (A), Föll et al. (B) and Ouyang et al. (C) [23, 26-27].

#### 2.1.4 Biosensors made from porous silicon

New biosensors and other sensing devices have also been constructed from porous silicon [16, 23, 32-33]. These biosensor platforms can produce optical signals (photoluminescence or interferometric reflectance changes) that are generated from the porous silicon surface from events such as chemical or biomolecule recognition and these signals form the readout of the sensing device. Other types of biosensors have become useful for biomedical and environmental applications such as monitoring health conditions, food and water quality, agricultural pesticides and water and air-borne contaminants [34-36]. Ideally, these biosensors should be adaptable for *in situ* use, offer a suitable sensitivity range and specificity for a given biomolecular target, produce a quick and easily interpretable signal, be compact in design and be relatively inexpensive. Of course, most of the published biosensor platforms can usually be improved in some of these areas. Therefore, continuing the research in this field is appropriate and developing new and improved biosensors is desirable.

#### 2.1.5 Functionalisation of porous silicon biosensors

For some porous silicon-based sensors, the substrate surface layer is left hydride-terminated (Si-H) [37]. In other cases, a thin oxide (Si-O<sub>x</sub>) is generated [38-39]. For yet other applications, the surface may require some surface modification, usually with a thin functional organic film [23]. Common approaches for generating functional porous silicon surfaces include surface silylation with alkoxy silane molecules (that are bonded to the surface through Si-O-Si-R linkages) or through alkylation by alkene or alkyne organic linkers (to produce Si-C-R surface bonded layers). Oxidised and functionalised porous silicon surfaces are generally more stable in aqueous solutions, but usually possess weaker photoluminescence properties than hydride-terminated porous silicon [40-42]. Therefore, if the sensor requires strong porous silicon photoluminescence or changes in photoluminescence as a readout, the degree of surface oxidation is usually kept to a minimum. However, for porous silicon used in aqueous environments, which is a common requirement for biosensors, such as the one described in this part of the thesis, surface oxidation and subsequent silylation, or alternatively hydrosilylation on hydride-terminated silicon, protect the underlying porous silicon substrate from hydrolytic attack and therefore prevent undesired material degradation.

Also, reactive groups can be easily generated on porous silicon by functionalising the surface with alkoxy silane molecules or other organic linkers containing functional end groups, which can be used as attachment points for biomolecules. Two examples are shown in **Figure 2.5** [23, 32].

In **Figure 2.5 A**, a  $\beta$ -glucuronidase enzyme was linked to porous silicon by an activated *N*-hydroxysuccinimide (NHS) ester on the end of an organic linker that was attached to the porous silicon surface via a Si-C linkage [32]. This article also demonstrated that the enzyme, which was covalently linked to the porous silicon substrate (by the described mechanism), could still retain its intended enzymatic activity.

In **Figure 2.5 B**, oxidised porous silicon was functionalised with a monoalkoxy silane (by a Si-O linkage) to generate reactive thiol groups for protein attachment. The surface was subsequently biotinylated to enable specific molecular recognition of streptavidin at a concentration of 10  $\mu$ M [23]. Binding of streptavidin inside the pores of porous silicon was detected by means of interferometric reflectance spectroscopy. In this experiment, the spectral shift of the interference pattern generated from the reflection of light off the porous silicon-bulk silicon interface was monitored over time. The authors found that the interference pattern shifted to the red region of the spectrum when streptavidin was captured inside the biotinylated pores. The shift of the interference pattern was attributed to the bound protein having a higher refractive index in comparison to the medium that was used in this experiment. This corresponded to an increase in the effective optical thickness (EOT) (that was calculated from the experimentally obtained interference patterns). Interferometric reflectance spectroscopy is described in more detail on **pages 172-175** of this introduction.

### **2.1.6 Patterning of biosensor platforms with biomolecules**

In other studies, biomolecules have been loaded onto glass and silicon substrates (that were first coated with silane or other polymeric films) at defined regions by following simple photo-patterning procedures [43-45]. As a specific example, Christman et al. patterned an array of streptavidin molecules onto a modified silicon substrate surface [43]. The silicon substrates were coated with poly(3,3'-diethoxypropyl methacrylate) (PDEPMA). This polymer contains acetal side chains that can be converted to

aldehydes for subsequent protein attachment. In the presence of a photoacid generator, defined regions of aldehyde groups were formed upon illuminating the surface with deep ultraviolet light through a patterned mask. By using this photo-patterning technique, an array of streptavidin molecules could be loaded onto the modified silicon surface at site-specific locations (**Figure 2.6 A**). Furthermore, Christman et al. demonstrated that the streptavidin molecules remained biologically active by showing that biotin could only bind specifically to locations of patterned streptavidin (**Figure 2.6 B**). These patterning techniques can also be adapted for use on porous silicon substrates (because the material is similar in surface chemistry to that of glass and silicon). This opens the possibility for array type biosensor designs on porous silicon platforms.

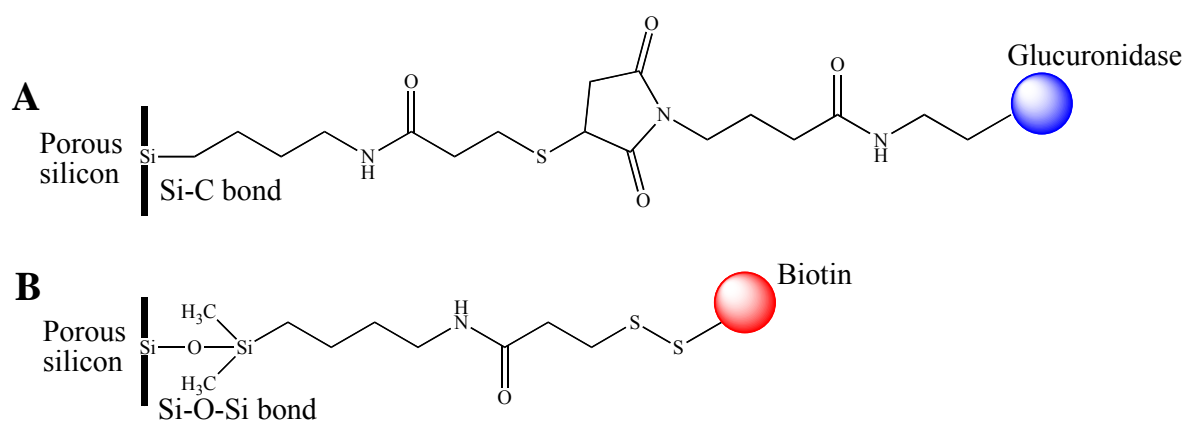


**Figure 2.5.** Two possible methods for tethering proteins to porous silicon. On the top,  $\beta$ -glucuronidase (an enzyme) (shown as a blue circle) is covalently linked to the porous silicon substrate by an intermediate organic linker (**A**) and the scheme below shows biotin (red circle) linked to the substrate by an intermediate silane molecule (**B**). The mechanisms were adapted from Létant et al. and Janshoff et al. [32, 23].

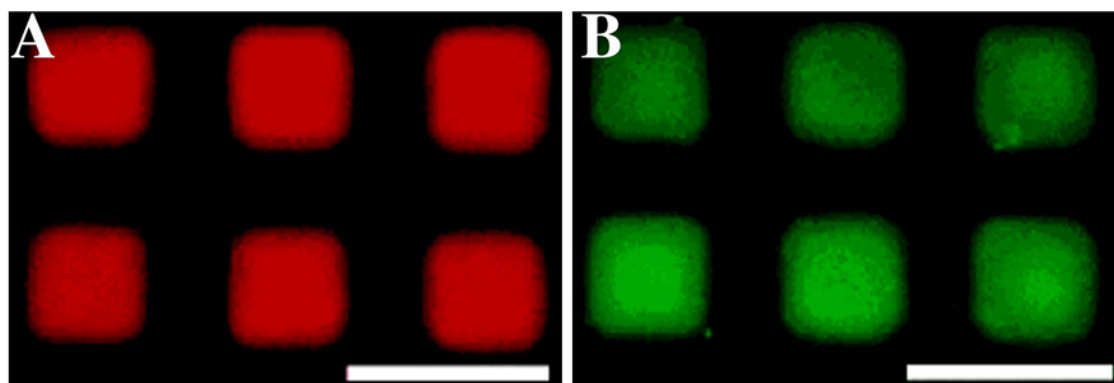


**Figure 2.6.** Fluorescence micrographs of site-specific patterned proteins on a film of PDEPMA that was exposed to deep ultraviolet light through a patterned mask in the presence of a photoacid generator. **A** shows patterned regions of red fluorescent streptavidin and **B** shows fluorescein biotin bound specifically to locations of patterned streptavidin. Scale bars = 25  $\mu\text{m}$ . The images were adapted from Christman et al. [43].

### 2.1.7 Readout signal of porous silicon biosensors

Porous silicon based biosensors and sensors have been applied for the detection of many other biological molecules and chemicals as well as gases [33, 46-48]. For example, Gao et al. developed a porous silicon biosensor for detecting ethanol, methyl ethyl ketone and *n*-hexane vapours on porous silicon [38-39, 46]. In these experiments, the porous silicon surface was probed with a diode laser at a fixed wavelength rather than with a white light that was used by Janshoff et al. [23]. The authors found that a shift in the interference pattern on porous silicon (upon exposure to a target vapour analyte with a refractive index that differs from that of background  $\text{N}_2$  vapour used in this experiment) yields a large intensity change of the reflected laser light and this change in laser intensity could be used as a readout signal to detect vapours down to the parts per billion range.

Generally, porous silicon based sensors have been developed to produce an end optical signal that acts as a readout mechanism, but electrochemical signals can also be used [48-50]. The reported ‘end-point’ optical signals derived from the porous silicon substrate are usually from the measured levels of photoluminescence emission or changes in reflection interference patterns (measured by optical interferometry) [6, 16, 23, 32-33, 51]. The following section will introduce the concept of optical

interferometry as a transducer mechanism for optical biosensors. This technique was employed for developing the biosensor in Part Two of this thesis.

### 2.1.8 Porous silicon optical interferometry

Optical interferometry on porous silicon is performed using a simple experimental set-up shown in **Figure 2.7**. A tungsten white light source delivered through optical fibre illuminates the porous silicon surface and the reflected light is detected by a spectrometer that sends the signal to a computer for processing. Importantly, optical interferometry can be used to monitor reactions in solutions. For these experiments, the porous silicon sample is usually held in a plexiglass fluidic cell. Due to thin film interference, light is reflected from the porous silicon surface as an interference pattern (called a Fabry-Pérot fringe pattern). The interference pattern is generated from 2-phase reflections of white light from the air-porous silicon interface and the porous silicon-bulk silicon interface resulting in a Fabry-Pérot fringe pattern, which is recorded by a spectrometer and relayed to the computer. Processing software applies a Fast Fourier Transform (FFT) to the experimentally obtained interferogram to calculate an effective optical thickness (EOT).

The interference principle is defined by the equation  $m\lambda = 2nL$  where  $m$  = spectral order of the Fabry-Pérot fringe;  $\lambda$  = wavelength of the incident light striking the surface at an incident angle of  $0^\circ$ ;  $n$  = average refractive index of the porous silicon layer;  $L$  = porous silicon layer thickness and  $2nL = \text{EOT}$  [16]. A shift in the Fabry-Pérot fringe pattern towards the blue region of the spectrum results in a decrease of the EOT indicating that either the refractive index or the thickness of the porous silicon layer has decreased (**Figure 2.8**). The blue shift can be due to either or both of two effects: a refractive decrease occurs when a silicon layer is converted to a silicon dioxide because  $\text{SiO}_2$  has a smaller refractive index ( $n = 1.46$ ) to that of Si ( $n = 3.5$ ) [46]; or pore collapse occurred resulting in a decrease of the porous silicon layer thickness. Conversely, an increase in the EOT is seen when the Fabry-Pérot fringe has shifted towards the red region of the spectrum (**Figure 2.8**). This can be caused by the molecules or medium inside the pores having a higher refractive index than the background medium or if precipitate had deposited inside the pores.

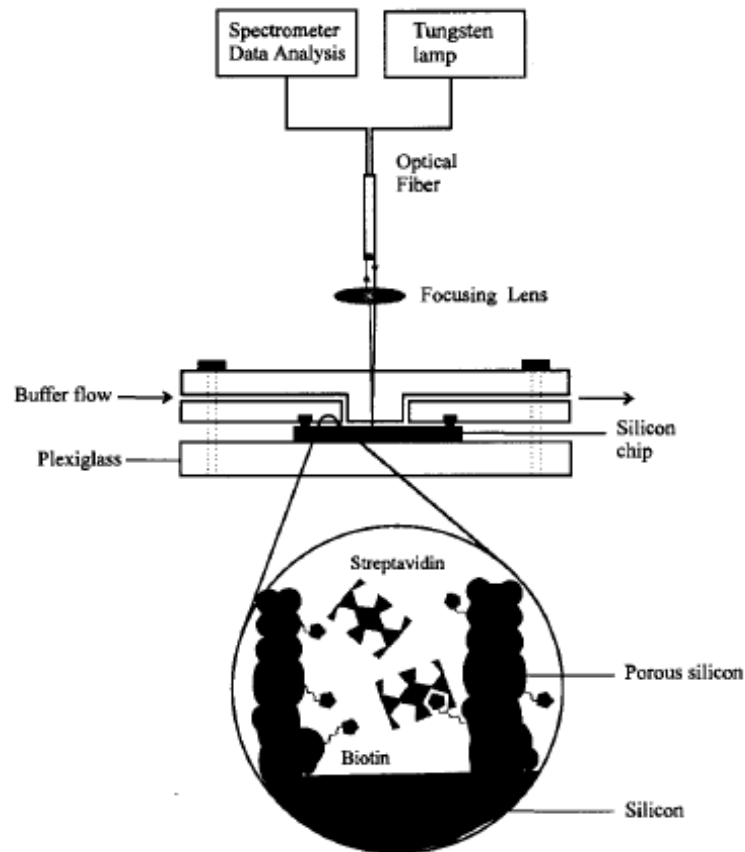


**Figure 2.7.** A scheme of the interferometric reflectance set-up taken from Janshoff et al. [23]. They used the set-up to monitor the interaction between immobilised biotin and streptavidin (the molecule to be analysed), which are shown in the magnified cartoon illustration.

### 2.1.9 Interferometric porous silicon biosensors

Interferometric porous silicon-based sensing has already been used to detect a variety of protein and DNA molecules and other biologically relevant compounds in solution [16, 23, 33, 47-48]. For example, Lin et al. showed that by employing the technique of optical interferometric reflectance spectroscopy on porous silicon, short 16-mer DNA oligonucleotides could be detected on porous silicon pre-loaded with complementary DNA strands [16]. The authors also demonstrated that both biotin and streptavidin could be detected on appropriately modified porous silicon biosensor platforms. Finally, by following a cascade of specific immune reactions on porous silicon, the authors could also use the interferometric porous silicon-based sensing device for detecting a steroid (digoxigenin) at a concentration of  $10^{-6}$  M.

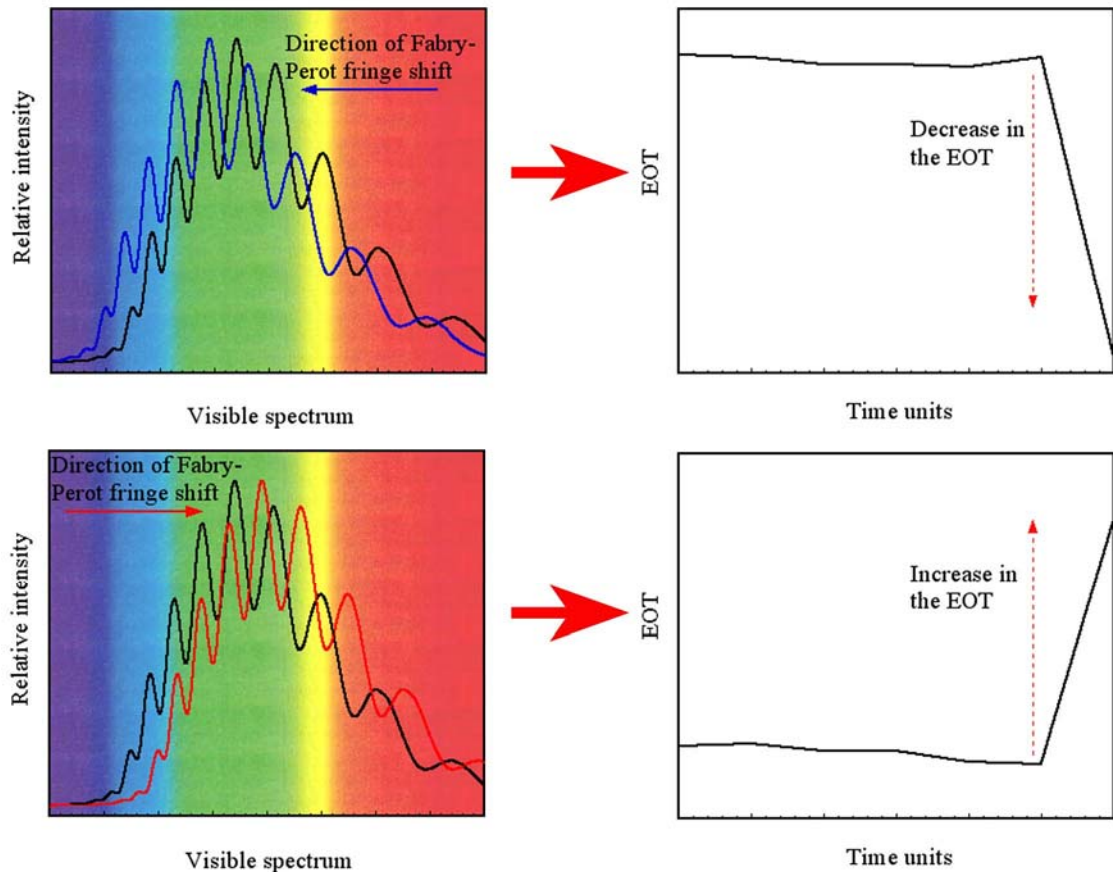


**Figure 2.8.** Graphs illustrating the relationship between the shift in the interferogram and the resultant change in the EOT. The top panel shows a shift in the interferogram to a lower wavelength (a blue shift) and a resulting decay in EOT. In the bottom panel the interferogram has shifted to a higher wavelength (a red shift) resulting in an increase in EOT. EOT denotes effective optical thickness (in nm).

More recently, a sensitive porous silicon-based sensor was developed for the detection of chemical vapours that involved monitoring reflectance changes at fixed wavelengths by laser interferometry, which illustrates the broad scope of porous silicon sensor devices [46]. The sensitivity of porous silicon sensors can be improved by altering the porous silicon morphological or surface chemistry characteristic features or by using catalysts to increase the resolution of the readout signal. For example, Voelcker et al. demonstrated that with the aid of a (transition metal complex) catalytic label to transduce biomolecule binding (inside the pores of porous silicon) to an amplified optical response, it was possible to detect DNA or protein to a relatively low concentration of 1  $\mu\text{M}$  [33]. Generally, these interferometric porous silicon-based sensors are not reusable when used in solution, especially when the readout signal involves a decrease in EOT, because these systems usually undergo a significant level of pore corrosion that can significantly alter the morphology or the chemistry of the

porous silicon surface. However, as described previously, photo-patterning procedures opens the possibility for biological molecules to be arrayed at a high-density on porous silicon that allows for a large number of assays to be performed simultaneously on a single porous silicon chip.

#### **2.1.10 Advantages of interferometric porous silicon biosensors**

Finally, all of these systems are relatively inexpensive and only simple data analysis is required to obtain quantitative results. For quantitative analysis, either the final change in EOT (either increase or decrease), or the change in the rate of EOT increase or decay can be used. As an example, an interferometric porous silicon-based biosensor developed by Janshoff et al. monitored the change in the EOT to detect streptavidin at a sensitivity of 1-10 ng of protein bound to 1 mm<sup>2</sup> of porous silicon (a sub-monolayer coverage of protein) [23]. In another example, Voelcker et al. monitored the change in the rate of EOT decay on a biotinylated porous silicon chip for detecting 1 μM of streptavidin [33]. Although this was not performed in this case, it could also be possible to construct a calibration curve by plotting the rate of EOT change over a specified protein concentration range. Similar to other biological assays such as an enzyme-linked immunosorbent assay (ELISA), the calibration curve can be used to determine the concentration levels of specific proteins in test solutions. This is useful for many biomedical or even environmental related applications.

In summary, the porous silicon-based transducer, which is readout by the technique of reflective interferometry, may lead to the development of new biosensors and sensors with increased sensitivity because the high surface area of porous silicon increases the potential molecular loading capacity compared to conventional 2-dimensional surfaces. Furthermore, optical signals are amplified by the effect of accelerated pore corrosion. The biosensor also offers wide applicability because the system is able to detect a wide range of target analytes (already demonstrated in the literature) and high-throughput capabilities are a real possibility (through simple photo-patterning procedures).

**2.1.11 Part two objectives**

The overall objective for Part 2 of this thesis was to develop an optical biosensor based on a porous silicon film (as the molecular recognition matrix and transducer) using an enzyme trigger to generate an optical signal detectable by interferometric reflectance spectroscopy. The main objectives are outlined below:

- Manufacture porous silicon films with an appropriate design (physical and chemical surface properties) for a protein biosensor.
- Find and characterise an enzymatic mechanism to catalyse the corrosion of porous silicon that can be measured by interferometric reflectance spectroscopy.
- Use this enzyme system to establish an interferometric biosensor based on functionalised porous silicon.
- Analyse the performance of the biosensor.
- Identify possible means of improving the sensitivity of the biosensor.

## 2.2 Materials and Methods

### 2.2.1 Porous silicon formation

Boron doped silicon wafers (Virginia Semiconductor Inc., Virginia) with a resistivity of 0.0005-0.001  $\Omega\cdot\text{cm}$  and  $\{100\}$  orientation were electrochemically etched in a 3:1 mixture of 48% (v/v) hydrofluoric acid (HF) 48% (v/v) (Merck) and ethanol (100%, Chem-Supply) in a custom built Teflon cell at 25°C. The Teflon cell, shown in **Figure 2.9**, has a hollowed centre with a diameter of 1.5 cm and a height of 1.5 cm that is filled with the electrolyte solution. A Viton O-ring sealed the solution over the polished side of the silicon. The back of the silicon wafer was contacted to the alligator clip via aluminium foil and a platinum-meshed electrode (Sigma) served as the counter electrode. An alligator clip was used to connect the platinum electrode to the negative terminal of the power supply (2425 Keithley SourceMeter) and the foil was connected to the positive terminal of the power supply. The current and treatment times were varied to alter either the current or charge densities, accordingly. At the completion of an etch cycle, the electrolyte was decanted and the sample was washed consecutively in ethanol, acetone and dichloromethane (DCM) (all solvents were of Analytical Grade and supplied by Chem-Supply) and dried under a gentle stream of  $\text{N}_2$ . The cell was then disassembled and the sample was removed and rinsed liberally again in DCM and dried under  $\text{N}_2$ . All samples were stored under vacuum.

Porous silicon samples were post-chemically etched by incubating the samples in a 1:10 mixture of  $\geq 99.9\%$  pure dimethyl sulfoxide (DMSO) (Sigma) and 48% HF at 25°C for 30 min. The samples were then washed, dried and stored as described above.

Structural features of the porous silicon samples were obtained by imaging the surface by means of AFM. SEM was employed for cross-sectional imaging. The surface chemistry was analysed by means of IR spectroscopy. Refer to **pages 182-183**.

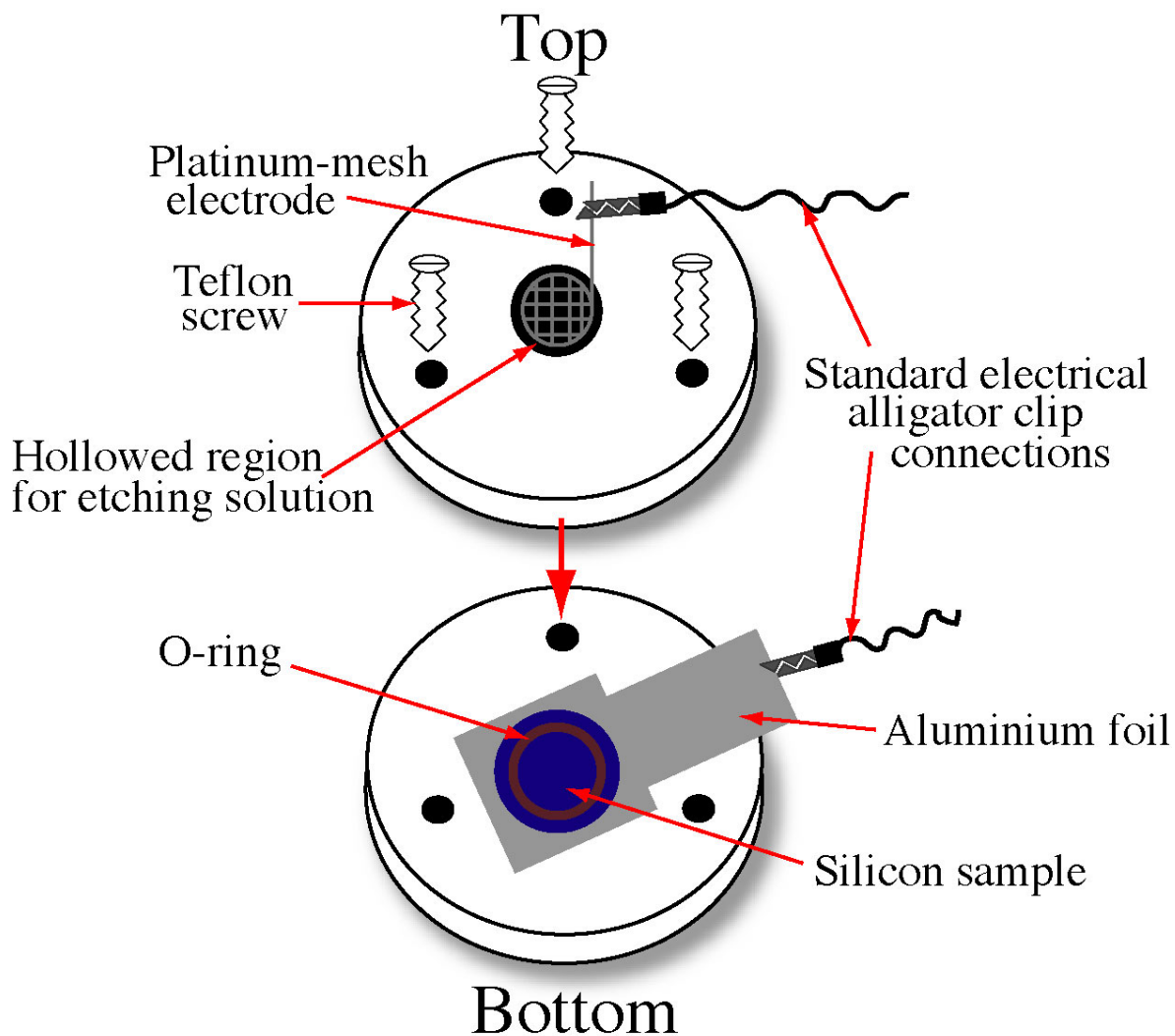


**Figure 2.9.** A diagram of the Teflon cell that was used to hold the silicon wafer and the electrolyte solution during electrochemical etching in the manufacturing process of porous silicon.

### 2.2.2 Porous silicon oxidation

Porous silicon was oxidised either by ozonolysis or bromination. Ozonolysis was carried out by purging  $O_2$  through a column filled with Drierite™ at 100 l/h (0.6 bar) into a Fisher ozon ozone generator (ozon-generator 500) connected to a glass desiccator containing the samples (positioned porous silicon side up). The generator was operated at 1.25 A and the reaction was allowed to proceed for 10 min at 25°C. Bromine oxidised samples were prepared by first evacuating the samples in a custom-built vessel (shown in **Figure 2.10**) and backfilling the vessel with dry  $N_2$ ; the procedure was repeated 3 times. Bromine vapour was allowed to leak into the vessel and react with the samples for 30 min, followed by a 30 min exposure to air. The chemistry of oxidised porous silicon samples was characterised by IR spectroscopy (refer to **pages 182-183**).

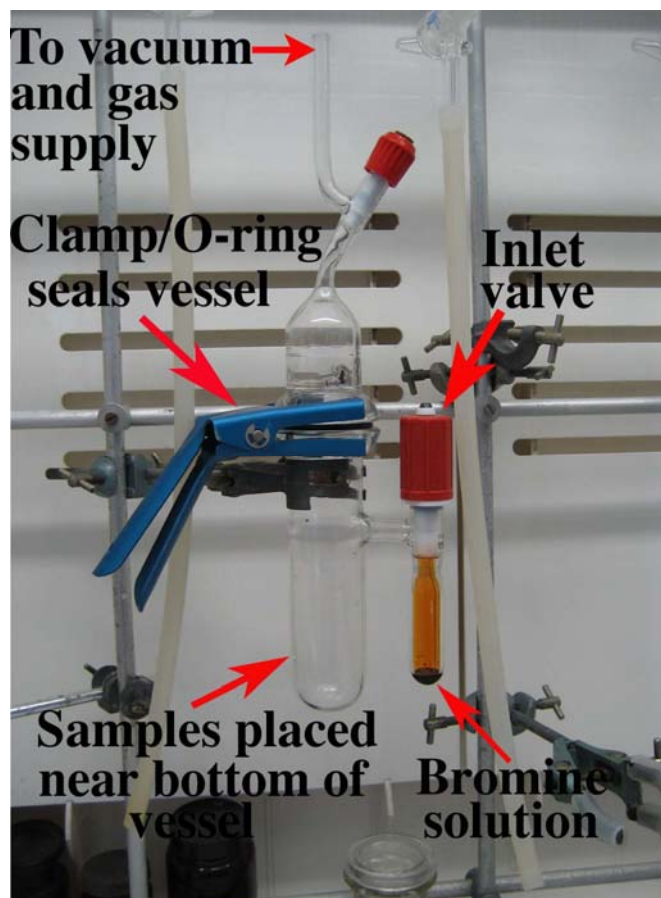


**Figure 2.10.** A photograph of the custom-built vessel used for oxidising porous silicon by bromination.

### 2.2.3 Optical interferometric reflectance spectroscopy

The effective optical thickness (EOT) of porous silicon was measured in time-lapse mode by optical interferometric reflectance spectroscopy (OIRS) **Figure 2.11**. The sample was assembled in a custom-built fluidic cell made from Plexi-glass (shown in **Figure 2.11**), which allowed fluid to be flowed over the porous silicon region while simultaneously measuring the EOT. The solution was injected into the fluidic cell with plastic syringes connected to the cell by Silastic tubing (Dow Corning). The components of the OIRS unit were purchased from Ocean Optics and consisted of a bifurcated fiber-optic probe, a tungsten halogen lamp (LS-1) and a spectrometer (USB 2000) capable of recording wavelengths between 300-1000 nm. Igor Pro software (version 4.06A) was used for data processing. Light reflected from the porous silicon surface to the spectrometer was recorded as a Fabry-Perot fringe pattern. The experimentally obtained information is used to calculate an effective optical thickness (EOT) of the porous silicon layer by applying a fast Fourier transform (FFT) to the interference spectrum. A shift in the fringe pattern represented a change in the EOT of the porous silicon layer. Porous silicon degradation was detected by a blue shift of the spectrum (EOT decrease) and a red shift corresponded to an increase in the EOT. The EOT was monitored at time intervals of 1 min.

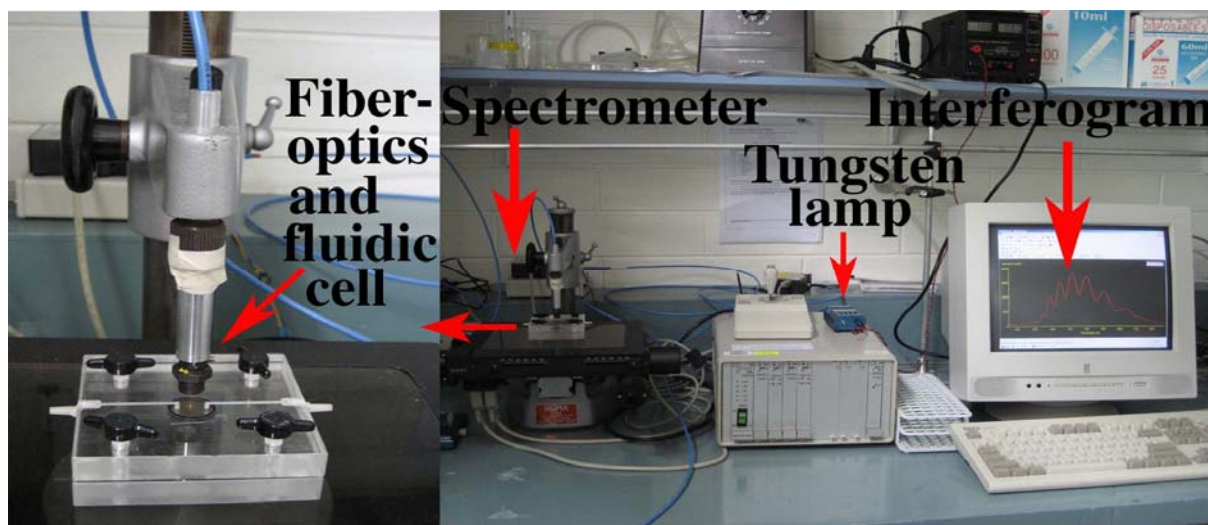


**Figure 2.11.** A photograph of the Plexi-glass fluidic cell (left side of figure) and a photograph of the complete OIRS unit (right side of figure) used for the biosensing experiments in this thesis.

### 2.2.4 Mechanism of enzyme-catalysed porous silicon degradation

Commercial precipitating and non-precipitating formulations of TMB were purchased from Sigma. Horseradish peroxidase (HRP) was purchased from Sigma in a lyophilised form and was reconstituted in (filtered and autoclaved) PBS (pH 7.4) to a concentration of 1 µg/ml (refer to **page 31** for description of PBS preparation). Absorbance measurements of all test solutions were recorded in a quartz cuvette using a Hewlett Packard 8452 UV-Vis spectrometer. During optical interferometry experiments, 2.5 ml volumes of test solutions were flushed over the substrate surface. Washes were performed using 10 ml of PBS. The EOT values were referenced to the initial reading for each experiment. Hydroquinone was purchased from Sigma in a crystalline form and was dissolved to a 10 mM concentration in PBS, pH 7.4. Sulfuric acid (Ajax Finechem) was diluted to a 100 mM concentration in water.

### 2.2.5 Immobilisation of anti-human IgG on porous silicon

3-isocyanatopropyl triethoxysilane IPTES (Fluka; purity  $\geq 95\%$ ) was prepared in distilled toluene (refer to **pages 36-37** for distillation procedure) to a concentration of 50 mM. The solution was incubated over oxidised porous silicon samples in a 50 mm glass dish at 25°C for 5 min. The samples were then rinsed in toluene and dried under N<sub>2</sub>. The samples were stored under vacuum.

Anti-human IgG was purchased from Chemicon. 1 ml of 12.5 µg/ml of anti-human IgG, prepared in PBS (PBS preparation described on **page 31**), was incubated over IPTES functionalised porous silicon at 25°C for 2 h with gentle mixing on a RATEK orbital mixer at a speed setting of 3.5. The sample was washed 3 times with PBS-Tween<sup>®</sup> 20 (0.5% v/v) (PBS-T) and 3 times with PBS. 1 mM of ethanolamine hydrochloride (Sigma), prepared in PBS, was incubated over porous silicon at 25°C for 30 min with gentle mixing on a RATEK orbital mixer at a speed setting of 3.5 to quench any unreacted isocyanate groups. The functionalised surface was washed 3 times with PBS. Alternatively, ozone oxidised porous silicon (not functionalised with IPTES) was incubated with 1 ml of 12.5 µg/ml of

anti-human IgG at 25°C for 2 h with gentle mixing on a RATEK orbital mixer set at 3.5. The sample was then washed 3 times with PBS-T (0.5% v/v) and 3 times with PBS before being used for the biosensing experiments.

### 2.2.6 Biosensing of human IgG

Anti-human IgG functionalised porous silicon samples (or control samples as will be described in the following sections) were assembled in the Plexi-glass fluidic cell (shown in **Figure 2.11**). 10 ml of PBS was flushed over the porous silicon surface and the sample was incubated in the buffer for 15 min to establish a baseline in the slope of the EOT. 2.5 ml of the Intragam solution (60 mg/ml of human protein comprising 94% IgG and the remainder IgA and IgM and 100 mg/ml maltose) (donated by Dr. Peter MacArdle's laboratory at Flinders University) or negative control (PBS not containing Intragam) solutions were injected over porous silicon and incubated over the surface for 20 min. Dilutions were prepared in PBS containing 50 µg/ml of BSA to reduce non-specific binding of immunoglobulins on porous silicon. The surface was washed by first flushing 3 ml of PBS-T (0.5% v/v) and then 10 ml of PBS over porous silicon and incubating the sample in PBS for 15 min. 2.5 ml of HRP conjugated anti-human IgG (diluted 1/500 in PBS from a commercial stock) was injected over porous silicon and incubated over the surface for 25 min. The surface was washed and incubated in PBS as described above. Finally, 2.5 ml of *o*-phenylenediamine dihydrochloride (OPD) (Sigma; substrate was prepared according to the manufacturers instructions by dissolving urea buffer tablet first in 20 ml of water followed by the OPD tablet) was injected over porous silicon and left in contact with the surface for 10 min. Non-specific protein binding sites of the Silastic tubing and the fluidic cell were blocked by incubating with 2.5% (w/v) of BSA prepared in PBS (pH 7.4) for 1 h at 25°C and then washing with 3 ml of PBS-T (0.5% v/v) and then 10 ml of PBS.

### 2.2.7 Infrared spectroscopy

Samples were analysed on a Nicolet Avatar<sup>®</sup> 370 MCT, by using the smart diffuse reflectance accessory supplied by the manufacturer. Background spectra were taken from a

clean silicon wafer (that had not been etched). The remainder of the analysis was performed according to the description on **page 46**.

### **2.2.8 X-ray photoelectron spectroscopy**

Refer to **pages 45-46**.

### **2.2.9 Atomic force microscopy**

Samples were analysed using a Nanoscope 4 Multimode microscope (Digital Instruments) in Tapping Mode in air. High frequency commercial silicon cantilevers (TESP, Veeco Instruments, USA) were used. The diameter of the porous silicon pores was determined by measuring the horizontal distance across each pore using cross-sectional analysis with Nanoscope v5.12r3 software (Digital Instruments).

### **2.2.10 Scanning electron microscopy**

Cross-sectional images of the porous layers were acquired on a Phillips XL30 operated at 10 kV. Samples were prepared by snap fracturing across the centre of the etched region of the silicon wafer. All samples were coated with a thin layer of platinum to a thickness of 2 nm to prevent charging effects during analysis.

## 2.3 Results and Discussion

### 2.3.1 Characterisation of porous silicon morphology and surface chemistry

Major consideration in the development of this porous silicon biosensor platform was given to the dimensions of the pore openings. Ideally, the pore dimensions throughout the porous layer should be large enough to allow biomolecular interactions (such as protein binding events) to occur inside the channels without steric hindrance. Here, highly boron-doped (p-type) silicon material was chosen because large pore diameters have previously been fabricated from this material for use in porous silicon-based optical interferometric biosensors [16, 23, 33, 51-53].

A typical porous silicon sample is shown in **Figure 2.12**. Porous silicon is not only reactive for further surface chemical modification, but the pores generate an optical interference pattern as light is reflected from the surface; whereas light is reflected from flat, untreated silicon as a broad reflectance band. Macroscopically, this effect gives rise to structural colour as seen in **Figure 2.12** [54]. Shifts in the interference pattern induced by changes in the refractive index of the porous material, or pore collapse caused by defined molecular interactions, were monitored in later experiments.

Atomic force microscopy (AFM) was used to acquire step-height images of the porous silicon surface. These images were processed using Nanoscope (version 5.12) software (Digital Instruments) to measure the diameter of the porous silicon pores. Pore diameters from samples produced at two current densities of 250 (low) and 450 (high) mA/cm<sup>2</sup> at a constant charge of 4.5 C/cm<sup>2</sup>, were compared. At the low current density, pores in the order of 200 nm are visible on the surface (**Figure 2.13 A**). When the current density was increased to 450 mA/cm<sup>2</sup>, the pore diameter doubled to approximately 400 nm (**Figure 2.13 B**). Also, pore size and distribution appeared relatively consistent across the surface (**Figure 2.13 C**). This small experiment simply demonstrated that pore diameter increased as the current was increased as expected from the literature [23]. For this work, the larger pore diameters of 400 nm are more

suitable because this allows relatively large biomolecules (such as immunoglobulin G (IgG), a large Y-shaped protein with a width of 14.5 nm and a height of 8.5 nm) to enter and interact inside the pore channels with minimal influences from limiting factors such as steric hindrance [55].

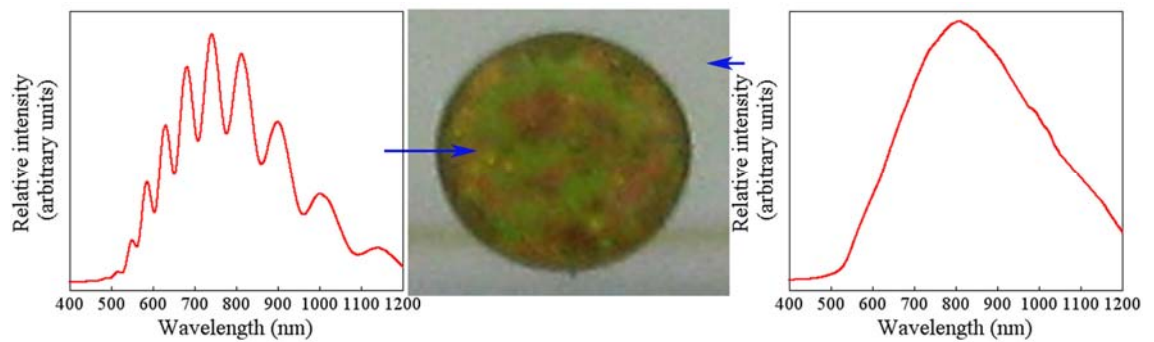


**Figure 2.12.** A photograph of a typical porous silicon sample (multi-coloured circular area of centre image) and the surrounding untreated silicon (grey region). A fringe pattern obtained from the porous silicon surface is shown on the left and the broad reflection band from the untreated silicon surface is shown on the right.

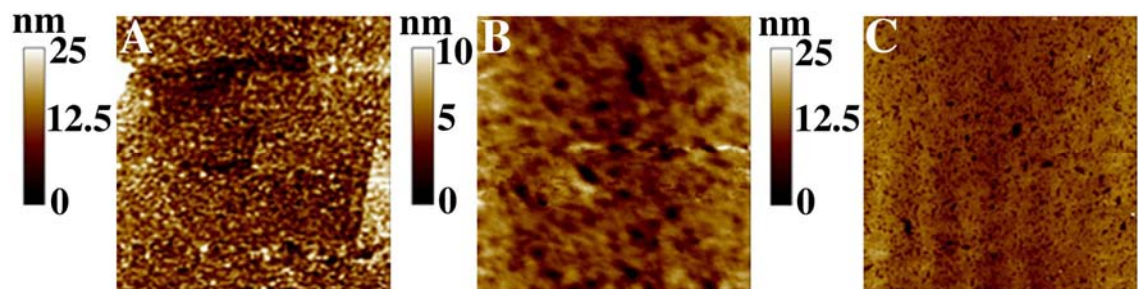


**Figure 2.13.** AFM height images of porous silicon manufactured at 250 (A) and 450 (B and C) mA/cm<sup>2</sup> at a constant charge of 4.5 C/cm<sup>2</sup>. 5 (A and B) and 10 (C) µm<sup>2</sup> scanned areas are shown.

Porous silicon cross-sectional SEM micrographs were also taken to gain information on the pore channels inside the porous layers. The depth of the measured porous layer was related to the applied charge density. At  $450 \text{ mA/cm}^2$  and  $4.5 \text{ C/cm}^2$ , the depth of the porous layer was  $2 \text{ }\mu\text{m}$  (**Figure 2.14 A**). The depth doubled in thickness (to  $4 \text{ }\mu\text{m}$ ) when the charge was increased to  $9.0 \text{ C/cm}^2$  (**Figure 2.14 B**). This is again consistent with previous reports [56]. Notably, the long cylindrical pore channels extending through the whole of the porous layer maintain a constant pore diameter. Furthermore, there does not appear to be branching and pore-to-pore communication. Each pore can therefore be regarded as an individual nano-compartment.

The maximum obtainable pore diameter and depth was constrained because of the fragile nature of the porous silicon material and also the chosen parameters were close to the electrochemical-polishing regime [25]. At a higher current density of  $500 \text{ mA/cm}^2$ , the pores collapse, which was evident from a dull grey looking surface (not shown). This was also found to be the case for porous silicon prepared at  $450 \text{ mA/cm}^2$  and a charge of  $18 \text{ C/cm}^2$ . This limited the depth of electrochemically manufactured porous silicon with large macropores (in the order of  $400 \text{ nm}$ ) to a maximum depth of  $4 \text{ }\mu\text{m}$  in this case.

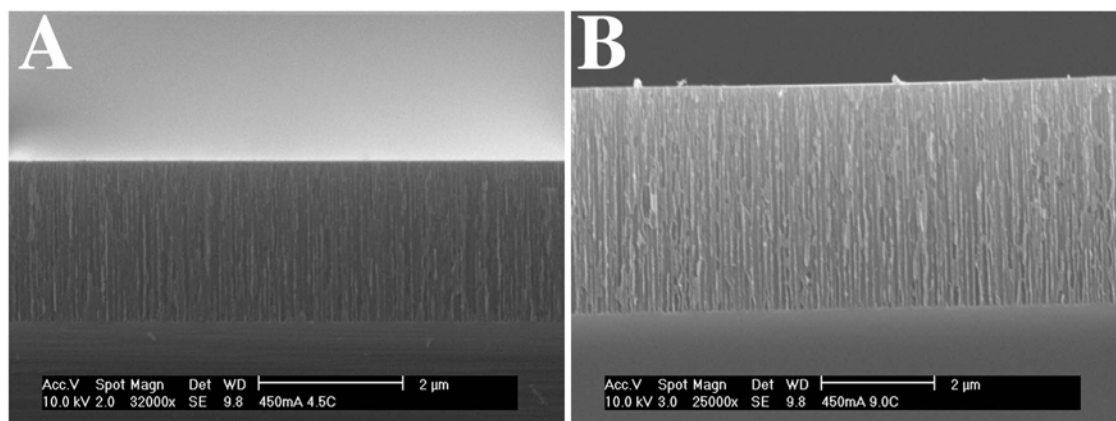


**Figure 2.14.** SEM cross-sectional micrographs of porous silicon. **A** is a cross-section of a porous silicon layer that was etched at  $450 \text{ mA/cm}^2$  and  $4.5 \text{ C/cm}^2$  and **B** was prepared at a higher charge density of  $9.0 \text{ C/cm}^2$  at the same current density. Both samples were coated with a thin layer of platinum ( $\sim 2 \text{ nm}$ ).

Anglin et al. have reported a post-chemical etch procedure to gently expand the pores of a deep porous layer [56]. Gentle pore expansion was accomplished by incubating electrochemically prepared porous silicon in a dimethyl sulfoxide (DMSO)/HF solution. DMSO slowly oxidises the material that is then immediately solubilised by the HF. This procedure was first applied to samples etched at a lower current density of  $25 \text{ mA/cm}^2$  and a higher charge density of  $18.0 \text{ C/cm}^2$  (compared to the previous samples) to produce a thicker layer of porous silicon. These samples possessed small pores even after treatment with a post-chemical etch (**Figure 2.15 E**). By increasing the current density to  $250 \text{ mA/cm}^2$  while maintaining a constant charge of  $18.0 \text{ C/cm}^2$ , a deeper porous layer measured at  $8 \text{ }\mu\text{m}$  was produced, but this sample still possessed smaller pores compared to porous silicon prepared at a higher current density of  $450 \text{ mA/cm}^2$  (**Figures 2.14 B and 2.15 A and C**). As anticipated, the pores of the porous silicon sample prepared at  $250 \text{ mA/cm}^2$  and  $18.0 \text{ C/cm}^2$  could be expanded by treatment with a post-chemical etch and these larger pores were visible by SEM (compare **Figure 2.15 C to D**). Also, the pore dimensions after chemical pore expansion were comparable to porous silicon made at the higher current density of  $450 \text{ mA/cm}^2$  and a lower charge density of  $9.0 \text{ C/cm}^2$  (**Figure 2.15 A and D**). Therefore, in this study, a thicker macroporous silicon layer could be produced by first electrochemically anodising silicon at a current density of  $250 \text{ mA/cm}^2$  and a relatively high charge density of  $18.0 \text{ C/cm}^2$  to produce a thick porous silicon layer of  $8 \text{ }\mu\text{m}$ , and then post-chemically etching this sample to obtain a macroporous silicon film with a depth of  $8 \text{ }\mu\text{m}$ .

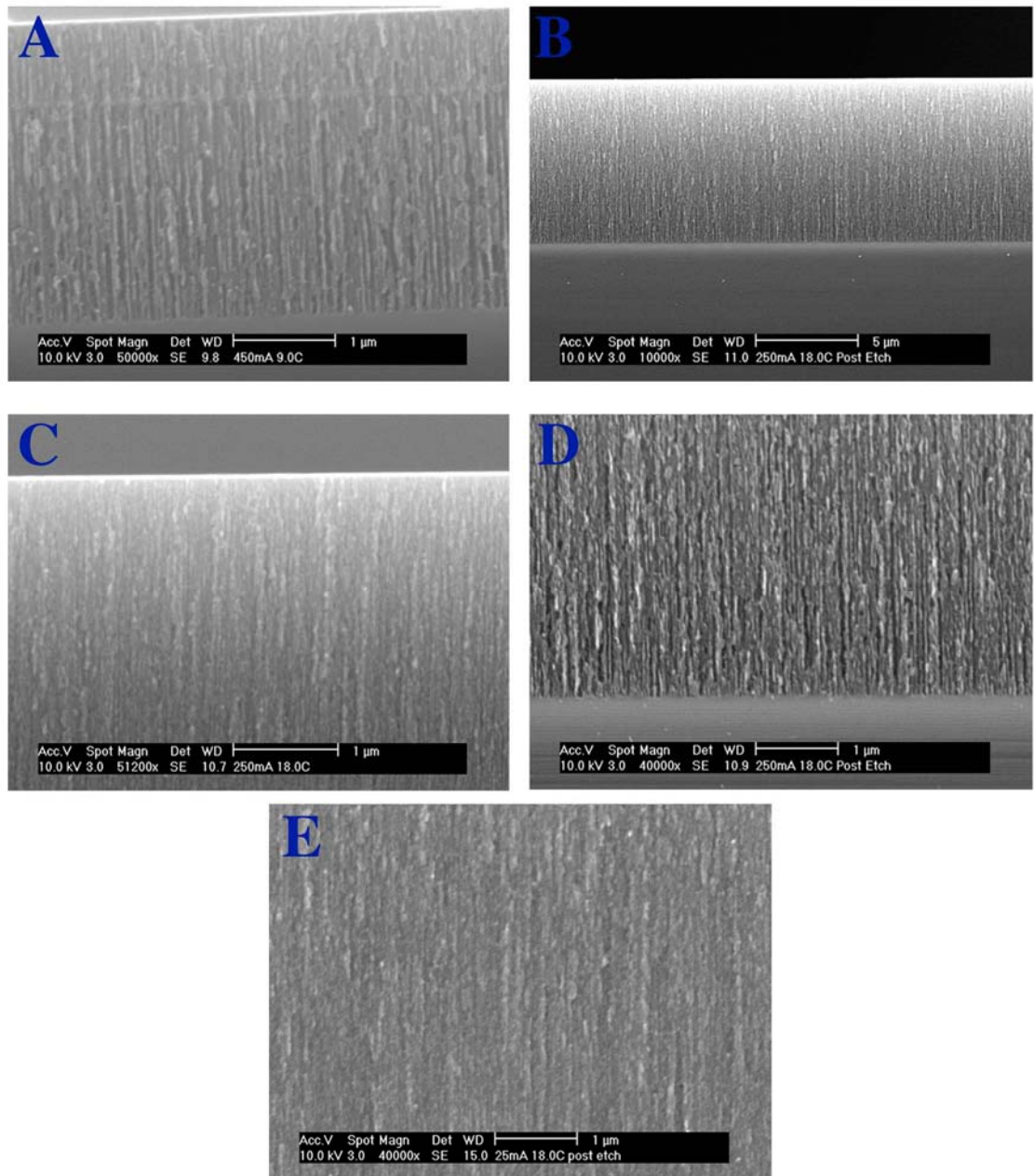


**Figure 2.15.** SEM cross-sectional micrographs of porous silicon. **A** is a high magnification micrograph of porous silicon prepared at  $450 \text{ mA/cm}^2$  and  $9.0 \text{ C/cm}^2$ ; micrographs of porous silicon prepared at  $250 \text{ mA/cm}^2$  and  $18.0 \text{ C/cm}^2$  and post-chemically etched are shown at low (**B**) and high (**D**) magnifications and before post-chemical treatment at a high magnification (**C**); **E** is a micrograph of post-chemically etched porous silicon prepared at  $25 \text{ mA/cm}^2$  and  $18.0 \text{ C/cm}^2$ . All samples were coated with a thin layer of platinum ( $\sim 2 \text{ nm}$ ).

Many other types of porous silicon layers with different arrangements of porous networks can be manufactured such as porous films with multiple porous layers, interconnected pores or branched pores [57-59]. This investigation only required cylindrical one-dimensional pores to be made. However, this study did confirm that pores could be tailored to specific dimensions by simply altering the current and charge density or by utilising a chemical post-etching procedure. Although limitations were experienced with the generation of deep ( $> 4 \mu\text{m}$ ) macroporous silicon films, suitable candidates for the desired porous silicon biosensor platform (with varying pore sizes and depths) were successfully manufactured. Relatively robust macroporous silicon films were formed at  $450 \text{ mA/cm}^2$  and  $4.5 \text{ C/cm}^2$  (with a calculated average pore diameter of  $400 \text{ nm}$  and a depth of  $2 \mu\text{m}$ ). These films displayed 9 interference fringes (**Figure 2.12**). These etching conditions were used in the development of an interferometric biosensor, which is presented in the following sections of Part 2: Results and Discussion. Future investigations could identify etching conditions for producing porous silicon with more optimal morphological characteristics, which improve the performance of the biosensor, such as its sensitivity.

The discussion so far has focussed on the morphological characteristics of the porous silicon films. The remainder of the discussion in this section will focus on the surface chemistry of the porous silicon film that was analysed by infrared (IR) spectroscopy and X-ray photoelectron spectroscopy (XPS).

When porous silicon is freshly prepared, the surface is hydride terminated (as detected by infrared spectroscopy) and is susceptible to hydrolytic attack in aqueous solution (**Figure 2.16 A**) [23, 51]. Characteristic peaks for a hydride-terminated porous silicon surface were observed at approximately  $900 \text{ cm}^{-1}$  ( $\text{SiH}_2$  scissor) and  $2100 \text{ cm}^{-1}$  for Si-H stretching in  $\text{Si}_2\text{H-SiH}$  or  $\text{Si}_3\text{-SiH}$  [60-62]. These silicon hydrides can be easily transformed into silicon oxides by various oxidation procedures such as through thermal heating, ozone or bromine oxidation [23, 63-65]. The oxide layer produced through these processes protects the underlying porous silicon material somewhat from hydrolytic corrosion.

The surfaces reported here were oxidised by means of bromination or ozonolysis. After oxidation, a strong peak for a silicon dioxide was observed in the region of  $1100 \text{ cm}^{-1}$

(SiO stretching in O-SiO) for both procedures (**Figure 2.16 B** and **C**) [60-62]. A small peak at about  $900\text{ cm}^{-1}$  (SiH<sub>2</sub> scissor) was still detected after bromination that was not seen after ozonolysis, which suggests the surface has not oxidised as efficiently compared to an ozone-oxidised surface. Therefore, bromination can be a useful technique for varying the dissolution properties of porous silicon and ozonolysis can be used when more stringent levels of oxidation are required to achieve a surface that is more stable in aqueous solution.

There was also a significant peak (referred to as an interference band) observed in all of the spectra (**Figure 2.16 A-C**). If this was derived from a laser reflection from the substrate surface, the peak should remain at a fixed wavelength (632.8 nm for the laser of the spectrometer used in this study). However, this peak shifted in position and varied in intensity between all the samples analysed. Therefore, the peak was attributed to a Fabry-Pérot interference effect generated from the porous silicon and bulk silicon interface (**Figure 2.16 A-C**). This phenomenon has been explained in a previous report [46].

To obtain quantitative information of the elemental species present on the surface of the porous silicon films, the samples were next analysed by XPS. After oxidation, three main elements were detected on the porous silicon surface mainly consisting of oxygen (54 at.%), silicon (34 at.%) and carbon (below 10 at.%) (**Figure 2.17 A**). A small amount of contamination from nitrogen (below 1 at.%) and fluorine (~ 2 at.%) was also detected, which is likely to be derived from the HF solution, the walls of the Teflon cell or from the Viton O-ring.

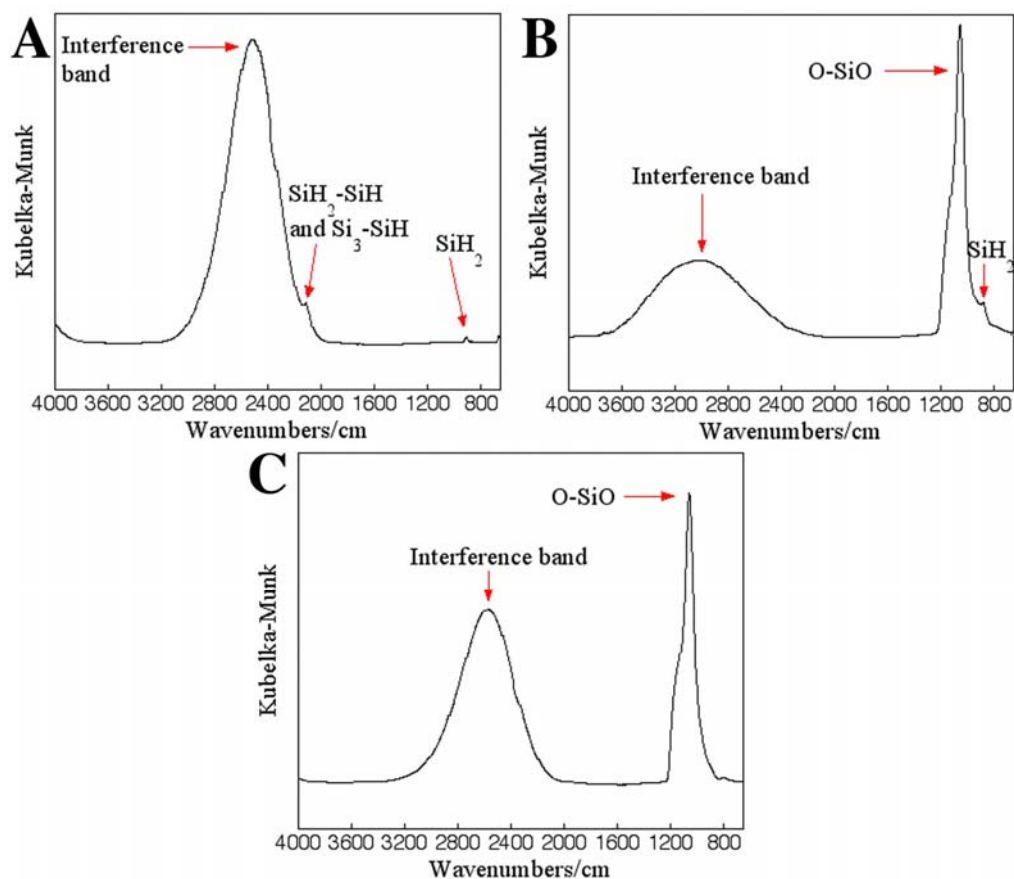


**Figure 2.16.** Diffuse reflectance infrared spectra taken on freshly prepared porous silicon (A); after bromine oxidation (B); and after ozone oxidation (C). All samples were etched at 450 mA/cm<sup>2</sup> and 4.5 C/cm<sup>2</sup>. The spectra were referenced to blank spectra taken on an untreated piece of silicon. Kubelka-Munk are relative units.

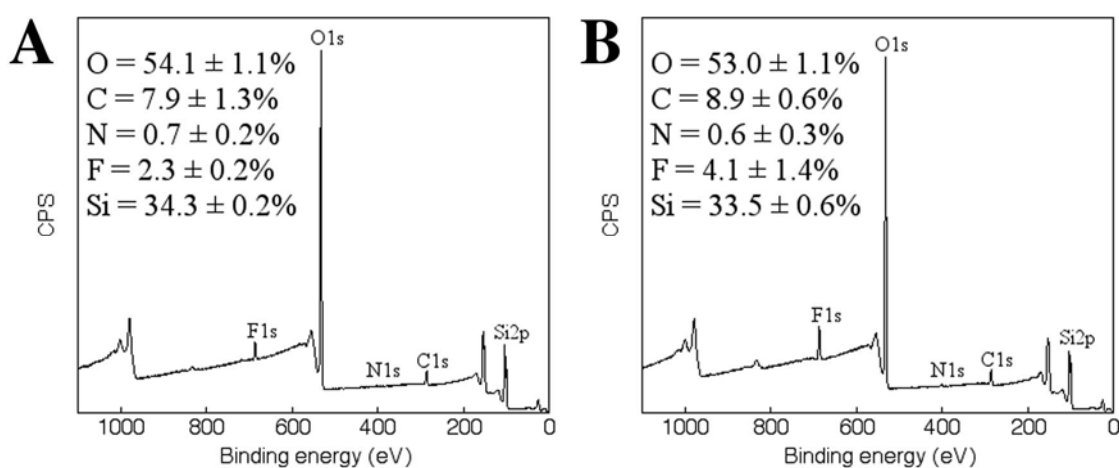


**Figure 2.17.** XPS survey spectra of ozone oxidised porous silicon (A) and after a reaction with 3,3,3-trifluoropropyl trimethoxysilane (B). Both samples were etched at 450 mA/cm<sup>2</sup> and 4.5 C/cm<sup>2</sup>. Percentages shown in the graphs denote atomic percentages.

Although hydroxyl groups could not be detected directly by IR where the depth of analysis is too deep, by XPS (the hydroxyl component expected at 531.5 eV in the O 1s high-resolution spectrum was absent; data not shown) or by trifluoroacetic anhydride (TFAA) derivatisation for reasons explained on **pages 57-67**, oxidation by bromine or ozone is known to generate surface silanol groups that are reactive with alkoxy silanes [23, 51, 63-65]. To avoid pores from being blocked by silane molecules, the reactions on porous silicon are generally performed with lower silane concentrations and at shorter reaction times compared to the more vigorous conditions used on non-porous PECVD-Si-Ti as outlined in **Table 1.2**. Following a surface reaction with a fluorinated silane (the same molecule that was used to model silanisation of PECVD-Si-Ti as discussed on **pages 69-80**), the fluorine content is increased almost 2-fold compared to an oxidised porous silicon surface (**Figure 2.17 A and B**) indicating that the silane had reacted with the surface. Given that porous silicon can be simply and rapidly modified with commercially available alkoxy silanes (5 min reaction times), these silanes were chosen as vehicles to generate reactive functional groups on the material surface, as will be discussed from **page 200**.

In summary, in this current investigation, the pore size and depth of the fabricated porous layers was varied under different current and charge parameters on low-resistivity p-type silicon. A previously reported post-chemical etching procedure to gently expand pores of deep porous layers on porous silicon was also found to be useful for producing deeper layers of macroporous silicon in this work. However, due to the fragile nature of the material, the maximum obtainable depth of the macroporous silicon layer was limited to 8  $\mu\text{m}$ . Nonetheless, possible porous silicon candidates for the biosensing platform were produced and characterised. Also, different degrees of surface oxidation were achieved on ozone and bromine oxidised porous silicon that can also have a bearing on the stability of the material in solution. Oxidised porous silicon was reactive with a model alkoxy silane and similar silanes will be used in subsequent surface modifications. Now that the surface morphology and chemistry of the porous silicon platform has been described, the next section will address the readout mechanism of the biosensor.

### 2.3.2 Enzyme-catalysed porous silicon degradation

Recently, Jenison et al. had developed a biosensor on a flat silicon substrate that was based on horseradish peroxidase (HRP)-catalysed oxidation of the benzidine derivative, 3,3',5,5'-tetramethylbenzidine (TMB) [66-67]. This chromogen has been heavily exploited for enzyme-linked immunological applications for many years and its reaction with HRP has been extensively characterised [68-77]. Under appropriate oxidative conditions, an insoluble final product is formed. The precipitate can be quantified chromometrically [69]. Jenison et al. found that the product could also be easily detected under white light illumination on the highly reflective silicon surface. This effect formed the basis of the readout mechanism for the biosensor that was used for the detection of various biological interactions (from proteins or nucleic acids) [66-67]. This led to the present investigation where HRP-catalysed oxidation of TMB was followed over porous silicon using interferometric reflectance spectroscopy. The reaction was monitored on porous silicon by measuring changes in the effective optical thickness (EOT) of the porous layer over time. The EOT measurements presented in this thesis have been normalised to the first EOT measurement taken at time 0 min by dividing each EOT measurement (EOT) over the EOT measured at time 0 min ( $EOT_0$ ) (represented on the y-axis of each graph as  $EOT/EOT_0$ ). It was found that the enzyme-catalysed reaction gave rise to an intricate optical signal. This signal represents the basis for the readout mechanism used in the present biosensor.

First, ozone oxidised porous silicon (prepared at  $450 \text{ mA/cm}^2$  and  $4.5 \text{ C/cm}^2$ ; measured average pore size of 400 nm and a porous layer depth of 2  $\mu\text{m}$ ) was shown to be relatively stable in a phosphate buffered saline (PBS) solution of a near neutral pH of 7.4 (**Figure 2.18**). Also, the HRP enzyme by itself has no significant influence on the stability of the porous silicon material in solution. Porous silicon was shown to be unstable in a high pH environment by the addition of 0.1 M NaOH (**Figure 2.18**). The rapid EOT decrease at high pH is due to oxidative hydrolysis [23, 51]. However, a characteristic and reproducible signal is observed when TMB is flushed over porous silicon loaded with adsorbed HRP (**Figures 2.19** and **2.21 A**). This signal can be divided into 4 components. When porous silicon is first exposed to TMB, an increase in the EOT is observed (1). Soon after, there is a rapid decrease in the EOT (2) before the

EOT increases again (3) and finally stabilises over time (4). To explain each component of the signal, the reaction mechanism between HRP and TMB needs to be introduced (**Scheme 2.2**).

When TMB is oxidised by HRP in the presence of  $H_2O_2$ , the colourless diamine with a  $\lambda_{max}$  of 285 nm, is first converted by a one-electron oxidation to an intermediate cation free radical or a diamine/diimine complex with a  $\lambda_{max}$  of 370 and 652 nm, respectively. By another one-electron oxidation, the intermediate products then form the final diimine product ( $\lambda_{max} = 450$  nm). Because the reduced form of TMB and the intermediate and final oxidised products have absorption maxima at distinct wavelengths, the reaction can be followed by ultra-visible (UV-Vis) spectroscopy.

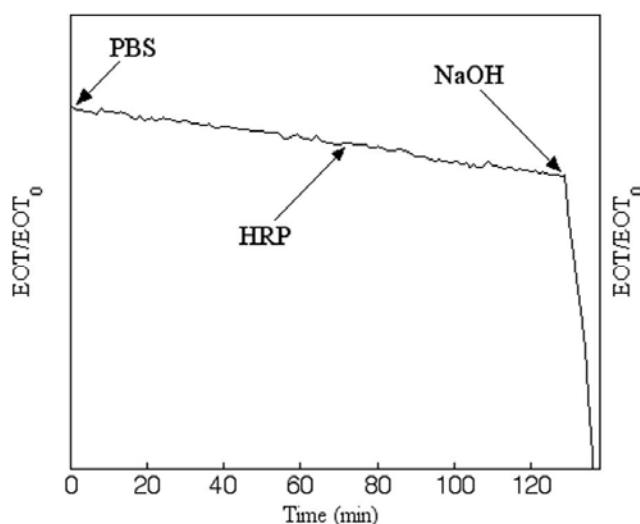


**Figure 2.18.** A time course graph displaying the EOT of the porous silicon material measured by means of interferometric reflectance spectroscopy. Phosphate buffered saline (PBS) at pH 7.4 was first injected for about 1 h followed by 50  $\mu$ M of HRP prepared in PBS. Finally, 3 ml of 0.1 M of NaOH was injected into the flow cell. EOT/EOT<sub>0</sub> denotes the effective optical thickness (EOT) measured at a given time divided by the first EOT measurement taken at time 0 min.

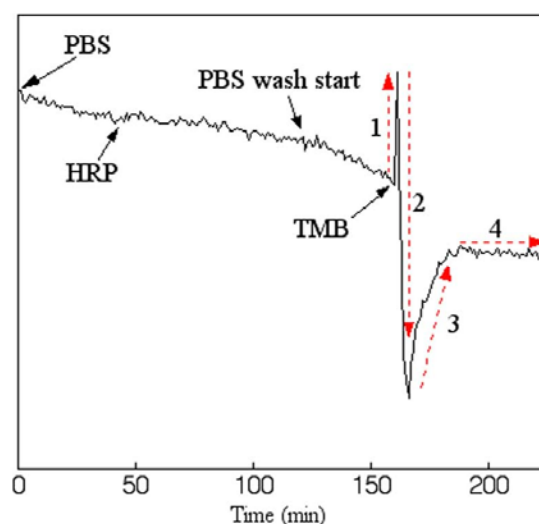
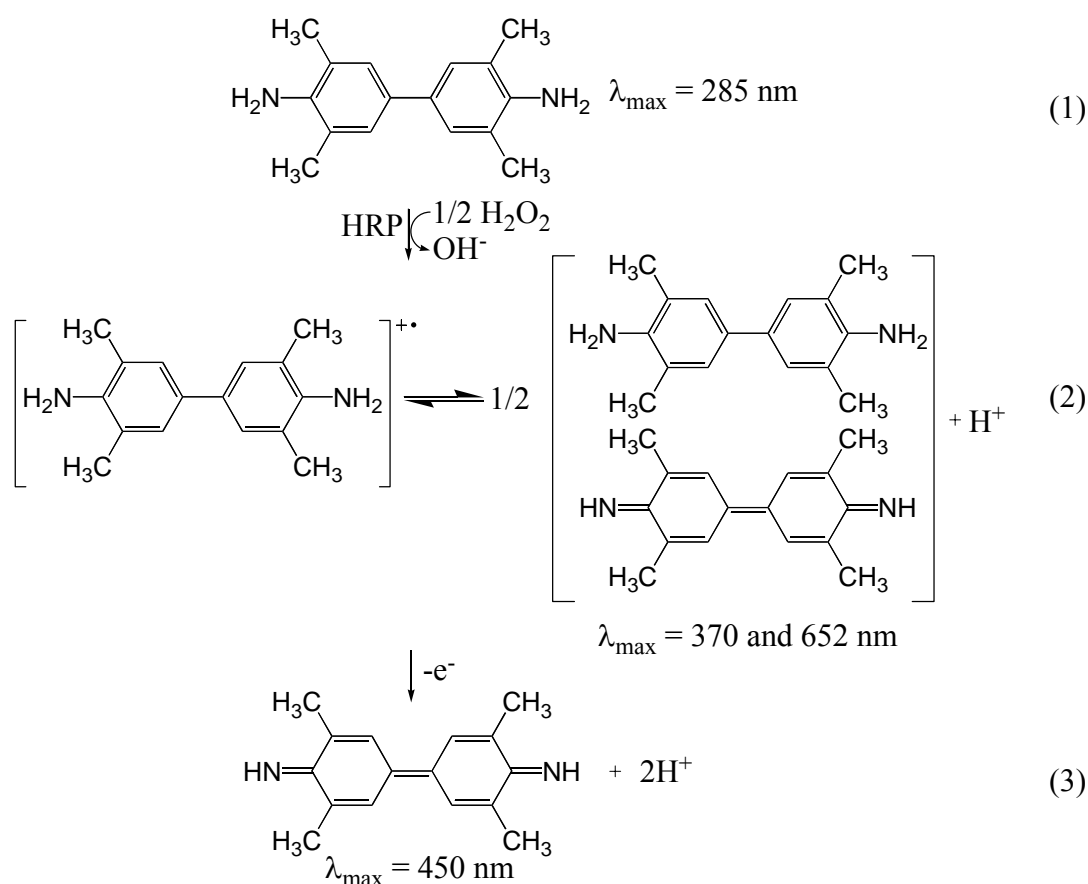


**Figure 2.19.** A time course graph displaying the EOT of the porous silicon material measured by means of interferometric reflectance spectroscopy. 50  $\mu$ M of HRP was adsorbed onto the surface for about 1 h and washed with PBS for 20 min before a commercial precipitating formulation of TMB was added. The resulting signal caused by HRP-catalysed oxidation of TMB is divided into 4 components, which are numbered in the graph and indicated by the broken red arrows.



**Scheme 2.2.** HRP-catalysed oxidation of TMB [70-71].

The initial, unreacted TMB molecule was confirmed to have a  $\lambda_{\max}$  of 285 nm (**Figure 2.20 A**). There was also a strong peak observed at 200 nm that was present in all of the spectra that corresponds to absorbance of  $\pi$  electrons of the aromatic rings (**Figure 2.20 A-D**). When TMB is reacted with HRP in the presence of  $\text{H}_2\text{O}_2$ , the peak for the reduced form of TMB at 285 nm decreases in intensity over time and the peaks for the intermediate (370 and 652 nm) and final (450 nm) oxidised products increase (**Figure 2.20 B**). This reaction is reversible by adding a reducing agent such as hydroquinone (HQ). After adding HQ to a 10 min reaction of TMB with HRP/ $\text{H}_2\text{O}_2$ , the oxidised products are reduced back to the parent TMB molecule (**Figure 2.20 C**). Alternatively, the reaction can also be driven to completion (although less effectively) by reducing the pH of the solution. For example, when the concentration of sulphuric acid (SA) was gradually increased from 1-3 mM (corresponding to a decrease of pH from 4.2 for the reaction mixture to 2.8, 2.5 and 2.3 after each sequential SA addition) in a reaction mixture containing reduced and oxidised TMB products, the peaks of the intermediate

TMB products gradually decreased and the intensity of the peak for the final diimine increased accordingly (**Figure 2.20 D**).

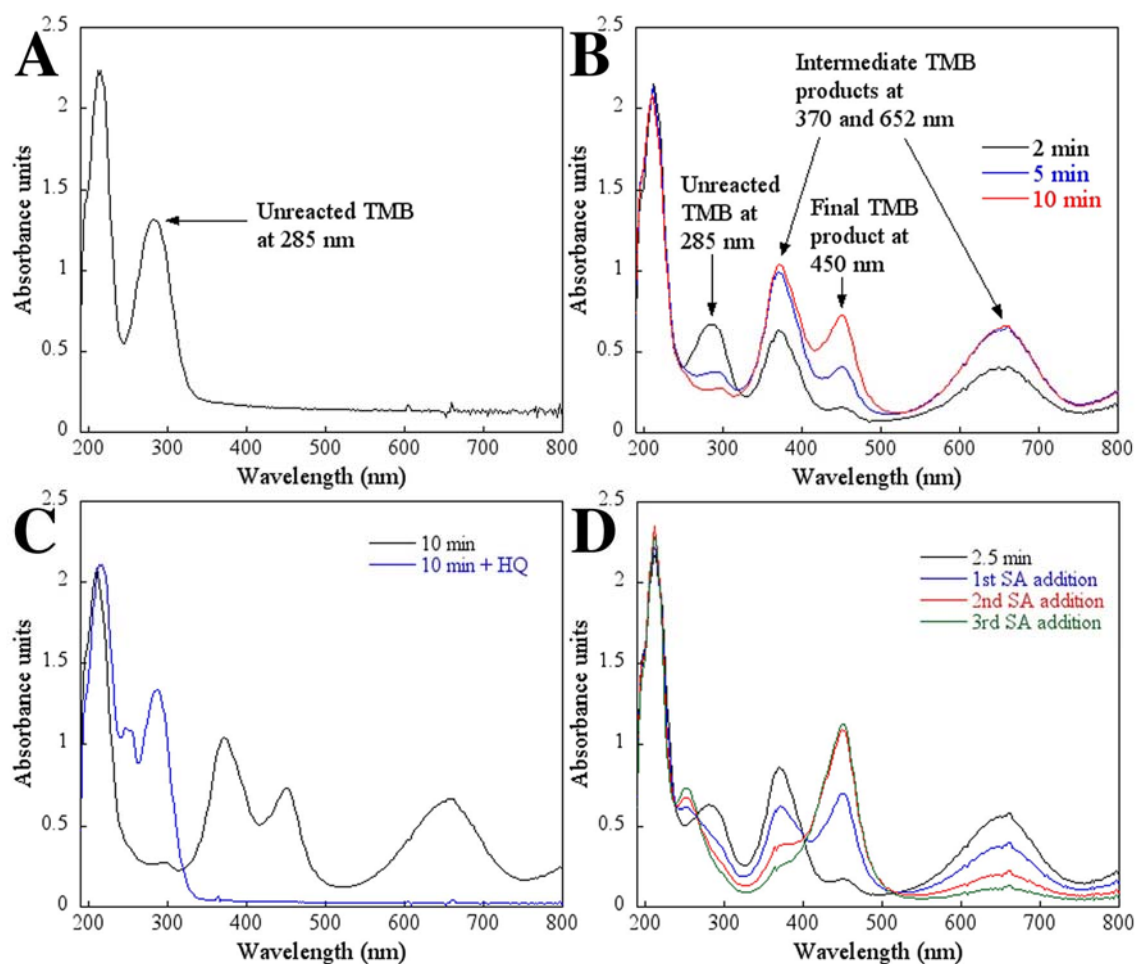


**Figure 2.20.** UV-Vis spectra of TMB and TMB oxidation products. A 20X dilution (in water) of a commercial non-precipitating TMB formulation is shown in **A**. Spectra of diluted TMB formulations reacted at room temperature with 10 ng/ml of HRP at 2, 5 and 10 min are shown in **B**. In **C**, a spectrum of TMB oxidised by HRP for 10 min is compared before and after addition of HQ to a final concentration of 1 mM. **D** shows the spectra after 2.5 min of HRP-catalysed TMB oxidation and after 3 sequential additions of SA to final concentrations of 1, 2 and 3 mM.

Now, the components of the optical signal resulting from the HRP-catalysed oxidation of TMB on porous silicon from **Figure 2.19** can be explained. The first initial increase in the EOT of porous silicon can be attributed to a bulk effect from injecting the TMB formulation with a refractive index that differs from that of PBS (**Figure 2.21 A**).

The second phase of the signal corresponds to a sharp decrease in the EOT due to an accelerated corrosion rate of the porous silicon material that is similar to that observed for material exposed to NaOH (compare **Figures 2.18** and **2.19**). Although the mechanism is not well known, a high oxidation state transition metal complex ( $\text{Ni}(\text{cyclam})^{3+}$ ) has been shown to catalyse porous silicon corrosion [33]. Similar to this previous study, the results obtained here suggest that a radical oxidation pathway induced porous silicon pore degradation.

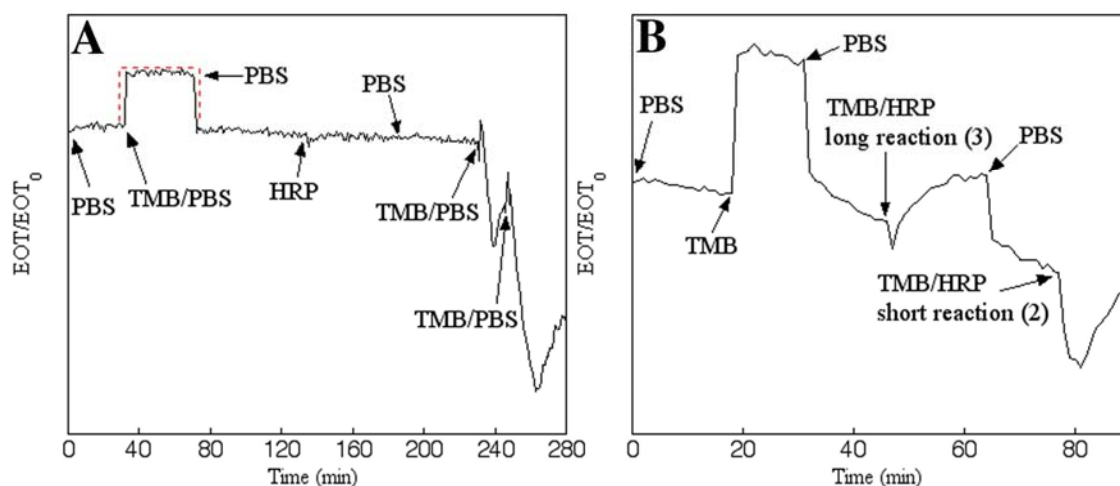


**Figure 2.21.** In graph **A**, the broken red lines highlight the bulk effect observed on porous silicon from the commercial precipitating formulation of reduced TMB. After allowing HRP (at a concentration of 50  $\mu\text{M}$ ) to adsorb on the same surface, two subsequent injections of TMB/PBS (1:1) mixtures were carried out to demonstrate the reproducibility of the signal. In graph **B**, the precipitating formulation of TMB after 30 min of incubation with HRP/ $\text{H}_2\text{O}_2$  (50  $\mu\text{M}$  of HRP) was injected over porous silicon (long reaction) as well as a freshly prepared mixture of TMB and HRP/ $\text{H}_2\text{O}_2$  (short reaction). The bracketed numbers correspond to the intermediate oxidised TMB products expected in the reaction solutions and shown in **Scheme 2.2**.

An intermediate cation radical produced during the oxidation of TMB (**Scheme 2.2**) was hypothesised to accelerate pore degradation. This was found to be the case when the EOT of porous silicon was monitored at different stages of the TMB oxidation pathway. At short reaction times (freshly prepared in **Figure 2.21 B**; or a 10 min reaction in **Figure 2.22**) where the intermediate cation radical is assumed to be present at the highest concentration, rapid pore degradation occurs. Conversely, this was not evident when hydroquinone reduced the oxidised TMB products back to the original diamine (**Figure 2.22**). Alternatively, at long reaction times of 30 min (**Figure 2.21 B**) and 1 h (**Figure 2.22**) where the final diimine product is assumed to be the prevalent species and only low amounts of intermediate products would be present, no considerable level of pore degradation was detected, but rather an increase in EOT was observed, which was attributed to the final oxidised product precipitating in the macropores (Component 3 – refer to **Figure 2.19** and **Scheme 2.2**). Eventually, the EOT stabilised when all the starting TMB material and intermediate products had oxidised or no more precipitate could enter the clogged pores resulting in no more increase in the EOT (Component 4 – refer to **Figure 2.19** and **Scheme 2.2**).

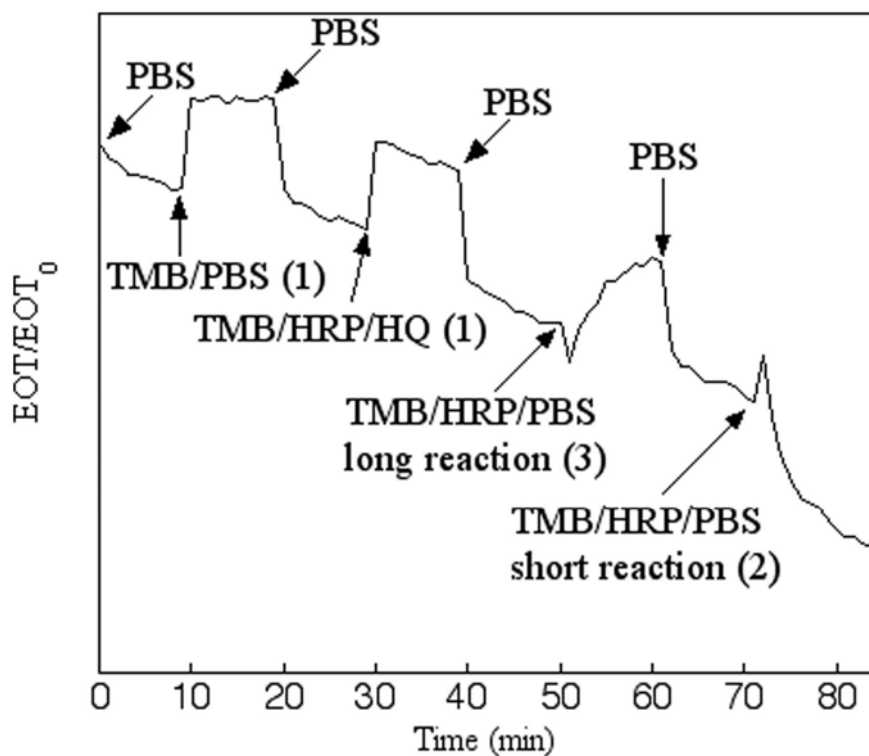


**Figure 2.22.** Porous silicon degradation resulting from: the diamine (1) of unreacted TMB (TMB/PBS) or the diamine of oxidised TMB (after a 10 min reaction with 10 ng/ml HRP), which was subsequently reduced with 1 mM HQ; the diimine produced after a 1 h reaction (TMB/HRP/PBS: long reaction) or from the intermediate products after a 10 min reaction (TMB/HRP/PBS: short reaction). Bracketed numbers correspond to intermediate oxidised TMB products shown in **Scheme 2.2**. The reaction mixtures were prepared to a constant volume by adding appropriate amounts of PBS.

In summary, a standard optical detection system that has been developed for immunological applications was adapted to porous silicon in this study. Enzyme (HRP) mediated oxidation of a TMB chromogen (in a commercial precipitating formulation) was easily detected through distinct changes in the EOT of the porous silicon material. At initial stages of TMB oxidation, a cation radical was shown to induce pore degradation before a precipitated thin organic layer at the end of the reaction eventually covered the surface. The characterised macroporous silicon film and the enzyme-chromogen system will next be combined to develop a procedure for the detection of a model protein molecule by interferometric reflectance spectroscopy.

### **2.3.3 Establishment of an enzyme-based interferometric biosensor for the detection of immunoglobulin G (IgG) on a functionalised porous silicon platform**

The next stage of the project aimed at developing a procedure for detecting a model protein molecule by combining the previously described porous silicon platform with an enzyme-chromogenic system. Immunoglobulin G (IgG) was chosen as a model protein for these studies. IgG is a Y-shaped protein containing two heavy and two light polypeptide chains that are linked together by disulphide bonds (refer to **Scheme 2.3**) [78]. The V region consists of both heavy and light chains that contain variable regions, which bind antigens. This diversifies the range of target antigens that an immunoglobulin can recognise during the immune response thereby enabling the protection of the body from a wide range of diseases.

Two other interferometric porous silicon optical biosensors have previously been reported for detecting IgG. Dancil et al. developed an optical porous silicon biosensor to detect human IgG at a concentration of 2.5 mg/ml [53]. Bonanno et al. detected a rabbit IgG at a limiting concentration of 70 µg/ml [11]. The readout signal in both cases consisted as an increase in the effective optical thickness (EOT) when IgG was captured in the porous silicon pores. The increase in EOT was explained by two factors: firstly, IgG filling the pores and secondly, IgG having higher refractive index than the aqueous medium. Both of these reports utilised a cascade of immunological reactions on the porous silicon platform to detect the target analyte.

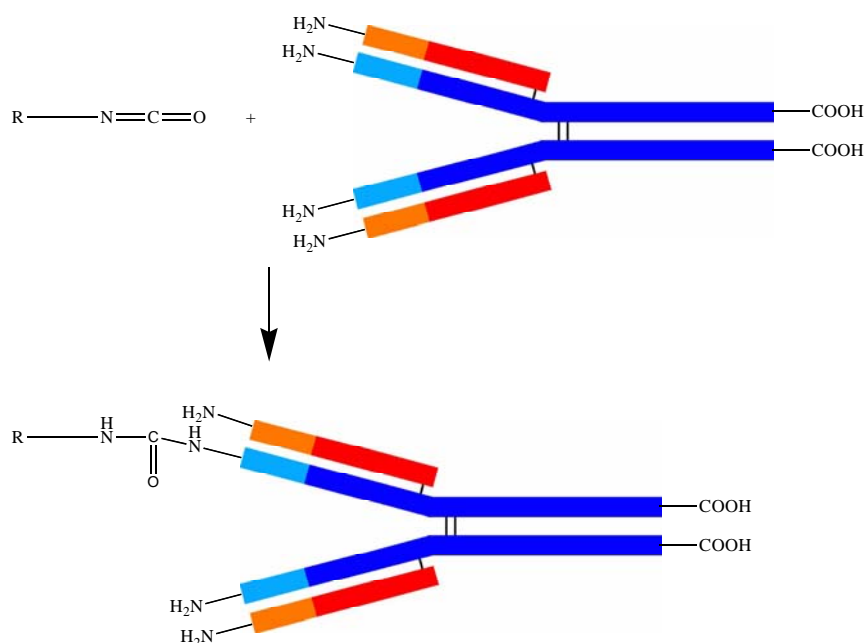
In this study, human IgG was used as a model protein for developing and optimising the experimental parameters that were used in the preparation of the biosensor platform and in the establishment of the biosensing experimental protocols. IgG is a therapeutic protein of significant importance, especially in antibody replacement therapy. For example, IgG is an active ingredient in a formulation known as Intragam that is used for replacing antibodies in patients who suffer from immune disorders. The Intragam formulation was used as the test solution in this study and is composed of 60 mg/ml of human protein and 100 mg/ml of maltose (a sugar). IgG makes up 98% of the total human protein content in the Intragam formulation and the remainder are

immunoglobulins A and M (IgA and IgM). If biosensing of IgG from a multi-component solution such as Intragam containing potential interferences (IgA and IgM) can be achieved, this biosensor could become a useful tool for protein detection from real-life samples such as body fluids where the biosensor platform would be exposed to all types of biological species (cells, proteins, hormones etc.).

Similar to the previous optical porous silicon IgG biosensors, the biosensor developed here also utilises a cascade of immune reactions to detect IgG. A sandwich immunoassay (comprising the HRP/TMB system) was adapted to the porous silicon platform, as described in the previous two sections, to develop a procedure for detecting IgG in solution. A polyclonal human antibody that has a main specificity for the heavy chain of human IgG (referred to as the capture antibody or anti-human IgG) was immobilised on porous silicon. This antibody formulation comprises over 94% of anti-human IgG of the overall protein content but also contains antibodies that can bind human IgA and IgM. Therefore, the biosensor can also be used for the detection of IgA and IgM antibodies (with appropriate secondary anti-human IgA and IgM) but this was not investigated in this study. The capture antibody was covalently immobilised via an intermediate silane tether (IPTES – this is the same silane that had been used in Part 1 of this thesis to couple IGF-1). The principle of the immobilisation procedure was described in Part 1 of this thesis (refer to **pages 90-103**). Briefly, the capture antibody was covalently attached to porous silicon by formation of a urea bond between amino groups on the protein reacting with isocyanate groups on the functionalised porous silicon (refer to **Scheme 2.3**). Possibly, the antibody could be tethered to the surface at its antigen-binding site as shown in **Scheme 2.3**. If this reaction occurred, the other antigen-binding site of the capture antibody would still remain available for binding human IgG. However, IgG can also be covalently linked through amino groups of the side chains of the antibody, such as lysine, leaving free both of its antigen-binding sites for antigen capture.

After having covalently immobilised the capture antibody to porous silicon, the biosensor platform was next assembled into the plexiglass fluidic cell (shown in **Figure 2.11**). The test (Intragam) solution containing the target analyte (human IgG) was injected over the porous silicon surface. As the molecule enters the macropores, it can interact with the available antigen-binding sites of the immobilised capture antibody. To

reduce the chance of non-specific protein binding, the test solution is prepared in buffer supplemented with a small amount (50  $\mu\text{g/ml}$ ) of BSA. Any protein that has not specifically reacted with the capture antibody is then washed away with Tween<sup>®</sup> 20 and PBS. HRP-conjugated antibody that is only specific for human IgG, was next injected and allowed to interact with the captured human IgG. Any HRP-conjugated antibody that had not specifically reacted inside the pores was washed away. The final step of this assay involved injecting a formulation of TMB. A cationic radical generated by the HRP/H<sub>2</sub>O<sub>2</sub> catalysed oxidation of TMB, as described in the previous section, causes accelerated corrosion of the porous silicon film that was detected as a slope change of the EOT. This procedure is illustrated in **Figure 2.23**.



**Scheme 2.3.** A possible reaction between an immunoglobulin and a surface isocyanate reactive group, resulting in the formation of a urea bond. R denotes the hydrocarbon chain of IPTES that is linked to the porous silicon chip. The immunoglobulin (G) is comprised of two heavy polypeptide chains (dark and light blue regions) and two light polypeptide chains (red and orange regions) that are linked together by disulphide bonds (black lines). The V structure contains both heavy and light chains with variable regions (light blue and orange regions), which bind antigens with high affinity and specificity. The antigen binding sites also contain free amino groups that can react with isocyanates. The stem region is made from the heavy polypeptide chains that contain free carboxylic end groups. The dark blue regions indicate the area of the immunoglobulin that is virtually constant within a class of immunoglobulins. Note – only the terminal amino groups of IgG are shown in the scheme; the antibody can also covalently link to IPTES functionalised porous silicon by other amino groups on the side chains of the antibody, such as lysine.

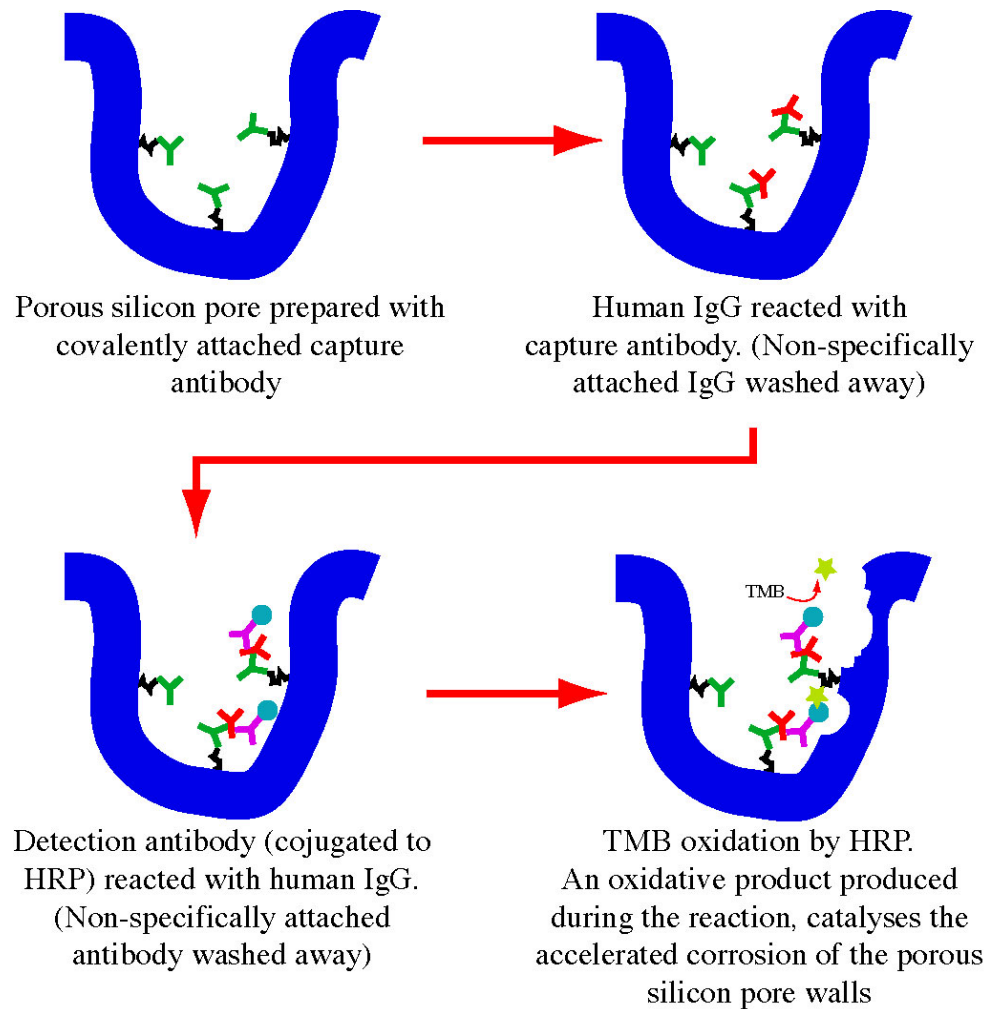


**Figure 2.23.** A cartoon illustrating an immunoassay inside a porous silicon pore. The capture antibody (green Y) is first covalently linked to porous silicon via a IPTES linker (black line). The antibody can then bind human IgG (red Y). The detection antibody (purple Y) conjugated to HRP (blue circle) then binds to human IgG. HRP finally catalyses the oxidation of TMB causing a rapid dissolution of porous silicon.

In the first experiment, the readout signal was compared on samples where the analyte injected was either Intragam or BSA at a concentration of 100  $\mu\text{g/ml}$  (**Figure 2.24**). The concentration of Intragam described in this thesis refers to the total human protein content of the formulation and therefore the total concentration of IgG that was detected in each experiment is slightly overestimated (by approximately 2%). In each of the experiments, the incubation times of antigen (20 min) and detection antibody (25 min) and the wash steps' times and volumes were kept constant. Also, the formulations containing the target antigen or the detection antibody were prepared in PBS containing 50  $\mu\text{g/ml}$  of BSA to reduce non-specific binding of these proteins (or other proteins that may be present in the test solutions) binding non-specifically to the porous silicon film, which can lead to false results. The wash steps referred to at the bottom of the graph in **Figure 2.24** involved first washing with 3 ml of PBS- Tween<sup>®</sup> 20 (PBS-T) (0.5% v/v of Tween<sup>®</sup> 20) and then immediately flushing the surfactant from the porous silicon surface with 10 ml of PBS. The first wash with PBS containing Tween<sup>®</sup> 20 detergent was used to remove non-specifically attached proteins and the second wash in PBS was required because the detergent with a higher refractive index of 1.48 to that of water (1.33) results in a bulk effect on the measured EOT, which complicates the interpretation of the data [79].

After injecting a precipitating formulation of TMB over both surfaces, the EOT sharply increased (due to the TMB bulk effect discussed in the previous section) (**Figure 2.24**). Soon after, the measured EOT significantly decreased for the sample that was reacted with Intragam and at a much faster rate compared to the corrosion rate prior to injecting TMB. In contrast, the corrosion rate was not accelerated on porous silicon exposed to BSA (**Figure 2.24**). Therefore, a distinct readout signal was generated on the sample exposed to Intragam compared to the sample exposed to BSA. This indicated that the biosensor specifically detected the target analyte (IgG). Also, no increase in EOT was observed as a result of TMB precipitation (that was to be expected from the response shown in **Figure 2.19** in the previous section) probably because the experimental conditions used in the previous section allowed for more HRP attachment on porous silicon in comparison to the biosensing conditions used here, resulting in faster substrate (TMB) oxidation and consequently precipitation. However, any precipitate entering the pores may also interfere with the readout signal, which was designated as an increase in the rate of EOT decay of the porous silicon film.

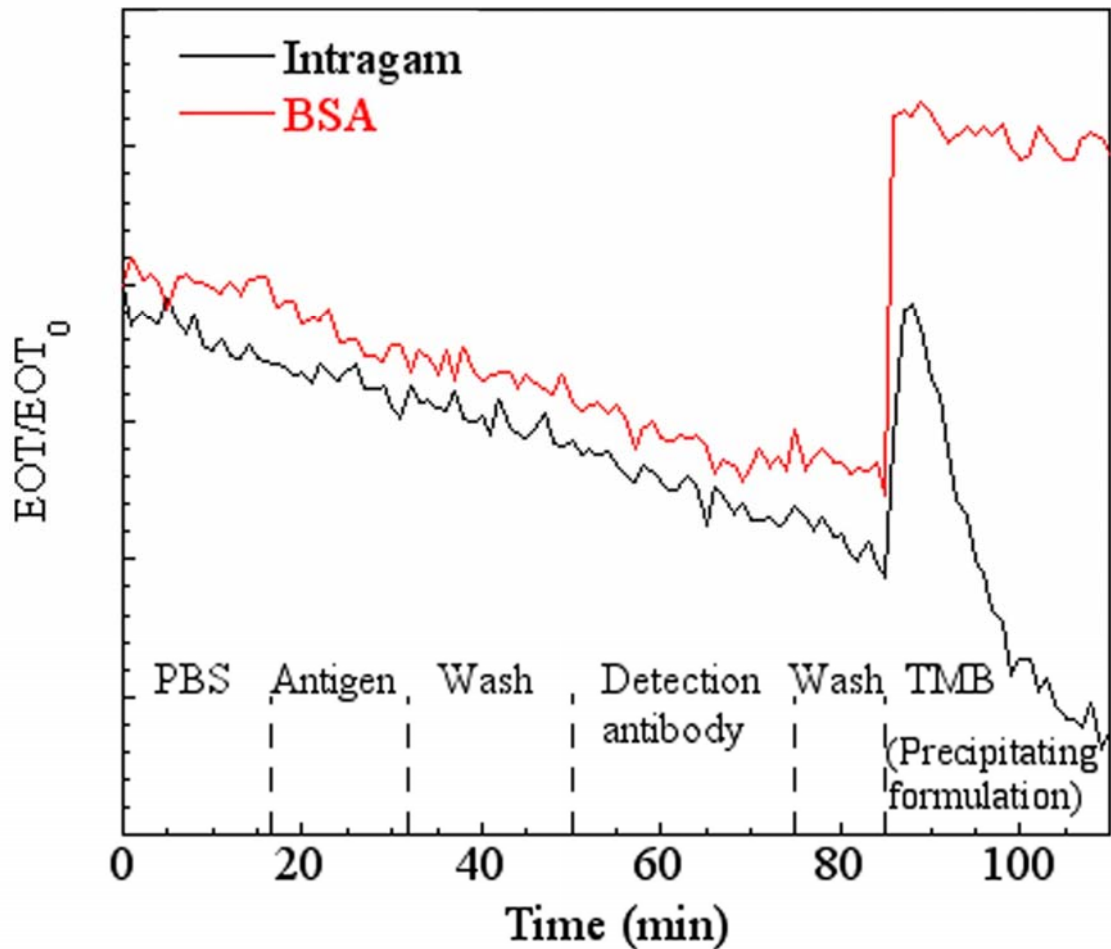


**Figure 2.24.** A time course graph of an Intragam biosensing experiment displaying the EOT of the porous silicon material measured by means of interferometric reflectance spectroscopy. Porous silicon, prepared at  $450 \text{ mA/cm}^2$  and  $4.5 \text{ C/cm}^2$ , was ozone oxidised and then functionalised with 3-isocyanatopropyl triethoxysilane (IPTES) and reacted with  $12.5 \text{ }\mu\text{g/ml}$  of the capture antibody (anti-human IgG). Shown at the bottom of the graph are the various steps performed during a typical biosensing experiment that was developed for detecting IgG. The surface was first incubated with PBS for 15 min before the antigen (Intragam) or the negative control (BSA) at  $100 \text{ }\mu\text{g/ml}$  was injected and incubated over the surface for 20 min. The surface was then washed with PBS-Tween<sup>®</sup> 20 (PBS-T; Tween<sup>®</sup> 20 concentration at 0.5% (v/v)) followed by a wash in PBS and allowed to incubate in PBS for 15 min. The detection antibody, HRP conjugated anti-human IgG, (used at a dilution of 1/500 from a commercial stock solution), was then injected and allowed to react with the target analyte for 25 min. Unreacted detection antibody was removed with a final PBS-T/PBS wash step and the surface was allowed to incubate in PBS for 10 min. A commercially available precipitating formulation of TMB was finally added and incubated over the porous silicon surface. Refer to **pages 181-182** for more detail of the biosensing experimental procedure.

Next, precipitating and non-precipitating TMB formulations were compared in the immunoassay described above. The non-precipitating TMB formulation is developed specifically for ELISA applications where the readout signal is a colour change measured spectroscopically and so no precipitation is desirable; whereas the precipitating formulation is used when precipitation is required as a visual aid to determine whether or not an immune reaction had taken place, such as for immunoblot applications.

The results of the immunoassay are shown in **Figure 2.25**, which compares the change in slope upon injecting precipitating and non-precipitating TMB formulations to the slope of the curve (that is the EOT/min) from PBS, as part of the last wash step of the assay, as outlined in **Figure 2.24**. Later, as will be discussed in the next section of Part 2: Results and Discussion, the change in slope after injecting the substrate formulation was used to calculate the readout signal to obtain quantitative data. In **Figure 2.25**, both samples displayed similar background porous silicon degradation rates in PBS. After injecting either precipitating or non-precipitating TMB formulations, there was a large sharp increase in EOT attributed to a bulk effect (refer to **Figure 2.21 A** in the previous section). The larger bulk effect observed when the non-precipitating TMB formulation was injected over porous silicon, in comparison to the precipitating TMB formulation, suggests the solvent type is different or the concentration of solvent is higher in the non-precipitating TMB formulation compared to the precipitating formulation. Both formulations are proprietary and information on the exact composition is not available from the supplier. Soon after, the EOT on both samples began to decay. However, the degradation rate of the porous silicon film appeared greater after injecting the precipitating TMB formulation compared to the non-precipitating formulation. This may be a consequence of a lower TMB concentration (to improve product solubility) in the non-precipitating TMB formulation compared to the precipitating formulation. A lower concentration of TMB would result in a lower concentration of TMB-derived free radicals degrading the porous silicon film as the TMB is oxidised by HRP/H<sub>2</sub>O<sub>2</sub>. Also, after injecting the precipitating TMB formulation, the slope of EOT/min was slightly different between the early stages of TMB oxidation (first 10 min) compared to the final 10 min (highlighted by the dashed lines in **Figure 2.25**). This was also observed in **Figure 2.24**. As shown in **Figures 2.24** and **2.25**, the EOT decay slowed down after the initial stages of TMB oxidation. Because this was not apparent when the non-

precipitating TMB formulation was injected (**Figure 2.25**), it can be assumed that this change in slope is caused by the onset of TMB precipitation deposition inside the porous silicon layer. This would cause a refractive index increase and therefore an EOT-increasing contribution. This would counteract the decrease in EOT caused by porous silicon degradation. Furthermore, the TMB-derived precipitation products coating the porous silicon film could also shield the surface from TMB-derived free radicals, slowing down or preventing further oxidative, hydrolytic corrosion of the porous silicon film.

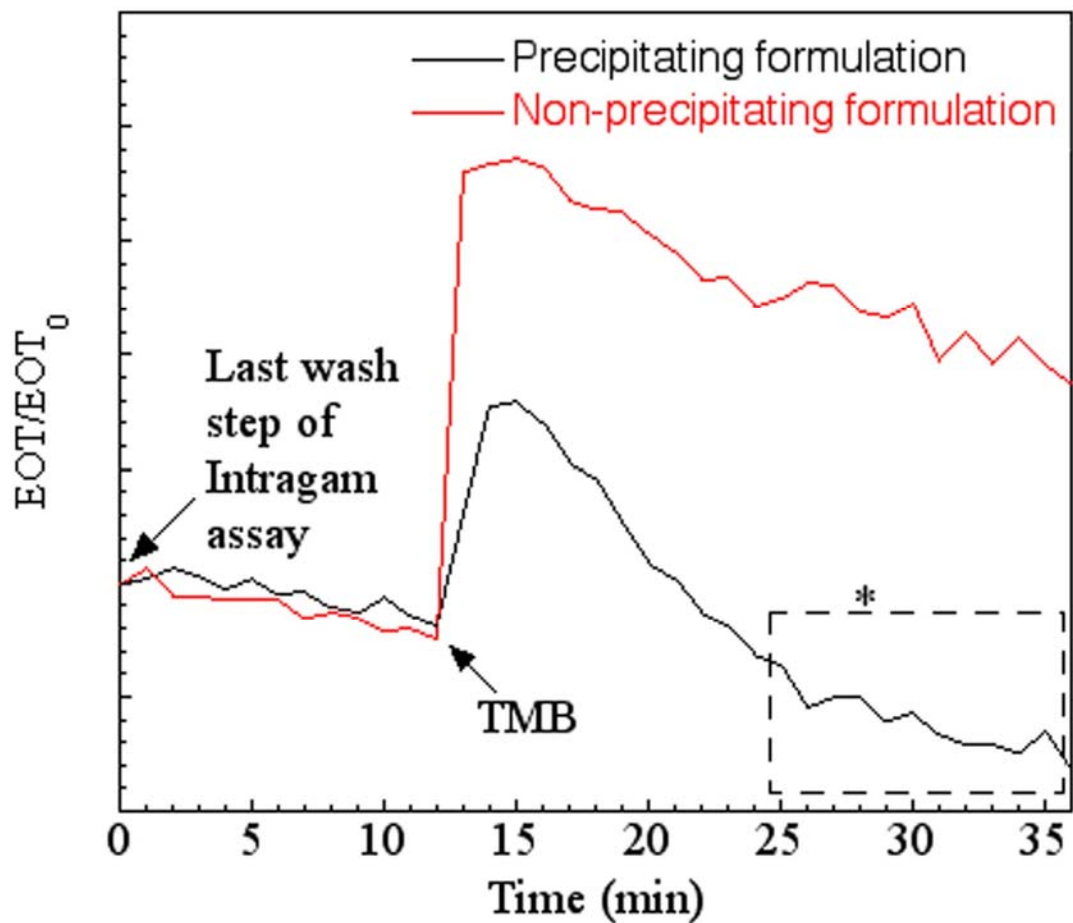


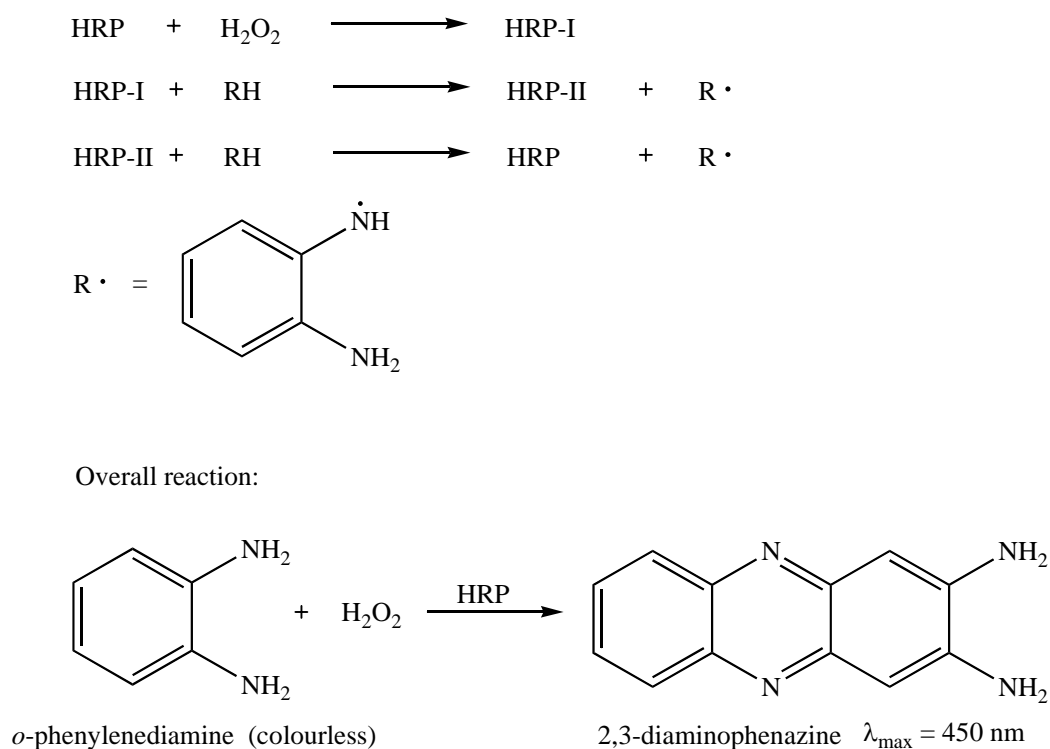
**Figure 2.25.** Intragam biosensing experiments where either commercially available precipitating or non-precipitating TMB formulations were compared. TMB solutions were injected over the surface in the final step of the assay. The EOT slope from the final wash step of the assay is also shown (refer to **Figure 2.24**). The porous silicon chip was prepared at  $450 \text{ mA/cm}^2$  and  $4.5 \text{ C/cm}^2$ , ozone oxidised, functionalised with IPTES and reacted with  $12.5 \text{ }\mu\text{g/ml}$  of anti-human IgG. Intragam was used at  $100 \text{ }\mu\text{g/ml}$  in both experiments. \* A highlighted region by the dashed lines where a slope change was observed possibly as a result of TMB precipitation inside the porous silicon layer. Refer to **pages 181-182** for more detail of the experimental procedure.

So far, the procedure for detecting IgG in an Intragam formulation has been established. The readout signal was chosen as the change in the degradation rate (EOT/min) of the porous silicon film after injecting TMB compared to the degradation rate obtained in PBS (prior to injection of TMB). A precipitating TMB formulation appeared to be more effective than the non-precipitating TMB formulation. However, the readout signal is still rather complicated and difficult to interpret for quantitative analysis because the TMB formulations cause initial increases in EOT (bulk effects) and also TMB precipitation can interfere with the readout signal.

Therefore, in another attempt to improve the readout signal, an alternative aromatic substrate molecule, *o*-phenylenediamine (OPD), was tried because the oxidation of OPD can also be catalysed by HRP/H<sub>2</sub>O<sub>2</sub>. When reconstituted in water, the concentration of each ingredient is 0.4 mg/ml OPD, 0.4 mg/ml of urea-H<sub>2</sub>O<sub>2</sub> buffer and 0.05 M of phosphate-citrate at a pH of 5.0. When OPD becomes oxidised by HRP/H<sub>2</sub>O<sub>2</sub>, a yellow-coloured product is formed and commercial microplate readers in ELISA experiments can readout the intensity of the yellow colour formed in microplate wells containing the test solutions. The final yellow product formed during the HRP/H<sub>2</sub>O<sub>2</sub> catalysed oxidation of OPD is thought to be produced from a free-radical intermediate [80-81]. As shown in **Scheme 2.4**, HRP undergoes two oxidation states (HRP-I and HRP-II) generating free radicals derived from OPD. These free radicals then combine in a ring-forming reaction to form a yellow product, 2,3-diaminophenazine, which has a  $\lambda_{\text{max}}$  of 450 nm. Similar to the induced degradation of porous silicon from TMB-derived free radicals (described in the previous section), the free radicals generated during the oxidation of OPD may also accelerate the corrosion of the porous film. This was tested in the next two experiments.

Referring to **Figure 2.26**, a baseline in the rate of ozone-oxidised porous silicon corrosion was first established in PBS at pH 7.4. Then a freshly prepared reaction mixture, consisting of a reconstituted OPD formulation and 50  $\mu\text{M}$  of HRP, was injected. After injecting the reaction mixture, a sharp decrease in EOT was immediately observed. The decrease in the EOT was likely caused by the porous silicon film being attacked by the free radical that was generated during the oxidation of OPD. Notably, there was no bulk effect observed on the porous silicon film by an increase in EOT after injecting the substrate, which was observed for both of the TMB (precipitating and non-

precipitating) formulations. Also, no precipitation products, as a result of HRP/H<sub>2</sub>O<sub>2</sub> catalysed oxidation of OPD, was detected in the OPD-HRP/H<sub>2</sub>O<sub>2</sub> reaction solution. The slope change detected 1-2 min after injecting the OPD-HRP/H<sub>2</sub>O<sub>2</sub> reaction solution, as shown in **Figure 2.26**, was attributed to all of the OPD starting material being consumed in the reaction solution, resulting in more decay of the EOT.



**Scheme 2.4.** A possible mechanism of HRP/H<sub>2</sub>O<sub>2</sub> catalysed oxidation of OPD. The scheme was adapted from Tarcha et al. and Bystryak et al. [80-81].

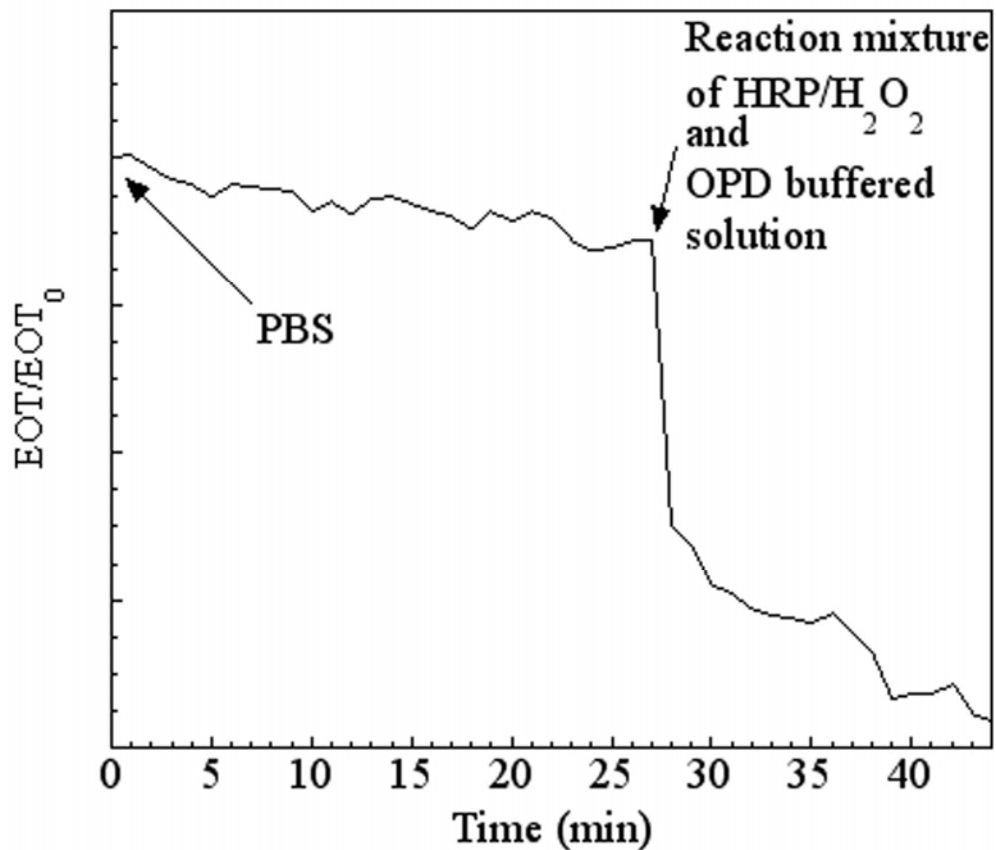


**Figure 2.26.** A time course graph displaying the EOT of the porous silicon material measured by means of interferometric reflectance spectroscopy. Porous silicon was prepared at  $450 \text{ mA/cm}^2$  and  $4.5 \text{ C/cm}^2$  and was ozone oxidised. In this experiment, a slope of the porous silicon EOT over time was established before a freshly made reaction mixture of OPD (prepared according the manufacturer's instructions) and  $50 \mu\text{M}$  of HRP was injected. The freshly made reaction mixture had a pH of 5.8 and this remained constant over the analysis time frame of 20 min that is shown in the graph.

Next, the readout signal was compared after injecting OPD, a precipitating TMB formulation and a non-precipitating TMB formulation during the final stages of the immunoassay. Intragam was used at a total human protein concentration of  $100 \mu\text{g/ml}$  in these experiments. The time course graphs of the EOT from the porous silicon films obtained after the last wash step of the assay (refer to **Figure 2.24**) are shown in **Figure 2.27**. As shown in this graph, when the substrate formulations (OPD and precipitating or non-precipitating TMB formulations) were injected over the positive controls (porous silicon biosensor platform exposed to Intragam), a readout signal was produced that was distinct to the negative controls (porous silicon biosensor platform exposed to BSA). Furthermore, the readout signal produced after injecting OPD was more pronounced compared to the TMB formulations that were tested in the assay.

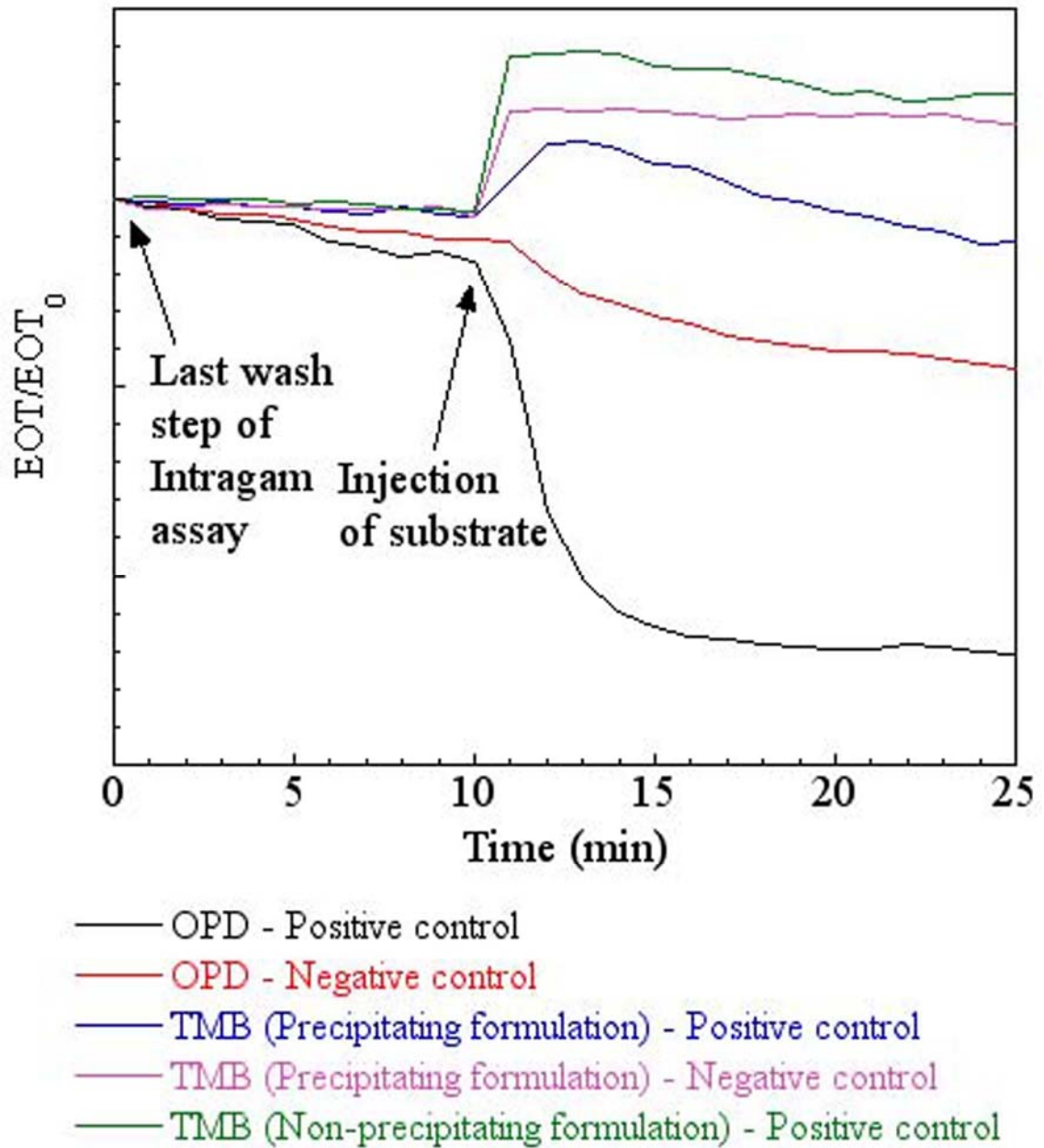


**Figure 2.27.** Intragam biosensing experiments where commercially available OPD and precipitating or non-precipitating TMB formulations were injected over the surface in the final step of the assay. The EOT slope of the porous silicon film from the final wash step of the assay is shown (refer to **Figure 2.24**). The porous silicon chip was prepared at  $450 \text{ mA/cm}^2$  and  $4.5 \text{ C/cm}^2$ , ozone oxidised, functionalised with IPTES and reacted with  $12.5 \text{ }\mu\text{g/ml}$  of anti-human IgG. Positive controls of Intragam or BSA as negative controls (both at a concentration of  $100 \text{ }\mu\text{g/ml}$ ) were used in these experiments. Refer to **pages 181-182** for more detail of the experimental procedure.

To summarise this section, the HRP/H<sub>2</sub>O<sub>2</sub> catalysed oxidation of TMB was used to establish an interferometric biosensor based on functionalised porous silicon for specifically detecting IgG from an Intragam test solution. It was demonstrated that a distinct readout signal was produced when the porous silicon biosensor platform was exposed to 100 µg/ml of the total human protein content of Intragam by using either precipitating or non-precipitating TMB formulations. Oxidation of a different type of aromatic substrate (OPD) produced a more pronounced and interpretable readout signal. Therefore, in the final set of experiments, the more suitable (OPD) substrate will be used to assess the performance of the biosensor and identify possible means of improving the biosensor's performance characteristics.

### 2.3.4 Assessing the performance of the enzyme-based interferometric biosensor on functionalised porous silicon

The purpose of the next set of experiments was to test the performance of the enzyme-based functionalised porous silicon interferometric biosensor. This was accomplished again by first immobilising the capture antibody on IPTES functionalised porous silicon (refer to **pages 181-182**). The molecule became covalently attached by formation of a urea bond. The biosensing procedure was the same as outlined in the previous section, except that OPD substrate was used. The time course graph of the EOT of the porous silicon film after exposing the surface to a range of Intragam (total human protein) concentrations (indicated in the graph), is shown after the last wash step of the assay in **Figure 2.28**. As illustrated in **Figure 2.28**, no significant change in EOT was detected after injecting OPD over the porous silicon biosensor platform that was not exposed to Intragam (0 ng/ml). This indicates that there is minimal non-specific protein (detection antibody) binding to the porous silicon film.

Similarly, after injecting Intragam at a (total human protein) concentration of 5 and 50 ng/ml over the porous silicon biosensor platform, no significant change in EOT was observed (**Figure 2.28**). Also, the readout signal, defined as the change in slope after injecting the substrate solution compared to the slope in PBS from the last wash step of the immunoassay, was indistinguishable to the background change in EOT (obtained on the porous silicon chip reacted with 0 ng/ml of Intragam). After injecting OPD over the porous silicon biosensor platform that was reacted with 100 ng/ml of Intragam, a distinct change in EOT slope was observed. Therefore, the detection limit for IgG of the biosensor was determined to be at 100 ng/ml. This readout signal importantly became more pronounced when the porous silicon biosensor platform was reacted with a higher Intragam (total human protein) concentration of 200 ng/ml (**Figure 2.28**). These results indicate that the biosensor could specifically detect IgG in a dose dependent manner.

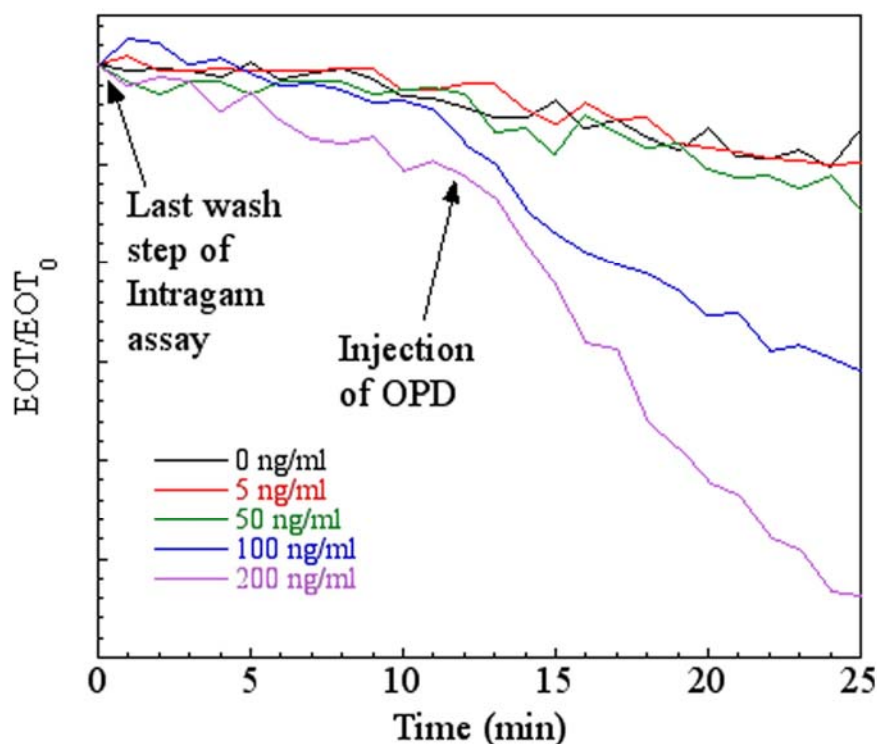


**Figure 2.28.** A time course graph displaying the EOT of porous silicon after the final wash step of the assay and after injecting an OPD formulation over the surface (refer to the previous section for the biosensing protocol). The porous silicon chip was prepared at  $450 \text{ mA/cm}^2$  and  $4.5 \text{ C/cm}^2$ , ozone oxidised, functionalised with IPTES and then reacted with  $12.5 \text{ }\mu\text{g/ml}$  of anti-human IgG. Intragam was injected over the surface at a range of concentrations as indicated in the graph. Refer to **pages 181-182** for more detail of the biosensing experimental procedures.

Next, a calibration plot was constructed to test the feasibility of obtaining quantitative results from the biosensor. The porous silicon biosensor platform was reacted with total human protein concentrations of 0, 100, 200 and 1000 ng/ml from the Intragam test solution. Then the readout signal, defined as the change in slope obtained after injecting the substrate solution, was calculated by dividing the rate of EOT change ( $\text{min}^{-1}$ ) from the first 5 min upon exposing the porous silicon film to OPD ( $\text{EOT}_{\text{OPD}}$ ) over the rate of EOT change calculated from the last 5 min when the porous silicon chip was exposed to PBS just prior to injecting OPD ( $\text{EOT}_{\text{PBS}}$ ). The calculated readout ( $\text{EOT}_{\text{OPD}}/\text{EOT}_{\text{PBS}}$ ) was then plotted against the corresponding concentration of Intragam. This calibration curve is shown in **Figure 2.29**. The results were referenced to the negative control sample that was reacted with 0 ng/ml of protein. At the high IgG concentration range (of 1000 ng/ml) that was tested in this study, the calibration curve was non-linear as often seen in immunoassays [82].

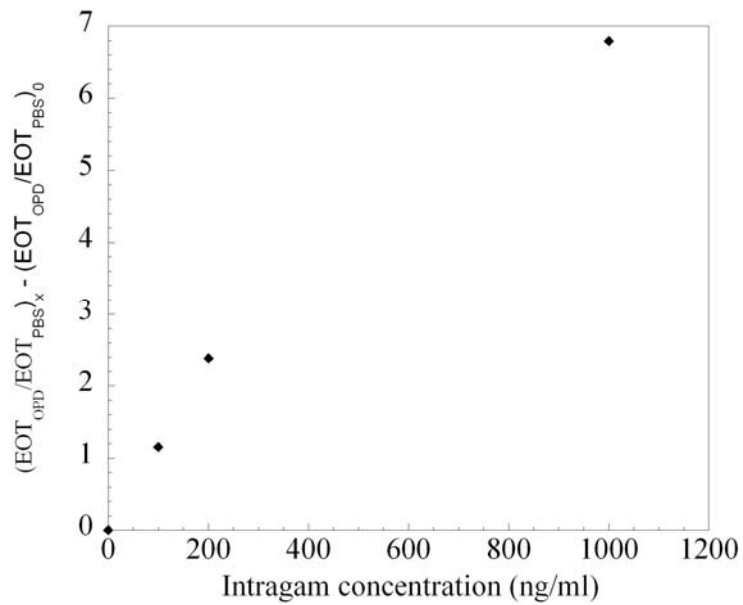


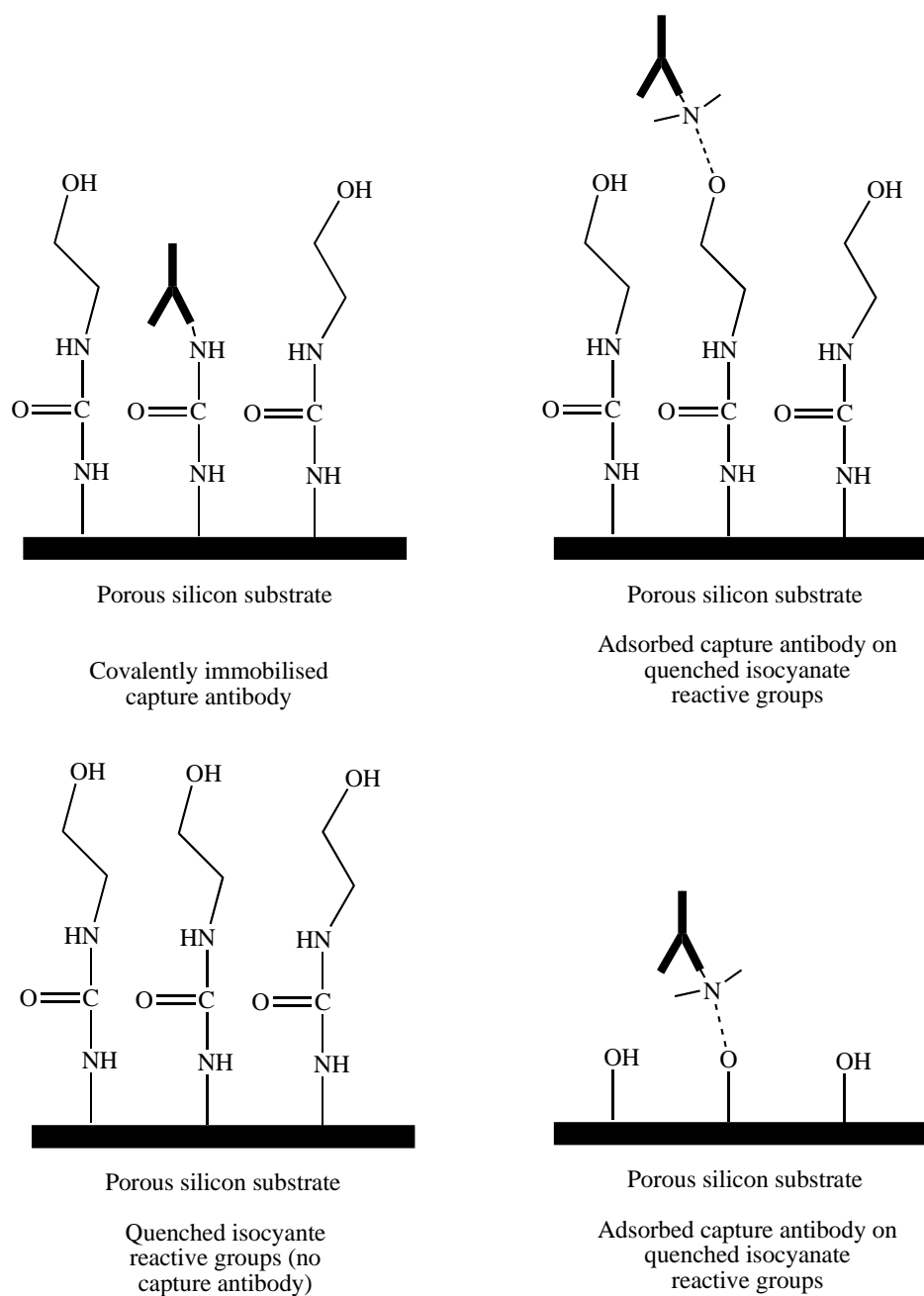
**Figure 2.29.** A calibration plot derived from biosensing assays for the detection of IgG (from Intragam). The readout signal (determined by dividing the rate of change of the EOT of the porous silicon material after injecting OPD (first 5 min) over the rate of change of the EOT that was obtained in PBS from the last 5 min of the final wash step of the assay) was plotted against the corresponding (total human protein) concentration of Intragam. The  $(EOT_{OPD}/EOT_{PBS})_x$  for each concentration (100, 200 and 1000 ng/ml) was subtracted from the  $(EOT_{OPD}/EOT_{PBS})_0$  of the 0 ng/ml negative control sample.

In order to characterise the efficiency of the covalent immobilisation methodology on the porous silicon biosensor platform, several control reactions (for the immobilisation of the capture antibody onto porous silicon) were carried out and the performance of the biosensor (for each immobilisation chemistry) was assessed. Four different surfaces were prepared: IPTES functionalised porous silicon was reacted with the capture antibody and any unreacted isocyanate groups were subsequently quenched with ethanolamine hydrochloride (covalently immobilised capture antibody) (this was the same immobilisation strategy as described above); isocyanate groups on IPTES functionalised porous silicon were quenched with ethanolamine hydrochloride before reacting the capture antibody with the surface (adsorbed capture antibody on quenched isocyanate reactive groups); IPTES functionalised porous silicon was incubated in PBS for the same period of time as the capture antibody (2 h) before quenching any unreacted isocyanate groups with ethanolamine hydrochloride (quenched isocyanate reactive groups, no capture antibody); and finally, oxidised porous silicon was incubated with the capture antibody (adsorbed capture antibody on oxidised surface). These four surfaces were subsequently used to detect IgG in an Intragam formulation at a total human protein concentration of 200 ng/ml. These surfaces are shown in **Scheme 2.5** and the results of the biosensing experiments are shown in **Figure 2.30**.

As anticipated, IgG was not detected on the IPTES functionalised porous silicon biosensor platform not loaded with the capture antibody (quenched isocyanate reactive groups, no capture antibody) (**Figure 2.30**). There was no significant change in the slope after injecting OPD indicating that the surface had not captured IgG. No definite response was observed because the surface was not loaded with a protein that could recognise IgG or contained any (known) functionality that could promote protein attachment (apart from the isocyanate groups that were quenched prior to the biosensing experiment). Also, the results confirmed that non-specific protein binding (from IgG or the detection antibody) was minimal because the readout signal ( $EOT_{OPD}/EOT_{PBS} = 1.33$ ) produced on this sample was the lowest of the samples compared in the graph.

When the capture antibody was adsorbed to oxidised porous silicon, the readout signal produced from the biosensing experiment was only slightly increased ( $EOT_{OPD}/EOT_{PBS} = 1.57$ ). This could be due to a number or combination of possible scenarios: the capture antibody adsorbed to porous silicon at a low surface density; the capture

antibody weakly adsorbed to porous silicon and then was washed away during the wash steps of the biosensing experiment, or the capture antibody had denatured during the adsorption process. All of these situations would prevent a large readout signal.



**Scheme 2.5.** Schemes of 4 different possible surface chemistries prepared for biosensing. The results of these experiments are shown in **Figure 2.30**. The porous silicon surface is shown as a solid black line. Hydrogen bonding is shown by the broken lines. Only a terminal amino group of IgG is shown to have reacted with the surfaces; the antibody can also covalently link to IPTES functionalised porous silicon by other amino groups on the side chains of the antibody, such as lysine.

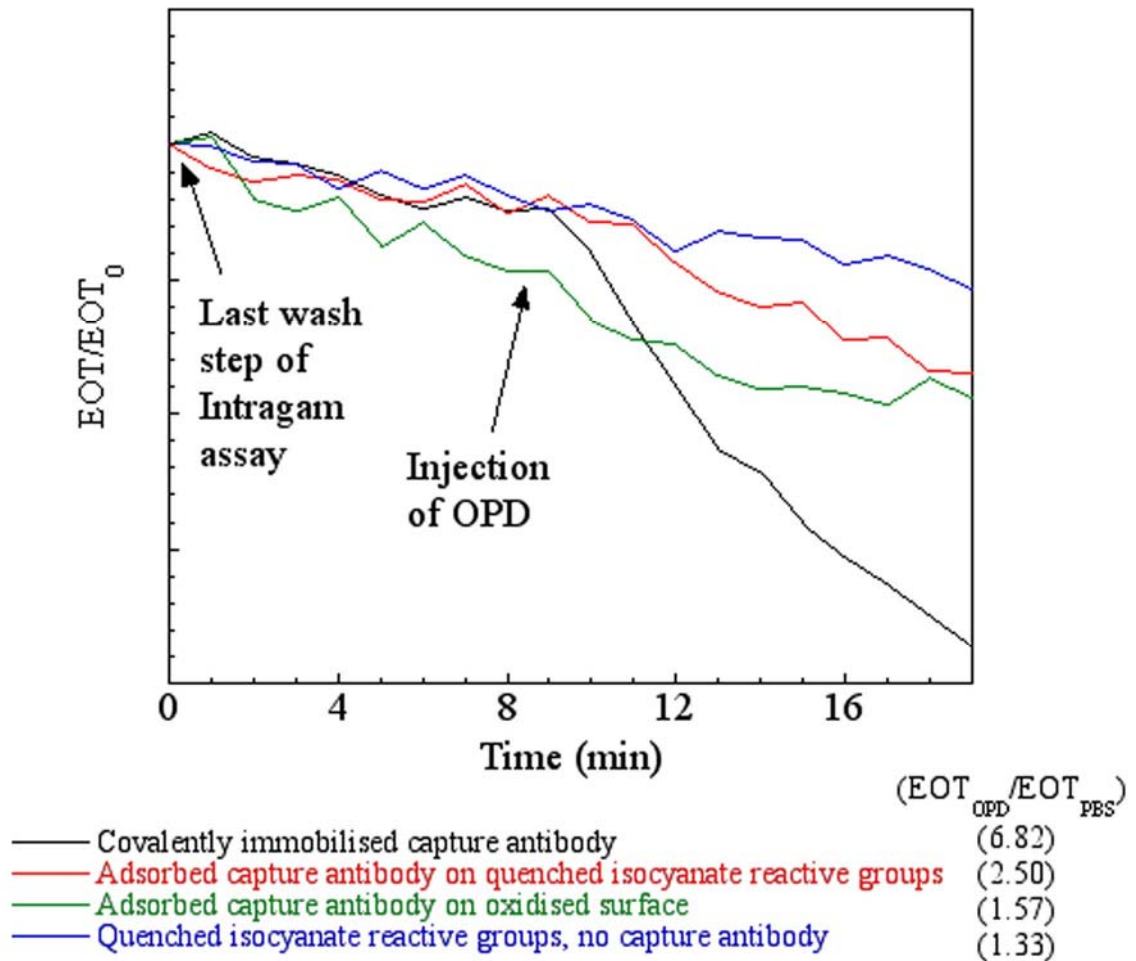


**Figure 2.30.** Graph obtained from the biosensing experiments performed on porous silicon samples with different surface chemistries that were used to detect IgG from an Intragam formulation at a total human protein concentration of 200 ng/ml. The porous silicon chip was prepared at 450 mA/cm<sup>2</sup> and 4.5 C/cm<sup>2</sup> and was ozone oxidised. The surface was then functionalised with IPTES and reacted with 12.5 µg/ml of anti-human IgG (Covalently immobilised capture antibody); the isocyanate groups of a second functionalised porous silicon surface were quenched with ethanolamine hydrochloride before allowing the capture antibody to adsorb onto the surface (**Adsorbed capture antibody on quenched isocyanate reactive groups**); a third IPTES functionalised surface was quenched with ethanolamine hydrochloride (**Quenched isocyanate reactive groups, no capture antibody**); finally, the capture antibody was adsorbed to oxidised porous silicon (**Adsorbed capture antibody on oxidised surface**). The EOT of porous silicon from the final wash step of the assay is shown.  $EOT_{OPD}$  was determined from the change in EOT/min from the first 5 min after injecting OPD and  $EOT_{PBS}$  corresponds to the change in EOT/min from the last 5 min of the final PBS-T and PBS wash step (just prior to injecting OPD). Refer to **pages 181-182** for more detail of the biosensing experimental procedures.

When the capture antibody was covalently immobilised on IPTES functionalised porous silicon, a conspicuous change in slope was observed after injecting OPD (**Figure 2.30**). The calculated readout signal ( $EOT_{OPD}/EOT_{PBS} = 6.82$ ) was over 4-fold compared to the readout obtained on the porous silicon biosensor platform loaded with the adsorbed capture antibody (but not functionalised with IPTES). Therefore, the performance of the biosensor was enhanced when the capture antibody was covalently attached to porous silicon in comparison to when it was adsorbed on to the biosensor platform. The readout signal produced on porous silicon loaded with the covalently attached capture antibody was also higher (2.6-fold) than the signal produced when the capture antibody was reacted with quenched isocyanate groups of IPTES functionalised porous silicon. This observation supports the view that the performance of the biosensor is enhanced when the capture antibody is covalently attached to the porous silicon film.

This outcome can be explained by stronger bonds being formed between the capture antibodies and the isocyanate groups on the porous silicon surface, in comparison to weaker chemisorption or physisorption interactions between the protein and the quenched isocyanates or the oxidised porous silicon surface. Alternatively, the covalent reaction may have occurred much more rapidly than the adsorption process. Therefore, more of the capture antibody would have reacted with the isocyanate groups of the IPTES functionalised porous silicon surface and less protein would have been removed during the washing steps.

In an attempt to further improve the performance of the biosensor, porous silicon samples were prepared at two levels of surface oxidation and at two different porous silicon layer thicknesses. Again, these biosensor platforms were used to detect IgG in an Intragam formulation at a total human protein concentration of 200 ng/ml. All surfaces were prepared in the same manner as described previously (refer to **pages 181-182 and 201**) by functionalising with IPTES and subsequently covalently attaching anti-human IgG, and all of the biosensing parameters were kept constant to those used in the previous experiments.

First, a comparison of the readout signal was made between ozone and bromine oxidised porous silicon prepared at  $450 \text{ mA/cm}^2$  and  $4.5 \text{ C/cm}^2$ . The only difference between these samples was the level of surface oxidation. As shown in the diffuse

reflectance infrared spectra, ozone oxidation resulted in a higher level of surface oxidation compared to surfaces oxidised by bromine (refer to **Figure 2.16 B** and **C**). These samples were then functionalised with IPTES and subsequently with the capture antibody. After injecting OPD at the final stage of the biosensing experiments carried out on these samples, the change in the rate of the EOT decay ( $EOT_{OPD}/EOT_{PBS}$ ) was determined to be 6.82 and 8.96 for ozone and bromine oxidised surfaces, respectively (**Figure 2.31**). The higher readout signal obtained on porous silicon oxidised by bromine compared to when it was oxidised by ozone, could be explained by the lower level of oxidation achieved through bromine oxidation. The induced degradation of the porous silicon film through silicon hydride groups undergoing oxidative hydrolysis from free radicals produced during the oxidation of OPD (by HRP/H<sub>2</sub>O<sub>2</sub>), could therefore occur more effectively on the bromine oxidised surface, which possessed a higher surface density of silicon hydride groups than the ozone oxidised porous silicon film (refer to the infrared spectra shown in **Figure 2.16 B** and **C**).

The performance of the biosensor could be even further improved when a thicker layer porous silicon layer was used as the sensing matrix. Porous silicon was prepared at 450 mA/cm<sup>2</sup> and at two different charge densities of 4.5 and 9.0 C/cm<sup>2</sup> to produce porous silicon films of a similar pore diameter in the order of 400 nm and porous silicon films with depths of 2 and 4 µm, respectively (**Figure 2.14 A** and **B**). In comparison to the signal obtained on 2 µm of porous silicon film, the readout signal became greatly enhanced by nearly 3-fold when the thicker porous silicon film of 4 µm was used as the sensing matrix (**Figure 2.31**). The deeper porous silicon layer of 4 µm would result in a larger surface area for capture antibody immobilisation. Therefore, the deeper porous silicon film can support higher surface loading of the capture antibody allowing for more IgG capture upon exposing the surface to Intragam. Subsequently, a greater concentration of the detection antibody (anti-human IgG conjugated to HRP) could react with human IgG resulting in a faster rate of OPD oxidation and a faster rate of oxidative, hydrolytic porous silicon corrosion.

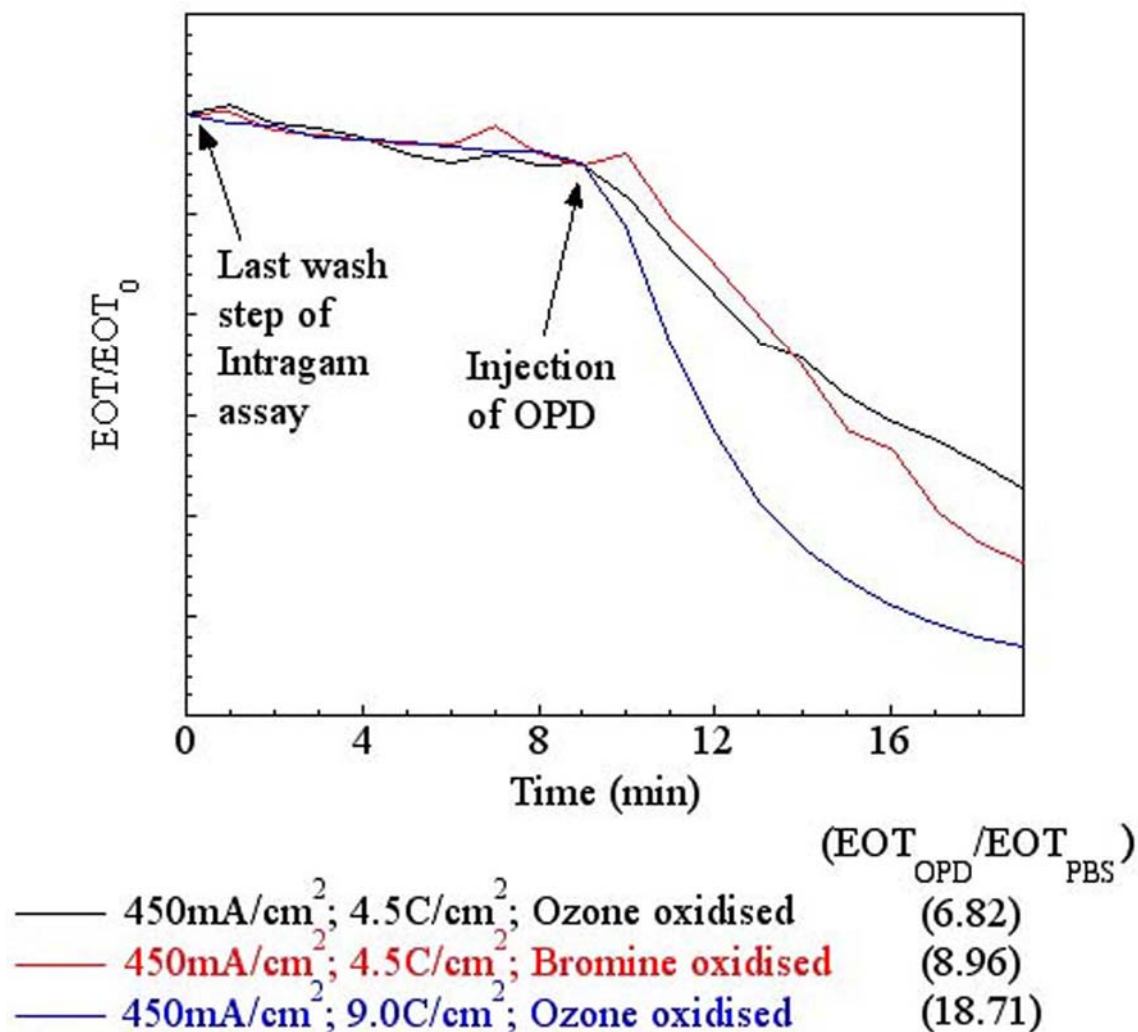


**Figure 2.31.** Biosensing experiments performed on modified porous silicon surfaces that were used to detect IgG from an Intragam formulation at a total human protein concentration of 200 ng/ml. Porous silicon was prepared at 450 mA/cm<sup>2</sup> and 4.5 C/cm<sup>2</sup> or 9.0 C/cm<sup>2</sup> and was ozone oxidised or porous silicon was prepared at 450 mA/cm<sup>2</sup> and 4.5 C/cm<sup>2</sup> and bromine oxidised. All surfaces were then functionalised with IPTES and reacted with 12.5 µg/ml of anti-human IgG. Refer to **pages 181-182** for more detail of the experimental procedures.

In summary, the readout signal of the enzyme-based interferometric porous silicon biosensor ( $EOT_{OPD}/EOT_{PBS}$ ) was established, defined and used to construct a calibration plot for a protein concentration range of 0-1000 ng/ml. Furthermore, the biosensor could detect IgG in an Intragam formulation to a sensitivity of 100 ng/ml (of total human protein concentration). Finally, the readout signal was enhanced by reducing the level of porous silicon surface oxidation, by tethering the antibody on porous silicon with covalent immobilisation (isocyanate-amino) chemistry and by increasing the depth of the porous silicon matrix.

## 2.4 Conclusions and Future Directions

Part 2 of this thesis discussed the development of a new optical interferometric biosensor. The biosensor platform was constructed from electrochemically-prepared thin films of porous silicon that acted as a sensing matrix and transducer element. Porous silicon layers were tailored specifically for this application by altering the pore size, depth and surface chemistry.

By using the technique of white light reflective interferometry to measure the effective optical thickness (EOT) of porous silicon, an enzyme-catalysed system was found (HRP/H<sub>2</sub>O<sub>2</sub>-mediated oxidation of TMB) that produced an intricate optical signal, which formed the basis of the biosensor's readout signal. The signal gave rise to 4 distinct changes in EOT during the HRP/H<sub>2</sub>O<sub>2</sub>-TMB reaction:

1. Increase in EOT caused by a bulk effect from TMB;
2. Decrease in EOT caused by accelerated corrosion of porous silicon from an intermediate TMB cationic radical produced during the oxidation of TMB by the enzyme HRP;
3. Increase in EOT due to the final oxidised TMB products precipitating on the porous silicon surface; and
4. Stabilisation of EOT when all the starting TMB material and intermediate products had oxidised or no more precipitate could enter the clogged pores resulting in no further increase in the EOT.

We used the enzyme-chromogen system for detecting human IgG from an Intragam formulation, containing a mixture of antibodies, on highly boron-doped (p-type) porous silicon that was electrochemically prepared with pore diameters in the order of 400 nm and a layer thickness of 2  $\mu$ m. Porous silicon was prepared for biosensing by first oxidising the surface with ozone, then functionalising the surface with 3-isocyanatopropyl triethoxysilane (IPTES) and finally covalently immobilising anti-human IgG on the functionalised porous

silicon surface through isocyanate-amino bioconjugate chemistry. The surface was then exposed to Intragam and the captured IgG was labeled with HRP-conjugated anti-human IgG. Finally, the surface was exposed to TMB and the EOT was measured in time lapse. We found that this sensor was sensitive and specific for the detection of IgG. However, we also discovered that another substrate, which is also oxidised by HRP, OPD, produces an even more pronounced readout signal.

We used the OPD substrate first for defining the readout signal and then for assessing and identifying means of improving the performance of the biosensor. We defined the readout signal as the change in the slope of EOT/min after injecting the OPD solution compared to the slope in PBS from the last wash step of the immunoassay ( $EOT_{OPD}/EOT_{PBS}$ ). We determined that the biosensor (as described above) could detect IgG from a total human protein concentration of Intragam to a sensitivity of 100 ng/ml. IPTES-functionalised ozone-oxidised porous silicon prepared with covalently immobilised IgG produced a readout signal over 4-fold to ozone-oxidised porous silicon prepared with adsorbed IgG. The readout signal was further enhanced on porous silicon platforms by reducing the level of surface oxidation (1.3-fold) and by increasing the thickness of the porous silicon layer to 8  $\mu\text{m}$  (2.7-fold). Therefore, the performance of the biosensor was improved by combining these features into the design of the porous biosensor platform.

In the future, it will be fundamentally important to determine if the biosensor can be used for the detection of a range of other proteins and biological species such as living cells, viruses and DNA. This will be important because if many types of biological species can be detected to a suitable sensitivity by the biosensor, the biosensor may become an extremely versatile tool in the field of life sciences such as for disease diagnostics and drug discovery.

## Overall Conclusions

This thesis described the surface modification of PECVD-Si-Ti and porous silicon biomaterials with an alkoxysilane, IPTES, for the covalent immobilisation of proteins through isocyanate-amino bioconjugate chemistry. On both surfaces, a functional surface was generated by covalently linking proteins to the respective surfaces.

IGF-1 was covalently immobilised on IPTES functionalised PECVD-Si-Ti for improving the growth of MG63 osteoblast-like cells. The immunological reactivity and biological activity of IGF-1 was enhanced when the growth factor was covalently coupled to PECVD-Si-Ti compared to when the growth factor was adsorbed on the same surface.

Anti-human IgG was covalently immobilised on IPTES functionalised porous silicon for the detection of human IgG in a sandwich immunoassay format by white light reflective interferometry. The readout signal of the biosensor was significantly higher when anti-human IgG was covalently coupled to porous silicon compared to when the antibody was adsorbed on the same surface.

By using isocyanate-amino chemistry for covalently immobilising IGF-1 on PECVD-Si-Ti, or anti-human IgG on porous silicon, and testing the performance of the protein-functionalised materials, we showed that this covalent immobilisation strategy was an ideal mechanism for delivering biologically active proteins for orthopaedic implant applications and in the design of a biosensor for biomedical diagnostics.

# References

## Part 1: Covalent immobilisation of IGF-1 on PECVD-Si-Ti for orthopaedic biomaterial applications

1. Hubbel, J.A., Langer, R. 1995, 'Tissue engineering' *Chemical and Engineering News*, **73**: p. 42-54.
2. Green, R., Davies, J., Davies, M., Roberts, C., Tendler, S. 1997, 'Surface plasmon resonance for real time *in situ* analysis of protein adsorption to polymer surfaces', *Biomaterials*, **18**: p. 405-413.
3. Santin, M., Motta, A., Denyer, S., Caanas, M. 1999, 'Effect of the urine conditioning film on ureteral stent encrustation and characterisation of its protein composition', *Biomaterials*, **20**: p. 1245-1251.
4. Mathieu, H.J. 2001, 'Bioengineered material surfaces for medical applications', *Surface and Interface Analysis*, **32**: p. 3-9.
5. Thull, R. 2001, 'Surface functionalization of materials to initiate auto-biocompatibilization *in vivo*', *Materialwissenschaft und Werkstofftechnik*, **32**: p. 949-952.
6. Helsen, J.A., Breme, H.J. 1998, '*Metals as Biomaterials*', John Wiley and Sons Ltd, West Sussex, United Kingdom.
  - a. Breme, H.J., Biehl, V., Helsen, J.A., *Metals as implants*, p. 37-71.
7. Nicholson, J.W. 2002, '*The Chemistry of Medical and Dental Materials*', The Royal Society of Chemistry, Cambridge, United Kingdom.
8. Long, M., Rack, H.J. 1998, 'Titanium alloys in total joint replacement – a materials science perspective', *Biomaterials*, **19**: p. 1621-1639.
9. Brunette, D.M., Tangvall, P., Textor, M., Thomsen, P. 2001, '*Titanium in Medicine: Material Science, Surface Science, Engineering, Biological Responses and Medical Applications*', Springer-Verlag, Berlin, Germany.
  - a. Ratner, B.D., *A perspective on titanium biocompatibility*, p. 1-12.
  - b. Tengvall, P., *Proteins at titanium interfaces*, p. 457-483.

- c. Textor, M., Sittig, C., Frauchiger, V., Tosatti, S., Brunette, D.M., *Properties and biological significance of natural oxide films on titanium and its alloys*, p. 171-230.
  - d. Esposito, M., *Titanium for dental applications (I)*, p. 827-873.
  - e. Windler, M., Klabunde, R., *Titanium for hip and knee prostheses*, p. 703-746.
  - f. Lausmaa, J., *Mechanical, thermal, chemical and electrochemical surface treatment of titanium*, p. 231-266.
  - g. Gruner, H., *Thermal spray coatings on titanium*, p. 375-416.
10. Black, J. 2006, '*Biological Performance of Materials: Fundamentals of Biocompatibility*', 4<sup>th</sup> Ed., CRC Press, Florida, United States of America.
  11. Ellingsen, J.E. 1990, 'A study on the mechanism of protein adsorption to TiO<sub>2</sub>', *Biomaterials*, **12**: p. 593-596.
  12. Steinemann, S.G. 1998, 'Titanium: the material of choice?', *Periodontology 2000*, **17**: p. 7-21.
  13. Puleo, D.A., Huh, W.W. 1995, 'Acute toxicity of metal ions in cultures of osteogenic cells derived from bone marrow stromal cells', *Journal of Applied Biomaterials*, **6**: p. 109-116.
  14. Davies, J.E. 2000, '*Bone Engineering*', Rainbow graphic and printing Ltd., Hong Kong.
    - a. Wieland, M., Sittig, C., Brunette, D.M., Textor, M., Spencer, N.D., *Measurement and evaluation of the chemical composition and topography of titanium implant surfaces*, p. 163-182.
    - b. Davies, J.E., Hosseini, M.M., *Histodynamics of endosseous wound healing*, p. 1-14.
    - c. Zaleski, D.J., *Morphogenesis of the skeletal system*, p. 15-18.
    - d. Aubin, J.E., *Osteogenic cell differentiation*, p. 19-30.
    - e. Sodek, J., Cheifetz, S., *Molecular regulation of osteogenesis*, p. 31-43.
    - f. Boskey, A.L., Paschalis, E., *Matrix proteins and biomineralization*, p. 44-62.
    - g. Parker, E., Shiga, A., Davies, J.E., *Growing human bone in vitro*, p. 63-77.

- h. Anderson, J.M., *The cellular cascades of wound healing*, p. 81-93.
  - i. Zandstra, P.W., *Challenges involved in the development of stem-cell-based technologies: hematopoiesis, osteogenesis, and beyond*, p. 94-107.
  - j. Gemmel, C.H., Park, J.Y., *Initial blood interactions with endosseous implant materials*, p. 108-117.
  - k. Thomsen, P., Esposito, M., Gretzer, C., Liao, H., *Inflammatory response to implant materials*, p. 118-136.
  - l. Lakey, L.A., Akella, R., Ranieri, J.P., *Angiogenesis: Implications for tissue repair*, p. 137-142.
  - m. Canfield, A.E., Doherty, M.J., Ashton, B.A., *Osteogenic potential of vascular pericytes*, p. 143-151.
  - n. Al-Saffar, N., Revell, P.A., *Frustrated wound healing: the immunopathogenesis of bone resorption*, p. 152-160.
  - o. Marx, R.E., *Platelet concentrate: a strategy for accelerating and improving bone regeneration*, p. 447-453.
  - p. Hosseini, M.M., Sodek, J., Franke, R.-P., Davies, J.E., *The structure and composition of the bone-implant interface*, p. 295-304.
  - q. Kokubo, T., Kim, H.M., Kawashita, M., Nakamura, T., *What kinds of materials exhibit bone-bonding?*, p. 190-194.
15. Arnold, F., West, D.C. 1991, 'Angiogenesis in wound healing', *Pharmacology and Therapeutics*, **52**: p. 407-422.
16. Clark, R.A., Lanigan, J.M., DellePelle, P., Manseau, E. Dvorak, H.F., Colvin, R.B. 1982, 'Fibronectin and fibrin provide a provisional matrix for epidermal cell migration during wound reepithelialization', *The Journal of Investigative Dermatology*, **79**: p. 264-269.
17. Madri, J.A., Pratt, B.M., Tucker, A.M. 1988, 'Phenotypic modulation of endothelial cells by transforming growth factor- $\beta$  depends upon the composition and organization of the extracellular matrix', *The Journal of Cell Biology*, **106**: p. 1375-1384.
18. Muller, G., Behrens, J., Nussbaumer, U., Böhlen, P., Birchmeier, W. 1987, 'Inhibitor action of transforming growth factor  $\beta$  on endothelial cells',

- Proceedings of the National Academy of Sciences of the United States of America*, **84**: p. 5600-5604.
19. Vander, A., Sherman, J., Luciano, D. 1998, '*Human physiology: the Mechanisms of Body Function*', 7<sup>th</sup> Ed., WCB/McGraw-Hill, USA.
  20. Lind, M. 1998, 'Growth factor stimulation of bone healing: effects of osteoblasts, osteomyelitis and implants fixation', *Acta Orthopaedica Scandinavica Supplementum*, **283**: p. 2-37.
  21. Aubin, J.E., Heersche, J.N.M. 2000, 'Osteoprogenitor cell differentiation to mature bone-forming osteoblasts', *Drug Development Research*, **49**: p. 206-215.
  22. Shen, X., Roberst, E., Peel, S.A.F., Davies, J.E. 1993, 'Organic extracellular matrix components at the bone cell/substratum interface', *Cells and Materials*, **3**: p. 257-272.
  23. McKee, M.D., Nanci, A. 1993, 'Ultrastructural, cytochemical and immunocytochemical studies on bone at its interfaces', *Cells and Materials*, **3**: 219-243.
  24. Hunter, G.K., Goldberg, H.A. 1993, 'Nucleation of hydroxyapatite of bone sialoprotein', *Proceedings of the National Academy of Sciences of the United States of America*, **90**: p. 8562-8565.
  25. Goldberg, H.A., Hunter, G.K. 1995, 'The inhibitory activity of osteopontin on hydroxyapatite formation in vitro', *Annals of the New York Academy of Sciences*, **760**: p. 305-308.
  26. Murphy-Ulrich, J.E., Lane, T.F., Pallero, M.A., Sage, E.H. 1995, 'SPARC mediates focal adhesion disassembly in endothelial cells through a follistatin-like region and the Ca<sup>2+</sup>-binding EF-hand', *Journal of Cellular Biochemistry*, **57**: p 341-350.
  27. Glowacki, J., Rey, C., Cox, K., Lian, J. 1989, 'Effects of bone matrix components on osteoclast differentiation', *Connective Tissue Research*, **20**: p. 121-129.
  28. Aarden, E.M., Nijweide, P.J., Burger, E.H. 1994, 'Function of osteocytes in bone', *Journal of Cellular Biochemistry*, **55**: p. 287-299.

29. Zambonini-Zallone, A, Teti, A, Primavera, M.V. 1984, 'Resorption of vital or devitalized bone by isolated osteoclasts in vitro. The role of lining cells', *Cell and Tissue Research*, **235**: p. 561-564.
30. Chambers, T.J., 2000, 'Regulation of the differentiation and function of osteoclasts', *Journal of Pathology*, **192**: p. 4-13.
31. Teitelbaum, S.L. 2000, 'Bone resorption by osteoclasts', *Science*, **289**: p. 1504-1508.
32. Khosla, S. 2001, 'Minireview: the OPG/RANKL/RANK system', *Endocrinology*, **142**: p. 5050-5055.
33. Boyle, W.J., Scott Simonet, W., Lacey, D.L. 2003, 'Osteoclast differentiation and activation', *Nature*, **423**: p. 337-342.
34. Kasemo, B. 2002, 'Biological surface science', *Surface Science*, **500**: p. 656-677.
35. Bagnò, A., Piovan, A., Dettin, M., Chiarion, A., Brun, P., Gambaretto, R., Fontana, G., Di Bello, C., Palù, G., Castagliuolo, I. 2007, 'Human osteoblast-like cell adhesion on titanium substrates covalently functionalized with synthetic peptides', *Bone*, **40**: p. 693-699.
36. Reyes, C.D., Petrie, T.A., Burns, K.L., Schwartz, Z., García, A.J. 2007, 'Biomolecular surface coating to enhance orthopaedic tissue healing and integration', *Biomaterials*, **28**: p. 3228-3235.
37. Jäger, M., Zilkens, C., Zanger, K., Krauspe, R. 2007, 'Significance of nano- and microtopography for cell-surface interactions in orthopaedic implants', *Journal of Biomedicine and Biotechnology*, **2007**: p. 1-19.
38. Petrie, T.A., Raynor, J.E., Reyes, C.D., Burns, K.L., Collard, D.M., García, A.J. 2008, 'The effect of integrin-specific bioactive coatings on tissue healing and implant osseointegration', *Biomaterials*, **29**: p. 2849-2857.
39. Balazic, M., Kopac, J., Jackson, M.J., Ahmed, W. 2007, 'Review: titanium and titanium alloy applications in medicine', *International Journal of Nano and Biomaterials*, **1**: p. 3-34.
40. Buser, D., Schenk, R.K., Steinemann, S., Fiorellini, J.P., Fox, C.H., Stich, H. 1991, 'Influence of surface characteristics on bone integration of titanium

- implants. A histomorphometric study in miniature pigs', *Journal of Biomedical Materials Research*, **25**: p. 889-902.
41. Larsson, C., Thomsen, P. Lausmaa, J., Rodahl, M., Kasemo, B., Ericson, L.E. 1994, 'Bone response to surface modified titanium implants: studies on electropolished implants with different oxide thickness and morphology', *Biomaterials*, **15**: p. 1062-1074.
42. Li, D.H., Liu, B.L., Zou, J.C., Xu, K.W. 1999, 'Improvement of osseointegration of titanium dental implants by a modified sandblasting surface treatment: an in vivo interfacial biomechanics study', *Implant Dentistry*, **8**: p. 289-294.
43. Berenzai, M., Pelsöczy, I., Tóth, K., Radnai, M., Bor, Z., Fazekas, A. 2003, 'Surface modifications induced by ns and sub-ps excimer laser pulses on titanium implant material', *Biomaterials*, **24**: p. 4197-4203.
44. Cacciafesta, p., Hallam, K.R., Watkinson, A.C., Allen, G.C., Miles, M.J., Jandt, K.D. 2001, 'Visualisation of human plasma fibrinogen adsorbed on titanium implant surfaces with different roughness', *Surface Science*, **491**: p. 405-420.
45. Chu, P.K., Chen, J.Y., Wang, L.P., Huang, N. 2002, 'Plasma-surface modification of biomaterials', *Materials Science and Engineering R*, **36**: p. 143-206.
46. Kim, H.J., Kim, S.H., Kim, M.S., Lee, E.J., Oh, H.G., Oh, W.M., Park, S.W., Kim, W.J., Lee, G.J., Choi, N.G., Koh, J.T., Dinh, D.B., Hardin, R.R., Johnson, K., Sylvia, V.L., Schmitz, J.P., Dean, D.D. 2005, 'Varying Ti-6Al-4V surface roughness induces different early morphological and molecular responses in MG63 osteoblast-like cells', *Journal of Biomedical Materials Research*, **74A**: p. 366-373.
47. Batzer, R., Liu, Y., Cochran, D.L., Szmuckler-Moncler, S., Dean, D.D., Boyan, B.D., Schwartz, Z. 1998, 'Prostaglandins mediate the effects of cells titanium surface roughness on MG63 osteoblast-like cells and alter cell responsiveness to  $1\alpha,25\text{-(OH)}_2\text{D}_3$ ', *Journal of Biomedical Materials Research*, **41**: p. 489-496.
48. Bizios, R. 1994, 'Mini-review: Osteoblasts: An in vitro model of bone-implant interactions', *Biotechnology Bioengineering*, **43**: p. 582-585.

49. Boyan, B.D., Lohmann, C.H., Dean, D.D., Sylvia, V.L., Cochran, D.L., Schwartz, Z. 2001, 'Mechanism involved in osteoblast response to implant surface morphology', *Annual Review of Materials Research*, **31**: p. 357-371.
50. Kieswetter, K., Schwartz, Z., Hummert, T.W., Cochran, D.L., Simpson, J., Dean, D.D., Boyan, B.D. 1996, 'Surface roughness modulates the local production of growth factors and cytokines of osteoblast-like MG-63 cells', *Journal of Biomedical Materials Research*, **32**: p. 55-63.
51. Price, R.L., Haberstroh, K.M., Webster, T.J. 2003, 'Enhanced function of osteoblasts on nanostructured surfaces of carbon and alumina', *Medical and Biological Engineering and Computing*, **41**: p. 372-375.
52. Davies, J.E. 1996, 'In vitro modeling of the bone/implant interface', *The Anatomical Record*, **245**: p. 426-445.
53. Lim, J.Y., Dreiss, A.D., Zhou, Z., Hansen, J.C., Siedlecki, C.A., Hengstebeck, R.W., Cheng, J., Winograd, N., Donahue, H.J. 2007, 'The regulation of integrin-mediated osteoblast focal adhesion and focal adhesion kinase expression by nanoscale topography', *Biomaterials*, **28**: p. 1787-1797.
54. Zhao, G., Raines, A.L., Wieland, M., Schwartz, Z., Boyan, B.D. 2007, 'Requirement for both micron- and submicron scale structure for synergistic responses of osteoblasts to substrate surface energy and topography', *Biomaterials*, **28**: p. 2821-2829.
55. Lim, J.Y., Donahue, H.J. 2007, 'Cell sensing and response to micro- and nanostructured surfaces produced by chemical and topographic patterning', *Tissue Engineering*, **13**: p. 1879-1891.
56. Lampin, M., Warocquier-Clerout, R., Legris, C., Degrange, M., Sigot-Luizard, M.F. 1997, 'Correlation between substratum roughness and wettability, cell adhesion, and cell migration', *Journal of Biomedical Materials Research*, **36**: p. 99-108.
57. MacDonald, D.E., Deo, N., Markovic, B., Stranick, M., Somasundaran, P. 2002, 'Adsorption and dissolution behaviour of human plasma fibronectin on thermally and chemically modified titanium dioxide particles', *Biomaterials*, **23**: p. 1269-1279.

58. Giordano, C., Sandrini, E., Del Curto, B., Signorelli, E., Rondelli, G., Di Silvio, L. 2004, 'Titanium for osseointegration: Comparison between a novel biomimetic treatment and commercially exploited surfaces', *Journal of Applied Biomaterials and Biomechanics*, **2**: p. 35-44.
59. Sandrini, E., Morris, C., Chiesa, R., Cigada, A., Santin, M. 2005, 'In vitro assessment of the osteointegrative potential of a novel multiphase anodic spark deposition coating for orthopaedic and dental implants', *Journal of Biomedical Materials Research Part B: Applied Biomaterials*, **73B**: p. 392-399.
60. Neel, E.A.A., Mizoguchi, T., Ito, M., Bitar, M., Salih, V., Knowles, J.C. 2007, 'In vitro bioactivity and gene expression by cells cultured on titanium dioxide doped phosphate-based glass', *Biomaterials*, **28**: p. 2967-2977.
61. Pham, M.T., Reuther, H., Matz, W., Mueller, R., Steiner, G., Oswald, S., Zyganov, I. 2000, 'Surface induced reactivity for titanium by ion implantation', *Journal of Materials Science: Materials in Medicine*, **11**: p. 383-391.
62. Chiesa, R., Sandrini, E., Santin, M., Rondelli, G., Cigada, A. 2003, 'Osteointegration of titanium and its alloys by anodic spark deposition and other electrochemical techniques', *Journal of Applied Biomaterials and Biomechanics*, **1**: p. 91-107.
63. Hench, L.L. 1991, 'Bioceramics: from concept to clinic', *Journal of the American Ceramic Society*, **74**: p. 1487-1510.
64. Oonishi, H. 1991, 'Orthopaedic applications of hydroxyapatite', *Biomaterials*, **12**: p. 171-178.
65. Oonishi, H., Kushitani, S., Yasukawa, E., Iwaki, H., Hench, L.L., Wilson, J., Tsuji, E., Sugihara, T. 1997, 'Particulate bioglass compared with hydroxyapatite as a bone graft substitute', *Clinical Orthopaedics and Related Research*, **334**: p. 316-325.
66. Hench, L.L., Wilson, J. 1984, 'Surface-active materials', *Science*, **226**: p. 630-636.
67. Davies, J.E., Baldan, N. 1997, 'Scanning electron microscopy of the bone-bioactive implant interface', *Journal of Biomedical Materials Research*, **36**: p. 429-440.

68. Peng, P., Kumar, S., Voelcker, N.H., Szili, E., Smart, R.St.C, Griesser, H.J. 2006, 'Thin calcium phosphate coatings on titanium by electrochemical deposition in modified simulated body fluid', *Journal of Biomedical Materials Research Part A*, **76A**: p. 347-355.
69. Mavis, B., Tas, C. 2000, 'Dip coating calcium hydroxyapatite on Ti-6Al-4V substrates', *Journal of the American Ceramic Society*, **83**: p. 989-991.
70. Cook, S.D., Thomas, K.A., Kay, J.F., Jarcho, M. 1988, 'Hydroxyapatite-coated titanium for orthopaedic implant applications', *Clinical Orthopaedics and Related Research*, **232**: p. 225-243.
71. Lemmons, J.E. 1988, 'Hydroxyapatite coatings', *Clinical Orthopaedics and Related Research*, **235**: p. 220-223.
72. Ducheyne, P., Cuckler, J.M. 1992, 'Bioactive ceramic prosthetic coatings', *Clinical Orthopaedics and Related Research*, **276**: p. 102-114.
73. Ong, J.L., Appleford, M., Oh, S., Yang, Y., Chen, W.-H., Bumgardner, J.D., Haggard, W.O. 2006, 'The characterization and development of bioactive hydroxyapatite coatings', *JOM Journal of the Minerals, Metals, and Materials Society*, **58**: p. 67-69.
74. Hench, L.L., Splinter, R.J., Allen, W.C., Greenlee, T.K. 1971, 'Bonding mechanisms at the interface of ceramic prosthetic materials', *Journal of Biomedical Materials Research*, **5**: p. 117-141.
75. Coreño, J., Martínez, A., Bolarín, A., Sánchez, F. 2001, 'Apatite nucleation on silica surface: A Z potential approach', *Journal of Biomedical Materials Research*, **57**: p. 119-125.
76. Li, P., Ohtsuki, C., Nakanishi, K., Soga, N., Nakamura, T., Yamamuro, T. 1992, 'Apatite formation induced by silica gel in a simulated body fluid', *Journal of the American Chemical Society*, **75**: p. 2094-2097.
77. Keeting, P.E., Oursler, M.J., Weigand, K.E. 1992, 'Zeolite A increases proliferation, differentiation, and transforming growth factor beta production in normal adult human osteoblast-like cells in vitro', *Journal of Bone and Mineral Research*, **7**: p. 1281-1289.

78. Xynos, I.D., Edgar, A.J., Buttery, L.D.K., Hench, L.L., Polak, J.M. 2001, 'Gene-expression profiling of human osteoblasts following treatment with the ionic products of Bioglass<sup>®</sup> 45S5 dissolution', *Journal of Biomedical Materials Research*, **55**: p. 151-157.
79. Xynos, I.D., Edgar, A.J., Buttery, L.D.K., Hench, L.L., Polak, J.M. 2001, 'Ionic products of bioactive glass dissolution increase proliferation of human osteoblasts and induce insulin-like growth factor II mRNA expression and protein synthesis', *Biochemical and Biophysical Research Communications*, **276**: p. 461-465.
80. Teghil, R., D'Alessio, L.D., Ferro, D., Barinov, S.M. 2002, 'Hardness of bioactive glass film deposited on titanium alloy by pulsed laser ablation', *Journal of Materials Science Letters*, **21**: p. 379-382.
81. Stevenson, M., Arora, P.S., Smart, R.St.C. 1998, 'XPS studies of low-temperature plasma-produced graded oxide-silicate-silica layers on titanium', *Surface and Interface Analysis*, **26**: p. 1027-1034.
82. Arora, P.S., Smart, R.St.C. 1996, 'Formation of silicate structures in oxidized nickel surfaces using low-temperature plasma reaction', *Surface and Interface Analysis*, **24**: p. 539-548.
83. Zhang, H., Simpson, D., Kumar, S., Smart, R.St.C. 2006 'Interaction of hydroxylated PACVD silica coatings on titanium with simulated body fluid', *Colloids and Surfaces A: Physicochemical and Engineering Aspects*, **291**: p. 128-138.
84. Soballe, K. 1993, 'Hydroxyapatite ceramic coating for bone implant fixation. Mechanical and histological studies in dogs', *Acta Orthopaedica Scandinavica Supplementum*, **255**: p. 1-58.
85. Abbott, J.R., Smart, R.St.C., Henneberg, M., Yuen, T., Skinner, W., Leigh, C.M., Hermanis, G.M., David, D.J. 2001, 'Functionally graded surface layers on titanium implants', *Journal of Craniofacial Surgery*, **8**: p. 17-19.
86. Hall, B.K. 1992, '*Bone*', Volume 1, CRC Press, Florida.
  - a. Hauschka, P.V., *Growth factor effects in bone*, p. 103-170.

87. Yamaguchi, A., Komori, T., Suda, T. 2000, 'Regulation of osteoblast differentiation mediated by bone morphogenetic proteins, hedgehogs, and Cbfa1', *Endocrine Reviews*, **21**: p. 393-411.
88. Chen, D., Zhao, M., Mundy, G.R.. 2004, 'Bone morphogenetic proteins', *Growth Factors*, **22**: p. 233-241.
89. Jones, J.I., Clemmons, D.R. 1995, 'Insulin-like growth factors and their binding proteins: Biological actions', *Endocrine Reviews*, **16**: p. 3-34.
90. LeRoith, D. 2000, 'Editorial: Insulin-like growth factor 1 receptor signalling – overlapping or redundant pathways?', *Endocrinology*, **141**: p. 1287-1288.
91. Linkhart, T.A., Mohan, S., Baylink, D.J. 1996, 'Growth factors for bone growth and repair: IGF, TGF- $\beta$  and BMP', *Bone*, **19**: p. 1S-12S.
92. Wergedal, J.E., Mohan, S., Lundy, M., Baylink, D.J. 1990, 'Skeletal growth factor and other growth factors known to be present in bone matrix stimulate proliferation and protein synthesis in human bone cells', *Journal of Bone Minerals Research*, **5**: p. 179-186.
93. Nilsson, A., Swolin, D., Enerback, S., Ohlsson, C. 1995, 'Expression of functional growth hormone receptors in cultured human osteoblast-like cells', *Journal of Clinical Endocrinology and Metabolism*, **80**: p. 3483-3488.
94. Jones, J.I., Clemmons, D.R. 1995, 'Insulin-like growth factors and their binding proteins: Biological actions', *Endocrine Reviews*, **16**: p. 3-34.
95. Canalis, E. 1985, 'Effect of growth factors on bone cell replication and differentiation', *Clinical Orthopaedics and Related Research*, **193**: p. 246-263.
96. Langdahl, B.L., Kassem, M., Møller, M.K., Eriksen, E.F. 1998, 'The effects of IGF-1 and IGF-II on proliferation and differentiation of human osteoblasts and interactions with growth hormone', *European Journal of Clinical Investigation*, **28**: p. 176-183.
97. Galiano, R.D., Zhao, L.L., Clemmons, D.R., Roth, S.I., Lin, X., Mustoe, T.A. 1996, 'Interaction between the insulin-like growth factor family and the integrin receptor family in tissue repair processes', *Journal of Clinical Investigation*, **98**: p. 2462-2468.

98. Robinson, S.A., Rosenzweig, S.A. 2004, 'Synthesis and characterization of biotinylated forms of insulin-like growth factor-1: Topographical evaluation of the IGF-1/IGFBP-2 and IGFBP-3 interface', *Biochemistry*, **43**: p. 11533-11545.
99. Jia, D., Heersche, J.N.M. 2000, 'Insulin-like growth factor-1 and -2 stimulate osteoprogenitor proliferation and differentiation and adipocyte formation in cell populations derived from adult rat bone', *Bone*, **27**: p. 785-794.
100. McQueeney, K., Dealy, C.N. 2001, 'Roles of insulin-like growth factor-1 (IGF-1) and IGF-1 binding protein-2 (IGFBP2) and -5 (IGFBP5) in developing chick limbs', *Growth Hormone and IGF Research*, **11**: p. 346-363.
101. Tabata, Y. 2003, 'Tissue regeneration based on growth factor release', *Tissue Engineering*, **9**: p. S5-S15.
102. Vasita, R., Katti, D.S. 2006, 'Growth factor-delivery systems for tissue engineering: a materials perspective', *Expert Review of Medical Devices*, **3**: p. 29-47.
103. Luginbuehl, V., Meinel, L., Merkle, H.P., Gander, B. 2004, 'Localized delivery of growth factors for bone repair', *European Journal of Pharmaceutics and Biopharmaceutics*, **58**: p. 197-208.
104. Klinger, A., Steinberg, D., Kohavi, D., Sela, M.N. 1997, 'Mechanism of adsorption of human serum albumin to titanium *in vitro*', *Journal of Biomedical Materials Research*, **36**: p. 387-392.
105. Müller, R., Abke, J., Schnell, E., Macionczyk, F., Gbureck, U., Mahrl, R., Ruszczak, Z, Kujat, R., Englert, C., Nerlich, M., Angele, P. 2005, 'Surface engineering of stainless materials by covalent collagen immobilization to improve implant biocompatibility', *Biomaterials*, **26**: p. 6962-6972.
106. Kohler, N., Fryxell, G.E., Zhang, M. 2004, 'A bifunctional poly(ethylene glycol) silane immobilized on metallic oxide-based nanoparticles for conjugation with cell targeting agents', *Journal of the American Chemical Society*, **126**: p. 7206-7211.
107. Halliwell, C.M., Cass, A.E.G. 2001, 'A factorial analysis of silanization conditions for the immobilization of oligonucleotides on glass surfaces', *Analytical Chemistry*, **73**: p. 2476-2483.

108. Matinlinna, J.P., Areva, S., Lassila, L.V.J., Vallittu, P.K. 2004, 'Characterization of siloxane films on titanium substrate derived from three aminosilanes', *Surface and Interface Analysis*, **36**: p. 1314-1322.
109. Pantano, C.G., Wittberg, T.N. 1990, 'XPS analysis of silane coupling agents and silane-treated E-glass fibers', *Surface and Interface Analysis*, **15**: p. 498-501.
110. Mansur, H.S., Oréfice, R.L., Vasconcelos, W.L., Lobato, Z.P., Machado, L.J.C. 2005, 'Biomaterial with chemically engineered surface for protein immobilization', *Journal of Materials Science: Materials in Medicine*, **16**: p. 333-340.
111. Puleo D.A., Nanci, A. 1999, 'Understanding and controlling the bone-implant interface', *Biomaterials*, **20**: p. 2311-2321.
112. Xiao, S.J., Textor, M., Spencer, N.D., Wieland, M., Keller, B., Sigrist, H. 1997, 'Immobilization of the cell-adhesive peptide Arg-Gly-Cys (RGDC) on titanium surfaces by covalent chemical attachment', *Journal of Materials Science: Materials in Medicine*, **8**: p. 867-872.
113. Nanci, A., Wuest, J.D., Peru, L., Brunet, P., Sharma, V., Zalzal, S., McKee, M.D. 1998, 'Chemical modification of titanium surfaces for covalent attachment of biological molecules', *Journal of Biomedical Materials Research*, **40**: p. 324-335.
114. Dee, K.C., Rueger, D.C., Andersen, T.T., Bizios, R. 1996, 'Conditions which promote mineralization at the bone-implant interface: a model *in vitro* study', *Biomaterials*, **17**: p. 209-215.
115. Morra, M., Cassinelli, C., Cascardo, G., Cahalan, P., Cahalan, L., Fini, M., Giardino, R. 2003, 'Surface engineering of titanium by collagen immobilization. Surface characterization and *in vitro* and *in vivo* studies', *Biomaterials*, **24**: p. 4639-4654.
116. Jose, B., Antoci, V., Zeiger, A.R., Wickstrom, E., Hickok, N.J. 2005, 'Vancomycin covalently bonded to titanium beads kills *Staphylococcus aureus*', *Chemistry and Biology*, **12**: p. 1041-1048.

117. Hench, L.L., West, J.K. 1990, 'The sol-gel process', *Chemical Reviews*, **90**: p. 33-72.
118. Curtis, A., Wilkinson, C. 1997, 'Topographical control of cells', *Biomaterials*, **18**: p. 1573-1583.
119. Yim, E.K.F., Leong, K.W. 2005, 'Significance of synthetic nanostructures in dictating cellular response', *Nanomedicine: Nanotechnology, Biology and Medicine*, **1**: p. 10-21.
120. Palin, E., Liu, H., Webster, T.J. 2005, 'Mimicking the nanofeatures of bone increases bone-forming cell adhesion and proliferation', *Nanotechnology*, **16**: p. 1828-1835.
121. Li, P., Ohtsuki, C., Nakanishi, K., Soga, N., Nakamura, T., Yamamuro, T. 1992, 'Apatite formation induced by silica gel in a simulated body fluid', *Journal of the American Chemical Society*, **75**: p. 2094-2097.
122. Moon, J.H., Shin, J.W., Kim, S.Y., Park, J.W. 1996, 'Formation of uniform aminosilane thin layers: an imine formation to measure relative surface density of the amine group', *Langmuir*, **12**: p. 4621-4624.
123. Heiney, P.A., Grünberg, K., Fang, J. 2000, 'Structure and growth of chromophore-functionalized (3-aminopropyl)triethoxysilane self-assembled on silicon', *Langmuir*, **16**: p. 2651-2657.
124. Shlyakhtenko, L.S., Gall, A.A., Filonov, A., Cerovac, Z., Lushnikov, A., Lyubchenko, Y.L. 2003, 'Silatrane-based surface chemistry for immobilization of DNA, protein-DNA complexes and other biological materials', *Ultramicroscopy*, **97**: 279-287.
125. Jesionowski, T., Krysztalkiewicz, A. 2001, 'Influence of silane coupling agents on surface properties of precipitated silicas', *Applied Surface Science*, **172**: p. 18-32.
126. Kim, T., Suh, S.-M., Girshick, S.L., Zachariah, M.R., McMurry, P.H., Rassel, R.M., Shen, Z., Campbell, S.A. 2002, 'Particle formation during low-pressure chemical vapor deposition from silane and oxygen: Measurement, modeling, and film properties', *Journal of Vacuum Science and Technology A: Vacuum, Surfaces and Films*, **20**: p. 413-423.

127. Bierbaum, K., Grunze, M., Baski, A.A., Chi, L.F., Schrepp, W., Fuchs, H. 1995, 'Growth of self-assembled *n*-alkyltrichlorosilane films on Si(100) investigated by atomic force microscopy', *Langmuir*, **11**: p. 2143-2150.
128. Hu, S.M. 1980, 'Infrared adsorption spectra of SiO<sub>2</sub> precipitates of various shapes in silicon: calculated and experimental', *Journal of Applied Physics*, **51**: p. 5945-5948.
129. Sakai, N., Fujishima, A., Watanabe, T., Hashimoto, K. 2003, 'Quantitative evaluation of the photoinduced hydrophilic conversion properties of TiO<sub>2</sub> thin film surfaces by the reciprocal of contact angle', *Journal of Physical Chemistry B*, **107**: p. 1028-1035.
130. Stevens, N., Priest, C.I., Sedev, R., Ralston, J. 2003, 'Wettability of photoresponsive titanium dioxide surfaces', *Langmuir*, **19**: p. 3272-3275.
131. Rinch, C.L., Chen, X., Panchalingam, V., Eberhart, R.C., Wang, J., Timmons, R.B. 1996, 'Pulsed radio frequency plasma polymerisation of allyl alcohol: controlled deposition of surface hydroxyl groups', *Langmuir*, **12**: p. 2995-3002.
132. Dickie, R.A., Hammond, J.S., deVries, J.E., Holubka, J.W. 1982, 'Surface derivitization of hydroxyl functional acrylic copolymers for characterization by X-ray photoelectron spectroscopy', *Analytical Chemistry*, **54**: p. 2045-2049.
133. Ertel, S.I., Chilkoti, A., Horbett T.A., Ratner, B.D. 1991, 'Endothelial cell growth on oxygen-containing films deposited by radio-frequency plasmas: the role of surface carbonyl groups', *Journal of Biomaterials Science, Polymer Edition*, **3**: p. 163-183.
134. Iler, R.K. 1955, *The Colloid Chemistry of Silica and Silicates*, Ithaca, New York: Cornell V.P.
135. Dang, T.A., Gnanasekaran, R. 1990, 'Determination of amino and silanol functional groups on glass via chemical derivitization and ESCA', *Surface and Interface Analysis*, **15**: p. 113-118.
136. McCafferty, E., Wightman, J.P. 1998, 'Determination of the concentration of surface hydroxyl groups on metal oxide films by a quantitative XPS method', *Surface and Interface Analysis*, **26**: p. 549-564.

137. Ivanov, V.B., Behnisch, J., Holländer, A., Mehdorn, F., Zimmermann, H. 1996, 'Determination of functional groups on polymer surfaces using fluorescence labelling', *Surface and Interface Analysis*, **24**: p. 251-262.
138. Feng, B., Chen, J.Y., Qi, S.K., He, L., Zhao, J.Z., Zhang, X.D. 2002, 'Characterization of surface oxide films on titanium and bioactivity', *Journal of Materials Science: Materials in Medicine*, **13**: p. 457-464.
139. Söderholm, K.J.M., Shang, S.W. 1993, 'Molecular orientation of silane at the surface of colloidal silica', *Journal of Dental Research*, **72**: p. 1050-1054.
140. Boerio, F.J., Armogan, L., Cheng, S.Y. 1980, 'The structure of  $\gamma$ -aminopropyltriethoxysilane films on iron mirrors', *Journal of Colloid and Interface Science*, **73**: p. 416-424.
141. Britcher, L.G., Kehoe, D.C., Matisons, J.G., Smart R.St.C., Swincer, A.G. 1993, 'Silicones on glass surfaces. 2. Coupling agent analogs', *Langmuir*, **9**: p. 1609-1613.
142. Baselja, J., Gonzalez-Benito, J., Cabanelas, J.C., Aznar, A.J., Vigil, M.R., Bravo, J., Baselga, J. 1996, 'Surface characterization of silanized glass fibers by labelling with environmental sensitive fluorophores', *Journal of Applied Polymer Science*, **62**: p. 375-384.
143. Kurth D.G., Bein, T. 1995, 'Thin films of (3-aminopropyl)triethoxysilane on aluminium oxide and gold substrates', *Langmuir*, **11**: p. 3061-3067.
144. Sudhölter, E.J.R., Huis, R., Hays, G.R., Alma, N.C.M. 1985, 'Solid-state silicon-29 and carbon-13 NMR spectroscopy using cross-polarization and magic-angle-spinning techniques to characterize 3-chloropropyl and 3-aminopropyl-modified silica gels', *Journal of Colloid and Interface Science*, **103**: p. 554-560.
145. Varncken, K.C., Possemiers, K., Van Der Voort, P., Vansant, E.F. 1995, 'Surface modification of silica gels with aminoorganosilanes', *Colloids and Surfaces A: Physicochemical and Engineering Aspects*, **98**: p. 235-241.
146. Wojcik, S.M., Puleo, D.A. 1997, 'Biochemical surface modification of Ti-6Al-4V for the delivery of protein to the cell-biomaterial interface', *Biomedical Sciences Instrumentation*, **33**: p. 166-171.

147. Chong, A.S.M., Zhao, X.S. 2003, 'Functionalization of SBA-15 with APTES and characterization of functionalized materials', *Journal of Physical Chemistry B*, **107**: p. 12650-12657.
148. Chrisey, L.A., Lee, G.U., O'Ferral, E. 1996, 'Covalent attachment of synthetic DNA to self-assembled monolayer films', *Nucleic Acids Research*, **24**: p. 3031-3039.
149. Puleo, D.A. 1995, 'Activity of enzyme immobilized on silanized Co-Cr-Mo', *Journal of Biomedical Materials Research*, **29**: p. 951-975.
150. Lyubchenko, Y., Shlyakhtenko, L., Harrington, R., Oden, P., Lindsay, S. 1993, 'Atomic force microscopy of long DNA: imaging in air and under water', *Proceedings of the National Academy of Sciences of the United States of America*, **90**: p. 2137-2140.
151. Wang, Z., Jin, G. 2004, 'Covalent immobilization of proteins for the biosensor based imaging ellipsometry', *Journal of Immunological Methods*, **285**: p. 237-243.
152. Porté-Durrieu, M.C., Labrugère, C., Villars, F., Lefebvre, F., Dutoya, S., Guette, A., Bordenave, L., Baquey, C. 1999, 'Development of RGD peptides grafted onto silica surfaces: XPS characterization and human endothelial cell interactions', *Journal of Biomedical Materials Research*, **46**: p. 368-375.
153. Arai, K., Matsunaga, A., Yoneyama, M., Takigami, S., Nakamura, Y., Edwards, H.E., Phillips, G.O. 1993, 'Amino acid end-group in commercial Heparin. III. Determination of the number of amino groups of amino acid and hexosamine residues per heparin molecule', *Journal of Polymer Science: Part A: Polymer Chemistry*, **31**: p. 249-258.
154. Brown, H.H. 1968, 'A study of 2,4,6-trinitrobenzenesulfonic acid for automated amino acid chromatography', *Clinical Chemistry*, **14**: p. 967-978.
155. Bubnis, W.A., Ofner III, C.M. 1992, 'The determination of  $\epsilon$ -amino groups in soluble and poorly soluble proteinaceous materials by a spectrophotometric method using trinitrobenzenesulfonic acid', *Analytical Biochemistry*, **207**: p. 129-133.

156. Palmer, D.W., Peters, T. 1969, 'Automated determination of free amino groups in serum and plasma using 2,4,6-trinitrobenzene sulfonate', *Clinical Chemistry*, **15**: 891-901.
157. Puleo, D.A., Kissling, R.A., Sheu, M.S. 2002, 'A technique to immobilize bioactive proteins, including bone morphogenetic protein-4 (BMP-4), on titanium alloy', *Biomaterials*, **23**: p. 2079-2087.
158. Sarantonis, E.G., Diamandis, E.P., Karayannis, M.I. 1986, 'Kinetic study of the reaction between trinitrobenzenesulfonic acid and amino acids with a trinitrobenzenesulfonate ion-selective electrode', *Analytical Biochemistry*, **155**: p. 129-134.
159. Spadaro, A.C.C., Draghetta, W., Lama, S.N.D., Camargo, A.C.M., Greene, L.J. 1979, 'A convenient manual trinitrobenzenesulfonic acid method for monitoring amino acids and peptides in chromatographic column effluents', *Analytical Biochemistry*, **96**: p. 317-321.
160. Puleo, D.A. 1997, 'Retention of enzyme activity immobilized on silanized Co-Cr-Mo and Ti-6Al-4V', *Journal of Biomedical Materials Research*, **37**: p. 222-228.
161. Gong, X., Dai, L.D., Griesser, H.J., Mau, A.W.H. 2000, 'Surface immobilization of poly(ethylene oxide): structure and properties', *Journal of Polymer Science: Part B: Polymer Physics*, **38**: p. 2323-2332.
162. Hozumi, A., Inagaki, M., Shirahata, N. 2006, 'Vapor phase formation of a well-ordered aldehyde-terminated self-assembled monolayer on a SiO<sub>2</sub> surface and formation of silver film on the surface based on the silver mirror reaction', *Surface Science*, **600**: p. 4044-4047.
163. Perruchot, C., Watts, J.F., Lowe, C., White, R.G., Cumpson, P.J. 2002, 'Angle-resolved XPS characterization of urea formaldehyde-epoxy systems', *Surface and Interface Analysis*, **33**: p. 869-878.
164. Gerenser, L.J., Grace, J.M., Apai, G., Thompson, P.M. 2000, 'Surface chemistry of nitrogen plasma-treated poly(ethylene-2,6-naphthalate): XPS, HREELS and static SIMS analysis', *Surface and Interface Analysis*, **29**: p. 12-22.

165. Hermanson, G.T. 1996, *Bioconjugate Techniques*, Academic Press, San Diego, California.
166. Peng, L., Calton, G.J., Burnett, J.W. 1987, 'Effect of borohydride reduction on antibodies', *Applied Biochemistry and Biotechnology*, **14**: p. 91-99.
167. Raspoet, G., Nguyen, M.T., McGarraghy, M., Hegarty, A.F. 1998, 'Experimental and theoretical evidence for a concerted catalysis by water clusters in the hydrolysis of isocyanates', *The Journal of Organic Chemistry*, **63**: p. 6867-6877.
168. Moses, P.R., Wier, L.M., Lennox, J.C., Finklea, H.O., Lenhard, J.R., Murray, R.W. 1978, 'X-ray photoelectron spectroscopy of alkylamine-silanes bound to metal oxide electrodes', *Analytical Chemistry*, **50**: p. 576-585.
169. Esser, P. "Principles in adsorption to polystyrene", Bulletin **No. 6**: p. 317-321. Retrieved on March 15, 2007 from [www.nuncbrand.com](http://www.nuncbrand.com).
170. Galli, C., Collaud Coen, M., Hauert, R., Katanaev, V.L., Wymann, M.P., Gröning, P., Schlapbach, L. 2001, 'Protein adsorption on topographically nanostructured titanium', *Surface Science*, **474**: p. L180-L184.
171. Langel, W., Menken, L. 2003, 'Simulation of the interface between titanium oxide and amino acids in solution by first principles MD', *Surface Science*, **538**: p. 1-9.
172. Zhang, M., Ferrari, M. 1997, 'Reduction of albumin adsorption onto silicon surfaces by Tween 20', *Biotechnology and Bioengineering*, **56**: p. 618-625.
173. Massia, S.P., Stark, J. 2001, 'Immobilized RGD peptides on surface-grated dextran promote biospecific cell attachment', *Journal of Biomedical Materials Research*, **56**: p. 390-399.
174. Schleicher, I., Parker, A., Leavesley, D., Crawford, R., Upton, Z., Xiao, Y. 2005, 'Surface modification by complexes of vitronectin and growth factors for serum-free culture of human osteoblasts', *Tissue Engineering*, **11**: p. 1688-1698.
175. American Type Culture Centre (ATCC) Product Information Sheet for cell line designation: MG63 (Catalogue number: CRL-1427). Retrieved on May 25, 2007 from [www.atcc.org](http://www.atcc.org).

176. O'Brien, J., Wilson, I., Orton, T., Pognan, F. 2000, 'Investigation of the Alamar Blue (resazurin) fluorescent dye for the assessment of mammalian cell cytotoxicity', *European Journal of Biochemistry*, **267**: p. 5421-5426.
177. Lusquinos, De Carlos, A., Pou, J., Arias, J.L., Boutinguiza, M., León, B., Pérez-Amor, M., Driessens, F.C.M., Hing, K., Gibson, I., Best, S., Bonfield, W. 2003, 'Calcium phosphate coatings obtained by Nd:YAG laser cladding: Physiochemical and biologic properties', *Journal of Biomedical Materials Research*, **64A**: p. 630-637.
178. AlamarBlue™ Product Information Booklet, *Biosource*, Retrieved on 28 June 2007, from [www.biosource.com/content/literatureContent/PDFs/alarbluebooklet.pdf](http://www.biosource.com/content/literatureContent/PDFs/alarbluebooklet.pdf).
179. Li, S., Gerrard, E.R., Balkovetz, D.F. 2004, 'Evidence for ERK 1/2 phosphorylation controlling contact inhibition of proliferation in Madin-Darby canine kidney epithelial cells', *American Journal of Cell Physiology – Cell Physiology*, **287**: p. C432-C439.
180. Holley, R.W., Kiernan, J.A. 1968, 'Contact inhibition of cell division in 3T3 cells', *Proceedings of the National Academy of Sciences of the United States of America*, **60**: p. 300-304.
181. Viñals, F., Pouysségur, J. 1999, 'Confluence of vascular endothelial cells induces cell cycle exit by inhibiting p42/p44 mitogen-activated protein kinase activity', *Molecular and Cellular Biology*, **19**: p. 2763-2772.
182. Stoker, M.G.P. 1973, 'Role of diffusion boundary layer in contact inhibition of growth', *Nature*, **246**: p. 200-203.
183. Lee, J.H., Khang, G., Lee, J.W., Lee, H.B. 1998, 'Interaction of different types of cells on polymer surfaces with wettability gradient', *Journal of Colloid and Interface Science*, **205**: p. 323-330.
184. Steele, J.G., Dalton, B.A., Johnson, G., Underwood, P.A. 1995, 'Adsorption of fibronectin and vitronectin onto Primaria™ and tissue culture polystyrene and relationship to the mechanism of initial attachment of human vein endothelial cells and BHK-21 fibroblasts', *Biomaterials*, **16**: p. 1057-1067.

185. Anselme, K. 2000, 'Osteoblast adhesion on biomaterials', *Biomaterials*, **21**: p. 667-681.
186. Brandley, B.K., Schnaar, R.L. 1988, 'Covalent attachment of an Arg-Gly-Asp sequence to peptide to derivatizable polyacrylamide surfaces: Support of fibroblast adhesion and long-term growth', *Analytical Biochemistry*, **172**: p. 270-278.
187. Danilov, Y.N., Juliano, R.L. 1989, '(Arg-Gly-Asp)<sub>n</sub>-albumin conjugates as a model substratum for integrin-mediated cell adhesion', *Experimental Cell Research*, **182**: p. 186-196.
188. Massia, S.P., Hubbel, J.A. 1990, 'Covalent surface immobilization of Arg-Gly-Asp- and Tyr-Ile-Gly-Ser-Arg-containing peptides to obtain well-defined cell-adhesive substrates', *Analytical Biochemistry*, **187**: p. 292-301.
189. Massia, S.P., Hubbel, J.A. 1990, 'Covalently attached GRGD on polymer surfaces promotes biospecific adhesion of mammalian cells', *Annals New York Academy of Sciences*, **589**: p. 261-270.
190. Reznia, A., Healy, K.E. 2000, 'The effect of peptide surface density on mineralization of a matrix deposited by osteogenic cells', *Journal of Biomedical Materials Research*, **52**: p. 595-600.
191. Kolch, W. 2000, 'Meaningful relationships: the regulation of the Ras/Raf/MEK/ERK pathways by protein interactions', *Biochemical Journal*, **351**: p. 289-305.
192. Seger, R., Krebs, E.G. 1995, 'The MAPK signalling cascade', *The Journal of the Federation of American Societies for Experimental Biology*, **9**: p. 726-735.
193. Luttrell, L.M. 2003, 'G protein-coupled receptor signalling in neuroendocrine systems', *Journal of Medical Endocrinology*, **30**: p. 117-126.
194. Pearson, G., Robinson, F., Beers, Gibson, T.B., Xu, B., Karandikar, M., Berman, K., Cobb, M.H. 2001, 'Mitogen-activated protein (MAP) kinase pathways: Regulation and physiological functions', *Endocrine Reviews*, **22**: p. 153-183.
195. AlphaScreen Surefire ERK Assay, Brochure, Retrieved on July 16, 2007 from [www.perkinelmer.com](http://www.perkinelmer.com).

196. Warner, G., Illy, C., Pedro, L., Roby, P., Bossé, R. 2004, 'AlphaScreen™ Kinase HTS platforms', *Current Medicinal Chemistry*, **11**: p. 721-730.
197. Howe, A., Aplin, A.E., Alahari, S.K., Juliano, R.L. 1998, 'Integrin signaling and cell growth control', *Current Opinion in Cell Biology*, **10**: p. 220-231.
198. El-Ghannam, A.R., Ducheyne, P., Risbud, M., Adams, C.S., Shapiro, I.M., Castner, D., Golledge, S., Composto, R.J. 2004, 'Model surfaces engineered with nanoscale roughness and RGD tripeptides promote osteoblast activity', *Journal of Biomedical Materials Research*, **68A**: p. 615-627.
199. Osmand, R.I.W., Sheehan, A., Borowicz, R., Barnett, E., Harvey, G., Turner, C., Brown, A., Crouch, M.F., Dyer, A.R. 2005, 'GPCR screening via ERK 1/2: A novel platform for screening G protein-coupled receptors', *Journal of Biomolecular Screening*, **10**: p. 730-737.
200. Zhang, W., Lee, J.C., Kumar, S., Gowen, M. 1999, 'ERK pathway mediates the activation of Cdk2 in IGF-1-induced proliferation of human osteosarcoma MG63 cells', *Journal of Bone Mineral Research*, **14**: p. 528-535.
201. Freshney, R.I. 2005, *Culture of Animal Cells: A Manual of Basic Technique*, Wiley-Liss, New York.
202. Belford, D.A., Rogers, M.L., Regester, G.O., Francis, G.L., Smithers, G.W., Liepe, I.J., Priebe, I.K., Ballard, F.J. 1995, 'Milk-derived growth factors as serum supplements for the growth of fibroblast and epithelial cells', *In Vitro Cellular and Developmental Biology – Animal*, **31**: p. 752-760.
203. Francis, G.L., Regester, G.O., Webb, H.A., Ballard, F.J. 1995, 'Extraction from cheese whey by cation-exchange chromatography of factors that stimulate the growth of mammalian cells', *Journal of Dairy Research*, **78**: p. 1209-1218.
204. Bockus, B.J., Stiles, C.D. 1984, 'Regulation of cytoskeletal architecture by platelet-derived growth factor, insulin and epidermal growth factor', *Experimental Cell Research*, **153**: p. 186-197.
205. Martin, S.S., Rose, D.W., Saltiel, A.R., Klippel, A., Williams, L.T., Olefsky, J.M. 1996, 'Phosphatidylinositol 3-kinase is necessary and sufficient for insulin-stimulated stress fiber breakdown', *Endocrinology*, **137**: p. 5045-5054.

206. Goh, E.L.K., Pircher, T.J., Wood, T.J.J., Norstedt, G., Graichen, R., Lobie, P.E. 1997, 'Growth hormone-induced reorganization of the actin cytoskeleton is not required for STAT5 (signal transducer and activator of transcription-5)-mediated transcription', *Endocrinology*, **138**: p. 3207-3215.
207. Stossel, T.P. 1993, 'On the crawling of animal cells', *Science*, **260**: p. 1086-1094.
208. Thian, E.S., Huang, J., Best, S.M., Barber, Z.H., Bonfield, W. 2007, 'Silicon-substituted hydroxyapatite: The next generation of bioactive coatings', *Materials Science and Engineering C*, **27**: p. 251-256.
209. Gronowicz, G., McCarthy, M.B. 1996, 'Response of human osteoblasts to implant materials: integrin-mediated adhesion', *Journal of Orthopaedic Research*, **14**: p. 878-887.

## Part 2: Covalent immobilisation of anti-human IgG on porous silicon for the detection of human IgG by reflective interferometry

1. Anderson, S.H.C., Elliott, H., Wallis, D.J., Canham, L.T., Powell, J.J. 2003, 'Dissolution of different forms of partially porous silicon wafers under simulated physiological conditions', *Physica status solidi (a)*, **197**: p. 331-335.
2. Canham, L.T. 1990, 'Silicon quantum wire array fabrication by electrochemical and chemical dissolution of wafers', *Applied Physics Letters*, **57**: p. 1046-1048.
3. Canham, L.T. 1995, 'Luminescence bands and their proposed origins in highly porous silicon', *Physica status solidi (b)*, **190**: p. 9-14.
4. Canham, L. 1997, '*Properties of Porous Silicon*', Short Run Press Ltd., London.
  - a. Sailor, M.J., *Sensor applications of porous silicon*, p. 364-370.
  - b. Canham, L.T., *Biomedical applications of porous silicon*, p. 371-376.
  - c. Allongue, P., *Porous silicon formation mechanisms*, p. 3-11.
  - d. Halimaoui, A., *Porous silicon formation and anodisation*, p. 12-22.
5. Cullis, A.G., Canham, L.T., Calcott, P.D.J. 1997, 'The structural and luminescence properties of porous silicon', *Journal of Applied Physics*, **82**: p. 909-965.
6. Dian, J., Holec, T., Jelínek, I., Jindrich, J., Valenta, J., Pelant, I. 2000, 'Time evolution of photoluminescence response from porous silicon in hydrocarbon gas sensing', *Physica status solidi (a)*, **182**: p. 485-488.
7. Simons, A.J., Cox, T.I., Loni, A., Canham, L.T., Blacker, R. 1997, 'Investigation of the mechanisms controlling the stability of a porous silicon electroluminescent device', *Thin Solid Films*, **297**: p. 281-284.
8. Soares, D.M., Teschke, O., dos Santos, M.C. 1996, 'Dynamics of the hydrogen oxidation and silicon dissolution reactions in the formation of porous silicon', *Langmuir*, **12**: p. 2875-2877.
9. Hirschman, K.D., Tsybeskov, L., Duttagupta, S.P., Fauchet, P.M. 1996, 'Silicon-based visible light-emitting devices integrated into microelectronic circuits', *Nature*, **384**: p. 338-341.
10. Wong, H. 2002, 'Recent developments in silicon optoelectronic devices', *Microelectronics Reliability*, **42**: p. 317-326.

11. Bonanno, L.M, DeLouise, L.A. 2007, 'Steric crowding effects on target detection in an affinity biosensor', *Langmuir*, **23**: p. 5817-5823.
12. Canham, L.T., Reeves, C.L., Newey, J.P., Houlton, M.R., Cox, T.I., Buriak, J.M., Stewart, M.P. 1999, 'Derivatized mesoporous silicon with dramatically improved stability in simulated human blood plasma', *Advanced Materials*, **11**: p. 1505-1507.
13. Drott, J., Lindström, K., Rosengren, L., Laurell, T. 1997, 'Porous silicon as the carrier matrix in microstructured enzyme reactors yielding high enzyme activities', *Journal of Micromechanics and Microengineering*, **7**: p. 14-23.
14. Laurell, T., Drott, J., Rosengren, L., Lindström, K. 1996, 'Enhanced enzyme activity in silicon integrated enzyme reactors utilizing porous silicon as the coupling matrix', *Sensors and Actuators*, **31**: p. 161-166.
15. Li, X., Coffey, J.L., Chen, Y., Pinizzotto, R.F., Newey, J., Canham, L.T. 1998, 'Transition metal complex-doped hydroxyapatite layers on porous silicon', *Journal of the American Chemical Society*, **120**: p. 11706-11709.
16. Lin, V.S.Y., Moteshareh, K., Dancil, K.S., Sailor, M.J., Ghadiri, M.R. 1997, 'A porous silicon-based optical interferometric biosensor', *Science*, **278**: p. 840-843.
17. Rosengren, A., Wallman, L., Bengtsson, M., Laurell, Th. Danielsen, N., Bjursten, L.M. 2000, 'Tissue reactions to porous silicon: a comparative biomaterial study', *Physica status solidi (a)*, **182**: p. 527-531.
18. Lewis, W.G., Shen, Z., Finn, M.G., Siuzdak, G. 2003, 'Desorption/ionisation on silicon (DIOS) mass spectrometry: background and applications', *International Journal of Mass Spectrometry*, **226**: p. 107-116.
19. Shen, Z., Thomas, J.J., Averbuj, C., Broo, K.M., Engelhard, M., Crowell, J.E., Finn, M.G., Siuzdak, G. 2001, 'Porous silicon as a versatile platform for laser desorption/ionisation mass spectrometry', *Analytical Chemistry*, **73**: p. 612-619.
20. Allongue, P., Kieling, V., Gerischer, H. 1995, 'Etching mechanism and atomic structure of H-Si(111) surfaces prepared in NH<sub>4</sub>F', *Electrochimica Acta*, **40**: p. 1353-1360.
21. Gerischer, H., Allongue, P., Kieling, V.C. 1993, 'The mechanism of the anodic oxidation of silicon in acidic fluoride solutions revisited', *Berichte der Bunsen-Gesellschaft für Physikalische Chemie*, **97**: p. 753-757.

22. Lehmann, V., Gösele, U. 1991, 'Porous silicon formation: a quantum wire effect', *Applied Physics Letters*, **58**: p. 856-858.
23. Janshoff, A., Dancil, K.S., Steinem, C., Greiner, D.P., Lin, V.S.Y., Gurtner, C., Motesharei, K., Sailor, M.J., Ghadiri, M.R. 1998, 'Macroporous p-type silicon Fabry-Perot layers. Fabrication, characterization, and applications in biosensing', *Journal of the American Chemical Society*, **120**: p. 12108-12116.
24. Ponomarev, E.A., Lévy-Clément, C. 2000, 'Macropore formation on p-type silicon', *Journal of Porous Materials*, **7**: p. 51-56.
25. Smith, R.L., Collins, S.D. 1992, 'Porous silicon formation mechanisms', *Journal of Applied Physics*, **71**: p. R1-R22.
26. Föll, H., Carstensen, J., Langa, S., Christophersen, M., Tiginyanu, I.M. 2003, 'Porous III-V compound semiconductors: formation, properties, and comparison to silicon', *Physica status solidi (a)*, **197**: p. 61-70.
27. Ouyang, H., Christophersen, M., Fauchet, P.M. 2005, 'Enhanced control of porous silicon morphology from macropore to mesopore formation', *Physica status solidi (a)*, **202**: p. 1396-1401.
28. Salonen, J., Paski, J., Vähä-Heikkilä, K., Heikkilä, T., Björkqvist, M., Lehto, V.P. 2005, 'Determination of drug load in porous silicon microparticles by calorimetry', *Physica status solidi (a)*, **202**: p. 1629-1633.
29. Searson, P.C. 1991, 'Porous silicon membranes', *Applied Physics Letters*, **59**: p. 832-833.
30. Solanki, C.S., Bilyalov, R.R., Bender, H., Poortmans, J. 2000, 'New approach for the formation and separation of a thin porous silicon layer', *Physica status solidi (a)*, **182**: p. 97-101.
31. Coffey, J.L., Whitehead, M.A., Nagesha, D.K., Mukherjee, P., Akkaraju, G., Totolici, M., Saffie, R.S., Canham, L.T. 2005, 'Porous silicon-based scaffolds for tissue engineering and other biomedical applications', *Physica status solidi (a)*, **202**: p. 1451-1455.
32. Létant, S., Hart, B.R., Kane, S.R., Hadi, M.Z., Shields, S.J., Reynolds, J.G. 2004, 'Enzyme immobilization on porous silicon surfaces', *Advanced Materials*, **16**: p. 689-693.
33. Voelcker, N.H., Alfonso, I., Ghadiri, M.R., 'Biosensor signal amplification via catalyzed oxidative corrosion of porous silicon', *Small*, submitted 2007.

34. Byfield, M.P., Abuknesha, R.A. 'Biochemical aspects of biosensors', *Biosensors and Bioelectronics*, **9**: p. 373-400.
35. Nakamura, H., Karube, I. 2003, 'Current research activity in biosensors', *Analytical and Bioanalytical Chemistry*, **377**: p. 446-448.
36. Rogers, K.R. 2006, 'Recent advances in biosensor techniques for environmental monitoring', *Analytica Chimica Acta*, **568**: p. 222-231.
37. Curtis, C.L., Doan, V.V., Credo, G.M., Sailor, M.J. 1993, 'Observation of optical cavity modes in photoluminescent porous silicon films', *Journal of The Electrochemical Society*, **140**: p. 3492-3494.
38. Gao, J., Gao, T., Li, Y.Y., Sailor, M.J. 2002, 'Vapor sensors based on optical interferometry from oxidized microporous silicon films', *Langmuir*, **18**: p. 2229-2233.
39. Gao, J., Gao, T., Sailor, M.J. 2000, 'Porous-silicon vapor sensor based on laser interferometry', *Applied Physics Letters*, **77**: p. 901-903.
40. Harper, J., Sailor, M.J. 1997, 'Photoluminescence quenching and the photochemical oxidation of porous silicon by molecular oxygen', *Langmuir*, **13**: p. 4652-4658.
41. Lauerhaas, J.M., Sailor, M.J. 1993, 'Chemical modification of the photoluminescence quenching of porous silicon', *Science*, **261**: p. 1567-1568.
42. Xu, Z.Y., Gal, M., Gross, M. 1992, 'Photoluminescence studies on porous silicon', *Applied Physics Letters*, **60**: p. 1375-1377.
43. Chrsitman, K.L., Maynard, H.D. 2005, 'Protein micropatterns using a pH-responsive polymer and light', *Langmuir*, **21**: p. 8389-8393.
44. Harris, B.P., Kutty, J.K., Fritz, E.W., Webb, C.K., Burg, K.J.L., Metters, A.T. 2006, 'Photopatterned polymer brushes promoting cell adhesion gradients', *Langmuir*, **22**: p. 4467-4471.
45. Nakanishi, J., Kikuchi, Y., Takarada, T., Nakayama, H., Yamaguchi, K., Maeda, M. 2004, 'Photoactivation of a substrate for cell adhesion under standard fluorescence microscopes', *Journal of the American Chemical Society*, **126**: p. 16314-16315.
46. Gao, T., Gao, J., Sailor, M.J. 2002, 'Tuning the response and stability of thin film mesoporous silicon vapor sensors by surface modification', *Langmuir*, **18**: p. 9953-9957.

47. Ouyang, H., Christophersen, M., Viard, R., Miller, B.L., Fauchet, P.M. 2005, 'Moacroporous silicon microcavities for macromolecule detection', *Advanced Functional Materials*, **15**: p. 1851-1859.
48. Thrust, M., Schöning, M.J., Frohnhoff, S., Arens-Fischer, R., Kordos, P., Lüth, H. 1996, 'Porous silicon as a substrate material for potentiometric biosensors', *Measurement Science and Technology*, **7**: p. 26-29.
49. Betty, C.A., Lal, R., Sharma, D.K., Yakhmi, J.V., Mittal, J.P. 2004, 'Macroporous silicon based capacitive affinity sensor – fabrication and electrochemical studies', *Sensors and actuators B*, **97**: p. 334-343.
50. Lillis, B., Jungk, C., Iacopino, D., Whelton, A., Hurley, E., Sheehan, M.M., Splinter, A., Quinn, A., Redmond, G., Lane, W.A., Mathewson, A., Berney, H. 2005, 'Microporous silicon and biosensor development: structural analysis, electrical characterisation and biocapacity evaluation' *Biosensors and Bioelectronics*, **21**: p. 282-292.
51. Steinem, C., Janshoff, A., Lin, S.-Y., Völcker, N.H., Ghadiri, M.R. 2004, 'DNA hybridization-enhanced porous silicon corrosion: mechanistic investigations and prospect for optical interferometric biosensing', *Tetrahedron*, **60**: p. 11259-11267.
52. Chan, S., Horner, S.R., Fauchet, P.M., Miller, B.L. 2001, 'Identification of gram negative bacteria using nanoscale microcavities', *Journal of the American Chemical Society*, **123**: p. 11797-11798.
53. Dancil, K.S., Greiner, D.P., Sailor, M.J. 1999, 'A porous silicon optical biosensor: detection of reversible binding of IgG to a protein A-modified surface', *Journal of the American Chemical Society*, **121**: p. 7925-7930.
54. Bjorklund, R.B., Zangoie, S., Arwin, H. 1996, 'Color changes in thin porous silicon films caused by vapor exposure', *Applied Physics Letters*, **69**: p. 3001-3003.
55. Silverton, E.W., Navia, M.A., Davies, D.R. 1977, 'Three-dimensional structure of an intact human immunoglobulin', *Proceedings of the National Academy of Sciences of the United States of America*, **74**: p. 5140-5144.
56. Anglin, E.J., Schwartz, M.P., Ng, V.P., Perelman, L.A., Sailor, M.J. 2004, 'Engineering the chemistry and nanostructure of porous silicon Fabry-Pérot films for loading and release of a steroid', *Langmuir*, **20**: p. 11264-11269.

57. Föll, H., Christophersen, M., Carstensen, J., Hasse, G. 2002, 'Formation and application of porous silicon', *Materials Science and Engineering R*, **39**: p. 93-141.
58. Theiß, W. 1997, 'Optical properties of porous silicon', *Surface Science Reports*, **29**: p. 91-192.
59. Vinegoni, C., Cazzanelli, M., Pavesi, L. 2001, 'Porous Silicon Microcavities', Nalwa HS Ed., *Silicon based materials and devices volume 2: properties and devices*, Academica Press HSTC, USA, p. 123-192.
60. Bisi, O., Ossicini, S., Pavesi, L. 2000, 'Porous silicon: a quantum sponge structure for silicon based optoelectronics', *Surface Science Reports*, **38**: p. 1-126.
61. Borghesi, A., Guizzetti, G., Sassella, A., Bisi, O., Pavesi, L. 1994, 'Induction-model analysis of Si---H stretching mode in porous silicon', *Solid State Communications*, **89**: p. 615-618.
62. Borghesi, A., Sassella, A., Pivac, B., Pavesi, L. 1993, 'Characterization of porous silicon inhomogeneities by high spatial resolution infrared spectroscopy', *Solid State Communications*, **87**: p. 1-4.
63. Carter, R.S., Harley, S.J., Power, P.P., Augustine, M.P. 2005, 'Use of NMR spectroscopy in the synthesis of air- and water-stable silicon nanoparticles from porous silicon' *Chemistry of Materials*, **17**: p. 2932-2939.
64. Kazor, A., Gwilliam, R., Boyd, I.W. 1994, 'Growth rate enhancement using ozone during rapid thermal oxidation of silicon', *Applied Physics Letters*, **65**: p. 412-414.
65. Petrova-Koch, V., Muschik, T., Kux, A., Meyer, B.K., Koch, F., Lehmann, V. 1992, 'Rapid-thermal-oxidized porous Si-The superior photoluminescent Si', *Applied Physics Letters*, **61**: p. 943-945.
66. Jenison, R., La, H., Haeberli, A., Ostroff, R., Polisky, B. 2001, 'Silicon-based biosensors for rapid detection of protein or nucleic acid targets', *Clinical Chemistry*, **47**: p. 1894-1900.
67. Jenison, R., Yang, S., Haeberli, A., Polisky, B. 2001, 'Interference-based detection of nucleic acid targets on optically coated silicon', *Nature Biotechnology*, **19**: p. 62-65.
68. Bovaird, J.H., Ngo, T.T., Lenhoff, H.M. 1982, 'Optimizing the *o*-phenylenediamine assay for horseradish peroxidase: effects of phosphate and

- pH, substrate and enzyme concentrations, and stopping reagents', *Clinical Chemistry*, **28**: p. 2423-2426.
69. Childs, R.E., Bardsley, W.G. 1975, 'The steady-state kinetics of peroxidase with 2,2'-azino-di-(3-ethyl-benzthiazoline-6-sulphonic acid) as chromogen', *Biochemical Journal*, **145**: p. 93-103.
70. Frey, A., Meckelein, B., Externest, D., Schmidt M.A. 2000, 'A stable and highly sensitive 3,3',5,5'-tetramethylbenzidine-based substrate reagent for enzyme-linked immunosorbent assays', *Journal of Immunological Methods*, **233**: p. 47-56.
71. Josephy, P.D., Eling, T., Mason, R.P. 1982, 'The horseradish peroxidase-catalyzed oxidation of 3,5,3',5'-tetramethylbenzidine', *The Journal of Biological Chemistry*, **257**: p. 3669-3675.
72. Mesulam, M. 1978, 'Tetramethyl benzidine for horseradish peroxidase neurohistochemistry: a non-carcinogenic blue reaction-product with superior sensitivity for visualizing neural afferents and efferent', *The Journal of Histochemistry and Cytochemistry*, **26**: 106-117.
73. Mesulam, M., Hegarty, E., Barbas, H., Carson, K.A., Gower, E.C., Knapp, A.G., Moss, M.B., Mufson, E.J. 1980, 'Additional factors influencing sensitivity in the tetramethyl benzidine method for horseradish peroxidase neurohistochemistry', *The Journal of Histochemistry and Cytochemistry*, **28**: p. 1255-1259.
74. Metelitzka, D.I., Naumchick, I.V., Karasyova, E.I., Polozov, G.I., Shdyro, O.I. 2003, 'Inhibition of peroxidase-catalyzed oxidation of aromatic amines by substituted phenols', *Applied Biochemistry and Microbiology*, **39**: p. 352-362.
75. Porstmann, B., Porstmann, T., Nugel, E. 1981, 'Comparison of chromogens for the determination of horseradish peroxidase as a marker in enzyme immunoassay', *Journal of Clinical Chemistry and Clinical Biochemistry*, **19**: p. 435-439.
76. Romero, M.I., Romero, M.A., Smith, G.M. 1999, 'Visualization of axonally transported horseradish peroxidase using enhanced immunocytochemical detection: a direct comparison with the tetramethylbenzidine method', *The Journal of Histochemistry and Cytochemistry*, **47**: p. 265-272.
77. Sentchouk, V.V., Grintsevich, E.E. 2004, 'Oxidation of benzidine and its derivatives by thyroid peroxidase', *Biochemistry*, **69**: p. 201-207.

78. Hood, L.E., Weissman, I.L., Wood, W.B., Wilson, J.H. 1984, '*Immunology*', The Benjamin/Cummings Publishing Company, Inc., Menlo Park, California.
79. Product Information sheet for Tween<sup>®</sup> 20, Product number P7949, Retrieved on June 1, 2007 from [www.sigmaaldrich.com](http://www.sigmaaldrich.com).
80. Tarcha, P.J., Chu, V.P., Whittern, D. 1987, '2,3-diaminophenazine is the product from the horseradish-catalyzed oxidation of *o*-phenylenediamine', *Analytical Biochemistry*, **165**: p. 230-233.
81. Bystryak, S.M., Mekler, V.M. 1992, 'Photochemical amplification for horseradish peroxidase-mediated immunosorbent assay', *Analytical Biochemistry*, **202**: p. 390-393.
82. Whittle, J.D., Bullet, N.A., Short, R.D., Douglas, C.W.I., Hollander, A.P., Davies, J. 2002, 'Adsorption of vitronectin, collagen and immunoglobulin-G to plasma polymer surfaces by enzyme linked immunosorbent assay (ELISA)', *Journal of Materials Chemistry*, **12**: p. 2726-2732.